

# Effects of Twinning and Detwinning on the Mechanical Behavior of Mg and Mg-Gd Alloy at the Micron Scale

Vom Promotionsausschuss der  
Technischen Universität Hamburg  
zur Erlangung des akademischen Grades

Doktor-Ingenieur (Dr.-Ing.)

genehmigte Dissertation

von  
Mohammadhadi Maghsoudi

aus  
Teheran, Iran

2023

**Gutachter:**

Prof. Dr. Erica Lilleodden

Institute of Material Research, Materials Mechanics  
Helmholtz-Zentrum Hereon, Germany

Dr. Jon M. Molina-Aldareguia

IMDEA Materials Institute, Spain

Prof. Dr.-Ing. habil. Marcus Rutner

Institute of Metal and Composite Structures  
Hamburg University of Technology, Germany

**Vorsitzender des Prüfungsausschusses:**

Prof. Dr.-Ing. Norbert Huber

Institute of Materials Physics and Technology  
Hamburg University of Technology, Germany

**Tag der mündlichen Prüfung:**

28. Oktober 2022

**DOI:** <https://doi.org/10.15480/882.5052>

**ORCID:** <https://orcid.org/0000-0002-4133-1768>

**License:** This thesis is licensed under the Creative Commons License Attribution CC BY-NC-ND 4.0 (<https://creativecommons.org/licenses/by-nc-nd/4.0/>).

# Abstract

In addition to dislocation slip, deformation twinning also plays an important role in plasticity of magnesium (Mg). While there have been many numerical and experimental studies of various aspects of twinning in polycrystalline Mg, little has been done to understand the role of an individual twin, uncoupled from the effect of its grain neighborhood, on the deformation of Mg. For this kind of analysis, micromechanical characterization has a great advantage due its site-specific nature. Furthermore, twinning behavior can also be strongly influenced by the presence of alloying elements. In this work, the scientific objective was to understand how a single twin boundary can affect the concurrent slip activity during twinning and detwinning in two material systems: (i) pure Mg and (ii) Mg-4wt.% Gd binary alloy, where Gd solutes can segregate into twin boundaries upon thermal treatment. Such a comparison of the cases (i) and (ii) could answer the question of how solutes influence the twinning, detwinning and slip behavior at room temperature. To this end, microcompression experiments were performed on differently oriented micropillars in the two materials: slip-favored [0001] single crystals, twinning-favored  $[10\bar{1}0]$  single crystals, and detwinning-favored bicrystals including the both orientations.

Microcompression along with TEM observations confirmed that Mg [0001] single crystals, as reference, deform by a typical stair-case  $c$ -axis hardening flow curve which is mainly governed by (double) cross-slip of pyramidal  $\langle c + a \rangle$  dislocations. The  $[10\bar{1}0]$  single- and  $[0001]/[10\bar{1}0]$  bicrystalline micropillars underwent twinning and detwinning, respectively, leading to a reorientation into the nominal [0001] orientation. Further compression of the (de)twinning micropillars exhibited strong  $c$ -axis hardening with a considerably higher yield stress and strain hardening rate than the reference samples. TEM investigations highlighted a unique defect structure in the wake of a migrated twin boundary, comprised of a dense array of basal stacking faults (SFs) along with numerous dislocations both of which are considered as immobile and thus serve as a source for the observed (de)twinning-mediated hardening.

Mg-Gd micropillars with equal orientations as in the pure Mg were tested in the non-heat-treated alloy as well as after heat-treatment at 300°C for 3.5 hours. Alloying with Gd strengthened pyramidal slip and (de)twinning stress-strain characteristics. Such a solute strengthening found to be the highest for the detwinning mechanism in the heat-treated bicrystalline micropillars, where the pre-existing twin boundary was decorated with Gd after heating, as confirmed by STEM-EDS analysis. The comparison of the normalized resolved shear stresses at the onset of pyramidal slip and (de)twinning showed that the relative activity of these deformation modes is modified in the Mg-Gd system. The experimental results in this work suggest that the critical aspects regarding the twinning microstructure and the effects of solutes on concurrent slip and twinning must be included in any continuum-based modelling approach for understanding the deformation of Mg.

# Zusammenfassung

Neben dem Versetzungsgleiten spielt auch Verformungszwillingsbildung eine wichtige Rolle bei der Plastizität von Magnesium (Mg). Während es viele numerische und experimentelle Studien zu verschiedenen Aspekten der Zwillingsbildung in polykristallinem Mg gibt, wurde bisher die Rolle eines einzelnen Zwillings, losgelöst von der Wirkung seiner Kornumgebung, auf die Verformung von Mg wenig studiert. Dafür hat die mikromechanische Charakterisierung aufgrund ihrer ortsspezifischen Natur einen großen Vorteil. Darüber hinaus kann Zwillingsverhalten auch durch Legierungselemente stark beeinflusst werden. In dieser Arbeit war es das Ziel, zu verstehen, wie eine einzelne Zwillingsgrenze die gleichzeitige Gleitaktivität in zwei Materialsystemen beeinflussen kann: (i) reines Mg und (ii) Mg-4wt.% Gd binäre Legierung, in der sich gelöste Gd-Elemente bei thermischer Behandlung in Zwillingsgrenzen entmischen können. Dazu wurden Mikrokompressionsversuche an unterschiedlich orientierten Mikrosäulen der beiden Materialien durchgeführt: [0001] Einkristalle, die Gleiten, [10 $\bar{1}$ 0] Einkristalle, die Zwillingsbildung und Bikristalle, die beide Orientierungen beinhalten, die Entzwilligung begünstigen.

Mikrokompression zusammen mit TEM Untersuchungen bestätigten, dass sich die Mg [0001]-Referenzeinkristalle durch eine typische treppenförmige  $c$ -Achsenverfestigungs-Fließkurve verformen, die hauptsächlich durch Kreuzgleiten von pyramidalen  $\langle c + a \rangle$  Versetzungen bestimmt wird. Die [10 $\bar{1}$ 0]-Einkristall- und [0001]/[10 $\bar{1}$ 0]-Bikristall-Mikrosäulen unterlagen einer Zwillingsbildung bzw. einer Entzwilligung, was zu einer Umorientierung in eine [0001] nahe Orientierung führte. Eine weitere Kompression dieser Mikrosäulen zeigte eine starke  $c$ -Achsenverfestigung mit einer wesentlich höheren Fließspannung und Verfestigungsrate als bei den [0001] Referenzproben. TEM Untersuchungen zeigten eine einzigartige Defektstruktur im Gefolge einer migrierten Zwillingsgrenze, bestehend aus einer dichten Anordnung von basalen Stapelfehlern (SFs) zusammen mit zahlreichen Versetzungen, die beide als unbeweglich angesehen werden und somit als Quelle für die beobachtete Verfestigung dienen.

Mg-Gd Mikrosäulen wurden sowohl in der nicht wärmebehandelten Legierung getestet, als auch nach einer Wärmebehandlung bei 300°C für 3,5 Stunden. Die Legierung mit Gd verstärkte pyramidales Gleiten und das Zwillings-, und Entzwilligungs-Spannungs-Dehnungsverhalten. Eine solche Verstärkung durch gelöste Elemente wurde für den Entzwilligungs-Mechanismus in den wärmebehandelten bikristallinen Mikrosäulen am stärksten festgestellt, wo die bereits existierende Zwillingsgrenze nach dem Erwärmen mit Gd belegt wurde, was durch STEM-EDS-Analyse bestätigt wurde. Der Vergleich der normalisierten aufgelösten Schubspannungen zeigte, dass die relative Aktivität dieser Deformationsmodi im Mg-Gd-System verändert ist. Die Ergebnisse dieser Arbeit deuten darauf hin, dass die kritischen Aspekte in Bezug auf die Zwillingsmikrostruktur und die Auswirkungen von gelösten Elementen in jeden kontinuumsbasierten Modellierungsansatz zum Verständnis der Verformung von Mg einbezogen werden müssen.

# Contents

<b>1 Introduction</b>	<b>1</b>
1.1 Motivation and research objectives	1
1.2 Approach	4
<b>2 Fundamentals of slip and twinning in Mg</b>	<b>5</b>
2.1 Dislocation slip in Mg	5
2.1.1 The effect of solute elements on the slip activity	6
2.2 Deformation twinning in hcp metals	9
2.2.1 Crystallography of twinning	9
2.2.2 $\{10\bar{1}2\}$ twinning mechanisms: Classical twinning dislocations vs. atomic shuffling	12
2.3 Overview on micromechanics of twinning	16
<b>3 Materials, experimental methods and analysis</b>	<b>19</b>
3.1 Materials	19
3.2 Preparation and processing of bulk polycrystals	20
3.2.1 Thermal processing	21
3.3 Fabrication and testing of micron-sized samples	22
3.3.1 Focused ion beam (FIB) microscopy	22
3.3.2 Micropillar fabrication	22
3.3.3 Microcompression testing	24
3.3.4 Schmid factor and the required stress to initiate slip	25
3.4 Post-mortem characterization of micron-sized samples	26
3.4.1 FIB lift-out technique	26
3.4.2 Electron backscatter diffraction (EBSD)	27
3.4.3 Transmission electron microscopy (TEM)	29
<b>4 Influence of twinning and detwinning on the <math>[0001]</math> compression response in pure Mg</b>	<b>35</b>
4.1 Experimental details	35

4.2	Microcompression of [0001] single crystals	38
4.3	Microcompression of [1010] single crystals	46
4.4	Microcompression of [0001]/[1010] bicrystals	59
4.5	The impact of twinning defect structure on the subsequent <i>c</i> -axis hardening	66
4.6	Chapter summary	74
<b>5</b>	<b>Twinning and detwinning in Mg-4.7 wt.% Gd alloy</b>	<b>77</b>
5.1	Experimental details	77
5.2	Solute segregation at {1012} twin boundary	78
5.3	Microcompression of [0001] single crystals	82
5.4	Microcompression of [1010] single crystals	83
5.5	Microcompression of [0001]/[1010] bicrystals	86
5.6	Chapter summary	89
<b>6</b>	<b>A comparison of the microcompression results in pure Mg and Mg-4.7 wt.% Gd alloy</b>	<b>91</b>
6.1	Effect of Gd solutes on the [0001] compression response	91
6.2	Effect of Gd solutes on the [1010] compression response	94
6.3	Effect of Gd solutes on the [0001]/[1010] compression response	97
6.4	Effect of Gd solutes on the relative activities of slip and twinning	98
6.5	Chapter summary	100
<b>7</b>	<b>Concluding remarks and future directions</b>	<b>103</b>
7.1	Concluding remarks	103
7.2	Future directions	104
<b>8</b>	<b>Bibliography</b>	<b>106</b>
<b>A</b>	<b>Appendix</b>	<b>121</b>
A.1	Conversion from Miller-Bravais notation to orthonormal coordinate system	121
A.1.1	Transformation of directions (shear)	122
A.1.2	Transformation of plane normals	122
A.2	Schmid factor for different slip and twinning systems	123
<b>B</b>	<b>Curriculum vitae</b>	<b>125</b>

# 1 Introduction

## 1.1 Motivation and research objectives

Metals with a hexagonal close-packed (hcp) crystal structure, are widely used as structural materials in industries due to their low density and relatively high specific strength [1]. In this sense, magnesium (Mg) alloys offer a great weight saving potential, as they are up to 37% lighter than aluminum (Al) while maintaining an excellent strength to weight ratio [2]. Accordingly, Mg alloys have attracted increasing attention as one of the best metallic lightweight candidates in the automotive industry, where weight reduction is a top priority in order to decrease the fuel consumption and the corresponding  $CO_2$  emissions [3]. Such a valuable investment on Mg alloys, also, takes advantage of the easy machining at low cutting speeds, easy castability and the improved recycling capabilities [4, 5]. However, the goal of widespread adoption and replacement of conventionally used materials such as steel and Al with Mg products has been restricted because of the challenges associated with the limited formability at low temperatures, corrosion resistance and high temperature applications of these materials [6]. The challenging issues related to the weak formability of Mg alloys arise mostly from their hcp crystallographic structure, which holds a reduced number of available deformation modes at room temperature compared to body-centered cubic (bcc) and face-centered cubic (fcc) structures. This originates from the ability of close-packed shear deformation modes occurring at room temperature to only provide plasticity on the basal plane. Deformation mechanisms that supply out of basal plane deformations are critically important.

Due to the scarcity of easy dislocation glide systems,  $\{10\bar{1}2\}$  deformation twinning (also known as mechanical twinning) plays an important role in the room temperature plastic deformation of Mg [7]. The boundaries of a  $\{10\bar{1}2\}$  twin are generally mobile under straining, which appears as either thickening or shrinkage of the twin depending on the direction of loading. Detwinning is associated with the shrinkage of existing twin bands under reverse loading [8, 9]. It has been generally accepted that under twinning-dominated deformation, the yielding is governed by the twin nucleation, propagation and growth, whereas further plastic deformation proceeds with dislocation slip within the twinned grains. To understand the twinning mechanisms, numerous numerical and experimental works have studied various aspects of twinning in polycrystalline Mg, such as twin transmission across grain boundaries [10, 11], local stress fields around twins [12], twin-twin interactions [13, 14] and interfacial structure of twin boundaries [15]. Comparatively, little is known about the impacts of twinning on the subsequent mechanical response. In this regard, some researchers have reported an

increased strain hardening rate after primary twinning [16, 17]. On the contrary, it has been argued that profuse twinning has little or no effect on the overall strain hardening behavior of Mg polycrystals [18, 19]. Common to all of these works is that the reported mechanical properties associated with twinning (or detwinning) is influenced by the polycrystallinity of the samples. In this macroscale testing scheme, neighboring grains lead to variations in the stress field and deformation constraints. Accordingly, due to the unknown local stress state at the respective twins in a polycrystalline sample, a true assessment of mechanical characteristics associated with twinning alone should be carried out where an individual twin can be isolated.

Recent technological developments such as the widespread application of focused ion beam (FIB) microscopes have significantly facilitated specimen fabrication and testing at small length scales. Uchic et al. [20] developed the microcompression testing methodology for the direct measurement of stress-strain behavior in volumes of materials that have microscale dimensions. The methodology consists of machining of micron-sized samples via the FIB and testing these samples in uniaxial compression using a commercial nanoindentation system equipped with a flat punch [21]. Advantages of testing at this scale include the ability to probe mechanical properties of site-specific single- and bicrystalline grains in a bulk polycrystalline sample. The method can thus be used to systematically investigate the mechanical response and the corresponding microstructures associated with individual slip and twinning mechanisms in the compressed volumes, which is isolated from the collective response of several grains in a typical polycrystalline aggregate.

Addition of rare-earth (RE) solute elements to Mg alloys has attracted considerable attention driven mainly by their improved mechanical properties including enhanced ductility, higher specific strength and excellent creep resistance [22, 23]. Due to the large atomic size and wide solubility in Mg, RE elements are effective solution strengthening constituents and contribute more to the material strength than other alloying additions used in conventional Mg alloys [22]. The material's increased strength is often associated with improved workability at room and elevated temperatures, adding to the favorable combination of alloy properties. Such a desirable combination of strength and ductility is considered as an important advantage of using RE elements which is manifested by their influence on the material's texture [22, 24]. Gadolinium (Gd) is one of the most effective solution strengthening elements in Mg-RE alloys [23]. Recent works on Mg-Gd alloys has revealed strong segregation of Gd to grain and twin boundaries [25, 26]. Deformation mechanisms, and in particular, twinning behavior can be strongly influenced by the Gd solute segregation. Using atomic-resolution transmission electron microscopy (TEM), Nie et al. [26] recently found that after annealing a pre-compressed polycrystalline sample, the generated twins were decorated by a periodic distribution of Gd-rich columns at the boundary. The mobility of such Gd-decorated twin boundaries was examined under further compression and it was found that the solute segregation provides a pinning effect on twins leading to a restricted twin growth during reloading. The observation highlights an important role that Gd solute element plays in the deformation response of Mg alloys. Most of the studies of the effect of Gd on the mechanical properties of

Mg alloys available in the literature have been carried out at the macroscopic level [23, 27, 28].

In general, the objective in this work was to understand how twinning and detwinning affect the concurrent slip activity in Mg and Mg alloys. More specifically, the goal was to examine the micromechanical response associated with twinning, detwinning and pyramidal slip in two material systems: (i) a pure Mg and (ii) a Mg-4.7 wt.% Gd binary alloy. For the microcompression experiments ran on the pure Mg, the key questions were:

- How the stress-strain response of [0001] single crystals, dominated by pyramidal slip, is affected by twinning and detwinning
- What is the specific defect structure in the wake of a migrating twin
- What is the relationship between the (de)twinning structure and the hardening response of pyramidal dislocations

For the Mg-4.7 wt.% Gd alloy, the experiments were particularly designed to:

- Characterize the potential segregation of Gd solutes into  $\{10\bar{1}2\}$  twins during heat-treatment
- Study the micromechanical response of twinning and detwinning in terms of the twin boundary structure
- Examine the post-twinning hardening behavior of the [0001] single crystals in the solid-solution

Finally, a comparison of the results obtained from the microcompression experiments performed on the pure Mg and Mg-Gd alloy enabled us to study how Gd solutes serve to influence the twinning, detwinning and pyramidal slip mechanisms.

Accordingly, the thesis is structured as follows: Chapter 2 briefly introduces fundamentals of plasticity and twinning in Mg. Particular focus is on the current understanding of the  $\{10\bar{1}2\}$  twinning mechanisms and the published data on the impact of solute elements on the slip and twinning activity in Mg alloys. The used materials, experimental methods and results analysis are described in Chapter 3. After the compositional analysis of the pure material and the alloy, the methods of preparation and processing of bulk polycrystals and the techniques used for fabrication and testing of micron-sized samples are described in this chapter. This covers details of the microcompression tests and post-mortem microstructural characterizations including FIB lift-out technique, electron backscattered diffraction (EBSD) and TEM. In addition, analytical approaches to analyse the experimental results are given in this chapter. Chapter 4 presents microcompression experiments in pure Mg. The results of microcompression testing are discussed to investigate the impact of  $\{10\bar{1}2\}$  (de)twinning-inherited defect substructure on the subsequent pyramidal slip. The chapter includes an analysis of the mechanical characteristics such as the yield stress and strain hardening rate, which are extracted from the stress-strain curves of each orientation. The mechanical results

will be discussed based on the EBSD and TEM microstructural observations on the FIB cross-sections of the compressed micropillars. Using the same set of orientations, Chapter 5 discusses the twinning and detwinning response in the Mg-4.7 wt.% alloy. The chapter points to an important role that changing of the twin boundary structure from a solute-free state (before heat-treatment) to a Gd-rich boundary (after heat-treatment) might play in the micromechanics of the  $\{10\bar{1}2\}$  twin. Chapter 6 provides a comparison of the microcompression results in the pure Mg and Mg-Gd solid solution to examine the effects of Gd solutes on the plasticity mechanisms occurring in the micropillars. Final concluding remarks and directions for future works based on the open questions from the current work that require further investigations are proposed in Chapter 7.

## 1.2 Approach

The experiments started with homogenization and then macro-scale compression of a polycrystalline pure Mg and a Mg-4.7 wt.% Gd alloy to produce deformation twins in the grains of interest. Single- and bicrystals of  $[0001]$ ,  $[10\bar{1}0]$  and  $[0001]/[10\bar{1}0]$  orientations, that are targeted for activating respectively pyramidal slip, twinning and detwinning mechanisms selected in the polycrystals of both materials. Using FIB milling, cylindrical micropillars were machined in the selected grains. Bicrystalline micropillars were fabricated at the twin boundary areas, where a single twin can be included inside the pillars. Uniaxial compression tests were performed on a statistically reliable number of micropillars using microcompression testing approach. For the Mg-Gd alloy, micropillar fabrication and microcompression tests were also carried out on the same grains after heat-treating the polycrystal. The aim was to investigate the effect of heat-treatment on the twin boundary structure.

The entire compression volumes were characterized post-mortem. In order to examine the post-deformation structures, FIB lift-out technique was used to take out lamellae from the compressed micropillars. Microstructural characterizations were then carried out on the lifted-out lamellae using EBSD and TEM. The crystallographical information obtained from the EBSD measurements were used to quantify the local deformation inside the compressed micropillars via different misorientation angle distribution analyses. To further analyse the defect structures, TEM observations were conducted using scanning transmission electron microscopy (STEM) technique under various two-beam diffraction conditions. In addition, high-angle annular dark-field (HAADF) imaging mode in STEM combined with energy dispersive spectroscopy (EDS) was used to study the twin boundary structures and examine the potential segregation of Gd solutes into the twin boundaries in the Mg-Gd solid solution after heat-treatment. The results obtained from the microstructural observations were used to establish a characteristic defect structure inherited from twinning and detwinning and to link this microstructure to the corresponding stress-strain behavior of the compressed micropillars in the two material systems.

## 2 Fundamentals of slip and twinning in Mg

Understanding plastic deformation in Mg is particularly complex as a result of the large anisotropy of active deformation modes. Different dislocation slip and twinning systems can be activated on various planes and directions to provide plasticity. The contribution of slip and twinning modes to the total plastic strain is largely affected by the crystal orientation and the presence of alloying constituents. Therefore, it is crucial to review the basics of slip and twinning systems in this chapter. More specifically, the effect of alloying elements on the slip and twinning activity are important to be covered, as they will be later referred in this thesis for discussing the discrepancies in the mechanical behaviors of pure Mg and Mg-Gd alloy systems. In order to give the reader an idea about the position of the current work in the context of micromechanics of slip and twinning, an overview of the available literature will be summarized, and the relevant lack-of-knowledge will be accordingly highlighted.

### 2.1 Dislocation slip in Mg

Dislocation slip and deformation twinning are the two fundamental modes by which hcp metals can deform plastically. Slip happens when crystal planes glide past each others through passage of dislocations on well-defined glide planes. The most commonly observed slip systems in Mg are summarized in [Figure 2.1](#). The three modes of basal  $\{0002\}\langle 11\bar{2}0\rangle$ , prismatic  $\{1\bar{1}00\}\langle 11\bar{2}0\rangle$ , and pyramidal  $\{1\bar{1}01\}\langle 11\bar{2}0\rangle$  slip systems have a Burgers vector along the  $\langle a \rangle$  direction. These slip systems lack a  $\langle c \rangle$  component in their Burgers vector and therefore are not able to provide any axial strain. First-order pyramidal ( $\pi 1$ )  $\{1\bar{1}01\}\langle \bar{2}113\rangle$ , and second-order pyramidal ( $\pi 2$ )  $\{2\bar{1}\bar{1}2\}\langle \bar{2}113\rangle$  systems having a  $\langle c + a \rangle$  Burgers vector can accommodate deformation along the crystal  $c$ -axis ( $[0001]$ ).

However, these pyramidal  $\langle c + a \rangle$  slip systems are very difficult to activate at room temperature due to their relatively high values of critical resolved shear stress (CRSS) compared to the easy basal slip system. The CRSS for dislocation slip in the basal slip system for pure Mg is about 0.5 MPa, whereas pyramidal systems possess high CRSS values of about 80 MPa [\[29, 30\]](#). According to the Taylor [\[31\]](#) criterion, the general homogeneous plastic deformation in polycrystals requires five independent slip systems. The basal slip only provides 2 independent slip systems [\[32\]](#) and the CRSS value for the first-order and second-order pyramidal systems that can fulfill the Taylor criterion is relatively large. Consequently, the large differences in the CRSS values to activate dislocation slip can lead to a strong anisotropy of the active deformation systems and thus the poor formability at room temperature. A promising strategy to reduce the mechanical anisotropy is the balancing of the CRSSs of the different slip systems

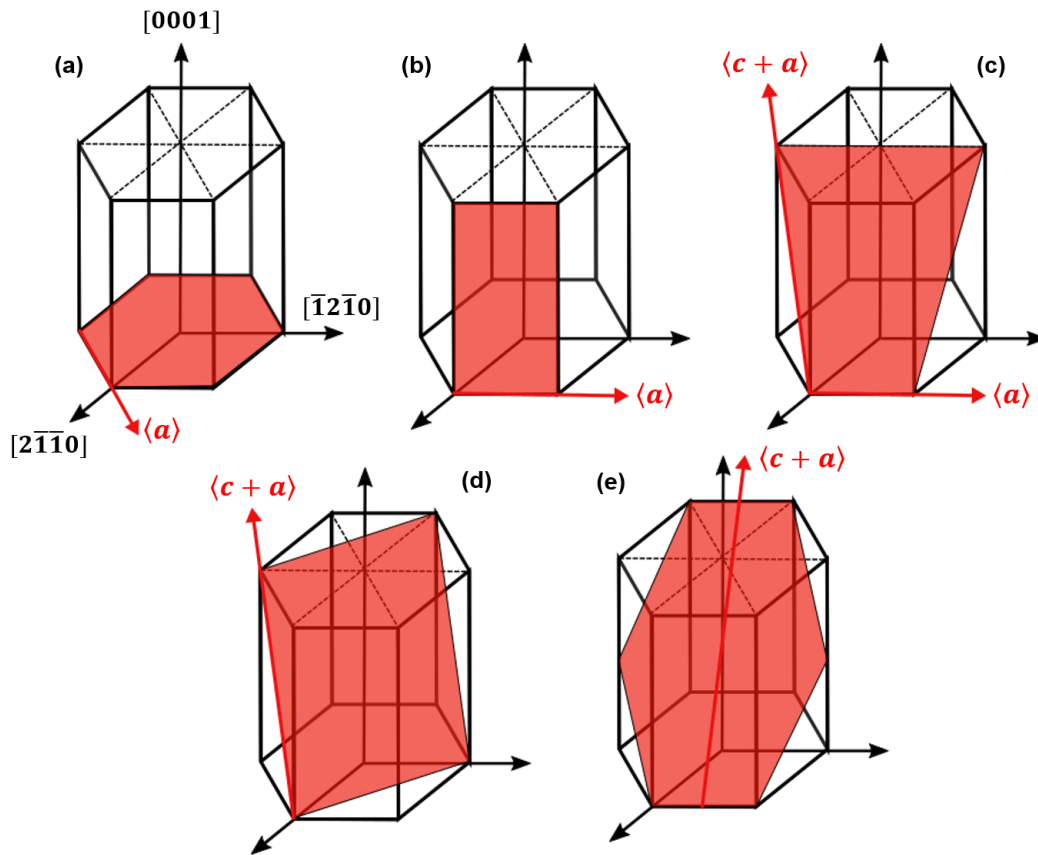


**Figure 2.1.** The common slip and twinning systems in hcp Mg. (a)  $\{0002\}\langle 11\bar{2}0 \rangle$  basal slip, (b)  $\{11\bar{0}0\}\langle 11\bar{2}0 \rangle$  prismatic slip, (c)  $\{11\bar{0}1\}\langle 11\bar{2}0 \rangle$  and  $\{11\bar{0}1\}\langle \bar{2}113 \rangle$  pyramidal slip, (d)  $\{2\bar{1}\bar{1}2\}\langle \bar{2}113 \rangle$  second-order pyramidal slip and (e)  $\{1012\}\langle 101\bar{1} \rangle$  extension twinning. The slip planes and shearing directions are shown in red color.

by reducing the differences in the CRSS values between the basal and non-basal slip systems, as they generally scale as  $CRSS_{basal} < CRSS_{twinning} < CRSS_{prismatic} < CRSS_{pyramidal}$  [24]. The addition of solid solution elements, in particular rare-earth (RE) elements, has been shown to be a convenient approach to achieve this goal through the strengthening of basal slip or softening of pyramidal slip systems [33–35]. The effect of solute atoms on the CRSS of  $\langle a \rangle$ -type basal and prismatic slip as well as  $\langle c+a \rangle$ -type pyramidal slip has been documented in the following section.

### 2.1.1 The effect of solute elements on the slip activity

Early works by Akhtar and Teghtsoonian [36, 37] have investigated the effects of Al and Zn solutes in Mg alloy single crystals oriented for basal and prismatic slip. For the case of basal slip, the CRSS of Mg-Zn alloy increased with Zn concentration. After separating the CRSS into an athermal and a thermally activated component, the authors ascribed the solute hardening of the basal slip to the increased athermal stress component of the CRSS, since the thermally activated component is very small at room temperature [36]. The increased

athermal stress arises from an increased long range stress field at the presence of Zn solutes and also an increase in the friction stress involving elastic and modulus interactions [36]. In line with this work and characterized at a smaller length scale, the solute hardening of basal slip was recently assessed using an experimental methodology based on the diffusion-couples and micromechanical testing in Mg-Al and Mg-Zn alloys [33]. Compression of single crystalline micropillars showed that the solid solution strengthening of basal slip follows a  $Kc^{2/3}$  model, where  $K$  is a constant depending on the alloying element and temperature, and  $c$  is the solute element content in atomic percent. For the case of prismatic slip, tensile tests showed that the CRSS decreases continuously with increasing the concentration of Zn and Al solutes [37]. In hcp metals, the axial ratio,  $c/a$ , where  $a$  and  $c$  are the lattice constants, affects the difference in the CRSS between the basal and the non-basal slips [32]; namely, a reduction in the  $c/a$  ratio enhances the activity of non-basal slips [38]. Accordingly, it has been the conclusion of Hauser and his coworkers [39] that only those elements which decrease the  $c/a$  ratio of Mg would be effective in decreasing the room temperature CRSS for prismatic slip. However, the axial ratio remained unaffected by Zn addition while it increased due to alloying with Al, yet both these elements were effective in lowering the room temperature CRSS of prismatic slip [37]. The solute softening of prismatic slip is attributable to the effect that solutes have on the ease of dislocation cross slip. Solute can improve the ability of dislocations to form a jog-pair, and this is likely to be the reason that solute softening is observed [37, 40].

Addition of RE elements has been shown to promote non-basal slip systems in Mg at room temperature [35, 38, 41-43]. The origin of the increased non-basal dislocation activity is generally linked with the alteration of the CRSS of non-basal slip systems. The actual mechanisms that have been proposed for the higher activity of certain deformation modes out of the basal plane include changes in the (i)  $c/a$  ratio, (ii) modified Peierls potentials and (iii) changed stacking fault energies (SFEs) [42, 43]. Considering the axial ratio effects, Yttrium (Y) is capable of decreasing the  $c/a$  ratio and thus stimulating the activation of non-basal slip systems [38]. Contradictory to this report, the lattice parameters of pure Mg and Mg-Y alloys were measured using synchrotron radiation by Sandlöbes et al. [42] and a slightly decreasing tendency of the  $c/a$  ratio was found with increasing Y content. The change in the axial ratio was almost negligible and therefore it was concluded that there is no direct connection between changes in the slip activity and the  $c/a$  ratio in Mg alloyed with RE elements. Similar conclusion was made in Cerium (Ce)-containing Mg alloys, where very small Ce addition had no effect on the  $c/a$  ratio, but it had an effect on the enhancement of non-basal slips [41, 44].

The Peierls potential describes the energy required to move a dislocation from one stable position to the next. Density functional theory (DFT) calculations by Tsuru et al. [45] showed that the use of an Y solution results in an alteration in the dislocation core structure and lubrication of the dislocation motion on non-basal planes. This was attributed to the reduced Peierls stresses with higher Y concentrations and therefore a softening effect of solid solution on plastic deformation in Mg alloys. Consistently, the enhanced activity of pyramidal dislocation slip in Mg-Y could, in principle, be a result of a decreased Peierls potential on the

pyramidal planes or increased Peierls potential on the basal planes through the addition of Y [42]. Nevertheless, the increased activity of compression and secondary twins in the cited work could not be explained by the changed Peierls potentials, because activation of these twins is related to the activation of twinning dislocations, which are only minorly influenced by the Peierls potential. It is therefore important to consider other materials characteristics that are critical for the enhanced non-basal slip activity, such as the SFEs.

It is assumed that RE elements can influence the SFE of certain types of dislocations. The modified SFE would also affect the CRSSs associated with competing slip/twinning mechanisms and hence their relative contributions to the overall deformation. Details have been revealed by TEM and SEM microstructural observations, as well as by *ab initio* calculations on the effects of RE elements on the SFE of different  $\langle a \rangle$  and  $\langle c + a \rangle$  dislocation types [42, 46, 47]. Microstructural examinations through TEM combined with EBSD slip trace analysis showed frequent activation of pyramidal  $\langle c + a \rangle$  dislocations in Mg-Y alloys [42]. The observed higher activity of  $\langle c + a \rangle$  dislocations has been also reported for Mg-Li alloys (a non-RE solid solution) [48]. The high pyramidal activity in Mg solid solutions has been accompanied by large amounts of stacking faults, while in the pure Mg stacking faults were observed only inside twins [42]. The same observation was reported for recrystallized and then slightly deformed specimens of other RE-containing Mg-3Er, Mg-3Tb, Mg-3Ho and Mg-3Dy alloys [46]. TEM examinations showed also wide splitting of the partial dislocations bounding the stacking faults. From the high density and widths of the observed stacking faults, it has been concluded that the SFEs are reduced compared to pure Mg in all Mg solid solutions studied. Therefore, since the stacking faults provide sessile defect structures on both, basal and pyramidal planes, in the light of the experimentally observed reduced SFEs it is assumed that the sessile stacking faults act as the heterogeneous source for the enhanced  $\langle c + a \rangle$  dislocation activity in Mg alloys. Understanding why RE elements cause the observed reduction of the SFE in Mg has been possible using quantum mechanical calculations.

With the advent of high-performance computing and efficient techniques to deal with the long-range elastic fields of dislocations, it is now possible to compute geometric and electronic effects of RE elements on the SFE using *ab initio* quantum mechanical calculations based on the DFT [46, 49]. Within the presented *ab initio* calculations the origin of the reduction in SFE in Mg-RE alloys was revealed to be a complex interplay of the solutes acting in a number of manners on the internal materials characteristics [46]. The effect is therefore due to the combination of thermodynamic, structural and energetic (elastic energy) contributions. The fundamental atomistic parameters associated with these structural, thermodynamic and energetic parts of the SFE in solid-solution systems are related to the atomic radius, the electronegativity and the bulk modulus difference of Mg and the solutes. The atomic radius determines the contributions of structure, electronegativity (both structural and thermodynamic), and bulk modulus to the (elastic) energetic component of the SFE. Theoretical analysis confirmed by experimental observations showed that the SFE and all these parameters contributing to the value of this energy are reduced in Mg with RE additions. Accordingly, the structure of the stacking faults is effectively thermodynamically destabilized with respect

to the hcp phase, and it is thus made structurally and elastically better matching the hcp matrix surrounding the stacking fault. The combination of these phenomena is proposed to be the underlying mechanism for the theoretically and experimentally observed reduction in the SFE [46].

In light of the literature reviewed here, there is a consensus on the effect of solute elements (mostly RE elements) in promoting  $\langle c + a \rangle$  and prismatic slip, which is attributed to a change in the stacking fault energy on non-basal planes, and a mitigation of dislocation motion and ability to cross slip as solutes diffuse in dislocation cores. At the macroscopic level, these solutes-induced modifications makes most wrought Mg alloys with proper additions of RE elements to exhibit improved ductility, reduced anisotropy, and thereby enhanced formability [24, 41, 43]. On the importance of such an improvement in the material properties at the presence of solutes, it is worth mentioning that researchers use the SFE of Mg solid solutions systematically as a guiding parameter for the design of a general class of ductile Mg alloys. Based on *ab initio* predictions of the SFEs, promising alloys, i.e. those characterized by a modified SFE and enhanced room-temperature ductility, can be practically produced [46].

## 2.2 Deformation twinning in hcp metals

### 2.2.1 Crystallography of twinning

In addition to dislocation slip, twinning is another important deformation mechanism in hcp metals. A deformation twin is a region of a grain that has experienced a homogeneous shape change in such a way that the twinned domain possesses the same crystalline structure as the matrix domain but of a different orientation. What differentiates a twin from a grain boundary is the specific boundary misorientation between the adjacent grains. In the classical theory of deformation twinning which has been comprehensively reviewed by Christian and Mahajan [50], the parent lattice is reoriented by atom displacements which are equivalent to a simple shear of the lattice points. Two planes remain undistorted (or invariant) by the action of this homogeneous shear, see Figure 2.2 reproduced from [50].

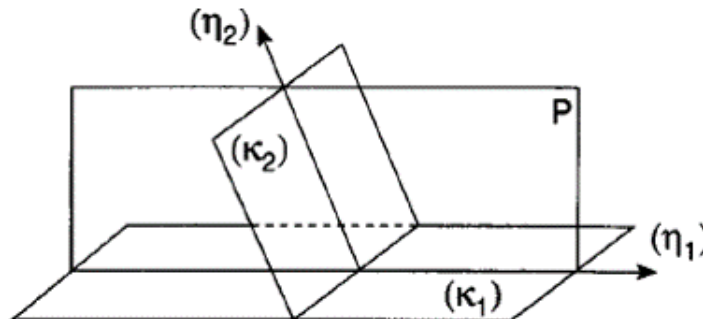


**Figure 2.2.** Schematic representation of the four twinning elements. The twinning plane and its conjugate (reciprocal) are  $K_1$  and  $K_2$ . The twinning shear direction and its conjugate are  $\eta_1$  and  $\eta_2$ . The plane of shear,  $P$ , contains all the twinning directions ( $\eta_1$  and  $\eta_2$ ) and the normals of the twinning planes ( $K_1$  and  $K_2$ ). The image is reused from [50] with permission from Elsevier.

The first invariant plane is called  $K_1$ . The twinning shear on this plane is along the  $\eta_1$  direction. The second undistorted (or conjugate) plane is  $K_2$ . This plane contains the reciprocal twinning direction (conjugate shear direction) along  $\eta_2$ . The plane of shear is denoted here by  $P$ . This plane contains the shear direction  $\eta_1$  and the normal to  $K_1$ . The plane  $P$  intersects the second invariant twinning plane,  $K_2$ , along the  $\eta_2$  direction. The two planes  $K_1$  and  $K_2$ , and the twinning directions  $\eta_1$  and  $\eta_2$ , together with the plane of shear are collectively termed as the twinning elements [51]. Obviously, among the four elements,  $K_1$  and  $\eta_2$  or  $K_2$  and  $\eta_1$  can be independent. Twinning causes a sphere to become an ellipsoid and this shape change can be conveniently illustrated by sections parallel to a plane of shear. This is shown schematically in Figure 2.3 [52], where a sphere of crystalline material undergoes a twinning shear in the direction  $\eta_1$ .

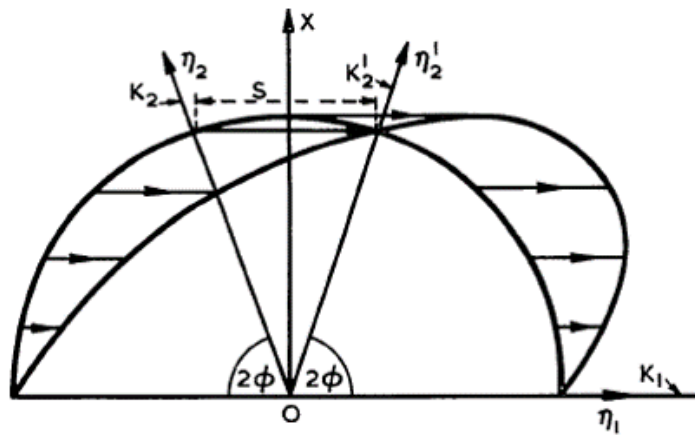


**Figure 2.3.** Schematic illustration of conversion of a sphere into an ellipsoid by the twinning shear  $S$  along  $\eta_1$  direction. Section is parallel to the plane of shear.  $S$  is the magnitude of shear. The image is reused from [52] with permission from Taylor & Francis.

The sphere is transformed into an ellipsoid by the shear, the origin of the orthogonal axes in the figure being taken as the center of both sphere and ellipsoid. The angle between the  $K_1$  twinning plane and its conjugate,  $K_2$ , is  $2\phi$ . While the twinning plane  $K_1$ , containing the twinning shear direction  $\eta_1$ , does not change its position,  $K_2$  is displaced to  $K_2'$  by the twinning shear,  $S$ . The lines of intersection of the plane of shear with  $K_2$  and  $K_2'$  are  $\eta_2$  and  $\eta_2'$ , respectively. The twinning shear,  $S$ , is related to the acute angle ( $2\phi$ ) between  $K_1$  and  $K_2$  and is given by  $S = 2\cot(2\phi)$  [51, 52]. The magnitude of twinning shear for a specific twinning mode is determined by the  $c/a$  ratio of the hcp crystal [52]. The most predominant twinning mode for most hcp materials at room temperature is  $K_1 = \{10\bar{1}2\}$ ,  $\eta_1 = \langle 10\bar{1}1 \rangle$  and  $P = \{11\bar{2}0\}$ . The elements of this twinning mode are illustrated in Figure 2.4.

The twinning shear for this mode is written as  $(\gamma^2-3)/\gamma\sqrt{3}$  [7], where  $\gamma = c/a$ . For Mg with  $c/a = 1.624$  [52], this type of twinning is called ‘extension twinning’; elongating the crystal  $c$ -axis under tension along the  $c$ -axis or compression perpendicular to the  $c$ -axis. The extension twinning shear equals to 0.129 resulting in a lattice reorientation of about  $86^\circ$ . In addition to extension twinning, there are also other twinning modes available in Mg either on  $K_1 = \{10\bar{1}1\}$  or on  $K_1 = \{10\bar{1}3\}$  twinning planes (see Figure 2.4). These twinning

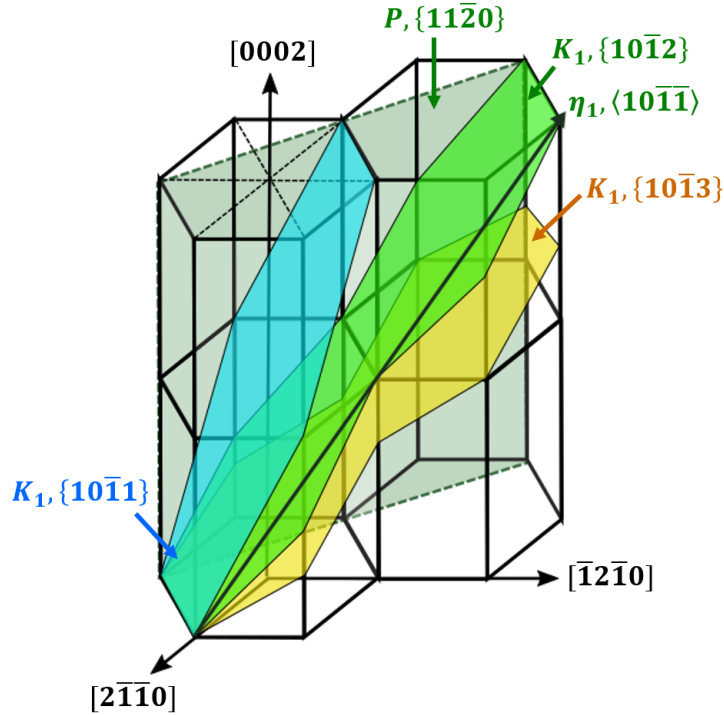


**Figure 2.4.** Crystallographic planes and directions corresponding to different twinning modes in Mg. Extension twinning is shown in green with twinning plane  $K_1 = \{10\bar{1}2\}$ , shear direction  $\eta_1 = \langle 10\bar{1}\bar{1} \rangle$  and plane of shear  $P = \{11\bar{2}0\}$ . Contraction twinning modes are denoted either on blue with  $K_1 = \{10\bar{1}\bar{1}\}$  or on yellow with  $K_1 = \{10\bar{1}\bar{3}\}$ .

modes are known as ‘contraction twins’ in Mg which are activated under compressive load parallel to the  $c$ -axis and can accommodate the associated strain. The twinning shear for these contraction modes is written as  $(4\gamma^2-9)/4\gamma\sqrt{3}$  [7]. The twinning shear resulting from this twinning type is therefore 0.138, higher than that for extension twinning. Accordingly, contraction twinning might contribute more effectively in plastic deformation than extension twinning, however, since the CRSS for contraction twinning is quite high, 76-153 MPa [53], compared to the CRSS for extension twinning, 2-3 MPa [53], a higher resolved shear stress is required to activate contraction twinning at room temperature. This fact makes them less observed than extension twins in deformed structures.

The deformation processes of twinning and detwinning are schematically illustrated in a single crystalline domain in Figure 2.5. A twin-free domain is shown in Figure 2.5(a) which is referred to as ‘matrix’. The dashed blue lines represent the basal planes of the matrix. Under a tensile stress along the  $c$ -axis of the matrix crystal and when the resolved shear stress reaches the CRSS for  $\{10\bar{1}2\}$  twinning, the grain starts twinning and is then split into a twinned domain (red dashed lines), and the original untwinned matrix, as is depicted in Figure 2.5(b). At the twin boundaries, which are shown by solid green lines, the basal planes of the matrix and the twin are mirrored. After nucleation of the twin in the matrix, Figure 2.5(b), the twinned crystal has two potential operations associated with twin growth or detwinning. Figure 2.5(c) shows the growth of the nucleated twin into the matrix. This

occurs when the sign of the resolved shear stress is the same as the initial loading required for nucleating the twin. The twin will then thicken by the migration of the twin boundaries via the glide of twinning dislocations. The volume fraction of the twinned region will therefore increase. Once the stress is applied in the reverse direction, detwinning can occur, as is sketched in Figure 2.5(d). Detwinning (also known as untwinning) is associated with the disappearance of existing twin bands under reverse loading. The crystal deformation process of detwinning is similar to twinning, although nucleation is not required [8]. It is a shrinkage of the already propagated twin and simply means that the twin boundaries retreat from the matrix into the twin. Hence, the twin volume fraction decreases.

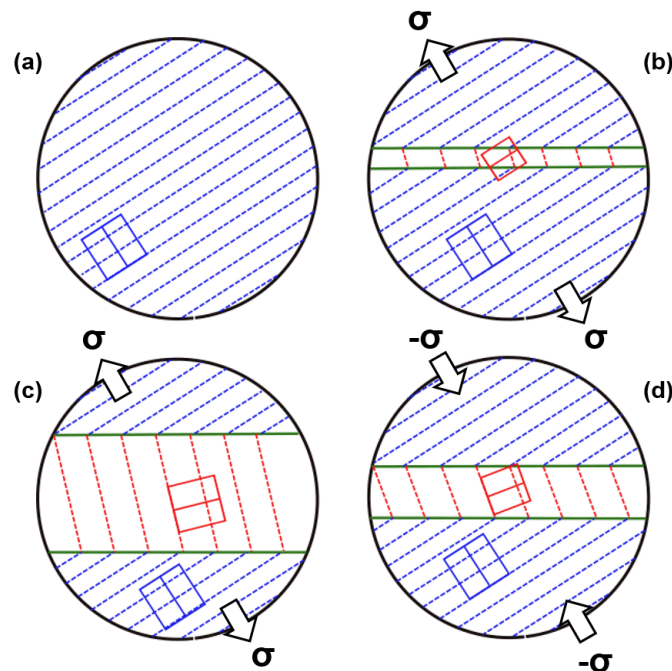


**Figure 2.5.** Schematic representation of  $\{10\bar{1}2\}$  twinning and detwinning in a single crystalline grain. (a) The grain is free of any twin and is referred to as the ‘matrix’ in the text. The blue dashed lines show the basal planes of the matrix. (b) The matrix undergoes twin nucleation resulting in splitting the crystal into the twinned domain (red lined) and the original matrix (blue lined). Solid green lines show the twin boundaries. The basal planes of the matrix and the twin are mirrored at the twin boundaries. (c) The growth of the twin into the matrix under a continued positive loading, the same the case required for twin nucleation. (d) Shrinkage of the twinned domain by detwinning under a reverse loading compared to the condition in (c).

### 2.2.2 $\{10\bar{1}2\}$ twinning mechanisms: Classical twinning dislocations vs. atomic shuffling

According to the classical twinning theory, the deformation associated with twinning is represented by shear. Twinning dislocations (TDs) are required to accomplish the shear deformation and they can only glide on the twinning plane ( $K_1$ ) so that the matrix-twin lattice correspondence is not disrupted. Twin boundaries coincide with the twinning plane showing

fully coherent interfaces. The misorientation between the matrix and twinned crystals is uniquely defined under the invariant plane strain condition, so the twinning plane basically remains undistorted during the twinning process. Twin boundary migration is mediated by TDs on the microscopic level; under an external stress a layer-by-layer glide of TDs on  $\{10\bar{1}2\}$  twinning plane can result in twin growth. The Burgers vector of TDs is given by  $(3-\gamma^2/3+\gamma^2)\langle 10\bar{1}\bar{1}\rangle$  [54], where  $\gamma$  is the crystal  $c/a$  ratio. A detailed schematic representation of twin growth related to TDs can be found in [50, 55].

Following the classical theory, a one-to-one lattice correspondence can be established between the atoms in the matrix and the twin lattice. Since the shear deformation does not necessarily move all the atoms into their correct positions, an atomic shuffling is required in addition to the shear to achieve the lattice correspondence between the two crystals. This idea has been schematically introduced by Bilby and Crocker [56] and later analyzed by Christian and Mahajan [50]. More recently, Li and Zhang [57] showed that the lattice correspondence in  $\{10\bar{1}2\}$  twinning is such that a matrix basal plane is transformed to a twin prismatic plane and a matrix prismatic plane to a twin basal plane. Figure 2.6 provides an example of how this transformation is possible in the  $\{10\bar{1}2\}\langle 10\bar{1}\bar{1}\rangle$  twinning mode through a combined shear and shuffle. The analysis has been reported by [58, 59].

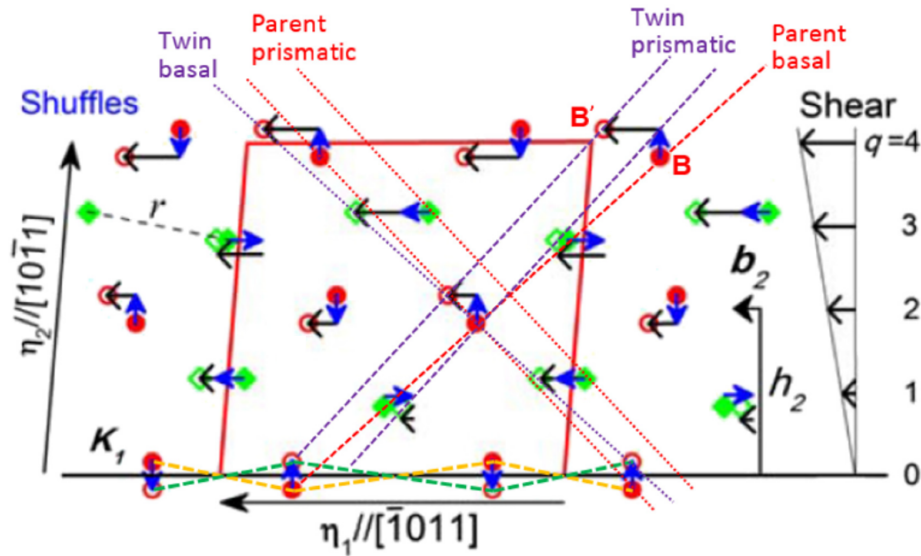


**Figure 2.6.** Analysis of atomic shear and shuffle using the classical  $\{10\bar{1}2\}$  twinning theory. The matrix (parent) lattice and the twin lattice are represented by solid and hollow symbols, respectively. The black arrows represent the homogeneous simple shear on layers 0 to 4. Atomic shuffles are shown by the blue arrows. A complete transformation of a  $(0002)$  basal plane in the matrix into an  $\{10\bar{1}0\}$  prismatic plane in the twin is accomplished by a combined shearing and shuffling of atoms. The image is reused from [58] with permission from Elsevier.

Atomic positions in the matrix (parent) and the twin are represented by the solid and hollow symbols, respectively. On the right, an array of black arrows shows the homogeneous simple shear distributed on layers 0 to 4. The atomic shear displacements are along the twin shear direction,  $\eta_1$ . Obviously, the matrix atoms cannot land on the twin positions only by a simple shear. Therefore, shuffles are needed to bring the sheared atoms into the final atomic

sites in the twin. For example, atom B on the matrix basal plane must shuffle upward after shear, as depicted by the blue arrow, to reach the twin position B' on the prismatic plane. Note that the atoms in the prismatic plane reside on two planes, i.e. it's a corrugated plane. In contrast to shear, the adjacent atoms move in different directions relative to the twinning plane and therefore it is possible that the net strain produced by atomic shuffling will be zero [60]. Such atomic movements off the twinning plane during shuffles indicate that the lattice transformations can distort the twinning plane [58]. This is a breakdown of the invariant plane strain condition which is denoted by the dashed zigzag lines across the atoms on layer 0 in Figure 2.6. It is seen that the twinning plane must be distorted by the shuffles. Once the shear and shuffles are complete, the basal plane of the matrix is transformed into the prismatic plane of the twin. Instead of the classical viewpoint of a combined shear and shuffle, recent theories have proposed a twinning mechanism including only atomic shuffles.

The shuffling-dominated twinning mechanism was proposed by Li and Ma [61] for  $\{10\bar{1}2\}$  twinning in Mg. By considering the shear strain for this type of twinning, 0.129, and the  $\{10\bar{1}2\}$  interplanar spacing,  $\sim 0.19$  nm, the authors calculated the shear involved on each  $\{10\bar{1}2\}$  plane, equivalent to the Burgers vector of a twinning dislocation, to be  $(0.129)(0.19 \text{ nm}) \sim 0.025$  nm. Owing to the small size of such a Burgers vector,  $\sim 1/31$  of the lattice vector in the  $\langle 10\bar{1}\bar{1} \rangle$  direction, it was concluded that the existence of such small dislocations is quite unlikely. Using atomic simulation, they claimed that the growth of the  $\{10\bar{1}2\}$  twins is mainly mediated through large atomic shuffles and that the shear displacement of an atomic plane relative to the next plane is so small that it can be reached by the net result of all shuffles without any action of twinning dislocations. In this scheme, the transformation of a matrix prismatic plane to a twin basal plane is accomplished by only shuffling atomic rearrangements, as is shown in Figure 2.7.

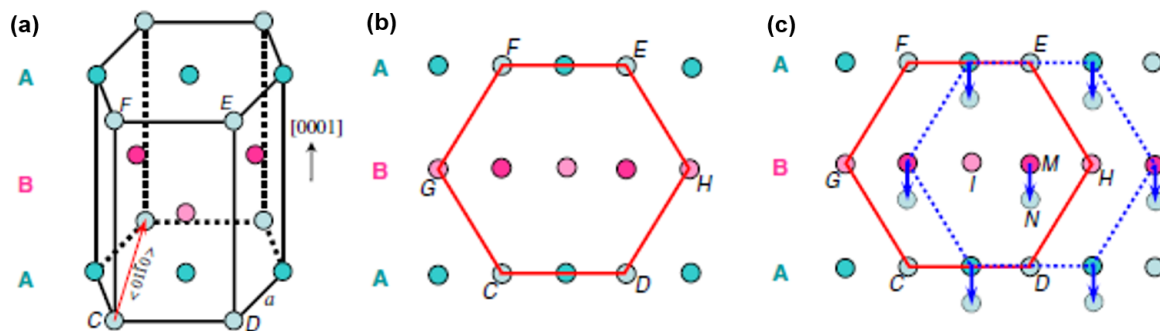


**Figure 2.7.** The shuffling-dominated  $\{10\bar{1}2\}$  twinning. (a) 3D view of the hcp lattice, (b) The projection view of the lattice along  $\langle 01\bar{1}0 \rangle$ . A new basal plane is constructed from the prismatic planes of the original lattice. The rotation degree between the prismatic and the basal plane is here  $90^\circ$ ; this different from the classical twinning-induced reorientation of about  $86^\circ$ . (c) The necessary shuffling to establish the correct hcp stacking sequence after twinning. The arrows show the atomic movements (shuffles). The final positions are seen by the dashed circles. The image is reused from [61] with permission from American Physical Society (APS).

Figure 2.7(a) shows a 3D view of a typical hcp lattice. Basal planes are in the sequence of

$ABAB\dots$  with different colors. The atoms lying in different prismatic planes are also marked. A projection view parallel to the  $\langle 01\bar{1}0 \rangle$  zone (perpendicular to the crystal  $[0001]$  axis) is shown in Figure 2.7(b). Through connecting some of the atoms in this 2D pattern, one can observe the possibility of constructing a new basal plane from the existing lattice points, see the red hexagon. This new basal plane comes from the prismatic planes of the original lattice in Figure 2.7(a) and is  $90^\circ$  oriented with respect to the original basal planes. This basal-prismatic conversion and the  $90^\circ$  misorientation in the absence of any actual crystal rotation, is similar to the results of in-situ compression tests on submicron-sized Mg pillars [62], where twinning happened without an obvious twinning shear and the reoriented lattice did not hold the crystallographic orientation relationship with the matrix as expected for the  $\{10\bar{1}2\}$  twinning. But, the lattice reconstruction shown in Figure 2.7(b) does not have the correct hcp packing, yet. Some structural deviations have to be adjusted and therefore atomic shuffling is required to accomplish the conversion. To accomplish the hcp  $ABAB\dots$  stacking sequence in the direction perpendicular to the new basal plane ( $A$ ), another basal plane ( $B$ ) has to be reconstructed in the right position. As depicted in Figure 2.7(c), this requires that the atoms in the second basal (dashed blue line connections) to be projected to the center of the triangles in the first basal; examples are shown by the dashed circles such as position N. This requirement is not satisfied in Figure 2.7(b). Atoms such as M have to shuffle down to new positions like N, as shown by the arrows. The magnitude of all the necessary shuffling is calculated to be much smaller than any existing Burgers vectors for dislocations in Mg [61]. A question that may raise in the shuffling-dominated scenario is how global strain is generated without involving shear. To address this question, Li and Zhang [63] showed that due to the misfit between the matrix and twin lattices, a normal strain is generated along the crystal  $c$ -axis. This misfit strain,  $\varepsilon$ , is calculated by  $\varepsilon = (\sqrt{3}-\gamma)/\gamma$ . Using  $\gamma = 1.624$  for Mg, the value of misfit strain is  $\sim 0.067$  which is comparable to the longitudinal strain generated by twinning shear,  $\sim 0.065$  (see Section 4.3).

By neglecting the role of TDs and the associated shear, the shuffling-dominated twinning mechanism contradicts some aspects of the classical twinning theory. This has raised a controversy on the actual  $\{10\bar{1}2\}$  twinning mechanisms in the community. Some researchers have questioned the new shuffling mechanism using experimental high resolution characterization techniques as well as computer calculations. Using a Burgers circuit at a twin boundary that showed a step of TDs in Li and Ma's simulation results, Serra et al. [64] proved that the absence of TDs in shuffling mechanism is only a misinterpretation of the results. Furthermore, observation of TDs using high-resolution TEM in hcp Zn [65] and Co [66] negates the argument that the Burgers vector for TDs is too small to have physical significance; small Burgers vector simply means small shear [64]. In addition, considering energy changes along the transformation path from matrix to twin, Ostapovets and Molnár [60] concluded that the energy at the final stage of twinning transformation is the same for pure shuffle and pure shear, and this energy is comparable to the barrier for the simultaneous shuffling and shear. Hence, only concurrent shuffling and shear can result into a twin with a correct hcp structure. Despite these facts, the authors in [63] believe that the shuffling-dominated twinning

mechanism should not be considered as contradictory to the classical mechanism where a homogeneous shear and atomic shuffling are involved. According to their calculations, the Burgers vector of TDs and the magnitude of the shuffle vary from one twinning mode to another. The  $\{10\bar{1}2\}\langle 10\bar{1}\bar{1}\rangle$  twinning mode should be treated as an extreme case of classical twinning in which shear is not involved and shuffling is dominant.

Even though the shuffling-dominated twinning mechanism is not well accepted in the community, it is still used to explain some abnormal twinning features that are not consistent with the classical twinning theory. According to some experimental evidences [67], the actual twin boundary can deviate from the  $\{10\bar{1}2\}$  plane. Since shuffling is not required to be confined in the twinning plane, this mechanism was used to explain the observed deviations from the actual twinning plane [67]. A deeper discussion of this case will be provided in Section 4.3.

### 2.3 Overview on micromechanics of twinning

Among all the twinning systems, the relatively low critical resolved shear stress (CRSS) of the  $\{10\bar{1}2\}$  mode and high mobility of the twin boundary make it the most frequently observed [68]. For Mg, this twinning mode produces an extension along the crystal  $c$ -axis and hence it is termed extension or tensile twinning [32]. Apart from numerous aspects of extension twinning that has been studied over the past decades, establishment of a characteristic defect substructure in the  $\{10\bar{1}2\}$  twins has received experimental microstructural characterization and numerical efforts in recent years. Using transmission electron microscopy (TEM) observations within and around twins, it has been found that while the matrix contains mostly  $\langle a \rangle$  dislocations, abundant  $\langle c \rangle$ -containing dislocations, commonly in form of pure  $\langle c \rangle$  or perfect  $\langle c + a \rangle$ , exist within the twinned lattice [69, 70]. The generation of such  $\langle c \rangle$ -containing dislocations is in turn surprising, if one considers the relatively very low plateau stress level, at which  $\langle c + a \rangle$  dislocations form. The observed dislocation structure within a twin is thus attributed to the transformation of matrix  $\langle a \rangle$  dislocations once they meet an advancing twin boundary, leaving  $\langle c + a \rangle$  dislocations inside the twin crystal, the process is known as ‘dislocation transmutation’ in the Mg community [69, 71]. This matrix-twin boundary interaction and the resultant microstructure is expected to affect the subsequent slip-based plasticity of the twinned lattice. So far, the mechanical impact of such a twinning-inherited defect substructure has not been explored thoroughly, and to the author’s best knowledge, a systematic mechanical characterization to find out the effect of the twinning microstructure obtained within the stress plateau on the subsequent strain hardening response has not been advanced. To address this issue, a mechanical testing method that can deform a representative volume associated with a single twinning phenomenon is of great advantage. Microcompression offers the possibility to assess the mechanical properties at the micrometer scale, where the response of an isolated twin decoupled from the stress field arising from neighboring grain, and twin boundaries could be traced.

As observed from conventional compression testing of bulk samples, once  $\{10\bar{1}2\}$  twin-

ning occurs, the material exhibits a stress plateau in the corresponding stress-strain curve, followed by a slip-dominated strain hardening [72]. Apart from numerous aspects of extension twinning that has been studied over the past decades, establishment of a characteristic defect substructure at the plateau regime in  $\{10\bar{1}2\}$  twins has received experimental microstructural characterization and numerical efforts in recent years. Using transmission electron microscopy (TEM) observations within and around twins, it has been found that while the matrix contains mostly  $\langle a \rangle$  dislocations, abundant  $\langle c \rangle$ -containing dislocations, commonly in form of pure  $\langle c \rangle$  or perfect  $\langle c + a \rangle$ , exist within the twinned lattice [69, 70]. The generation of such  $\langle c \rangle$ -containing dislocations is in turn surprising, if one considers the relatively very low plateau stress level, at which  $\langle c + a \rangle$  dislocations form. The observed dislocation structure within a twin is thus attributed to the transformation of matrix  $\langle a \rangle$  dislocations once they meet an advancing twin boundary, leaving  $\langle c + a \rangle$  dislocations inside the twin crystal, the process is known as ‘dislocation transmutation’ in the Mg community [69, 71]. This matrix-twin boundary interaction and the resultant microstructure is expected to influence the subsequent slip-based plasticity of the twinned lattice. So far, the mechanical impact of such a twinning-inherited defect substructure has not been explored thoroughly, and to the author’s best knowledge, a systematic mechanical characterization to find out the effect of the twinning microstructure obtained within the stress plateau on the subsequent strain hardening response has not been advanced. To address this issue, a mechanical testing method that can deform a representative volume associated with a single twinning phenomenon is of great advantage. Microcompression offers the possibility to assess the mechanical properties at the micrometer scale, where the response of an isolated twin decoupled from the stress field arising from neighboring grain, and twin boundaries could be traced.

Microstructure-mechanical properties relation associated with isolated twinning phenomena has been provided in the literature. Microcompression experiments has been mostly conducted on single crystals of orientations  $[2\bar{1}\bar{1}0]$  and  $[10\bar{1}0]$  that favor twinning; compression parallel to the basal planes. The  $[2\bar{1}\bar{1}0]$  loading direction twins in a way that the reoriented crystal is favorably aligned for further basal slip; easy slip after twinning. Loaded along this direction, Jeong et al. [30] studied the mechanism of twin nucleation, twinning size effect and strain rate dependency of twinning using in-situ TEM observation of micropillars. Their results showed that the pile-up of prismatic  $\langle a \rangle$  dislocations acts as local stress concentration for twin nucleation. This twin nucleation stress exhibited a strong size effect arising from the fact that dislocation pile-up depends on the crystal size. Similarly, a stronger size effect was found for twinning-dominated orientations relative to slip-assisted ones, as reported by Kim [73]. Moreover, increasing the strain rate promoted twinning because higher strain rates can effectively raise the stress to the level required for dislocation pile-up and the resultant twin nucleation [30].

Compression along  $[10\bar{1}0]$  direction reorients the micropillar to an orientation unfavorable for easy basal slip; hard slip after twinning. Liu et al. [74] compressed micropillars along  $[10\bar{1}0]$  axis to quantify the critical stress associated with twinning. Kim [73] loaded micropillars of  $[10\bar{1}0]$  orientation up to a strain within the plateau regime. Pillar cross-sections

revealed a fully twinned micropillar, confirming a reorientation of the micropillar to roughly [0001] ( $c$ -axis) direction. The reoriented micropillar, however, was not further compressed beyond the plateau to see whether the twin follows the stress-strain path typical of  $c$ -axis compression behavior, where the micropillar deforms by a strong strain hardening. The latter, i.e. [0001] compression response, was studied by Lilleodden [\[75\]](#) and it was shown that  $\langle c + a \rangle$  dislocation slip dominates the strong hardening after the yield without any contribution of deformation twinning.

# 3 Materials, experimental methods and analysis

This chapter presents the materials, methods of preparation and testing, and principles of the analysis that were used in the current study. The work was conducted on a pure Mg and a Mg-Gd alloy. General properties of these two materials are covered. The experimental scheme includes preparation and processing of bulk polycrystalline samples, fabrication and testing of micron-sized samples in the grains of interest, and post-mortem structural characterization of the deformed volumes. For the bulk sample preparation, details of macro scale testing and the applied thermal processing are important to be discussed. For the micron scale experiments, the electron microscopy techniques employed for micropillar fabrication using focused ion beam (FIB) milling, and those facilitating characterization of deformation structures such as transmission electron microscopy (TEM) and electron backscatter diffraction (EBSD) are discussed. Details of the microcompression testing method along with the approaches to extract and analyze the resulted mechanical data are also covered.

## 3.1 Materials

The present research was conducted on a pure Mg and a binary Mg-Gd alloy produced at the Magnesium Innovation Centre (MagIC) in Helmholtz-Zentrum Geesthacht. Sample volumes of 1 cm<sup>3</sup> were cut from the cast ingots and used for chemical analysis. The composition of the constituent elements for the investigated materials are listed in [Table 3.1](#). Both materials were homogenized at 450°C for 24 hours to remove the dendritic structure from the casting process. The samples possessed a very coarse grain size of about 700-800 μm after homogenization. The atomic percentage of Gd in the Mg-Gd alloy can be calculated based on the composition results in [Table 3.1](#):

**Table 3.1.** Elemental composition of the major constituents of the tested materials given in weight percent.

Material	Mg	Zn	Zr	Fe	Cu	Ni	Gd
Pure Mg	99.85	0.0006	<0.0005	0.032	0.0005	<0.0002	-
Mg-Gd alloy	95.27	0.0012	0.0005	0.031	0.0022	<0.003	4.69

$$at.\%Gd = \frac{(wt.\%Gd)/(at.wt.Gd)}{(wt.\%Gd)/(at.wt.Gd) + (wt.\%Mg)/(at.wt.Mg)} \times 100 \quad (3.1)$$

where wt.% Gd = 4.7, at.wt.Gd is gadolinium atomic weight = 157.25, wt.% Mg = 95.3 and at.wt.Mg is magnesium atomic weight = 24.30. Therefore, the atomic percent of the alloying solutes is about 0.76% in the Mg-Gd system. According to the equilibrium phase diagram for the Mg-Gd binary system [76] shown in Figure 3.1, this amount of Gd should not produce any precipitate or compounds, the first reaction is an eutectic equilibrium on the Mg side requiring 8.8 at.% Gd. Therefore, a contribution of pre-existing precipitates into the deformation and more specifically twinning response is not expected.

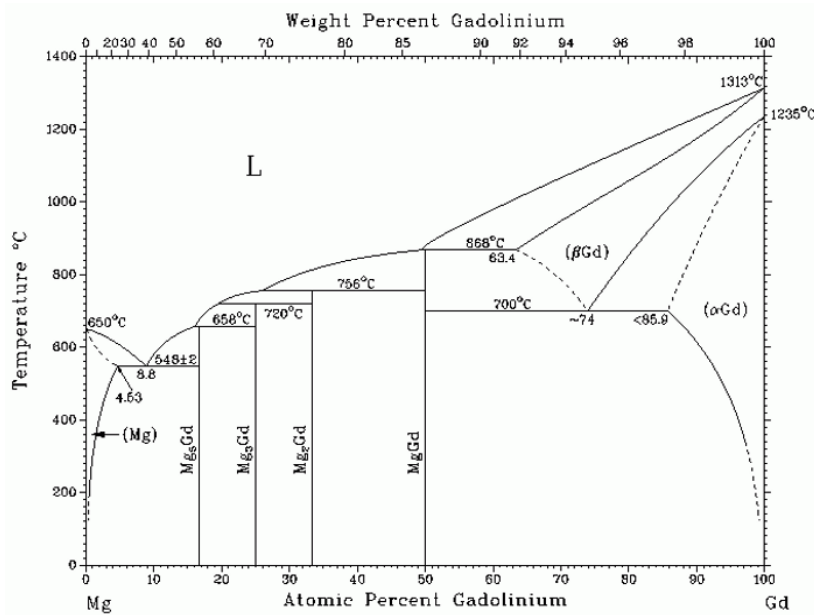


**Figure 3.1.** The equilibrium phase diagram for Mg-Gd binary system. The image is reused from [76] with permission from Taylor & Francis.

### 3.2 Preparation and processing of bulk polycrystals

Polycrystalline pure Mg (99.85 wt.% Mg) and Mg-4.7 wt.% Gd samples were cut from the homogenized ingots using a band saw. Rectangular shaped samples with dimensions of ca.  $4.4 \times 4.4 \times 9.3$  mm were then cut using a WELL Diamond Wire Saws SA cutting machine and grinded on all sides with sandpaper to remove large scale cut damage. Special care was taken to ensure planarity of the surfaces. For microstructural observations before and after deformation, one of the surfaces of the samples was further polished on a polishing cloth using an OP-S NonDry suspension having silica particles and Ethylenglycol as a lubricant. Final polishing was performed using OP-S (dry). A mirror like surface finish, which was required for EBSD analysis and micropillar fabrication, was achieved finally through submerging into a 0.5% Nital solution for few seconds. Figure 3.2 shows a simplified example of the bulk polycrystalline samples of the two materials that were prepared for macro scale testing. The well-polished side surfaces were characterized by EBSD technique (details are given later in this chapter) to reveal the initial microstructures and then to select the single grains of

interest.

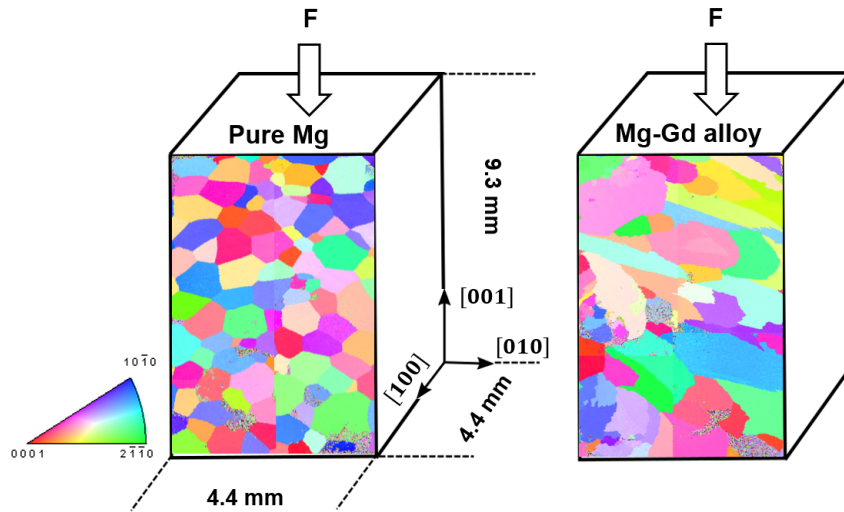


**Figure 3.2.** Simplified views of the bulk polycrystalline pure Mg and Mg-Gd alloy prepared for macro scale testing. The surfaces of the samples were grinded, polished and characterized using EBSD. The corresponding [001] EBSD maps of the initial microstructures are shown. The arrows labeled with **F** show the direction of macro compression. Compressions were performed to about 4.4% strain.

In order to produce deformation twins inside the grains, the bulk polycrystalline samples were compressed using a SCHENCK pressing machine up to about 4.4% accumulative strain. The test speed was 0.1 mm/min. The compression tests were interrupted at some interval strains to check through measuring the sample dimensions whether the desired strain has been achieved. The polished side surfaces of the samples were kept untouched during mechanical testing, in order to avoid repolishing after deformation.

### 3.2.1 Thermal processing

The compressed polycrystalline pure Mg sample was heat-treated at 350°C for 2 hours using a push oven built at Helmholtz-Zentrum Geesthacht, which was connected to protective Ar gas. The furnace was set to 392°C leading to a temperature of 350°C at the thermocouples connected to the sample holder. The heat-treatment was started once the sample holder temperature remained almost constant. The deformation structure was relieved in this way from the stored energy of the introduced dislocations as a result of previous bulk compression. The single grains for further micromechanical characterizations were therefore considered as deformation free volumes.

In order to investigate solute segregation at twin boundaries, the compressed polycrystalline Mg-Gd sample was heat-treated in the same furnace as mentioned above. The set temperature for the furnace was 324°C leading to a nominal temperature of 300.0°C for the sample holder. The sample was kept in this temperature range for 3.5 hours. The annealing time and temperature were selected based on the available data in the literature [26, 77, 78],

that have reported the segregation of Gd atoms in the grain/twin boundaries. The annealed sample was cooled in the furnace under an increased pressure of cold protective Ar atmosphere to prevent oxidation.

### 3.3 Fabrication and testing of micron-sized samples

#### 3.3.1 Focused ion beam (FIB) microscopy

A FEI Nanolab 200 Dualbeam scanning electron and focused ion beam (FIB) microscope was used in this work to fabricate micron-sized samples for further micromechanical investigations and also to characterize the deformation structures. The dual-beam microscope combines a high resolution field emission scanning electron microscope (FE-SEM), and a highly focused beam of gallium ( $\text{Ga}^{2+}$ ) ions that allows to switch between the two beams for navigation and milling. The SEM is typically used for imaging with secondary or backscattered electrons that also allows us to have access to crystallographic information and chemical composition of the sample using EBSD and energy dispersive x-ray spectroscopy (EDS) detectors, respectively. The FIB can be operated with different voltages and currents for imaging and precise site-specific sputtering or milling of various shapes into a bulk sample. The microscope is also equipped with an in-situ platinum (Pt) injection system and an Omniprobe micromanipulator for lifting-out of cross-sections milled by FIB. In the following, the usage of the dual-beam microscope for micropillar fabrication, FIB lift-out of cross-sections for further EBSD and TEM observations and EBSD measurement are given in details.

#### 3.3.2 Micropillar fabrication

Micropillars were fabricated in the selected grains from the bulk polycrystalline samples using FIB milling. An annular milling protocol with an accelerating voltage of 30 kV and varying currents was used. Micropillars were machined in two circular milling procedures; (*i*) first multi pass rough cut with a current of 3.0 nA and a depth of 3.0  $\mu\text{m}$  and (*ii*) final single pass fine cut with a current of 0.5-1.0 nA and dwell time of 2 ms. Attempts were made to ensure a roughly 4  $\mu\text{m}$  mid-plane diameter and an aspect ratio of height to mid-plane diameter between 3 and 4 for all the fabricated micropillars. Due to the annular cutting method used, a slightly larger base diameter than top diameter is achieved with a typical taper angle of  $\sim 3-4^\circ$ . Although this taper leads to some variation in axial stress along the column, the taper helps to stabilize the pillar, if there is any misalignment between the micropillar and the flat punch. A typical micropillar prior to compression and its corresponding FIB machined cross-section are shown in [Figure 3.3](#). The light gray in [Figure 3.3\(b\)](#) corresponds to a protective Pt layer deposited prior to sectioning. This helps to visualize the boundaries of the pillar's cross-section. Such a cross-sectional analysis of a sacrificial column is helpful in assessing the true pillar geometry. This is very important to avoid errors in geometry measurement that can lead to significant inaccuracies in the stress and strain analysis, since accurate measurement of the dimensions from SEM images of a non-sectioned pillar is difficult due to the surrounding

material and the images projection.

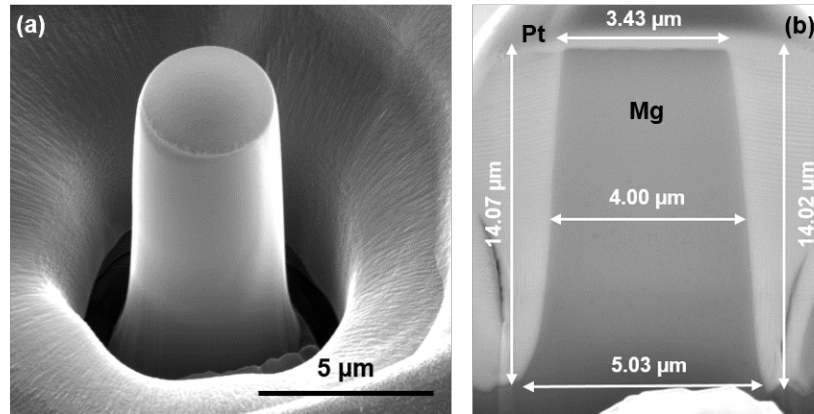


**Figure 3.3.** SEM micrographs of (a) a roughly 4 μm diameter micropillar and (b) its corresponding FIB machined cross-section showing the pre-deformation geometry of a typical pillar.

In order to perform microcompression on pre-existing twin boundaries, bicrystalline micropillars were fabricated in a way that a single twin is included inside the sample. Circular milling patterns were carefully positioned inside the selected twin band, an example is shown in Figure 3.4. Taking the inclination of the twin into account, the inner diameters of patterns were located close to the boundary from the twin side; in this way the twin boundary crosses edge of the fabricated micropillar leaving the twin part located at the top part of sample, this can be later verified from a cross-section of a sacrificed bicrystalline pillar before compression, see Figure 4.16(b).

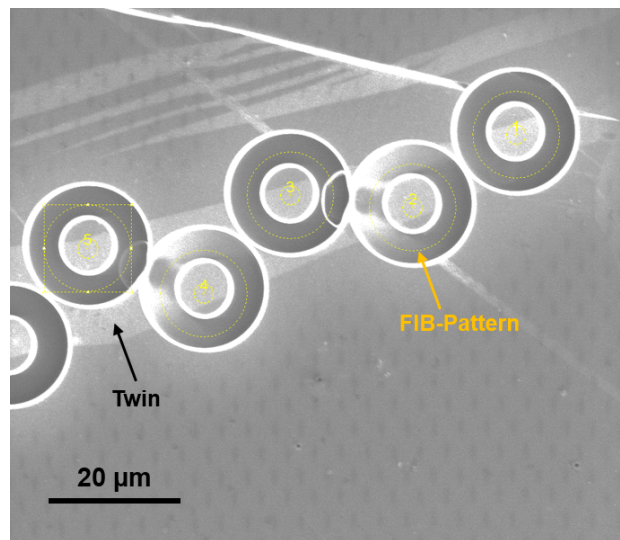


**Figure 3.4.** FIB-view of circular milling patterns to machine bicrystalline micropillars at a selected twin. The inner diameters of the patterns are carefully positioned close to the twin boundary; the machined micropillar will include the twin part at the top. An example of a bicrystalline cross-section is shown in Figure 4.16(b).

### 3.3.3 Microcompression testing

The advent of microcompression testing technique was pioneered by the inspiring works of Uchic et al. [20, 79], with the intention to characterize the mechanical properties of materials at small length scales. They developed a test methodology that allows analyzing the stress-strain characteristics of localized volumes from a bulk material in a simple uniaxial compression stress state. In this method a focused ion beam (FIB) microscope is used to machine cylindrical micropillars into the surface of a bulk crystal. The prepared samples are then compressed using a conventional nanoindentation device equipped with a flat-punch indentation tip. Micropillar compression testing has been widely used to investigate the plasticity of single crystals in a broad range of materials having face-centered (e.g. [80, 81]) and body-centered (e.g. [82, 83]) cubic as well as hexagonal closed-packed (e.g. [73, 75]) structures.

Extracting the mechanical response of individual interfaces is a new objective in this field. Micropillar compression offers a unique possibility to locate an individual interface (e.g. grain or twin boundaries) inside the deformation volume out of a polycrystalline sample; this might be a bicrystalline micropillar including the interface of interest. By testing the bicrystalline micropillar including only two grains separated by their grain/twin boundary, the mechanical impact of the interface can be individually identified; the results are not influenced by the collective behavior of several grains in a polycrystalline aggregate. Up to now, bicrystalline micropillar compression has been used to examine various grain/twin boundary characteristics. As some examples, dislocation slip transmission through copper high angle grain and twin boundaries has been investigated in terms of strain rate sensitivity [84, 85] and size effect [86]. In this regard, a comprehensive overview of the micromechanics of individual interfaces is given in [87].

The microcompression tests in this work were conducted with a Nanoindenter XP (Agilent) equipped with a flat-ended conical indenter with a 10  $\mu\text{m}$  diameter circular punch. The indenter diameter was chosen to ensure that it is larger than the pillar diameter and smaller than diameter of the trench milled around the pillar. All the compressions were carried out at a constant strain rate of 0.001 1/s up to varying targeted engineering strains of approximately 2.5-12%. The surface approach velocity, prescribed unloading rate and data acquisition rate were selected to be 10 nm/s, 5 mN/s and 10 Hz, respectively. Series of micropillars were tested at a same initial condition, e.g. pillar size, applied strain and microstructure, in order to show the reproducibility of the experimental data. The raw data taken from the microcompression experiments were processed offline; the governing equations for calculation of the load, displacement, stress, strain and modulus are given in Eq. (3.1) to Eq. (3.5), respectively:

$$P_{\text{sample}} = P_{\text{raw}} - k_s h_{\text{raw}} \quad (3.2)$$

$$h_{\text{sample}} = h_{\text{raw}} - h_{\text{surface}} - h_{\text{LF}} - h_{\text{substrate}} \quad (3.3)$$

$$\sigma_{\text{eng}} = P_{\text{sample}} / \frac{\pi}{4} D_{\text{mid}}^2 \quad (3.4)$$

$$\varepsilon_{\text{eng}} = h_{\text{sample}} / H_0 \quad (3.5)$$

$$E = S \frac{4}{\pi} H / D^2 \quad (3.6)$$

where  $h_{\text{LF}} = P_{\text{sample}} / S_{\text{LF}}$ . Here, the substrate deformation was accounted for by using the Sneddon equation [88]. The displacement of the substrate is accordingly given as:  $h_{\text{substrate}} = (1 - \nu)^2 P_{\text{sample}} / E D_{\text{foot}}$ . In the above equations  $P_{\text{sample}}$  is the load on the sample,  $P_{\text{raw}}$  the raw load,  $k_s$  the instrument spring constant,  $h_{\text{raw}}$  the raw displacement,  $h_{\text{surface}}$  is the surface position,  $h_{\text{LF}}$  is the load-frame displacement,  $h_{\text{substrate}}$  is the substrate displacement and  $S_{\text{LF}}$  is the load-frame stiffness.  $\nu$  and  $E$  are the Poisson's ratio and the Young's modulus of the substrate, respectively.  $D_{\text{foot}}$  is the diameter of pillar foot,  $D_{\text{mid}}$  is the mid-plane pillar diameter,  $H_0$  is the initial pillar height and  $S$  is the harmonic contact stiffness [81, 89].

### 3.3.4 Schmid factor and the required stress to initiate slip

The use of the four-index Miller-Bravais notation in hcp structures makes crystallographic calculations difficult, compared to the cubic structures. This is because some useful algebraic operations like lattice rotation or vectors multiplication are not valid in a non-orthogonal coordinate system, or at least some corrections must be applied. Therefore, for numerical calculations involving the hcp lattice, it is convenient to convert the four-index Miller-Bravais indices of crystallographic planes and directions into a three-index orthogonal coordinate system. All computations can thus be carried out in terms of the orthogonal system. The transformation equations from hexagonal Miller-Bravais index notation into the orthogonal system are given in Appendix A.1.

The Schmid factor,  $m$ , is classically used to predict slip and twinning activity in single crystals. It is calculated based on the angle between loading axis and slip (or twinning) plane normal,  $\phi$ , and the angle between loading axis and slip (or twinning) direction,  $\lambda$ , by the following expression [52]:

$$m = \cos \phi \cos \lambda = \tau_{\text{rss}} / \sigma_{\text{app}} \quad (3.7)$$

where  $\tau_{\text{rss}}$  is the shear stress resolved on the slip or twin plane and in the slip or twinning direction, and  $\sigma_{\text{app}}$  is the applied stress. It should be noted that  $m$  is an absolute value for slip and is independent of the loading direction along a given axis; i.e. tension or compression,

but the value can be negative for twinning modes, since twinning can be deactivated upon changing the loading mode from tension to compression or vice versa. Schmid factors for the deformation systems and loading directions that are important in this work were calculated based on Eq. (3.6). The maximum values for each slip and twinning mode are listed in Table 3.2. Grains **A** and **B** refer to the grains selected in the pure Mg as well as Mg-Gd alloy for microcompression of single crystals along the [0001] and [10 $\bar{1}$ 0] directions, respectively. Bicrystals hold a combination of these orientations. The corresponding microstructures of these grains will be shown later in Figures 4.1 and 5.1. In addition, variation of the Schmid factor with the angle between the crystal  $c$ -axis and the loading axis for different slip and twinning systems are presented in Appendix A.2.

Before slip/twinning will occur, the resolved shear stress on the slip/twinning plane ( $\tau_{\text{RSS}}$ ), must attain a critical value, called the critical resolved shear stress (CRSS). Thus, based on Eq. (3.6) the applied stress required to activate a deformation mode is obtained by  $\text{CRSS}/m$ . The stress was accordingly calculated for basal and pyramidal slip systems at varying loading conditions and was used to discuss the experimental results.

**Table 3.2.** Schmid factors for the slip and twinning systems in different loading directions that are used in this study. The maximum value for each deformation mode is given. Grains **A** and **B** are selected in the pure Mg (Figure 4.1) and Mg-Gd alloy (Figure 5.1) for microcompression along the [0001] and [10 $\bar{1}$ 0] directions, respectively.

Deformation system	Loading direction				
	[0001]	[10 $\bar{1}$ 0]	[10 $\bar{1}$ 30]	Normal to Grain <b>A</b>	Normal to Grain <b>B</b>
Basal slip- $\{0001\}\langle 11\bar{2}0\rangle$	0	0	0.03	0.07	0.09
Prismatic slip- $\{1\bar{1}00\}\langle 11\bar{2}0\rangle$	0	0.43	0	0	0.48
Pyramidal slip $\pi_1$ - $\{10\bar{1}1\}\langle \bar{1}\bar{1}23\rangle$	0.40	0.40	0.42	0.44	0.47
Pyramidal slip $\pi_2$ - $\{11\bar{2}2\}\langle \bar{1}\bar{1}23\rangle$	0.45	0.33	0.46	0.47	0.42
Extension twinning- $\{10\bar{1}2\}\langle \bar{1}011\rangle$	-0.50	0.50	-0.50	-0.50	0.49

## 3.4 Post-mortem characterization of micron-sized samples

### 3.4.1 FIB lift-out technique

Post-deformation structures were carefully characterized by EBSD and TEM on lamellae taken from the compressed micropillars, using the lift-out technique. The lift-out technique has proven to have unique advantages where mechanical sample preparation is difficult or impossible [90]. A major advantage of the lift-out technique is that specimens can be made directly from a bulk sample; cutting or mechanical polishing are not required. The lamella containing the feature of interest is mounted onto a carrier using a micromanipulator, and is thinned by FIB. The thinned lamella is then ready for microstructural characterization. The detailed steps used in this work are summarized in Figure 3.5 as follows:

- (a) Deposition of Pt layer using 500 nm depth and a current of 1.0 nA on the pillar of

interest. The aim is to cover the whole column to protect from FIB damage and visualize the boundaries of the sectioned pillar.

- (b) Coarse regular staircase cross section milling on either side of the to-be prepared lamella at an over tilt angle of  $2^\circ$  using 3.0 nA current and a depth of 6  $\mu\text{m}$  (Figure 3.5(a)). The lamella should be located at the center of the pillar having a thickness not larger than 2  $\mu\text{m}$  (Figure 3.5(b)). Further cleaning cross section milling is performed afterwards using a same depth as the trenches and a current of 1.0 nA, to remove the rough surfaces left from the coarse milling step and to reduce taper at the base of the lamella.
- (c) Through-section cutting with 0.3 nA current and a depth larger than the thickness of the lamella at an angle of  $7^\circ$  to free the lamella partially from the bulk, one corner is still connecting the lamella to the bulk (Figure 3.5(a)).
- (d) Attaching the free edge of the lamella to the inserted Omniprobe with a 500 nm thick layer of Pt (Figure 3.5(c)).
- (e) Lifting out of the attached lamella after FIB cutting of the connecting corner and attaching it to a copper grid with a 500-700 nm thick layer of Pt and a current of 0.1 nA (Figure 3.5(d)). The tip of the Omniprobe has now to be detached from the glued lamella using FIB. A cleaning cross section with a current of 1.0 nA is then performed to clean the glued lamella for further EBSD measurement. The following steps (f) and (g) are required once the lamella is going to be observed by TEM.
- (f) Thinning down the lamella applying a cleaning cross section with a current of 0.3 nA to a thickness between 100 and 200 nm to make it electron transparent.
- (g) Final low voltage cleaning at an over- and undertilt of  $\pm 5^\circ$  with a voltage and current of 5 kV and 70 pA, respectively. This will remove the Ga ion-damage surface layer from the transparent lamella.

### 3.4.2 Electron backscatter diffraction (EBSD)

Post-mortem crystallographic orientation characterization was performed on lifted-out cross-sections of the deformed micropillars using EBSD. EBSD measurements were carried out at 15-20 kV accelerating voltage and 2.2 nA electron beam current using an EDAX/TSL detector operating in the FEI Nanolab 200 Dualbeam microscope at a working distance of 10 mm. The EDAX OIM Analysis<sup>TM</sup> 7 software was used to process the data. Various scans were performed on several samples compressed to varying strains using a 50 nm step size. Due to the risk of damage during high angle tilting, the holder for lamellae was attached to a  $45^\circ$  pre-tilt sample holder for ease of tilting to  $70^\circ$  required for EBSD measurement. Figure 3.6 shows the arrangement of a  $25^\circ$  tilted sample holder carrying FIB-prepared lamellae, and the inserted EBSD camera.

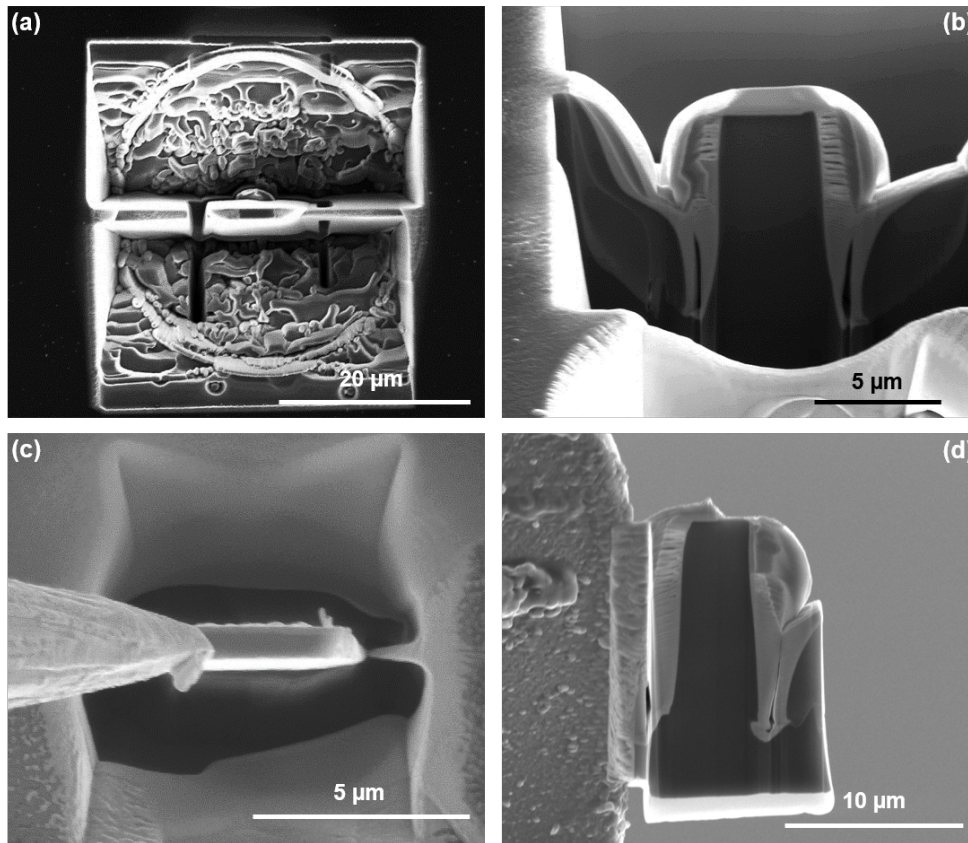


**Figure 3.5.** SEM micrographs showing the main steps of the FIB lift-out technique. (a) Regular cross-sectioned trenches at the top and bottom of the lamella. (b) The sectioned lamella from the center part of micropillar. The brighter contrast is the deposited Pt layer. (c) An Omniprobe attached to the corner of the lamella. (d) A lamella glued onto a Cu grid using Pt deposition.

EBSD is sensitive to the collective effects of dislocations that accumulate in the lattice during deformation. These dislocations can be divided into two categories: those termed ‘geometrically necessary’ dislocations (GNDs) and those which are ‘statistically stored’ dislocations (SSDs). It is somewhat imprecise to say that EBSD is ‘measuring plasticity’. Instead, EBSD measures the effects of plasticity upon the crystallite lattice in the form of lattice bending (GNDs) and lattice imperfection (GNDs and SSDs) [91]. Local deformation inside the compressed micropillars was quantified in this study using correlated and uncorrelated misorientation angle distribution analysis. Such analyses were used in the microstructure analysis as a measure of the dislocation density, which quantifies the local lattice curvature and is retrieved directly from the EBSD measurement. In correlated measurements, the misorientation is measured between each scan point and its nearest neighbors. Correlated data is used for example in the kernel average misorientation (KAM) analysis [91], in which each scan point is assigned to the average of the misorientation measured between that point and its nearest neighbors. KAM maps can be displayed as color-coded maps since each scan point is assigned to one value of misorientation [92]. In the current work, the KAM maps were constructed from the pillars cross-sections by calculating the average misorientation of every scan point up to its third nearest neighbors. In uncorrelated measurements, the misorientation is

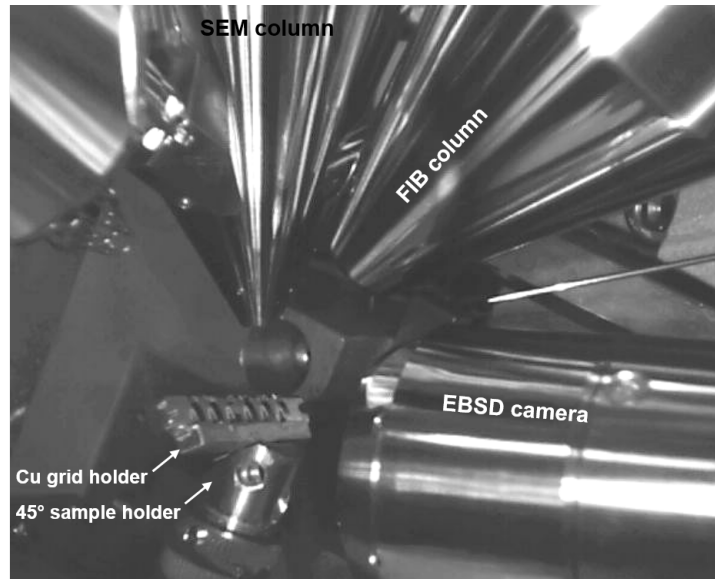


**Figure 3.6.** Arrangement of a 45° pre-tilted sample holder carrying a FIB-prepared lamellae, totally tilted to 70° for EBSD measurement. The EBSD camera is inserted.

calculated between each point and all other points in the scanned area. The uncorrelated misorientation angle distribution is more sensitive to plastic strain, since it includes all the possible misorientation pairs in the scanned area [92]. The difference between correlated and uncorrelated misorientation is illustrated schematically in Figure 3.7. Bulk polycrystalline samples were also characterized by EBSD in order to find the crystals of interest with the desired orientation. The step size used for the scans varied from 4 to 10  $\mu\text{m}$ .

### 3.4.3 Transmission electron microscopy (TEM)

Transmission electron microscopy (TEM) was carried out in a FEI Talos F200X double tilt holder microscope equipped with a four-quadrant energy dispersive spectroscopy (EDS) system operated at 200 kV at Hamburg University of Technology (TUHH). Observations were made on FIB-prepared lamellae glued to Cu grids. The principles of operation of a TEM are given briefly. When an electron beam strikes an electron transparent crystalline sample, the transmitted electrons are either diffracted or they travel through the sample without any angular deviation. The scattered electrons may be inelastic or elastic; i.e. the electrons may or may not suffer a measurable loss of energy. The elastically scattered electrons can be further classified as either coherent or incoherent depending on whether they are in phase with one another or out of phase. Consequently, different types of contrasts are associated with these different forms of electrons-sample interactions that occur in the TEM. In order to translate the electron scatter into interpretable amplitude contrast, either the direct beam or a diffracted beam is selected in the selected area diffraction pattern (SADP) to form bright field (BF) and dark field (DF) images, respectively [93]. The principle diffraction patterns for the hexagonal closed packed (hcp) structure are given in [93]. Most of the TEM observations were conducted such that the incident beam direction,  $\mathbf{B}$ , was nearly parallel to  $\mathbf{B} = [2\bar{1}\bar{1}0]$ ,

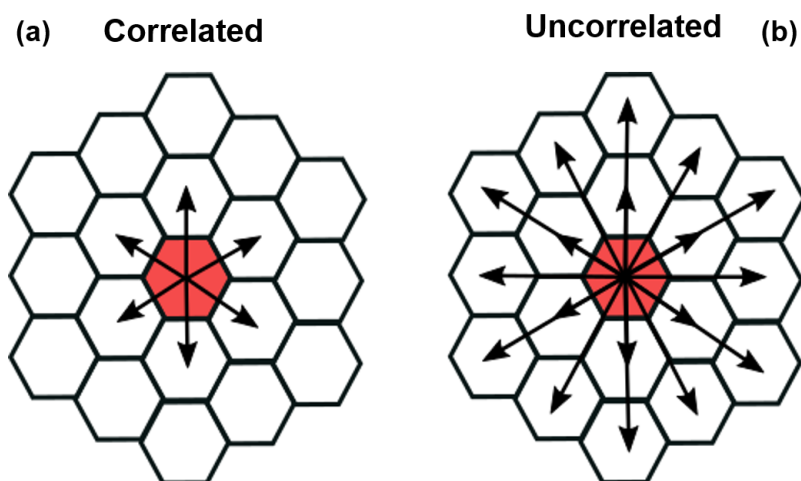


**Figure 3.7.** Schematic illustration of difference between (a) correlated and (b) uncorrelated misorientation calculation. Correlated data represents misorientation of a scan point to its nearest neighbors. The first immediate neighbors are considered in (a). Uncorrelated data represents misorientation of all the scan points with respect to one point. The scan points are shown by the hexagons. The red hexagons show the scan point which its misorientation is calculated.

the corresponding diffraction pattern is shown in [Figure 3.8](#). Such diffraction patterns allow the achievement of appropriate imaging conditions and accurate result analysis.

Sub-micron dislocation imaging was performed using scanning transmission electron microscopy (STEM). Unlike conventional TEM that images are formed by electrons passing through a sufficiently thin specimen, in the STEM the electron beam is focused to a fine spot and rasters across the sample point by point and line by line ([Figure 3.9](#)). The transmitted electrons are collected and counted for each point by STEM detectors. Scattering to different angles can produce complementary images. The bright field (BF) detector collects from unscattered electrons and electrons scattered to very low angles, whereas annular dark field (ADF) detectors measure electrons scattered to specific angular ranges, between the inner,  $\theta_1$ , and outer,  $\theta_0$ , cutoff angles in [Figure 3.9\(b\)](#). The acceptance angles for the detectors,  $\theta$ , can be tuned by changing the camera length,  $L$ , so that  $\theta = r/L$ , where  $r$  is the detector segment radius [\[94\]](#). Indeed, in STEM the user can select and define groups of electrons from the sample to fall on specific detectors by controlling the camera length. The detectors then function as an aperture, allowing only a certain group of electrons to be detected by BF or ADF and to participate in the formation of an image [\[93\]](#). As opposed to TEM imaging, where the objective lens refocuses electrons scattered by the sample onto the camera, [Figure 3.9\(a\)](#), STEM images are collected in ‘diffraction mode’, without formation of an image. Keeping the STEM probe beam in focus on the specimen avoids contrast inversions that must be corrected in TEM via the contrast transfer function. Chromatic aberration is also not an issue in STEM. The wavelength of illuminating electrons changes as they lose energy due to inelastic collisions in the specimen. In TEM this creates an out of focus haze on the camera, which is typically removed by an energy filter (spectrometer) that retains only unscattered or

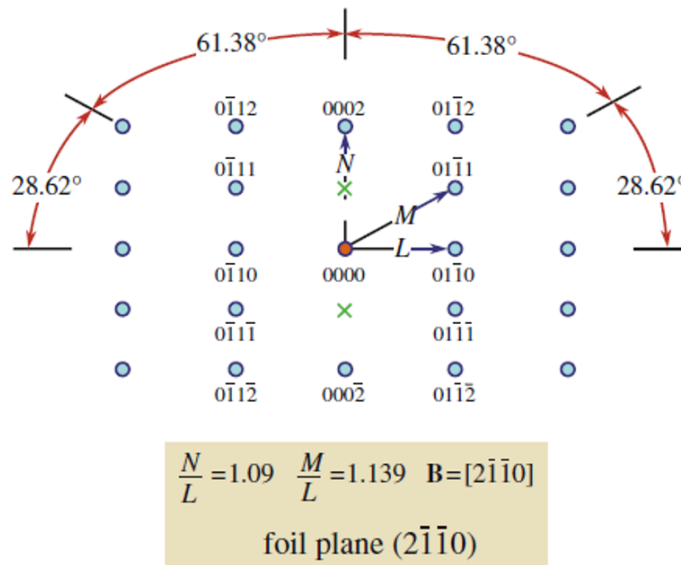


**Figure 3.8.** The standard diffraction pattern for hcp single crystals obtained from the  $\mathbf{B} = [2\bar{1}\bar{1}0]$ , where  $\mathbf{B}$  is the beam direction. Ratios of the principal spot spacings are shown as well as the angles between principal plane normals. The image is reused from [93] with permission from Springer Nature.

elastically scattered electrons to form the image. The image is clarified of haze by the filter but the sample still suffers damage from the exposure [94].

The interface chemical composition analysis at the twin boundaries was performed in this work using a high-angle annular dark-field (HAADF) imaging in STEM combined with energy dispersive spectroscopy (EDS). The HAADF imaging is undoubtedly the most popular imaging technique in STEM. The technique produces an annular dark field (ADF) image formed by a very high scattered angle, see Figure 3.10. The detector is therefore called a high-angle ADF or HAADF detector. Imaging with electrons scattered to angles larger than 40 mrad using a HAADF detector was proposed by Howie [95], in order to eliminate the presence of Bragg scattering in images. The resulting signal is shown to be incoherent and have a strong dependence on the atomic number, also known as Z-contrast imaging [96]. The term ‘Zeta’ originates from the fact that the intensity of the signal (elastically scattered electrons) is proportional to the square of the atomic number,  $Z^2$ , of the elements crossed by the beam. Since the normal ADF detector will always collect some Bragg electrons, it was necessary to design an ADF detector with a very large central aperture. Bragg effects are avoided if the HAADF detector only gathers electrons scattered through an angle of  $>50$  mrad (Figure 3.10). Thus only the electrons scattered through very high angles contribute to the image [93]. HAADF-STEM is not a chemical imaging method per se, but by collecting only a limited amount of all the possible scattering angles, HAADF detectors provide great contrast difference and give information about the various types of atoms present in the sample. Since HAADF detectors do not recover electrons from Bragg scattering, which often occurs when working with diffracting materials, HAADF imaging was initially devoted to the analysis of crystals and defects in crystals. Since the signal is proportional to the atomic mass of the

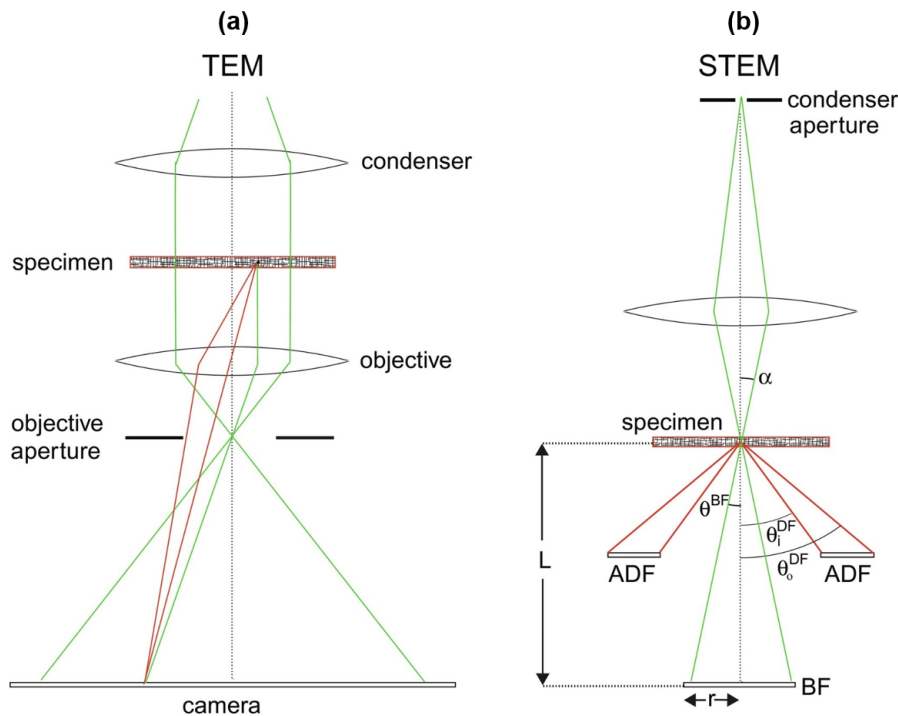


**Figure 3.9.** Schematic structures of (a) TEM and (b) STEM imaging modes. ADF and BF are the annular dark field and the bright field detectors, respectively. The semi-convergence angle is shown by  $\alpha$ . The inner and outer acceptance angles are  $\theta_i$  and  $\theta_o$ , respectively. The detector segment radius is  $r$  and the camera length is shown by  $L$ . The image is reused from [94] with permission from Elsevier.

element, HAADF produces a highly contrasted image, as compared to the resulted obtained with BF imaging and standard TEM [97].

To get good strong diffraction contrast in both BF and DF images, the specimen is tilted to two-beam conditions, in which only one diffracted beam is strong. Of course, the direct beam is the other strong spot in the pattern. The specimen can be tilted to set up several different two-beam conditions. To set up a series of two-beam conditions, a precise tilt control is needed, which explains why a double-tilt eucentric holder is the holder of choice for viewing crystalline specimens. The two-beam imaging conditions are not only necessary for good contrast but they also greatly simplify interpretation of the images [93]. To set up two-beam conditions, the specimen is tilted around while looking at the diffraction pattern until only one diffracted beam is strong. The specimen should be tilted close to the Bragg condition, in order to get the best possible strong-beam image contrast. Figure 3.11(a) shows a typical two-beam diffraction condition that was set up and used in the current work.

The type of the dislocations;  $\langle a \rangle$ ,  $\langle c \rangle$  and  $\langle c + a \rangle$  could be determined using the  $g \cdot b = 0$  invisibility criterion under two beam conditions, where  $g$  is the reflection vector and  $b$  is the dislocation Burgers vector. Dislocations are invisible or exhibit only weak contrast if  $g \cdot b = 0$ . This can be used for a Burgers vector analysis by imaging the same dislocation with different diffraction vectors and observing the contrast. As is exemplified in Figure 3.11(b),

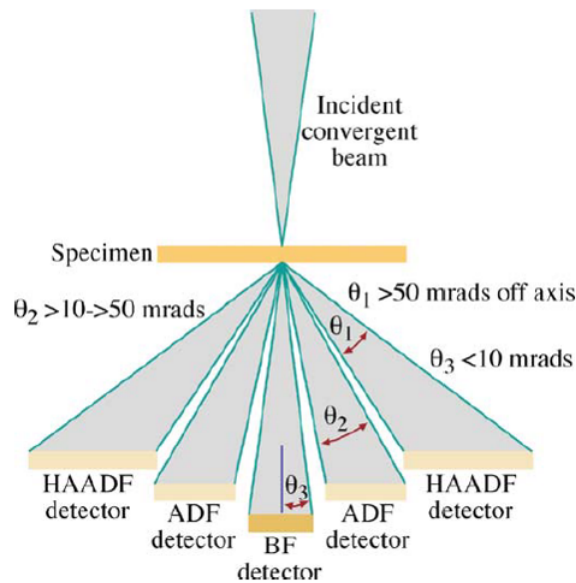


**Figure 3.10.** Schematic of HAADF detector set-up for Z-contrast imaging in a STEM. The conventional annular dark field (ADF) and bright field (BF) detectors are also depicted. The range of electron scattering angles gathered by each detector is shown. The image is reused from [93] with permission from Springer Nature.

dislocations of type *A* and *B* can be visualized or vanished using the same electron beam but at different chosen reflection vectors. If we use the reflection vector  $g_1$ , the Burgers vector for dislocation *A* is parallel to the  $g_1$  resulting in a non-zero  $g \cdot b$  value. Dislocation *A* is hence visible once using the reflection  $g_1$ . The  $g \cdot b$  product is, however, zero for the dislocation *B* once imaging with the same reflection vector,  $g_1$ , since  $g_1 \perp b_B$ . Therefore, dislocation *B* is invisible if the image is taken using  $g_1$ . Consequently, dislocations *A* and *B* can be in and out of contrast once imaging with a same beam direction but with different reflection vectors. Opposite story can happen for the reflection vector  $g_2$ , dislocation *A* is not captured in the image, while dislocation *B* shows up in the micrograph. Imaging dislocations using a same beam axis with different reflection conditions is useful in visualizing a certain type of dislocations in the studied microstructure and in determining the dislocations Burgers vectors. The practical usage of this criterion will be discussed in Chapter 4.

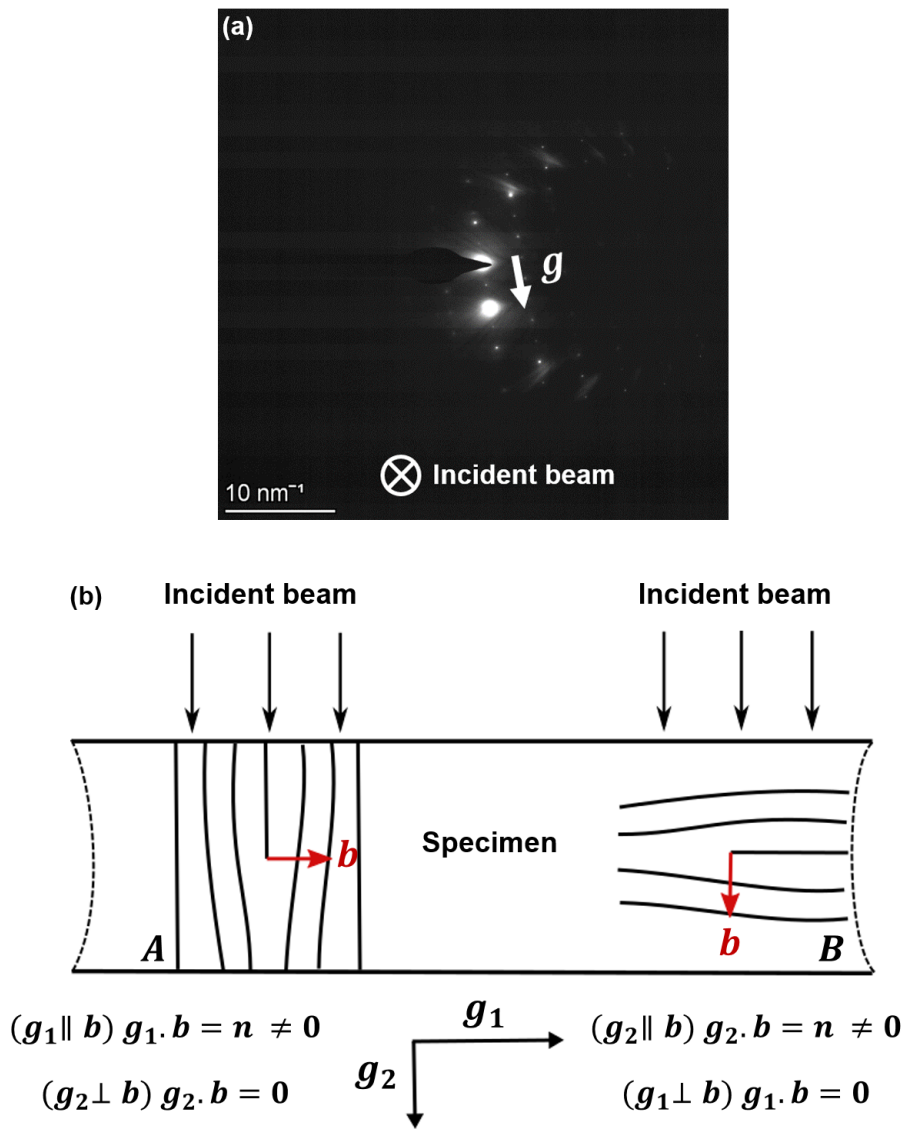


**Figure 3.11.** (a) A typical two-beam diffraction condition that was set up and used in this study to image defects. Directions of the reflection vector,  $g$ , the incident beam are shown. (b) Schematic representation of the (in)visibility  $g \cdot b$  criterion, where  $g$  is the reflection vector and  $b$  is the dislocation Burgers vector. Dislocations  $A$  and  $B$  are imaged using a same incident beam but with different reflection vectors. Dislocation type  $A$  is visible in the image taken with the reflection vector  $g_1$ , however this dislocation is out of contrast in the image captured with  $g_2$ . To visualize dislocation  $B$ , one should use the reflection vector  $g_2$ , since  $g_2 \parallel b_B$ . The reflection  $g_1$  makes this dislocation invisible, because the  $g_1 \cdot b = 0$  invisibility criterion is fulfilled.

## 4 Influence of twinning and detwinning on the [0001] compression response in pure Mg

As it was reviewed in Section 2.3, deformation twinning can reorient the crystal close to the [0001] ( $c$ -axis) orientation. The twinning mechanisms of this reorientation and the active slip systems in the  $c$ -axis oriented single crystals have been investigated by other researchers, however mostly independently. Understanding of the influence of twinning on the concurrent slip activity in [0001] single crystals is of great importance. The objective in this chapter is, therefore, to understand the origins of differences in deformation of nominally same oriented [0001] crystals with and without twinning histories. Microcompression testing is performed on three sets of micropillars in pure Mg: (i) [0001] single crystals favored for pyramidal slip, (ii)  $[10\bar{1}0]$  single crystals favored for  $\{10\bar{1}2\}$  extension twinning and (iii) [0001]/ $[10\bar{1}0]$  bicrystals favored for detwinning. This experimental schedule allows for comparing the compression response of  $c$ -axis oriented single crystals, without any twinning history, with those [0001] crystals produced as a result of twinning or detwinning reorientation. Such a comparison requires a sub-micron analysis of the defect structures after (de)twinning.

### 4.1 Experimental details

Microcompression experiments were to be performed on single as well as bicrystalline micropillars. In order to have a bicrystalline micropillar, a pre-existing twin has to exist in the grain of interest. The pre-existing twins were created through compressing a randomly textured bulk polycrystalline pure Mg sample to  $\sim 4.4\%$  strain. See Section 3.2 for details of the macro scale compression testing. The inverse pole figure (IPF) map of the sample surface after deformation is shown in Figure 4.1(a). The compressed polycrystalline sample was then heat-treated at  $350^\circ\text{C}$  for 2 hours in order to relax the deformed structure from the stored energy of defects created upon deformation. The heat-treated sample was then polished using a polishing cloth to make the sample surface appropriate for EBSD measurement and micropillar fabrication. The corresponding IPF map is shown in Figure 4.1(b). By comparing the two EBSD maps, it is shown that the total grain structure remains largely unchanged after heat-treatment. However, as marked by arrows in Figure 4.1(b), some new grains appear in the sample after heat-treatment. These grains were likely present in the sample before heat-treatment, however not reached the surface yet. The polishing step after heat-treatment made them visible. The grains of interest for further micropillar fabrication were then selected at the dashed line areas, labeled by **A**, **B** and **C**, targeted for compression of [0001] and

[10 $\bar{1}0$ ] single crystals, and [0001]/[10 $\bar{1}0$ ] bicrystals, respectively. A detailed description of the fabricated micron-sized samples and the corresponding crystallographic orientations is presented in Figure 4.2.

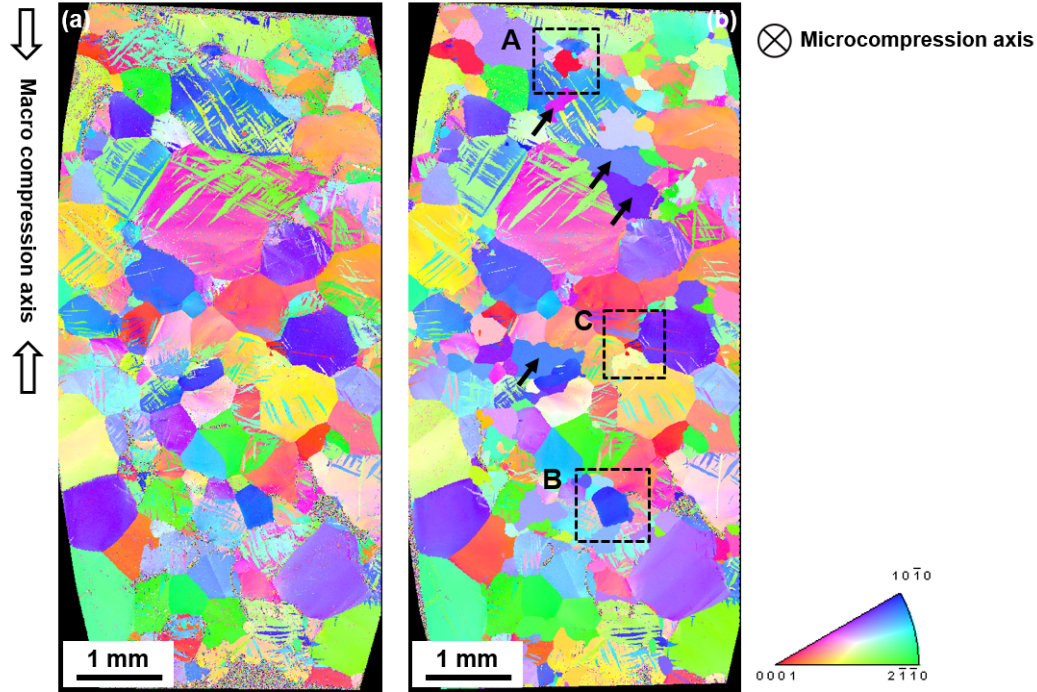


**Figure 4.1.** [001] IPF map of a bulk polycrystalline pure Mg subjected to (a) 4.4% compression followed by (b) heat-treatment at 350°C for 2 hours. Arrows mark some of the newly appeared grains after polishing. Labeled dashed line areas, **A**, **B** and **C**, show the grains selected for micropillar fabrication. Microcompression is performed along normal to the image. As is can be found from the color code IPF, the red grain **A** is oriented for compression of [0001] single crystals. The blue grain **B** is aligned for compression of [10 $\bar{1}0$ ] single crystals. The grain **C** is selected for compression of [0001]/[10 $\bar{1}0$ ] bicrystals. Further crystallographic information related to these grains together with higher magnification IPF maps and the fabricated micropillars will be presented in Figure 4.2.

A relatively large [0001] grain, grain **A**, was selected and micropillars were fabricated as shown in Figures 4.2(a) and 4.2b. No pre-existing twins are found in the grain. The micropillars are compressed roughly along the [0001] direction (Figure 4.2(c)). In fact, the loading axis approximately had 7.8° deviation from the ideal  $c$ -axis of the crystal. Such a misalignment would allow the easy activation of  $\langle a \rangle$  basal dislocations, this will be later discussed in Figure 4.6. However, the basal dislocations are not able to accommodate the applied strain along  $c$ -[0001] direction, therefore the plastic strain is expected to be governed by pyramidal  $\langle c + a \rangle$  slip [73]. This is consistent with Table 3.2, where the highest Schmid factor for the [0001] loading direction belongs to pyramidal slip.

Figures 4.2(d) and 4.2(e) show the selected [10 $\bar{1}0$ ] single crystal and the fabricated micropillars in this crystal, respectively. As shown in Figure 4.2(f), the micropillars are deformed along [10 $\bar{1}0$ ] direction, perpendicular to the crystal  $c$ -axis. As already reviewed in Section 2.3, this loading condition activates  $\{10\bar{1}2\}$  extension twinning and the twin will reorient the

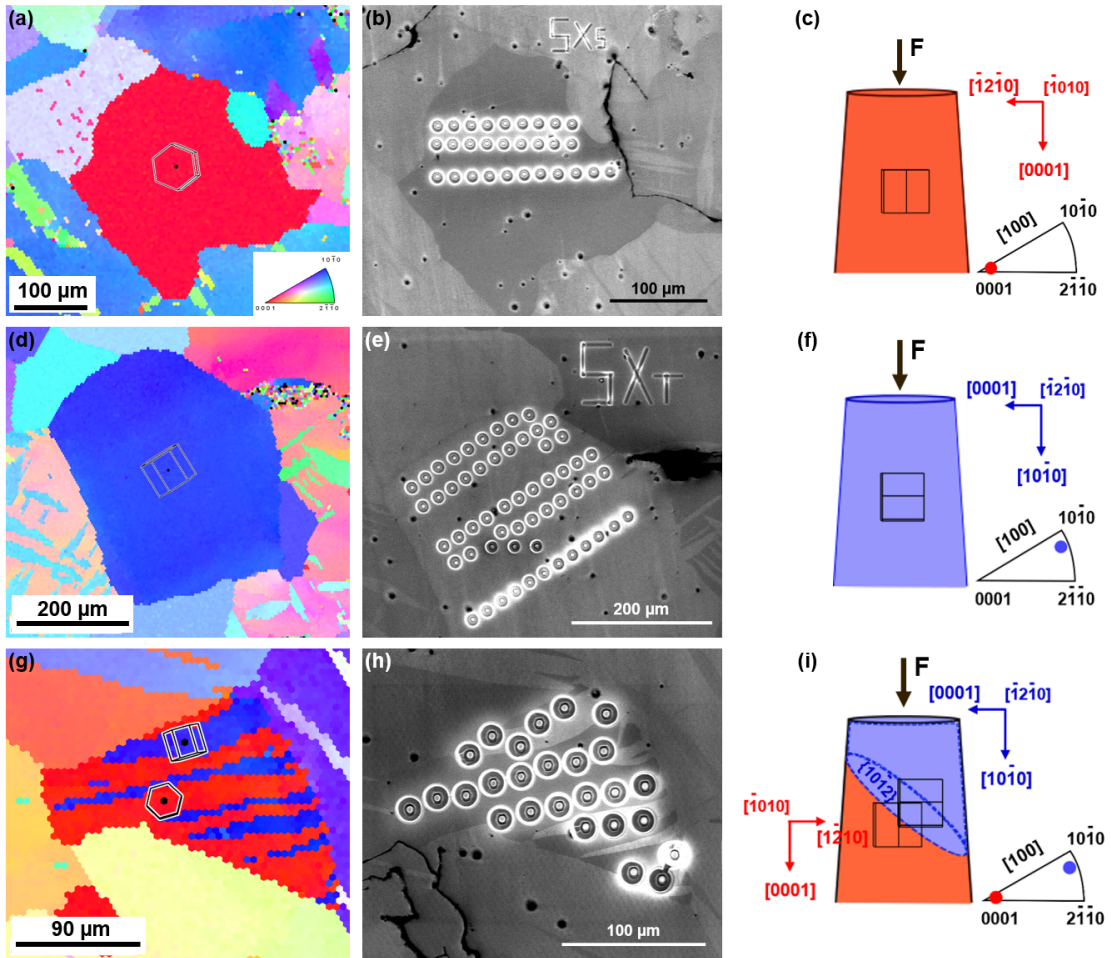


**Figure 4.2.** [001] IPF maps, scanning electron micrographs and schematic representations of the deformation conditions for the micropillars machined in (a-c) [0001] single crystals targeted for pyramidal slip, (d-f) [10 $\bar{1}$ 0] single crystals targeted for {10 $\bar{1}$ 2} twinning and (g-i) [0001]/[10 $\bar{1}$ 0] bicrystals targeted for detwinning. The rows (a-c), (d-f) and (g-i) correspond to the grains labeled by **A**, **B** and **C** in Figure 4.1. **F** represents the axis of microcompression. The IPF map in (g) characterizes the produced {10 $\bar{1}$ 2} twins in the grain. In (i), the bicrystalline micropillar includes the matrix and the twin. The samples are loaded along the [0001] direction in the matrix and along the [10 $\bar{1}$ 0] direction in the twin.

crystal close to [0001] direction [72, 73]. The highest twinning Schmid factor for this orientation is 0.5 (Table 3.2). Upon loading along [10 $\bar{1}$ 0] direction, prismatic slip operates before twin nucleation to accommodate the  $\langle a \rangle$  component of the applied strain [30, 73]. This is predictable by considering the highest Schmid factor for prismatic slip in the [10 $\bar{1}$ 0] orientation, 0.43, whereas basal slip has no chance to occur, see Table 3.2.

The [001] IPF map of the selected grain for bicrystalline deformation shown in Figure 4.2(g) characterizes the twin/matrix misorientation relationship to be a characteristic of the common {10 $\bar{1}$ 2} extension twinning in Mg. This misorientation relationship is associated with a rotation of the  $c$ -axis in the matrix grain of ca. 86° about the  $\langle 1\bar{2}10 \rangle$  axis [98]. Prior to the fabrication of the micropillars at the twin-matrix region (Figure 4.2(h)), an EBSD measurement was also conducted on the cross-section of the selected twin band. A [100] IPF

map of the twin cross-section exhibits an inclination of the twin boundary, as shown in [Figure 4.3](#). While the interface inclination with respect to the loading axis plays an important role in studying the dislocation-interface interactions [\[87, 99\]](#), the focus of the current work is on the impact of the twin boundary migration on the mechanical behavior. Bicrystalline micropillars were fabricated in a way that the columns include a twin boundary. The boundary intersects preferably the column's side, as is schematically shown in [Figure 4.2\(i\)](#). In the bicrystalline micropillars, the load is applied along  $[10\bar{1}0]$  direction in the twin. This direction is parallel to the crystal  $c$ -axis in the matrix (see [Figure 4.2\(i\)](#)). The highest twinning Schmid factors for the twin and the matrix are 0.50 and -0.5 (Table 3.2), respectively. Therefore, compression of the bicrystalline volumes is expected to be governed by a reverse twinning reorientation of the twin grain; i.e. detwinning, followed by pyramidal  $\langle c + a \rangle$  slip in the  $c$ -axis reoriented single crystal.

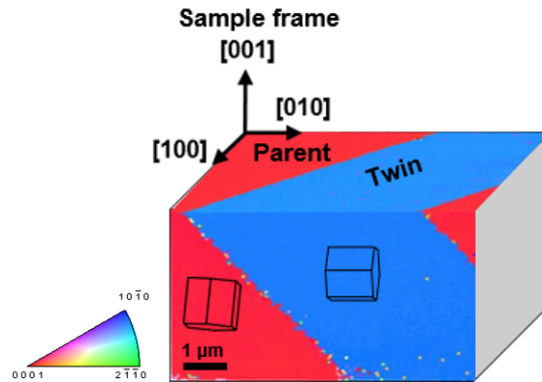


**Figure 4.3.** [001] and [100] IPF maps of a twin band showing the crystallographic arrangement of the parent grain and the twin, and the inclination of the twin boundary.

## 4.2 Microcompression of [0001] single crystals

The engineering stress-strain curves obtained from compression of the [0001] oriented single crystalline micropillars to a final engineering strain of 12% are presented in [Figure 4.4](#). A total number of 16 micropillars were successfully tested. For clarity, only four curves are shown. The deformation behavior of the micropillars is shown to be reproducible. They deform with a yield point at a nominal stress level of 170 MPa followed by a ‘stair-case’ hardening regime and then a massive strain burst at a stress level of around 365 MPa. The term ‘stair-case’ structure is referred to a sequence of discrete strain bursts occurring in the course of micropillar compression and has been used by other researchers as well [\[100, 101\]](#). The stress-strain curves look like the typical ones found for microcompression of  $c$ -axis oriented Mg single crystals, already reported by Kim [\[73\]](#), Lilleodden [\[75\]](#) and Byer and Ramesh [\[102\]](#). In particular, the similarities hold for the trend in hardening. Nonetheless, some differences in the stress-strain response are still to be expected due to the  $\sim 8^\circ$  offset from the ideal  $c$ -axis orientation in this work, along with the size of the tested samples and the deformation rates

used for microcompression testing.

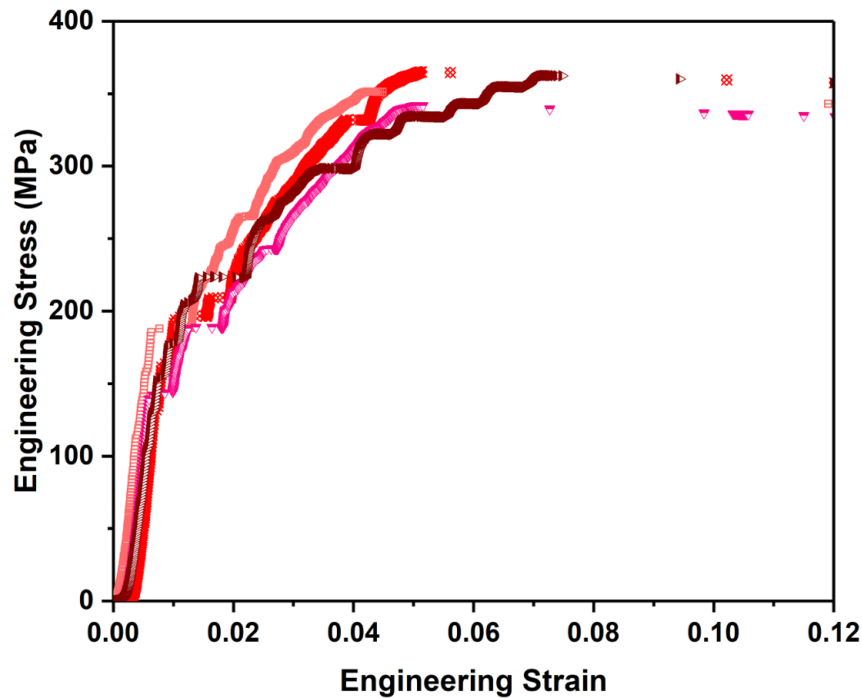


**Figure 4.4.** Engineering stress-strain curves for approximately [0001] oriented single crystalline micropillars compressed to 12% engineering strain. For pre-deformation condition, see [Figures 4.2\(a\)](#), [2\(b\)](#) and [2\(c\)](#).

Post-mortem secondary electron micrographs and the corresponding EBSD measurements performed on FIB-milled cross-sections of the micropillars compressed to varying strains are shown in [Figure 4.5](#). By increasing the unloading strain from 2.5% to 10% ([Figures 4.5\(a\)](#), [4.5\(d\)](#) and [4.5\(g\)](#)), a massive shearing of material on distinct slip planes is the main morphological characteristic of the compressed pillars. This shear instability results in the outward displacement of a top section of the column, see [Figure 4.5\(g\)](#). The sheared volume is perfectly oriented with the basal plane, serving to verify negligible misalignment issues upon microcompression. The observed deformation morphology is characteristic of the final stages of *c*-axis microcompression of Mg [[73](#), [75](#)].

The microstructures corresponding to the micropillars unloaded at 2.5% ([Figure 4.5\(b\)](#)), 5% ([Figure 4.5\(e\)](#)) and 10% ([Figure 4.5\(h\)](#)) strain show that deformation of the [0001] single crystals is governed by dislocation slip, while no evidence of twinning is observed. An increasing orientation gradient with increasing applied strain is reflected as the color gradient in the IPF maps on the cross-sections of the deformed single crystals. To quantitatively confirm the idea, uncorrelated misorientation angle distributions (introduced in [Section 3.4.2](#)) were calculated from the presented IPF maps, the results are shown in [Figures 4.5\(c\)](#), [4.5\(f\)](#) and [4.5\(i\)](#). The misorientation of the columns increases with strain up to about  $9^\circ$  after 10% strain. The increased in-grain misorientation results in a further deviation of the crystal *c*-axis from the loading direction, leading to a decrease in the required stress to initiate basal slip, see [Figure 4.6\(a\)](#), and consequent massive basal shear. This explains why basal slip occurs at the final

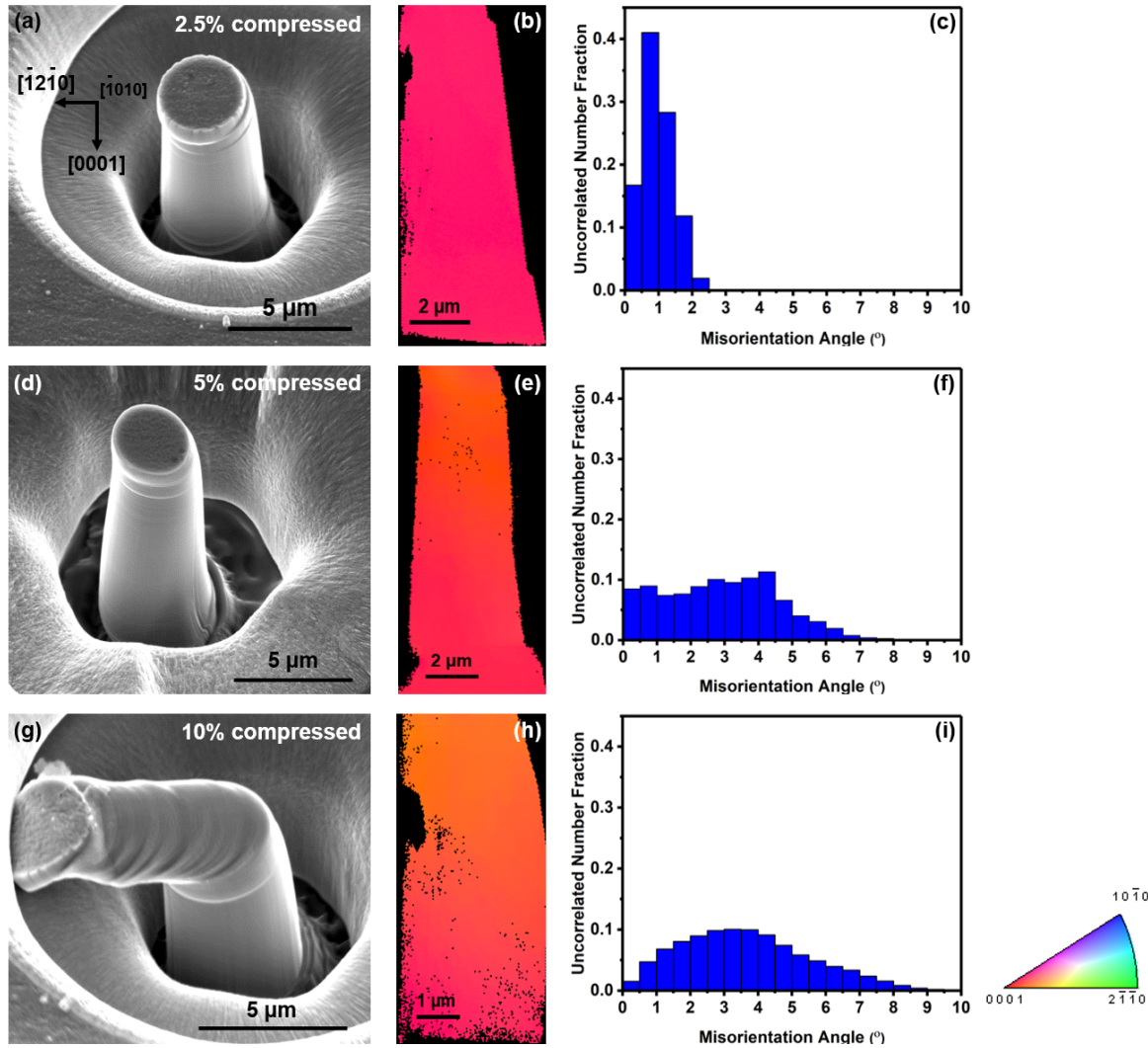


**Figure 4.5.** Post-mortem secondary electron images, the corresponding  $[100]$  IPF maps and uncorrelated misorientation angle distributions of pillars cross-sections compressed close to the  $[0001]$  axis to varying strains of (a-c) 2.5%, (d-f) 5% and (g-i) 10%. Magnifications are different. The color-code is valid for all IPF maps.

stages of  $[0001]$  compression while the Schmid factor for all the  $\langle a \rangle$ -type slip systems is zero at the start (Table 3.2).

The activation stress for basal slip at the yield point is only around 8 MPa, as is shown in Figure 4.6(a). Nevertheless, the stress increases up to about 170 MPa prior to yielding, a value nearly 21 times larger than the required stress for basal slip. Additionally, the amount of in-plane shear displacement associated with the given axial strain would be significantly greater than what is provided by the basal slip. Therefore, basal slip is definitely not the dominant plasticity mechanism in compression of  $[0001]$  single crystals. Indeed, the yield stress value in the stress-strain curves of the compressed micropillars,  $\sim 170$  MPa, is comparable to the initiation stress for pyramidal slip systems, as is seen in Figure 4.6(b). At the  $\sim 8^\circ$  deviation angle from the crystal  $c$ -axis, pyramidal dislocations would contribute to the applied load only

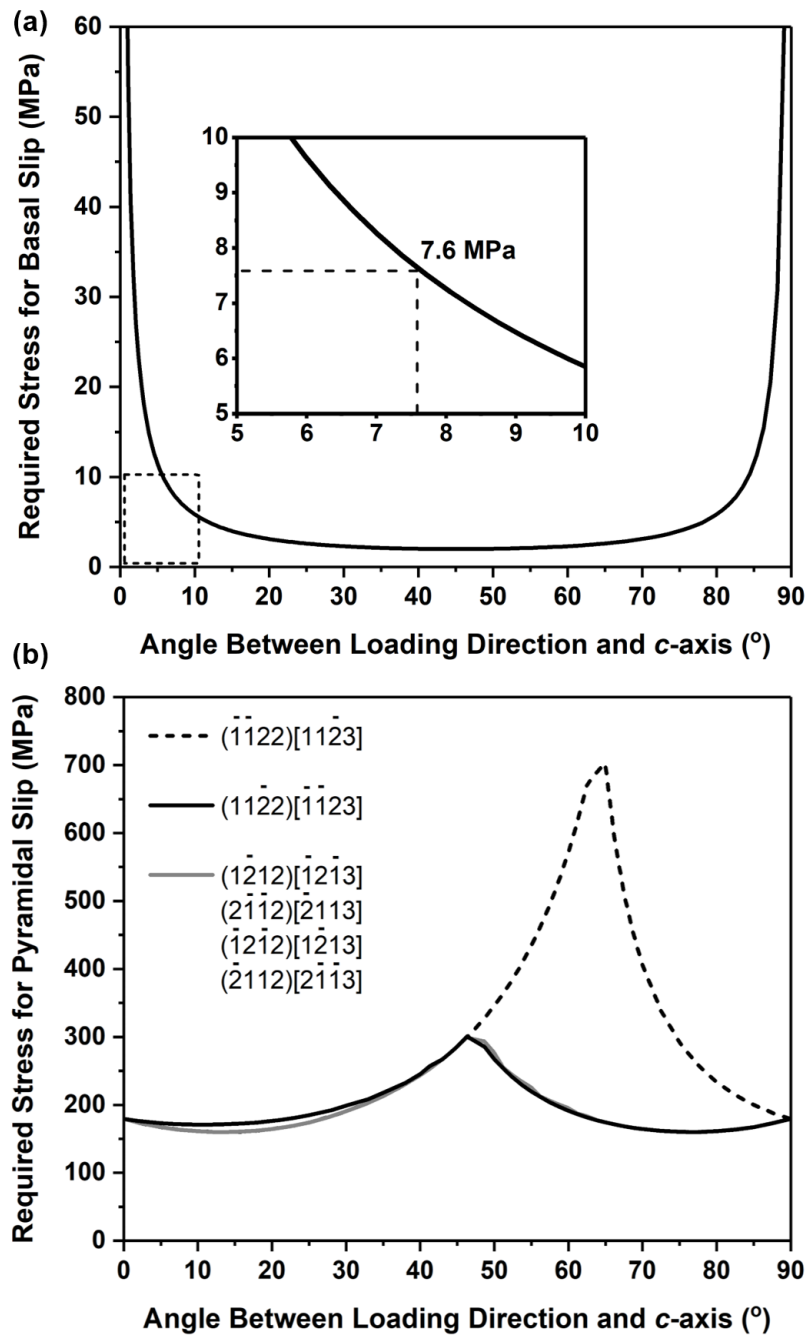


**Figure 4.6.** Required applied stress for activation of (a) basal slip and (b) pyramidal slip as a function of the angle between crystal  $c$ -axis and loading direction. All the six possible pyramidal  $\pi_2$  slip systems have been considered in (b). The critical resolved shear stress (CRSS) for basal and pyramidal slip is assumed to be 0.5 MPa and 80 MPa, respectively, according to [29, 30]. The loading axis is nearly  $8^{\circ}$  off from the crystal  $c$ -axis in the tested micropillars. There exists a strong anisotropy in the initiation stress for basal and pyramidal slip systems at a fixed deviation angle from the crystal  $c$ -axis.

once a resolved stress higher than 150 MPa is achieved, which is far beyond the requirement for easy basal slip.

A more detailed discussion about the active slip systems and, in particular, the origins of the observed work hardening capacity in compression of [0001] oriented single crystalline micropillars was achieved using transmission electron microscopy (TEM). Scanning transmission electron microscopy (STEM) was used for dislocation imaging. A bright-field image taken from a sample interrupted at 5% engineering strain is shown in Figure 4.7. The diffraction pattern presented in Figure 4.7(a) indicates that the zone axis is close to  $[2\bar{1}\bar{1}0]$ , parallel to the basal plane. A two-beam condition with the  $g = \{0002\}$  reflection was used to image the dislocations, as indicated in Figure 4.7(b). As described in Section 3.4.3, the  $g \cdot b = 0$  invisibility criterion where  $g$  is the reflection vector and  $b$  is the dislocation Burgers vector, was used to determine the character of dislocations present in the sample. Table 4.1 shows the values of  $g \cdot b$  for all the perfect  $\langle a \rangle$ ,  $\langle c \rangle$  and  $\langle c + a \rangle$ -type dislocations in Mg for the reflection and the zone axes used in our TEM measurements.

Based on the  $g \cdot b$  values, all the  $\langle a \rangle$ -type dislocations will be out of contrast, while the  $\langle c \rangle$  and  $\langle c + a \rangle$ -type dislocations will be in contrast for the  $g = \{0002\}$  reflection. The  $\langle c \rangle$  and  $\langle c + a \rangle$ -type dislocations cannot be unambiguously distinguished by using  $\{0002\}$  reflection alone. At least one more reflection condition, where only  $\langle a \rangle$ -type dislocations are visible, is required. Therefore, Figure 4.7(c) shows a typical dense array of either  $\langle c \rangle$  or  $\langle c + a \rangle$  dislocations for a micropillar compressed nearly parallel to the  $c$ -axis. The pure  $\langle c \rangle$  dislocations are generally immobile since they do not have a specific slip plane, therefore  $\langle c + a \rangle$  dislocations would be the governing carriers of plasticity during compression of Mg single crystals along the crystal  $c$ -axis. This has been supported in literature by measurements of the resolved shear stress [75], as well as by direct observation of the active slip systems achieved through TEM [73, 102-106].

**Table 4.1.** The  $g \cdot b$  values for perfect dislocations in Mg using a  $[2\bar{1}\bar{1}0]$  zone axis and a  $g = \{0002\}$  reflection.

Dislocation type	$\mathbf{b}$	$\mathbf{g} \cdot \mathbf{b}$
$\langle a \rangle$	$1/3 [11\bar{2}0]$	0
	$1/3 [\bar{1}2\bar{1}0]$	0
	$1/3 [2\bar{1}\bar{1}0]$	0
$\langle c + a \rangle$	$1/3 [\bar{1}\bar{2}13]$	$\pm 2$
	$1/3 [2\bar{1}\bar{1}3]$	$\pm 2$
	$1/3 [11\bar{2}3]$	$\pm 2$
	$1/3 [\bar{1}2\bar{1}3]$	$\pm 2$
	$1/3 [2\bar{1}13]$	$\pm 2$
	$1/3 [\bar{1}\bar{1}23]$	$\pm 2$
$\langle c \rangle$	$[0001]$	$\pm 2$

Close examination of the image shown in Figure 4.7(c) reveals that many of the dislocations are present in a zigzag configuration, some examples are marked by dashed circles. This observation is very similar to the  $\langle c + a \rangle$  dislocation structure achieved in  $c$ -axis compression of Mg in other studies [103, 104, 106]. The zigzag configuration for individual dislocations might result from the double cross-slip of the screw components of  $\langle c + a \rangle$  dislocations be-

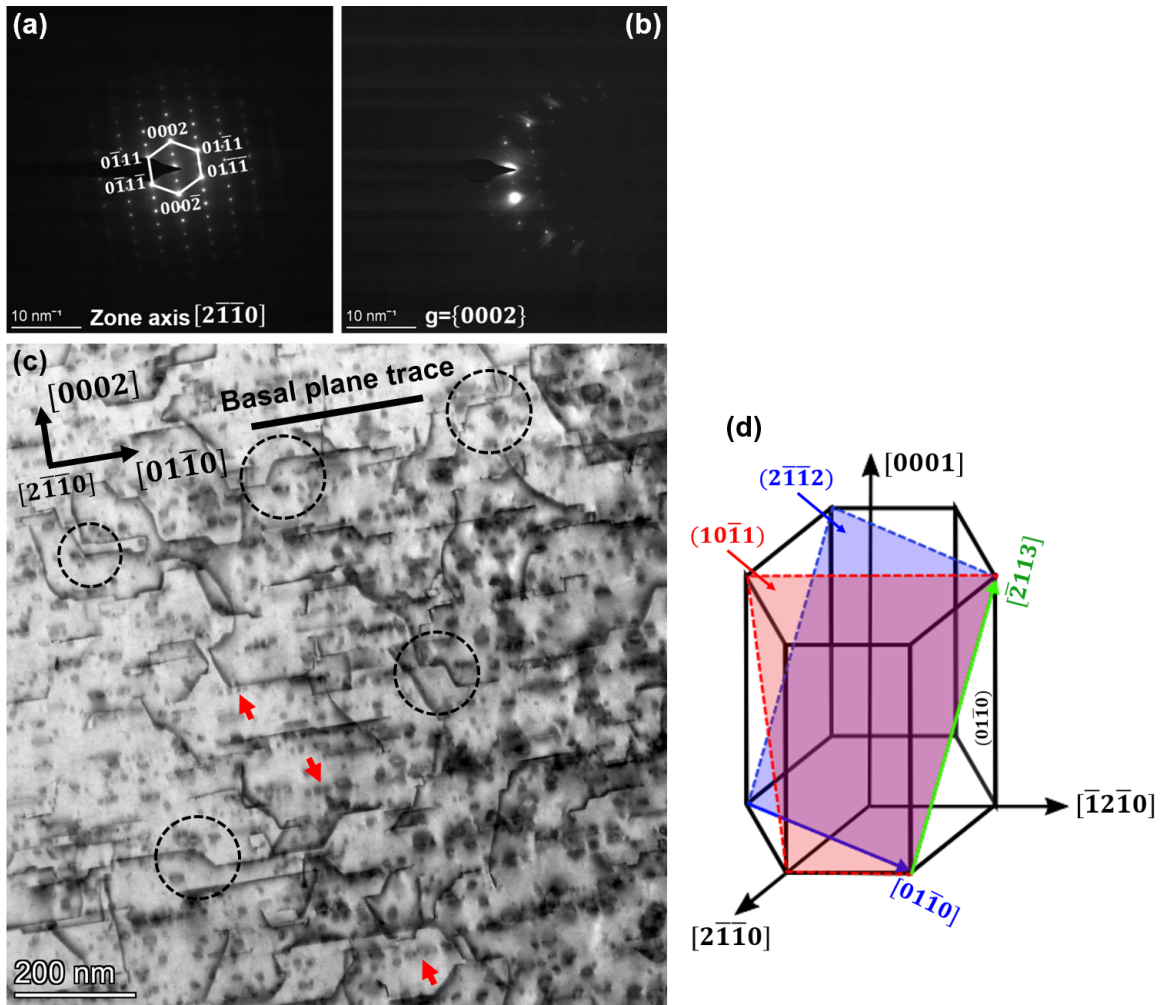
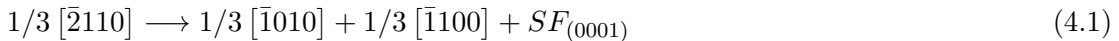


**Figure 4.7.** STEM observation of a  $\sim[0001]$  oriented single crystalline pillar compressed to 5% strain. (a) A  $[2\bar{1}\bar{1}0]$  zone axis electron diffraction pattern, (b) the selected two-beam condition for dislocation imaging using  $g = \{0002\}$  diffraction vector, (c) the bright-field image showing dislocations with either  $\langle c \rangle$  or  $\langle c + a \rangle$ -component Burgers vectors. Zigzag configurations of dislocations are marked by dashed circles. Rows of fine dislocation loops are shown by red arrows. (d) Schematic illustration of a hexagonal cell showing crystallographic planes and directions. First- and second-order pyramidal planes sharing a common  $\langle c + a \rangle$ - $[\bar{2}113]$  zone (green vector) are shown as red  $(10\bar{1}1)$  and blue  $(2\bar{1}\bar{1}2)$ , respectively. The  $[01\bar{1}0]$  intersection line between the basal and  $(2\bar{1}\bar{1}2)$  pyramidal planes is shown in blue, which is perpendicular to the green  $[\bar{2}113]$ .

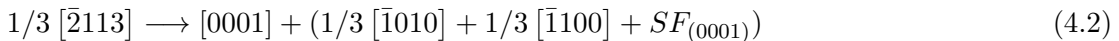
tween the first- and second-order pyramidal planes [104, 107]. As schematically illustrated in Figure 4.7(d), the first-order  $\{10\bar{1}1\}$  and second-order  $\{2\bar{1}\bar{1}2\}$  pyramidal planes are the only slip plane families that share a common  $\langle c + a \rangle$ -Burgers vector along the  $\langle \bar{2}113 \rangle$  zone. Therefore,  $\langle c + a \rangle$  dislocations moving on one pyramidal plane may cross-slip into the other plane and then again cross-slip back into the original plane unimpeded. This process would produce such a zigzag dislocation configurations. The zigzag dislocation pattern is made up of long straight dislocation segments lying preferentially parallel to the basal plane trace along  $\langle 01\bar{1}0 \rangle$  directions. As depicted in the schematic of the hexagonal cell in Figure 4.7(d), the basal and second-order  $\{2\bar{1}\bar{1}2\}$  pyramidal planes intersect at  $\langle 01\bar{1}0 \rangle$  zone. The dislocations

along this zone are bounded at the intersection between basal and  $\{2\bar{1}\bar{1}2\}$  pyramidal planes and possess both the  $\langle a \rangle$  and  $\langle c \rangle$  components. Moreover, these dislocations lying along the intersection line,  $\langle 01\bar{1}0 \rangle$ , are perpendicular to the  $\langle c + a \rangle$  Burgers vector along  $\langle \bar{2}113 \rangle$  zone, see Figure 4.7(d). Therefore, the straight dislocation segments, as part of the zigzag pattern shown in Figure 4.7(c), are likely those  $\langle c + a \rangle$  dislocations bounded at the intersection of the basal and pyramidal planes having a pure edge character. The presence of such straight edge dislocations along the pyramidal-basal intersection line as debris in the deformed structure has been attributed to the low mobility of  $\langle c + a \rangle$  edge dislocations [103, 104] and dissociation of  $\langle c + a \rangle$  dislocations into partials and basal stacking faults [48, 103, 108]. In the preliminary TEM work by Obara et al. [103] and more recent observations [104, 107], it was concluded that the strong binding of  $\langle c + a \rangle$  dislocations on basal planes implies that the edge dislocations are much less mobile than their screw counterparts. The process of  $\langle c + a \rangle$  (double) cross-slip is, therefore, facilitated by the higher mobility of the screw components leaving behind the progressive development of straight edge dislocation debris lying along  $\langle 01\bar{1}0 \rangle$  in the structure [104].

Regarding dislocation reactions, a common view outcoming from atomistic simulations is that dislocations on the pyramidal planes with the large  $\langle c + a \rangle$  Burgers vector might dissociate into partials. Several possible ways of the dissociation have also been proposed [108–111]. As speculated by Obara et al. [103] and later predicted by Ando et al. [108] using molecular dynamics simulation, one possibility is the dissociation of  $\langle c + a \rangle$  edge dislocations into two perfect dislocations of the  $\langle a \rangle$  and  $\langle c \rangle$ -type, such that the  $\langle a \rangle$  dislocation further dissociates into two Shockley partials on the basal plane leaving behind a basal stacking fault, according to:



The  $\langle c \rangle$  component is not dissociated into partials and therefore the dissociation of a  $\langle c + a \rangle$  edge dislocation at the intersection of the pyramidal and basal plane might be described as follows:



Using a Burgers vector analysis of individual dislocations under varying reflection conditions, this so-called nonplanar  $\langle c + a \rangle$  dissociation has been experimentally evidenced by Agnew et al. [48] and Sandlöbes et al. [112]. Accordingly, this decomposition into the basal plane may explain why the  $\langle c + a \rangle$  dislocation lines tend to lie along the intersection of the second-order pyramidal plane and the basal plane [48], as shown in Figure 4.7. The two  $1/3\langle \bar{1}010 \rangle$  partials introduced in Eqs. (4.1) and (4.2) are necessary to recombine in order to be able to move on the basal plane [108]. In addition, since the resolved shear stress for the dissociated  $\langle c \rangle$ -[0001] dislocations is zero while loading along the crystal  $c$ -axis, they may be immobile.

As a consequence, nonplanar dissociations such as those of Eqs. (4.1) and (4.2) represent locking configurations, having a very large Peierls-Nabarro friction stress [48], as supported by atomistic simulations [108, 113] and TEM observations [114].

Apart from the dislocation lines in Figure 4.7(c), rows of fine dislocation loops appear in the structure, as marked by red arrows. Their appearance is not easily visible at the provided magnification. Nevertheless, the loops array parallel to the straight dislocation segments along the basal plane trace. Similar to the dislocation lines, the loops might also have a  $\langle c \rangle$  or  $\langle c + a \rangle$ -type Burgers vector since they are visible under the  $g = \{0002\}$  reflection. In agreement with the current study, other researchers have also reported the presence of such fine dislocation loops along basal plane traces in  $c$ -axis compressed Mg single crystals [103, 106, 115, 116]. Geng et al. [116] analyzed the structure of such loops using TEM. By showing a symmetric change in the shape of a dislocation loop as it was tilted about the basal plane, the authors proposed that these loops might lie on (0001) basal planes. Their  $\langle c + a \rangle$  Burgers vector is therefore out of the plane of the loop, making the loops sessile. Price [117] was one of the first ones who observed these loops in deformed Cd, also having hcp structure, and attributed them to dislocation dipoles. Geng et al. [116] proposed that the dipoles might be produced by repeated intersection of a gliding screw dislocation segment with stationary edge segments, lying along the various  $\langle 01\bar{1}0 \rangle$  directions, which was observed in our TEM observation. This would produce edge dipoles where each arm of the dipole, lying along the  $\langle 01\bar{1}0 \rangle$  directions, would contribute to the generation of dislocation loops. The idea has been very recently supported by in-situ TEM nano-compression of [0001] oriented pillars [105], where the formation of an edge dislocation dipole resulted in a sessile  $\langle c + a \rangle$  dislocation loop.

Relative to other orientations, Mg single crystals exhibit the highest work hardening capacity under compression along the [0001] direction [73]. To understand the mechanisms responsible for this high work hardening, the possible roles of the dominant slip mechanism, i.e.  $\langle c + a \rangle$  pyramidal slip, and also the occurrence of twinning is considered here. The latter has been mostly reported in compression of bulk single crystals [72, 106, 118]. In the late 1960s, Kelley and Hosford [72] and Wonsiewicz [118] performed plane-strain compression on Mg single crystals and observed  $\{10\bar{1}1\}$ -contraction twinning as well as  $\{10\bar{1}2\}$ -extension twinning in the post-deformed structures. For the contraction twins, their number density was found to be extremely small as compared to the total volume of the bulk specimen [72], as more recently confirmed by TEM observations [106]. For the extension twins, the appearance of this unexpected twin type under compression along the  $c$ -axis has been attributed to the residual stresses due to non-homogeneous flow [118]. By this assumption, the cited author has pointed out that extension twins only occur during unloading; this was later confirmed by an in-situ optical observation of a  $c$ -axis compressed Mg single crystal [106]; extension twins appeared during unloading and disappeared upon reloading. In contrast to bulk samples and consistent with the presented results in Figure 4.5, deformation twinning has not been observed during compression of [0001] oriented micron-size pillars [73, 75]. This might be due to the more controlled stress state under microcompression where pre-existing twins and preferred nucleation sites for twinning can be avoided.

Activation of six equivalent pyramidal  $\pi 2$  slip systems having  $\langle c + a \rangle$  Burgers vector is suggested to account for the high strain hardening capacity in  $c$ -axis compression of Mg single crystals [75]. There are six slip systems in this family and no two are coplanar and all six are equally favorably disposed when compression is performed along the  $c$ -axis. Therefore, screw dislocations have ample opportunities to intersect other moving screw dislocations and also the relatively immobile straight edge dislocations. This may produce jogs that can contribute to work hardening as well [73, 116]. Furthermore, the fine dislocation loops observed in the deformed structure might act as obstacles to moving dislocations and thus contribute in part to the work hardening of compressed micropillars. At the final stages of compression, Kim [73] proposed that the massive strain burst observed in the corresponding stress-strain curves is associated with the escape of dislocations on the basal slip system. This might happen when the actual stress is sufficient to overcome the tangles of intersecting dislocations in the pyramidal slip system.

### 4.3 Microcompression of $[10\bar{1}0]$ single crystals

Representative engineering stress-strain curves associated with the microcompression of four single crystalline micropillars along the  $[10\bar{1}0]$  axis to an approximate engineering strain of 12% are shown in Figure 4.8. The mechanical response shows smooth, largely elastic loading up to a stress plateau in the range of 104-134 MPa. At this critical stress, a large strain extension to a strain of around 6% occurs. Upon continued loading, the stress linearly increases up to a secondary yield followed by a smooth strain hardening, reaching stress values between 470 to 550 MPa, values significantly higher than those found for the [0001] single crystals loaded to 12% strain (see Figure 4.4). Similar deformation behavior has been reported at macro [72, 119] and micron scale [73, 120] during compression testing of Mg single crystals along  $[10\bar{1}0]$  direction.

The observed strain burst (or stress plateau) is associated with  $\{10\bar{1}2\}$  extension twinning, as already confirmed in previous studies [73, 74, 120]. Indeed, extension twinning is expected to be activated under compression parallel to the basal plane, which is the case in the tested micropillars. Twinning will therefore contribute to the axial compressive stress. The longitudinal strain accommodated by twinning shear is given by [52, 121]:

$$\varepsilon = f_{\text{twin}} m \gamma \quad (4.3)$$

where  $f_{\text{twin}}$  is the twin volume fraction,  $m$  is the twinning Schmid factor (0.5 upon compression along  $[10\bar{1}0]$ ) and  $\gamma$  is the twinning shear for extension twinning. The twinning shear for Mg is 0.129, according to Yoo [32]. The maximum capacity of a twin to strain contribution is reached when the entire volume of a micropillar is twinned,  $f_{\text{twin}} \simeq 1$ . This would lead to a maximum axial strain of  $\varepsilon = (1) \times (0.5) \times (0.129) = 0.0645$ , consistent to the end of stress plateau at around 6% strain in Figure 4.8. The  $\{10\bar{1}2\}$  twinning exhausts at this strain level

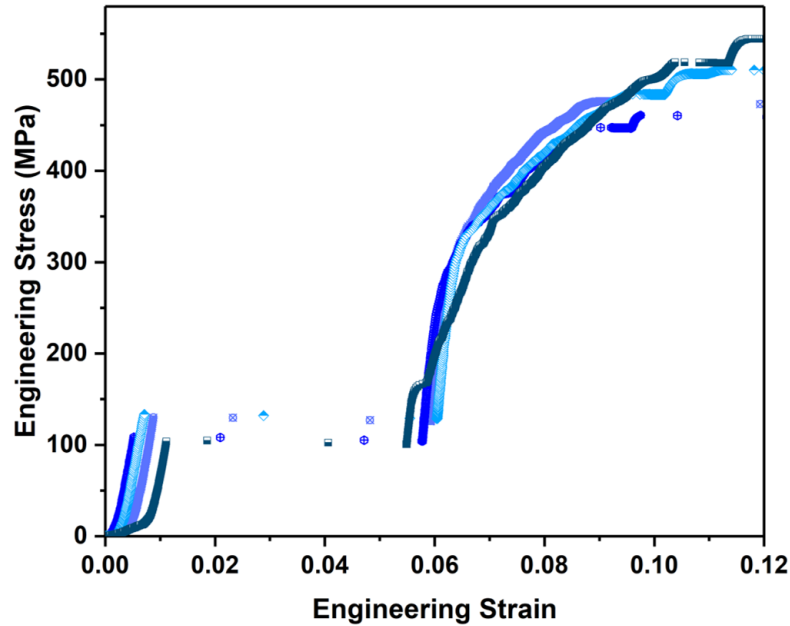


**Figure 4.8.** Engineering stress-strain curves for  $[10\bar{1}0]$  oriented single crystalline micropillars compressed to 12% engineering strain. For pre-deformation condition, see [Figures 4.2\(d\), 2\(e\)](#) and [2\(f\)](#).

and further compression must be accommodated by a reoriented crystal as a consequence of twinning. This hypothesis is further confirmed by revealing the deformation microstructures.

Post-mortem secondary electron micrographs and the corresponding EBSD measurements performed on FIB-milled cross-sections of the micropillars before and after microcompression to varying strains are presented [Figure 4.9](#). Prior to compression, the micropillar is a single crystal with basal planes parallel to the  $[10\bar{1}0]$  loading axis ([Figures 4.9\(a\)](#) and [4.9\(b\)](#)). The micropillar is free of any pre-existing twin. The uncorrelated misorientation angle distribution revealed in [Figure 4.9\(c\)](#) suggests a level of pre-deformation inside the crystal. This is because the initial grain shows up to  $2.5^\circ$  in-grain misorientation. This, however, is taken to be constant for all the fabricated micropillars inside the selected grain and therefore it would not influence our interpretation while comparing the results.

The SEM image of a micropillar unloaded at 5% strain, a strain still within the plateau stress, shows a slight tilt in the vertical pillar edge at the top, see [Figure 4.9\(d\)](#). The EBSD map shown in [Figure 4.9\(e\)](#) indicates a crystal reorientation of the whole pillar by about  $86^\circ$  from the initial  $[10\bar{1}0]$  direction, confirming the crystal reorientation induced by  $\{10\bar{1}2\}$  extension twinning. Therefore, the change of the sample edge geometry might be due to the nucleation of an extension twin and the associated crystal reorientation, the twin thickens via migration of the twin boundary throughout the pillar at a rather constant stress. The misorientation angle distribution corresponding to the formed twin (red crystal) shows higher values within the twin compared to the initial crystal ([Figure 4.9\(f\)](#)). Compared to the pre-compression state, the twin doesn't seem to have experienced a massive dislocation activity, and the maximum misorientation value is still around  $3^\circ$ . In this regard, activity of prismatic  $\langle a \rangle$  dislocations at early deformation stages of such twinning favored orientation may play a

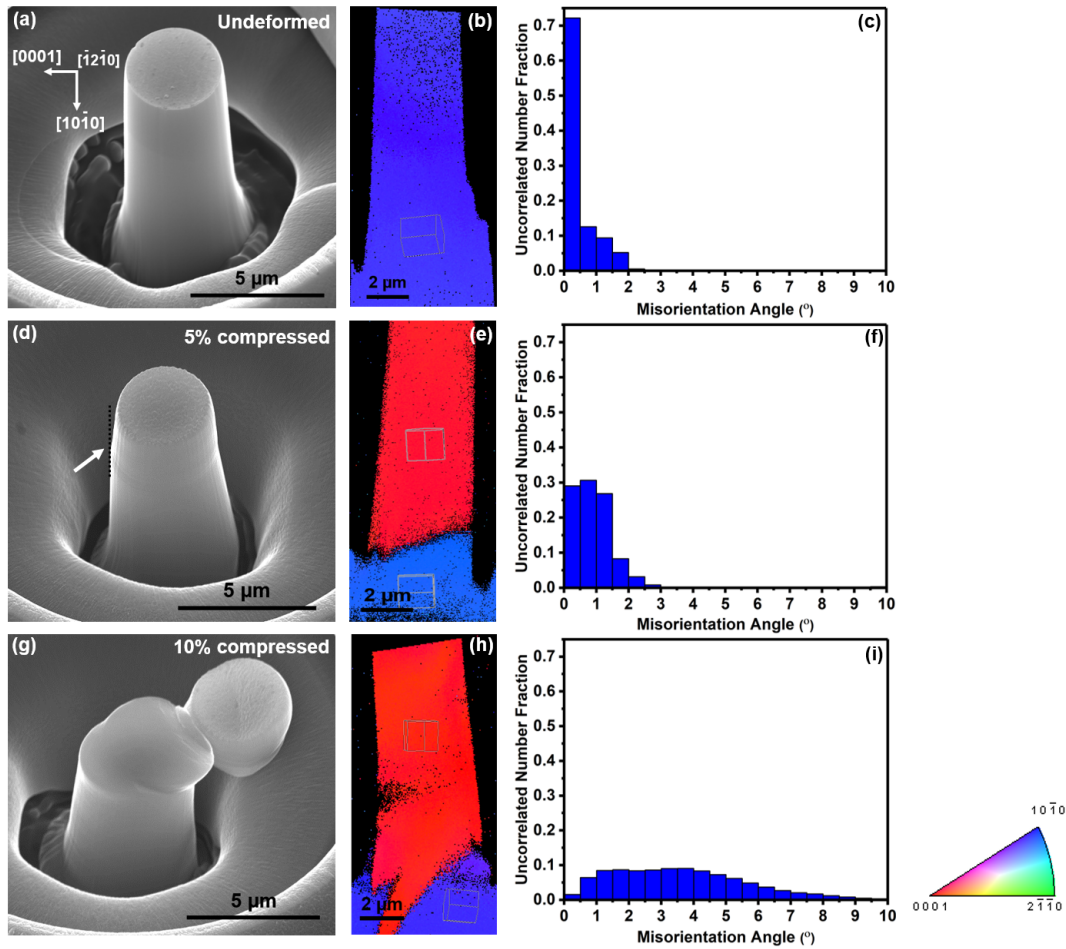


**Figure 4.9.** Post-mortem secondary electron images, the corresponding  $[100]$  IPF maps and uncorrelated misorientation angle distributions of pillars cross-sections in the (a-c) initial state, and compressed close to the  $[10\bar{1}0]$  axis to varying strains of (d-f) 5% and (g-i) 10%. The tilt in the vertical pillar edge after twinning reorientation is marked by white arrow in (d). The misorientation angle distributions in (f) and (i) were calculated for the red-colored twinned  $[0001]$  oriented crystals. The color-code is valid for all IPF maps.

critical role in twin formation and propagation, as reported by Kim [73] and very recently observed during in-situ testing by Jeong et al. [30]. Note that the highest Schmid factor for basal and prismatic slip in the tested orientation is 0 and 0.43 (Table 3.2), respectively. More details about the dislocation structure is discussed later in this section.

When the pillar is entirely twinned, the sample possesses a hard orientation with the  $c$ -axis close to  $[0001]$  direction (Figure 4.9(e)). The new loading axis is  $[10\bar{1}30]$  and is only  $3.8^\circ$  deviated from the  $[0001]$  direction. Loaded along this new direction, the highest Schmid factor for  $\{10\bar{1}2\}$  twinning, basal  $\langle a \rangle$  and pyramidal  $\pi 2 \langle c + a \rangle$  slip is -0.5, 0.03 and 0.46, respectively (see Table 3.2). Thus, compression beyond the plateau strain, where the micropillar is fully twinned, might be mainly accommodated by pyramidal  $\pi 2 \langle c + a \rangle$  slip with a final activation of basal dislocations, as described in the case of the  $[0001]$  samples in Section 4.2. Accordingly, the strong hardening following the plateau might be due to the cross-slip of  $\langle c + a \rangle$  dislocations

on equivalent pyramidal planes. This would lead to an increased misorientation inside the crystal compared to the as-twinned state accompanied by a higher deviation of the crystal  $c$ -axis from the loading direction, and leading to an increase in the resolved shear stress on the basal planes and consequent massive basal shear, see Figures 4.9(g), 4.9(h) and 4.9(i).

In order to investigate the defect structure inherited from  $\{10\bar{1}2\}$  twinning, the cross-section of the micropillar compressed to 5% strain (Figure 4.9(e)), where a single extension twin had propagated through almost the entire micropillar, was characterized using STEM. A bright-field micrograph taken from the sample is presented in Figure 4.10(a). The diffraction pattern taken from the twin crystal shows that the electron beam is nearly parallel to the  $[2\bar{1}\bar{1}0]$  zone axis (Figure 4.10(b)). A twin boundary crossing the width of the micropillar is located at the pillar's bottom. Convex- and concave-shaped sections together with a wedge-shaped twin extrusion have been developed on the twin boundary. The interface bounding the twin is curved and the extended trace of the  $\{10\bar{1}2\}_{\text{twin}}$  plane into the matrix (dashed line) does not coincide with the trace of the matrix twinning plane,  $\{10\bar{1}2\}_{\text{matrix}}$ . The observation suggests that the twin boundary deviated from the  $\{10\bar{1}2\}$  twinning plane during microcompression and thus the boundary is, at least partly, incoherent.

In the classical twinning framework, a twin boundary is expected to occur along the invariant  $\{10\bar{1}2\}$  plane to provide strain compatibility at homogeneous deformation conditions [60]. Similar observations of inclination of  $\{10\bar{1}2\}$  twin boundaries in hcp metals have been reported. Wang et al. [122] observed local bulging of twin boundaries during tension experiments of bulk Mg single crystals and it was attributed to the local interaction of gliding basal dislocations with the twin boundary. Extremely incoherent twin boundary regions due to local stresses were found after microhardness indentations of Zn and Mg [123]. The observed deviation of the twin boundary from the  $\{10\bar{1}2\}$  plane in Figure 4.10(a) might be related to local inhomogeneous deformation near the boundary in compressed micropillars. A rather large degree of inhomogeneity in twin-associated stress fields has been reported [124–126]. Numerical analysis has predicted that such stress inhomogeneity at the twin vicinity is related to the gradient distribution of twinning dislocations along the twin interface [124, 126]. This may cause diverse events of stress concentration, through dislocation pileup at the interface, and plastic relaxation, through dislocation emission from the twin tip [124]. As the defect content of the twin interfaces may not be symmetric, interactions of gliding dislocations with twin boundaries may vary from one interaction point to another. Such a non-classical  $\{10\bar{1}2\}$  twinning behavior has also been explained by other scenarios, where a shuffling-dominated growth mechanism is taken into account (see Section 2.2.2). Zhang et al. [67] observed twin boundaries in Co and Mg that were significantly deviated from the  $\{10\bar{1}2\}$  plane. They suggested that such large deviations can only be understood with the shuffling-dominated twinning mechanism. In this mechanism, a correct twin lattice is created only when the invariant plane strain condition is broken, and therefore the twinning plane is distorted [57]. Atomic shuffling does not have to be confined to the  $\{10\bar{1}2\}$  twinning plane and it is acceptable that twin boundaries can migrate off the twinning plane during growth [67].

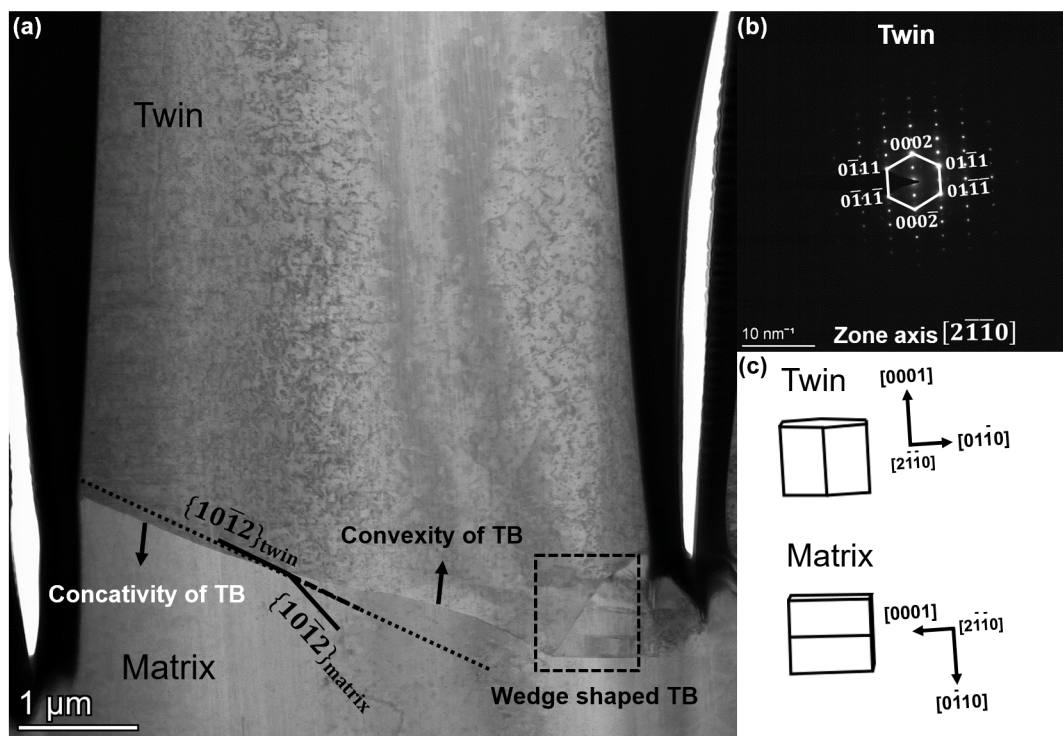


**Figure 4.10.** (a) A bright-field STEM micrograph from the cross-section of a single crystalline micropillar compressed along the  $[10\bar{1}0]$  to 5% strain. The micropillar is almost entirely twinned. The twin boundary (TB) shows convex- and concave-shaped sections together with a wedge-shaped twin extrusion, as specified in the image, the dotted line at the twin boundary is to guide the eye. Traces of the twinning plane in twin and matrix are marked. The twin boundary is shown to be locally incoherent, as evidenced by deviations from the invariant  $\{10\bar{1}2\}$  twinning plane. The extended trace of the twinning plane in the twin, marked by the dashed line, does not coincide with the twinning plane trace in the matrix. The corresponding EBSD map of the cross-section is shown in Figure 4.9(e). (b) The diffraction pattern of the twin crystal was captured using an electron beam close to the  $[2\bar{1}\bar{1}0]$  zone axis of the twin. (c) The crystallographic information of the matrix and twin lattices is given.

The twinned micropillar shown in Figure 4.10 was further examined at higher magnifications and at different two-beam diffraction conditions, where  $\langle c \rangle$ - and  $\langle a \rangle$ -containing defects are discernible. A dark-field STEM image taken at the vicinity of the twin boundary is shown in Figure 4.11(a). As is seen, a high density of well-defined long parallel fringes is clearly observed in the interior of the twin; some examples of which are marked by black arrows. The fringes are perfectly aligned along the trace of the basal plane in the twin. The selected two-beam diffraction condition using an electron beam with a zone axis close to the  $[2\bar{1}\bar{1}0]_{\text{twin}}$  and a  $g = (01\bar{1}0)_{\text{twin}}$  reflection vector is displayed in Figure 4.11(b). As indicated by white arrows, streaking of spots along the  $[0001]$  direction occurs in diffraction pattern, this is indicative of populated planar faults in the basal plane [127]. In reciprocal space, planar faults appear slender rods. The rods are cut by the Ewald sphere under certain diffraction conditions, resulting in a streaking that connects the diffraction spots corresponding to the planes the faults are lying in [128]. Indeed, the observation of fringes along the basal plane trace as well as streak-

ing in the diffraction pattern provide clear evidence that these are characteristics of basal stacking faults (SFs) formed on the basal plane in the twinned lattice. Interestingly, these SFs have lengths over hundreds of nanometers. In some cases the SFs were found to extend more than 700 nm, and this is believed to be two to three orders of magnitude larger than the equilibrium width of the basal SFs that are associated with partial dislocations [129, 130]. Additionally, the SFs appear to remain anchored with one end at the twin boundary, some examples marked by dashed white circles in Figure 4.11(a), and the other end terminating within the twin or probably crossing the free surface of the pillar (not shown here).

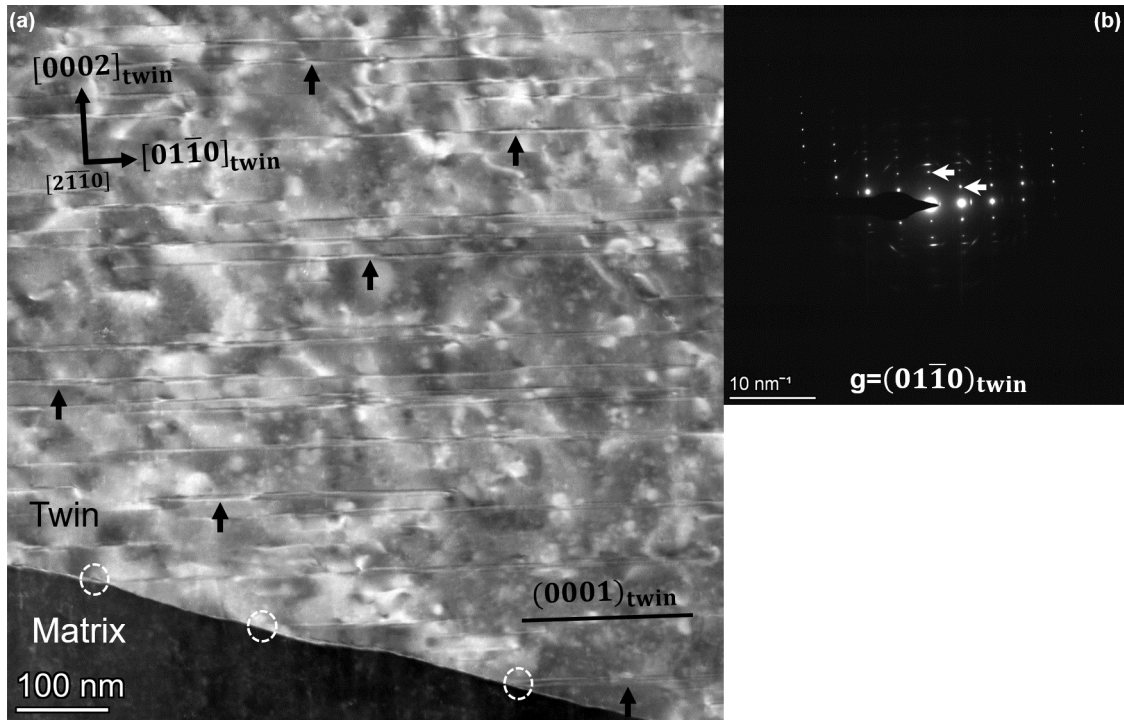


**Figure 4.11.** (a) A dark-field STEM micrograph at the vicinity of the twin boundary shown in Figure 4.10 corresponding to a single crystalline micropillar compressed along the  $[10\bar{1}0]$  to 5% strain. The new loading axis in the twin is close to  $[0001]_{\text{twin}}$ . A high density of long basal stacking faults (SFs) has been developed inside the pillar in the wake of the advancing  $\{10\bar{1}2\}$  twin boundary. Some examples of the SFs are marked by black arrows. Dashed white circles show some SFs pinned at the twin boundary. (b) The selected two-beam condition using an electron beam close to the  $[2\bar{1}\bar{1}0]$  zone axis and a  $g = (01\bar{1}0)_{\text{twin}}$  diffraction vector. The corresponding diffraction pattern has already been shown in Figure 4.10(b). The streaking of spots (indicated by white arrows) along the  $[0001]$  direction suggests that the faults are  $(0001)$  basal plane SFs.

The twinning defect structure was further characterized in two-beam diffraction condition using the same zone axis as in Figure 4.11,  $[2\bar{1}\bar{1}0]_{\text{twin}}$ , however with a different  $g = \{0002\}_{\text{twin}}$  reflection vector. The selected results are displayed in Figure 4.12. Based on the  $g \cdot b$  values presented in Table 4.2, the  $g = \{0002\}$  reflection will only give contrast to  $\langle c \rangle$ -containing dislocations, i.e. pure  $\langle c \rangle$  or  $\langle c + a \rangle$ . Thus, Figure 4.12(a) shows abundant  $\langle c \rangle$ -containing dislocations within the twinned micropillar. Most of these dislocations are rectilinear, lying parallel to the trace of the basal plane in the twin. As indicated by white arrows, frequent

rectilinear dislocations are pinned at the twin boundary. To further clarify, a magnified view of the marked dashed area containing the dislocation **A** is shown in Figure 4.12(b). As is seen, the single  $\langle c \rangle$ -containing dislocation **A** is connected to the twin boundary from the twin side.

**Table 4.2.** The  $\mathbf{g}\cdot\mathbf{b}$  values for perfect and partial dislocations in twin using a  $[2\bar{1}\bar{1}0]$  zone axis and reflection conditions of  $\mathbf{g} = (01\bar{1}0)$  and  $\mathbf{g} = \{0002\}$ .

Dislocation type	$\mathbf{b}$	$\mathbf{g} = (01\bar{1}0)$	$\mathbf{g} = \{0002\}$
		$\mathbf{g}\cdot\mathbf{b}$	$\mathbf{g}\cdot\mathbf{b}$
$\langle a \rangle$	$1/3 [1\bar{1}\bar{2}0]$	1	0
	$1/3 [\bar{1}2\bar{1}0]$	1	0
	$1/3 [2\bar{1}\bar{1}0]$	0	0
$\langle c + a \rangle$	$1/3 [1\bar{2}\bar{1}3]$	-1	$\pm 2$
	$1/3 [2\bar{1}\bar{1}3]$	0	$\pm 2$
	$1/3 [1\bar{1}\bar{2}3]$	1	$\pm 2$
	$1/3 [\bar{1}2\bar{1}3]$	1	$\pm 2$
	$1/3 [\bar{2}1\bar{1}3]$	0	$\pm 2$
	$1/3 [\bar{1}\bar{1}23]$	-1	$\pm 2$
$\langle c \rangle$	[0001]	0	$\pm 2$
$I_2$ partials	$1/3 [01\bar{1}0]$	2/3	0
	$1/3 [\bar{1}100]$	1/3	0
$I_1$ partials	$1/6 [02\bar{2}3]$	2/3	$\pm 1$
	$1/6 [\bar{2}203]$	1/3	$\pm 1$

The reflection vector used in the twin, can also be useful for imaging defects in the matrix based on the matrix-twin orientation relationship [71]. This crystallographic relationship is shown in Figure 4.13. An overlapping selected area diffraction pattern for both the matrix and the twin shows a typical  $\sim 86^\circ$  misorientation between the two crystals after  $\{10\bar{1}2\}$  twinning. Close alignment of the diffraction spots for the twin and the matrix is represented by dashed and solid squares, respectively. The labeled diffraction vectors indicated on the right show that the  $\mathbf{g} = [000\bar{1}]$  vector in the twin leads to the  $\mathbf{g} = [0\bar{1}10]$  reflection in the adjacent matrix, which gives contrast to two  $\langle a \rangle$  dislocations, according to  $\mathbf{g}\cdot\mathbf{b}$  values listed in Table 4.2. The  $\langle a \rangle$  dislocations that can be detected near the twin boundary from the matrix side, are indicated by white arrows labeled as **B** in Figure 4.12(b).

On the character of the marked dislocations in the matrix, they could also be of  $\langle c + a \rangle$ -type, as Table 4.2 provides four non-zero  $\mathbf{g}\cdot\mathbf{b}$  possibilities for them. However, dislocations in the matrix having a  $\langle c + a \rangle$  Burgers vector should also show up under  $\mathbf{g} = \{0002\}$  reflection, where only  $\langle c \rangle$ -containing dislocations appear. This is the case in the matrix in Figure 4.11, since the  $\mathbf{g} = [01\bar{1}0]$  in the twin leads to  $\mathbf{g} = [000\bar{1}]$  in the matrix (see Figure 4.13). An observable dislocation contrast is not detected in the matrix in Figure 4.11(a) and therefore the observed dislocations in the matrix in Figure 4.12(b) are likely of  $\langle a \rangle$ -type. Despite a weak contrast from these dislocations, they seem to be pinned to the twin boundary. This points to a critical finding from the Figures 4.11 and 4.12 that a dense array of highly extended

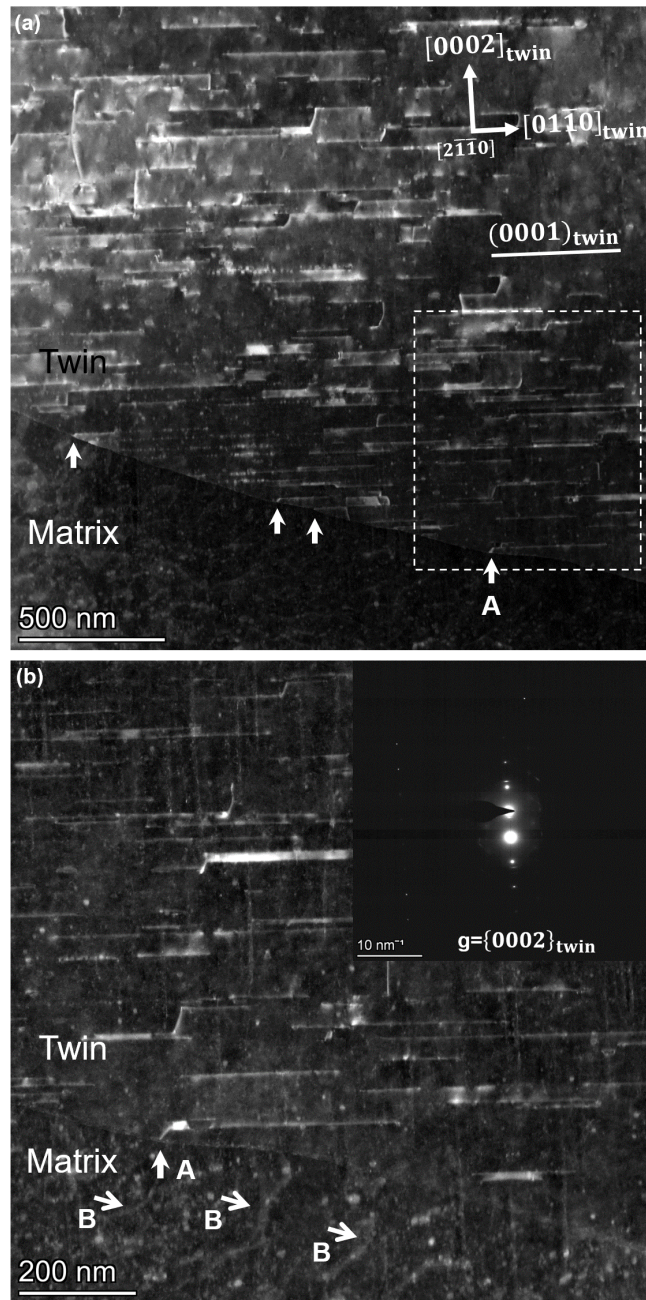


**Figure 4.12.** (a) A dark-field STEM micrograph at the vicinity of the twin boundary (TB) shown in Figures 4.10 and 4.11 corresponding to an  $[10\bar{1}0]$  oriented single crystalline micropillar compressed to 5% strain. The new loading axis in the twin is close to the  $[0001]_{\text{twin}}$ . Abundant  $\langle c \rangle$  or  $\langle c+a \rangle$  dislocations are found within the twin in the wake of the advancing TB. Some examples of the dislocations pinned at the TB are shown by arrows. (b) An enlarged view of the marked dashed area in (a) containing the dislocation **A** pinned at the TB. The selected two-beam condition using an electron beam close to the  $[2\bar{1}\bar{1}0]$  zone axis and a  $g = \{0002\}_{\text{twin}}$  diffraction vector is shown in the inset. The corresponding diffraction pattern has already been shown in Figure 4.10(b). The  $\langle c \rangle$ -containing dislocation **A**, already imaged in (a), is pinned at the TB. The presence of  $\langle a \rangle$  dislocations near the TB in the matrix is shown by arrows labeled as **B**. Despite the weak contrast for these defects in the matrix, a simultaneous attachment of  $\langle c \rangle$ -containing (from the twin side) and  $\langle a \rangle$  dislocations (from the matrix side) to the TB might be a signature of the transmutation reaction of  $\langle a \rangle_{\text{matrix}} \rightarrow \langle c+a \rangle_{\text{twin}}$  as a consequence of twinning.

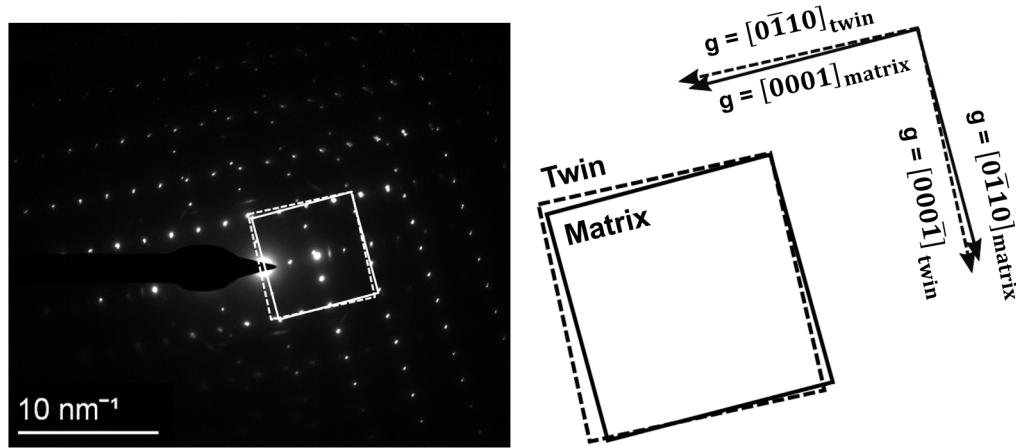


**Figure 4.13.** An overlapping selected area diffraction pattern for the matrix and twin showing a typical  $\sim 86^\circ$  misorientation relationship associated with  $\{10\bar{1}2\}$  twinning. The family of diffraction spots belonging to the twin and the matrix are shown by dashed and solid squares, respectively. The selected reflection vectors are indicated schematically on the right showing a crystallographic equivalence of the  $g = [000\bar{1}]$  in the twin and the  $g = [0\bar{1}10]$  in the matrix. Similarly, the  $g = [0\bar{1}10]_{\text{twin}}$  leads to  $g = [0001]_{\text{matrix}}$ . The zone axis is close to the  $[2\bar{1}\bar{1}0]$ .

basal SFs accompanied by populated  $\langle c \rangle$ -containing dislocations is confirmed to be a typical kind of a defect substructure, inherited from extension twinning in  $\langle 10\bar{1}0 \rangle$  oriented micropillars, interrupted within the stress plateau region. Interestingly, both features showing some evidence of being pinned to the twin boundary. The possible origins of such defects will be discussed subsequently.

Basal SFs are usually categorized in three types in Mg and its alloys. These faults are  $I_1$  (intrinsic),  $I_2$  (intrinsic) and  $E$  (extrinsic). The partial dislocations that bound these SFs are Frank partials with a Burgers vector of  $\pm 1/6 \langle 2\bar{2}03 \rangle$  ( $\langle c+a \rangle$  type) for  $I_1$  faults, Shockley partials with a Burgers vector of  $\pm 1/3 \langle 1\bar{1}00 \rangle$  ( $\langle a \rangle$  type) for  $I_2$  faults, and  $\langle c \rangle$  type partials with a Burgers vector of  $\pm 1/2 [0001]$  for extrinsic  $E$  faults [127, 131]. Basal SFs have been repeatedly reported to occur inside deformation twins in hcp metals. Using TEM observations along with computer simulations, they have been attributed to (i) non-classical twinning mechanisms, incoherent interfaces and non-dislocation-mediated boundary migration (shuffling mechanism) [127, 129, 130, 132], or to (ii) interactions of matrix dislocations with a twin boundary, the so-called ‘dislocation transmutation’ process with subsequent dissociation of  $\langle c+a \rangle$  dislocations [69–71, 122, 133]. The former idea, (i), is suggested to unravel some unusual features of basal SFs within the twins and the latter, (ii), might explain the co-existence of  $\langle c \rangle$ -containing dislocations and basal SFs inside the twins.

Song and Gray [127] observed SFs on the basal plane within deformation twins in Ti and Zr. No clearly visible dislocations that bound the faults were observed and the faults were usually in contact with the twin boundary. These features let them consider the observed SFs as ‘anomalous’ SFs; they are different in character from the SFs normally found in hcp crystals. The authors concluded that the formation of such anomalous SFs is tied to the twinning

process alone, since the faults were exclusively found inside twins. They finally suggested that the formation of such anomalous SFs inside twins is related to the motions of a large number of atoms involved in twinning; i.e. atomic shuffling, rather than partial dislocations. TEM measurements and atomistic simulations performed by Zhang et al. [129] have confirmed the anomalous basal SFs inside twins in Mg, Co and Ti. The authors called these defects ‘non-equilibrium’ SFs and suggested that the formation of such faults is closely associated with the migration of incoherent twin boundaries. Based on their molecular dynamics results, basal SFs can originate at initial defects, located at the incoherent twin boundary. One end of the SF is anchored at the twin boundary, and as the twin grows, the SF become longer and longer until it terminates either at the opposing twin boundary or reaches some pre-existing defects inside the twin. Such a simulated defect structure has been verified by microscopic observations, where SFs, attached to highly incoherent twin boundaries, can cross the entire twin.

The question of whether the twin boundary structure, i.e. its coherency, might influence the formation of such faults, has been addressed by assuming the initial twin boundary is fully coherent. By applying the same loading condition as in the case of incoherent twin boundaries, a perfectly twinned lattice without any appearance of SFs was found. The authors, therefore, concluded that the SFs form inside the twin as a result of incoherent twin boundary migration. Indeed, once the twin boundary is highly incoherent, this may cause the matrix atoms to land on the faulted sites of the basal plane in the twin, and the chances for this atomic jumping to the faulted sites of the twin is much less for a coherent twin boundary migration. The proposed mechanism in [129] supports the newly re-established  $\{10\bar{1}2\}$  twinning theory, in which twinning is solely accomplished by atomic shuffling (see Section 2.2.2). Under this scenario, the SFs do not involve partial dislocations. Such a non-dislocation-mediated mechanism has also been shown to explain anomalous basal SFs inside other twin types, e.g.  $\{10\bar{1}1\}$  contraction twins [130].

The incoherency of the twin boundary shown in Figure 4.10 along with the presence of lengthened SFs in connection to that twin boundary (Figure 4.11) is very similar to the characteristics of twinned structures observed by TEM and simulations in hcp metals [127, 129, 130, 132], as discussed. Accordingly, the basal SFs formed in the wake of the advancing incoherent twin boundary in this thesis are related to the  $\{10\bar{1}2\}$  twinning process. However, the question of whether the twinning mechanism is accomplished by the above suggested shuffling theory, resulting in zero contribution of partial dislocations to form such SFs, remains unanswered. Since no systematic experimental study has yet confirmed the shuffling theory, to the author’s knowledge, it is still under debate (Section 2.2.2). The role of partial dislocations, as by-products of matrix dislocation-twin boundary interactions in SF formation must be addressed.

New Burgers vectors and slip planes of dislocations after the twinning reorientation were determined uniquely by Niewczas, using a correspondence matrix establishing a one-to-one plane/direction correlation between the two crystals [134]. The correspondence matrix method is helpful in analyzing the interactions between slip dislocations and twin boundaries, and in

turn the nature of defects inherited by deformation twinning. For the particular  $\{10\bar{1}2\}\langle 10\bar{1}\bar{1}\rangle$  extension twinning mode in Mg considered here, the geometrical relations between slip planes and directions before and after twinning were reproduced from [134], and the results are given in Table 4.3. Only the transformation of matrix basal and prismatic slip systems with  $\langle a \rangle$ -type Burgers vectors are listed, as the activation of such dislocations is considered to occur prior to twin nucleation [30, 73]. After extension twinning, matrix  $\{0001\}$  basal planes are transformed to  $\{\bar{1}010\}$  prismatic planes in the twin. For both the basal and prismatic slip systems, two of three  $\langle a \rangle$ -type Burgers vectors of  $\langle 11\bar{2}0 \rangle$  in the matrix are transformed to  $\langle 11\bar{2}3 \rangle$  slip directions in the twinned lattice. Only one of the possible three Burgers vectors in the matrix keeps its slip direction within the twin. Indeed, most of the  $\langle a \rangle$  dislocations active in the matrix are expected to have larger Burgers vectors after the twinning transformation, possessing  $\langle c + a \rangle$ - $\langle 11\bar{2}3 \rangle$  Burgers vectors.

**Table 4.3.** Transformation of matrix basal and prismatic slip systems with  $\langle a \rangle$ -type Burgers vectors to slip systems within twin after  $\{10\bar{1}2\}\langle 10\bar{1}\bar{1}\rangle$  twinning shear in Mg. Data are reproduced from [134].

Slip type	Matrix slip system	Twin slip system
Basal slip systems	$(0001) \begin{bmatrix} 2\bar{1}\bar{1}0 \\ \bar{1}2\bar{1}0 \\ \bar{1}\bar{1}20 \end{bmatrix}$	$(\bar{1}010) \begin{bmatrix} \bar{1}2\bar{1}3 \\ \bar{1}2\bar{1}0 \\ \bar{1}2\bar{1}3 \end{bmatrix}$
	$(10\bar{1}0) \begin{bmatrix} \bar{1}2\bar{1}0 \\ 0\bar{1}10 \\ \bar{1}100 \end{bmatrix}$	$(000\bar{1}) \begin{bmatrix} \bar{1}2\bar{1}0 \\ \bar{1}2\bar{1}3 \\ \bar{1}2\bar{1}3 \end{bmatrix}$
		$(\bar{1}2\bar{1}2) \begin{bmatrix} \bar{1}2\bar{1}3 \\ \bar{1}2\bar{1}3 \end{bmatrix}$

The change of the slip plane and Burgers vector of a dislocation when incorporated into an extension twin in Mg has been termed a ‘dislocation transmutation’ by Wang and Agnew [69]. Based on TEM observations, they formulated dislocation reactions across a  $\{10\bar{1}2\}$  twin boundary:

$$2 \times 1/3 [\bar{1}2\bar{1}0]_{\text{matrix}} \rightarrow 2 \times 1/3 [1\bar{2}10]_{\text{twin}} \quad (4.4)$$

$$2 \times 1/3 [\bar{1}\bar{1}20]_{\text{matrix}} \rightarrow b_{\text{twin}} + 1/3 [\bar{1}2\bar{1}3]_{\text{twin}} \quad (4.5)$$

$$2 \times 1/3 [2\bar{1}\bar{1}0]_{\text{matrix}} \rightarrow b_{\text{twin}} + 1/3 [\bar{1}2\bar{1}3]_{\text{twin}} \quad (4.6)$$

where  $b_{\text{twin}}$  is the twinning dislocation which is a residual dislocation left on the twin boundaries. Equations agree well with the predictions of the lattice correspondence matrix presented in Table 4.3, and describe the transmutation reactions of  $\langle a \rangle$  dislocations from the matrix in two scenarios: (i) those with the  $1/3[\bar{1}2\bar{1}0]$  Burgers vector,  $[a_2]$ , which are parallel to the

intersection line of the basal slip and the twinning planes, remain unchanged (Eq.(4.4)) and (ii) those with a  $1/3[\bar{1}\bar{1}20]$  or a  $1/3[2\bar{1}\bar{1}0]$  Burgers vector,  $[a_3]$  or  $[a_1]$ , which are at  $60^\circ$  to the intersection line of the basal slip and the twinning planes (see Figure 4.14(a)), change to  $\langle c+a \rangle$ -type (Eqs. (4.5) and (4.6)). The interaction of these two groups of  $\langle a \rangle$  dislocations with a twin boundary leads to different products.

The transformation of  $[a_1]$  and  $[a_3]$  dislocations once penetrating a twin boundary has drawn attention by its potential to introduce defects into the twinned crystal through the creation of  $\langle c+a \rangle$  dislocations. Tomsett and Bevis [135] provided one of the first experimental evidence for dislocation transmutation at twin boundaries in Zn. They observed basal dislocations in the matrix and basal SFs within the twins. By determining the Burgers vectors of the partial dislocations bounding the SFs to be  $\pm 1/3\langle 1\bar{1}00 \rangle$ , it was suggested that the SFs inside the twin result from the propagation of Shockley partial dislocations and hence the SFs are of  $I_2$  type. Such faults can be formed by decomposition of transmuted  $\langle c+a \rangle$  dislocations within the twin into perfect  $\langle c \rangle$  and  $\langle a \rangle$  dislocations, and further dissociation of the  $\langle a \rangle$  dislocations into two Shockley partials [135], as is expressed by the following expression, a continuation of Eq. (4.5):

$$1/3 [\bar{1}2\bar{1}3]_{\text{twin}} \rightarrow [0001]_{\text{twin}} + 1/3 [\bar{1}2\bar{1}0]_{\text{twin}} \quad (4.7)$$

$$1/3 [\bar{1}2\bar{1}3]_{\text{twin}} \rightarrow [0001]_{\text{twin}} + (1/3 [01\bar{1}0]_{\text{twin}} + 1/3 [\bar{1}100]_{\text{twin}} + I_2) \quad (4.8)$$

Another type of dissociation of transmuted  $\langle c+a \rangle$  dislocations may cause the formation of an  $I_1$  fault bounded by two  $\pm 1/6\langle 2\bar{2}03 \rangle$  Frank partials. This non-coplanar reaction can be expressed as follows [115]:

$$1/3 [\bar{1}2\bar{1}3]_{\text{twin}} \rightarrow 1/6 [02\bar{2}3]_{\text{twin}} + 1/6 [\bar{2}203]_{\text{twin}} + I_1 \quad (4.9)$$

Both of the decomposition processes resulting in the generation of  $I_2$  (Eq. (4.8)) and  $I_1$  (Eq. (4.9)) faults, have recently been proven to be possible by molecular dynamics simulations [136].

The above discussion can be linked to the results presented in Figures 4.11 and 4.12. The co-existence of  $\langle a \rangle$  dislocations from the matrix side and  $\langle c \rangle$ -containing dislocations from the twin side, both of which attached to the twin boundary (Figure 4.12(b)), is likely an indication of transmutation of incoming  $\langle a \rangle$  dislocations into the twin boundary, resulting in generation of  $\langle c+a \rangle$  dislocations in the twin. The imaged microstructures in Figures 4.11 and 4.12 correspond to a micropillar interrupted at a stress plateau level of about 90 MPa. At such a relatively low stress level, the  $\langle c+a \rangle$  dislocations are generally not expected to be activated in the sample, see Figure 4.6 and [69]. Therefore, the presence of such  $\langle c+a \rangle$  dislocations

in the twin is additionally supported to be attributed to dislocation transmutation. Further dissociation of the transmuted  $\langle c + a \rangle$  dislocations according to Eq. (4.8) can give rise to deposition of  $\langle c \rangle$  dislocations (Figure 4.12) along with numerous basal  $I_2$  SFs (Figure 4.11) inside the twin. The  $\langle c \rangle$  dislocations are expected to be sessile since their Burgers vector is nearly parallel to the loading direction in the twin. Relying on Eq. (4.8), the SFs formed on the basal plane of the deformation twin, Figure 4.11, might be  $I_2$  faults, which is in agreement with the visible contrast of such faults under the  $g = (01\bar{1}0)$  reflection condition in Mg [69]. Partial dislocations bounding the  $I_2$  faults do not give contrasts under  $g = \{0002\}$  reflection, see Table 4.2, the rectilinear  $\langle c \rangle$  dislocations in Figure 4.12 are thus not misinterpreted as Shockley partial dislocations, if one assumes the reaction described by Eq. (4.8). The observed basal SFs could alternatively be considered as dissociation products of transmuted  $\langle c + a \rangle$  dislocations according to Eq. (4.9). Thus, the SFs captured in Figure 4.11 might be  $I_1$  faults and the  $\langle c \rangle$ -containing dislocations in Figure 4.12 are likely the bounding  $1/6 \langle 2\bar{2}03 \rangle$  Frank partial dislocations, as they are visible under the  $g = \{0002\}$  reflection, see Table 4.2. This dissociation reaction requires climb of the leading partial dislocations into the basal plane. This faulted configuration is also expected to be sessile [69].

At this point, a definitive conclusion with respect to the type of basal SFs observed in this work necessitates a more detailed Burgers vector determination of the bounding partial dislocations under additional reflection conditions. Regardless of being  $I_1$  or  $I_2$  type, to explain the extended length of basal SFs that can traverse the twin (Figure 4.11), one of the two partial dislocations must presumably be pinned at the incoherent twin boundary following the  $\langle c + a \rangle$  dissociation. The other partial dislocation, which is sessile in either case of being Shockley- $1/3 \langle 1\bar{1}00 \rangle$  or Frank- $1/6 \langle 2\bar{2}03 \rangle$ , may stay within the twin. Having one end of the fault anchored to the twin boundary and the other pinned inside the twin, the twin boundary would lengthen the fault as it advances under the applied stress. This process is schematically shown in Figure 4.14.

Under compression of the matrix along the  $\langle 10\bar{1}0 \rangle$  direction, a  $\{10\bar{1}2\}$  twin has been formed in the sample, Figure 4.14(a). If a pair of matrix  $[a_3]$  dislocations interact with the twin boundary, they will transmute into a single  $\langle c + a \rangle$  dislocation at the boundary. Further decomposition of the transmuted dislocation into partial dislocations will result in the formation of a basal SF in the twin, Figure 4.14(b). The bounding partial dislocations are likely sessile, as one end is positioned inside the twin and the other end is pinned to the residual defect at the interface. The twin boundary might also incorporate a new pair of matrix  $[a_3]$  dislocations at this step. As the interface further migrates downward, the already formed SF will be extended by the moving twin boundary, Figure 4.14(c). A second SF can be formed as a result of the preceding dislocation-interface interaction that occurred. The twin boundary may again interact with the matrix  $[a_3]$  dislocations, Figure 4.14(c). Continued twin boundary advancement will extend the already generated SFs and will leave a new SF from the  $[a_3]$  dislocation-twin boundary interaction in Figure 4.14(c), the result is sketched in Figure 4.14(d). As is seen from steps (a) to (d), the length of the generated SFs is not necessarily similar, as the twin boundary meets  $[a_3]$  dislocations randomly. Importantly, basal/prismatic

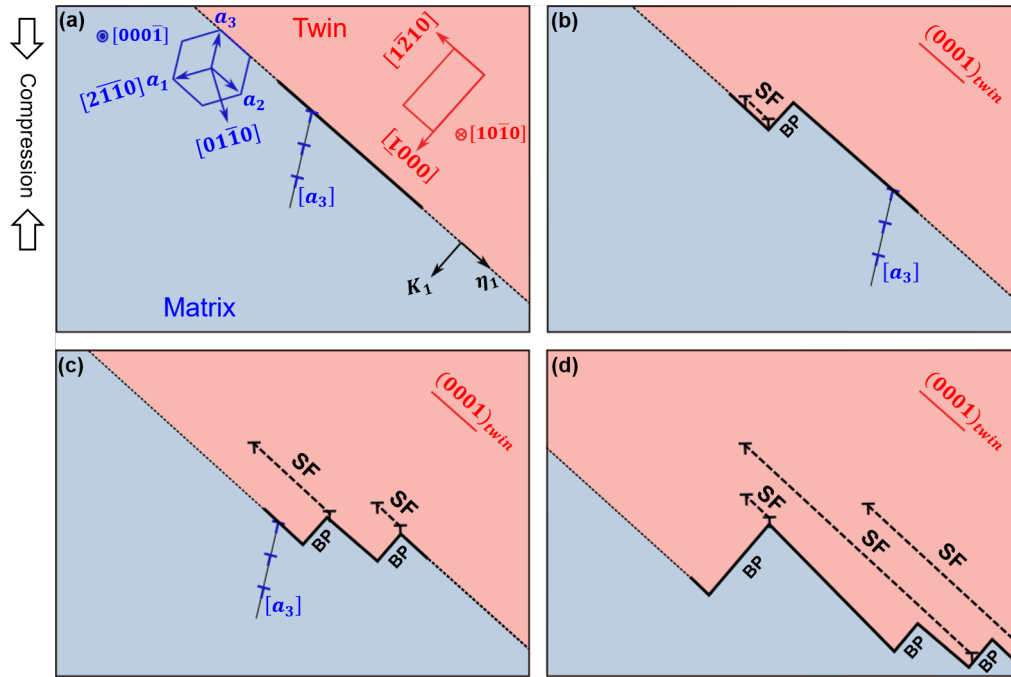


**Figure 4.14.** Schematic illustration of the development of the defect structure in the wake of an advancing twin boundary. The twinning plane and twinning shear direction are  $K_1 = \{10\bar{1}2\}$  and  $\eta_1 = \langle 10\bar{1}\bar{1} \rangle$ , respectively. Partial dislocations that bound a basal SF are generated after interaction of perfect  $[a_3]$  dislocations from the matrix with the twin boundary and further decomposition of the transmuted products. Having one end connected to the twin boundary and the other end pinned within the twin, the SFs are stretched as the twin boundary advances. Local incorporation of  $[a_3]$  dislocations into the twin boundary results in local incoherency of the boundary appearing as basal/prismatic (BP) interfaces on the twin boundary. All the features belonging to the matrix and twin are colored as blue and red, respectively. The black bold line separating the two crystals is the twin interface. Partial dislocations are shown in black. Note that the dislocation transmutation process transforming matrix  $[a_3]$  dislocations into  $\langle c+a \rangle$  dislocations in the twin is not shown here. The matrix and twin crystals are viewed along  $[000\bar{1}]$  and  $[10\bar{1}0]$  directions, respectively. For step-by-step evolution from (a) to (d) the reader is referred to the text.

(BP) interfaces develop on the twin boundary in response to the stress field of incoming matrix dislocations. Consequently, the initially coherent twin boundary can become locally incoherent under continued loading, consistent with the experimentally observed interface shown in Figure 4.10. Further deformation is expected to leave an array of basal SFs.

#### 4.4 Microcompression of $[0001]/[10\bar{1}0]$ bicrystals

The engineering stress-strain response obtained from microcompression of  $[0001]/[10\bar{1}0]$  bicrystalline micropillars is presented in Figure 4.15. A total number of 20 bicrystalline micropillars were successfully tested. For clarity, only four curves are shown. The stress increases linearly up to a stress plateau ranging from 17 to 41 MPa. At this critical stress a strain extension occurs. Note that this extension strain is different for each curve. After

the stress plateau, the stress linearly increases up to a secondary yield followed by a strain hardening up to stress values ranging from 450 to 507 MPa, values comparable to those found for the  $[10\bar{1}0]$ , but much higher than those for  $[0001]$  single crystals (see Figures 4.4 and 4.8). The observed stress plateau is similar to that shown for twinning in Figure 4.8, however with different stress and extension levels. Indeed, the strain burst in Figure 4.15 is thought to be associated with detwinning of the pre-existing twin included in the bicrystalline micropillars.

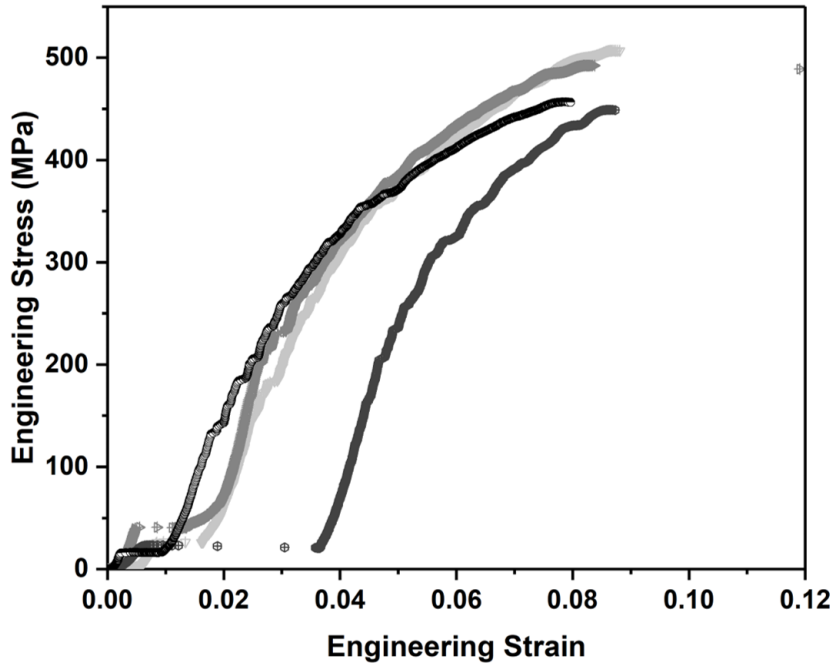


**Figure 4.15.** Engineering stress-strain curves for  $[0001]/[10\bar{1}0]$  oriented bicrystalline micropillars compressed to 12% engineering strain. For pre-deformation condition, see Figures 4.2(g), 2(h) and 2(i).

As expressed in Eq. (4.3) and verified in Figure 4.8, an entirely twinned micropillar contributes to about 6% longitudinal strain. The maximum strain accommodated by detwinning in the four curves presented in Figure 4.15 is around 3.7%. This is due to the fact that the included pre-existing twins inside the samples never reached the total volume of the pillar (see Figure 4.2(i)). A part of the pillar experiences detwinning, leading to a strain accommodation less than 6%. In addition, the plateau stress levels for detwinning are much less compared to twinning. This can be explained by the nucleation-free nature of detwinning. In the case of  $[10\bar{1}0]$  single crystals, a twin must be first nucleated, whereas in the bicrystals the pre-existing twin migrates through the pillar, once the propagation stress has been achieved. As can be found from Figure 4.15, it should be emphasized that detwinning in different micropillars manifests at different plateau stress-strain values. Since the volume fraction of the pre-existing twin in the bicrystals is not the same for all the micropillars, the stress and strain associated with twin migration varies with the volume of the included twin. An estimation of the exact quantitative correlation between the twin volume fraction and the corresponding stress-strain plateau requires an in-situ testing set-up, the volume of the included twin in

the micropillars was not measurable after running ex-situ tests, since the twin boundaries migrated during microcompression.

Microstructural examinations were conducted on cross-sections of micropillars compressed to varying strains. The SEM and EBSD results are shown in Figure 4.16. The initial bicrystalline pillar consists of two crystals of  $[0001]$  oriented matrix and its  $\{10\bar{1}2\}$  twin, Figure 4.16(b). The compressive load is performed along the  $c$ -axis of the matrix, the twin is compressed along the  $\langle 10\bar{1}0 \rangle$  axis. The misorientation angle distribution in Figure 4.16(c) shows an existence of pre-strain in the matrix and twin, this is likely the case for all the fabricated samples in the selected matrix-twin grain pair. At 4% strain, the vertical pillar edge has tilted slightly, Figure 4.16(d). This is similar to the 5% compressed  $[10\bar{1}0]$  single crystal shown in Figure 4.9(d), and is similarly attributed to (de)twinning shear. The corresponding EBSD map shown in Figure 4.16(e) reveals that the pre-existing twin has almost disappeared, with only a small trace of twin at the top right corner. It should be noted that 4% unloading strain was within the plateau stress for this micropillar. The matrix crystal shows a slight increase in the mean misorientation angle after twin boundary migration, as is found in Figure 4.16(f).

The deformation morphology of a micropillar unloaded at 10% strain shows many basal slip steps on the sample surface after compression, see Figure 4.16(g). As is clearly shown in Figure 4.16(h), the micropillar doesn't show any trace of the pre-existing twin in the cross-section. Consequently, it was observed that during microcompression of the bicrystals, the initial twin migrates out of the samples and the twin re-orientates into the nominal orientation of the matrix crystal, i.e. detwinning. At the exhaustion of detwinning, any subsequent straining is expected to be of a  $\sim[0001]$  single crystal. The idea is supported by consideration of the stress-strain response beyond the plateau region, see Figure 4.15. The micropillar follows a strong strain hardening after the second yield. Similar to the case of twinned  $[10\bar{1}0]$  micropillars, activation of pyramidal  $\langle c+a \rangle$  dislocations is suggested to govern the plastic response of detwinned bicrystals. The dislocation activity would lead to an increased mean misorientation angle within the micropillars, as is shown in Figure 4.16(i).

A dark-field STEM micrograph taken from a bicrystalline micropillar interrupted at 5% strain is presented in Figure 4.17. The diffraction pattern obtained from an electron beam nearly parallel to the  $[2\bar{1}\bar{1}0]$  zone axis, Figure 4.17(b), shows that the sample is a single crystal. This is confirmed by the  $[100]$  IPF map presented in Figure 4.17(c), where the initially bicrystalline micropillar had detwinned and reoriented to a single crystal of  $\sim[0001]$  orientation. Figure 4.17(a) shows a heterogeneous distribution of defects inside the detwinned sample. To further analyze the defect structure, the area marked by the dashed square, where a pre-existing twin boundary is supposed to have migrated through, was characterized at higher magnifications under different two-beam conditions, the results of which are shown in Figure 4.18.

A tangled distribution of dislocations is found from Figure 4.18(a). These are  $\langle c \rangle$ -containing dislocations, see the  $g = \{0002\}$  reflection in Table 4.2. They appear as either straight lines perfectly aligned with the basal plane, for edge type, or nearly straight and roughly parallel to the crystal  $c$ -axis, for screw type. If the dislocations Burgers vector is

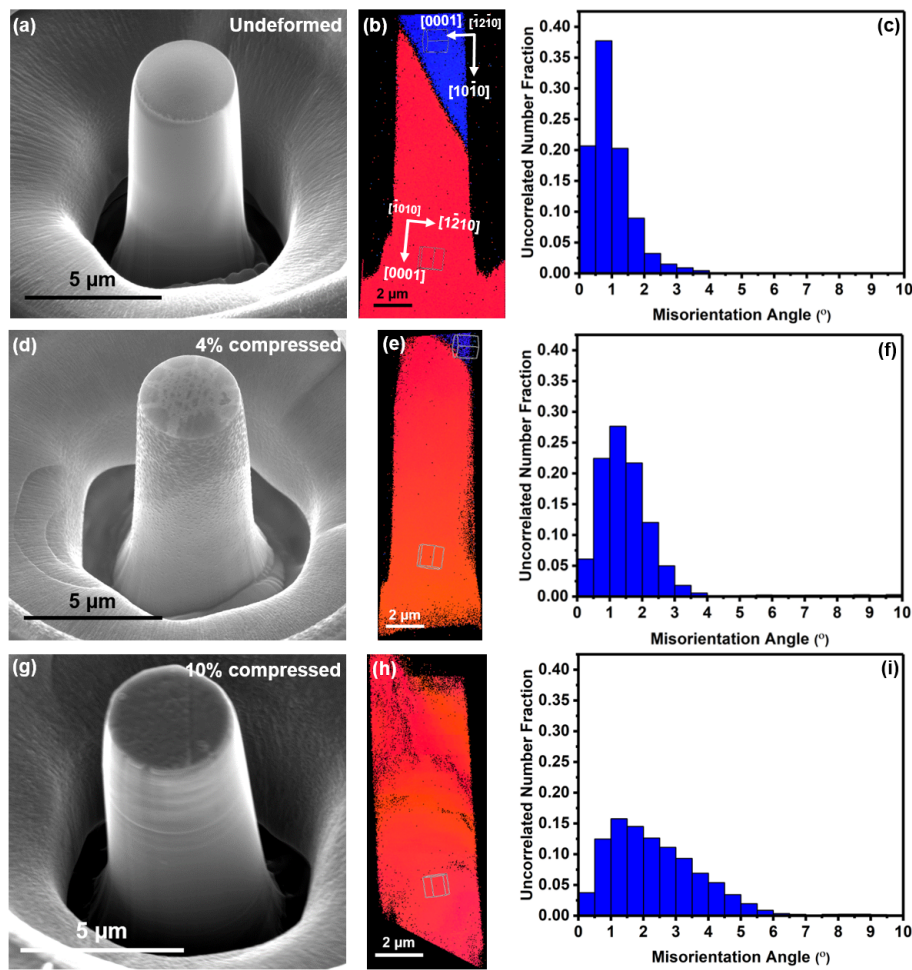


**Figure 4.16.** Post-mortem secondary electron images, the corresponding  $[100]$  IPF maps and uncorrelated misorientation angle distributions of bicrystalline pillars cross-sections in the (a-c) initial state, and compressed to varying strains of (d-f) 4% and (g-i) 10%. The bicrystals show detwinning during microcompression. Misorientation angle diagrams correspond to the red crystals. The color-code is valid for all the IPF maps.

pure  $\langle c \rangle$ , these dislocations are likely sessile, since the resolved shear stress upon loading along  $\sim[0001]$  direction is zero. A deterministic statement about the Burgers vectors, i.e.  $\langle c \rangle$  or  $\langle c + a \rangle$ , is not straightforward here, since dislocations show a weak contrast in the  $g = (01\bar{1}0)$  reflection, see Figure 4.18(b). On the other hand, this reflection reveals well-defined SFs aligned with the basal plane trace, as indicated by white arrows. These are basal SFs with one end at the pillar free surface and the other end terminating within the crystal. The co-existence of rectilinear  $\langle c \rangle$ -containing dislocations with basal SFs in the imaged area in Figure 4.18 is similar to the observations in Figures 4.11 and 4.12 and may therefore indicate a characteristic defect structure resultant from detwinning of a pre-existing twin boundary.

As already mentioned, the micropillar has been completely reoriented to a  $[0001]$  orientation along the pillar axis, and a trace of the pre-existing twin is not visible in the sample, see Figure 4.17(c). Detwinning was found to be exhausted at about 2% strain. Interrupted

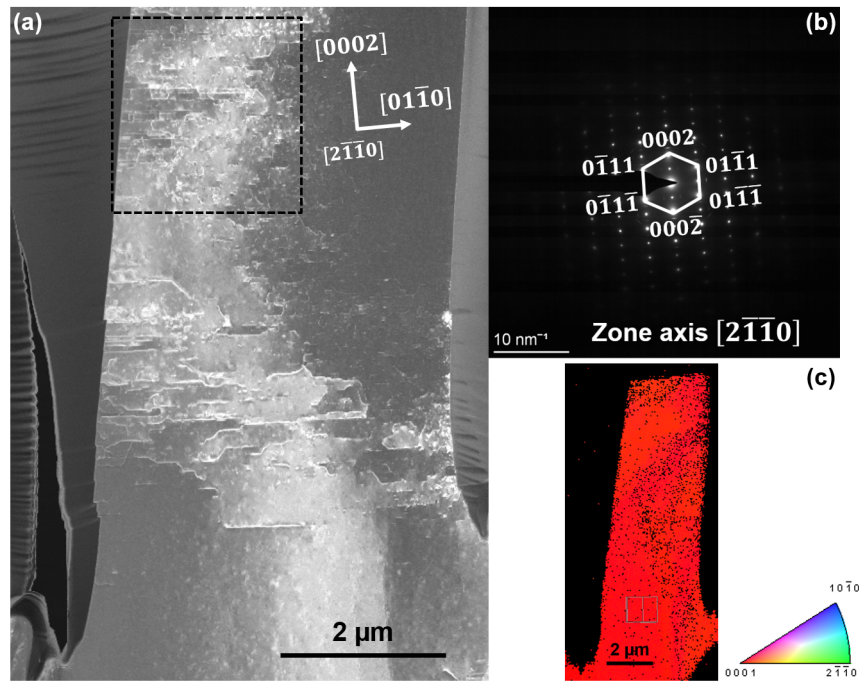


**Figure 4.17.** (a) A dark-field STEM micrograph from the cross-section of a  $[0001]/[10\bar{1}0]$  bicrystalline micropillar compressed to 5% strain. The micropillar had detwinned and holds a single crystal of  $\sim [0001]$  orientation after unloading. A trace of pre-existing twin boundary was not found in the unloaded sample. A heterogeneous defect distribution can be realized in the pillar. (b) The diffraction pattern of the sample obtained from an electron beam close to the  $[2\bar{1}\bar{1}0]$  zone axis of the crystal. (c) The corresponding  $[100]$  EBSD map, showing the crystallographic orientation of the unloaded sample.

at 5% strain, the micropillar had been compressed to 3% strain associated with compression along the  $[0001]$ . This second stage of deformation is dominated by pyramidal  $\langle c + a \rangle$  dislocations. The observed  $\langle c \rangle$ -containing dislocations in Figure 4.18(a) is a mixture of those defects, resulting from dislocation-twin boundary interaction during detwinning, and those activated upon  $c$ -axis compression beyond the detwinning stress plateau.

Further TEM examination was performed on a bicrystalline micropillar unloaded within the detwinning stress plateau, the corresponding EBSD map has been already shown in Figure 4.16(e). The result is presented in Figure 4.19. The image was taken using an electron beam close to the  $[2\bar{1}\bar{1}0]$  zone axis. The selected two-beam diffraction condition at a  $g = \{0002\}$  reflection vector in the matrix is shown in the inset. Fringes of planar faults appear to lie along the basal plane trace in both the matrix and the twin. These are basal SFs which are shown by black and white arrows in the matrix and the twin, respectively. Most of these faults are clearly pinned to the twin boundary in both the neighboring lattices. By applying a global compressive load, detwinning would happen and the twin boundary would migrate to the right, as indicated by the dashed arrow. Thus, the twin crystal reorients back to the orientation of the matrix, i.e.  $\sim [0001]$ . A comparison of the entirely detwinned structure presented in Figure 4.18(b), with the structure interrupted within detwinning in Figure 4.19

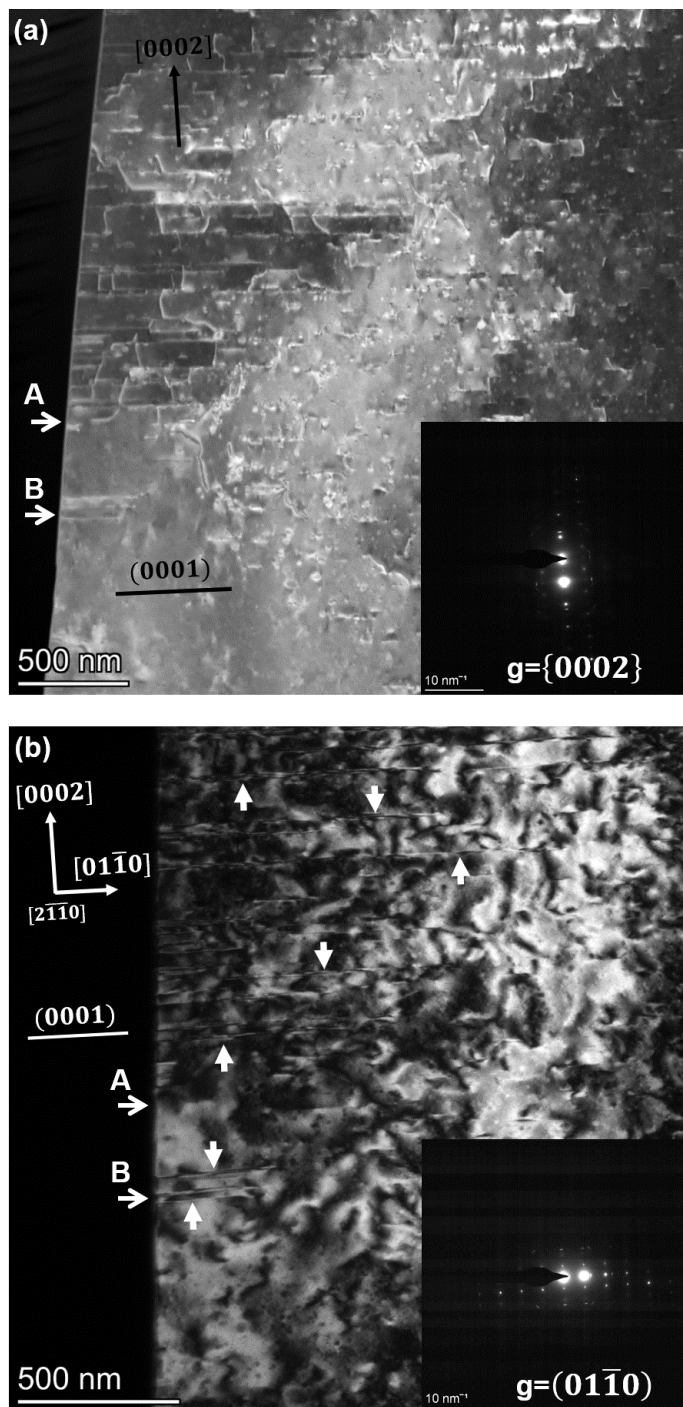


**Figure 4.18.** Magnified dark-field STEM view of the marked area in [Figure 4.17](#) at reflection conditions of (a)  $g = \{0002\}$  and (b)  $g = (01\bar{1}0)$ . The selected two-beam conditions are shown in the insets. The sample has been unloaded at 5% strain and detwinned. A tangled array of  $\langle c \rangle$ -containing dislocations is observed in (a). Basal SFs lying along  $(0001)$  basal planes, indicated by white arrows, are captured in (b). The labeled arrows show the same locations in the two images. The electron beam is close to the  $[2\bar{1}\bar{1}0]$  zone axis.

suggests that the basal SFs in the twin shrink during detwinning, since no obvious SF along the basal plane of the twin is found in the fully detwinned structure in [Figure 4.18\(b\)](#). A new

array of basal SFs might be formed within the detwinned region at the expense of SFs inside the twin, see [Figure 4.19](#).

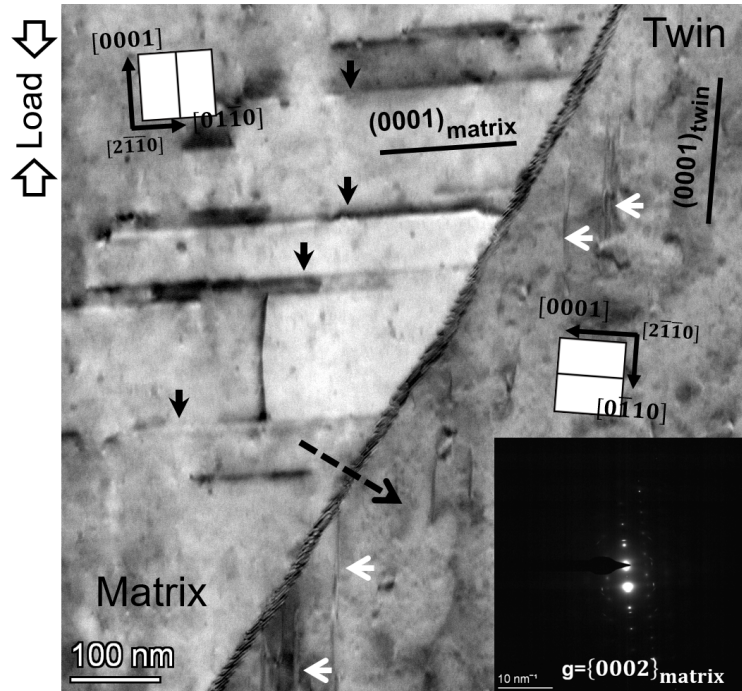


**Figure 4.19.** Dark-field STEM micrograph at the vicinity of the twin boundary in the bicrystalline micropillar shown in [Figure 4.16\(e\)](#). The loading axis in the matrix and the twin crystals is  $\sim\langle 0001 \rangle$  and  $\sim\langle 10\bar{1}0 \rangle$ , respectively. The selected two-beam diffraction condition using  $g = \{0002\}_{\text{matrix}}$  reflection is shown in the inset. The electron beam is nearly parallel to the  $[2\bar{1}\bar{1}0]$  zone axis. Basal SFs in the matrix and the twin are indicated by black and white arrows, respectively. Upon a global compressive loading along the shown direction by opposite arrows, the twin lattice would detwin through the rightward movement of the twin boundary, as indicated by the dashed arrow on the interface. New array of basal SFs might be created in the detwinned region at the expense of the SFs in the twin.

The basal SFs formed in the  $\sim[0001]$  crystal in the wake of the reversed twin boundary are thought to be a result of twin boundary migration, since they are attached to the interface and also they did not show up during microcompression of  $[0001]$  oriented single crystals ([Figure 4.7](#)). These results are consistent with atomistic simulations performed by Zhang et al. [\[129\]](#), where the defect structure inside the matrix behind a reversing incoherent twin boundary in Mg has been modeled. As they reported, basal SFs in the twin disappeared during detwinning and new SFs on the basal planes formed in the detwinned region in the matrix. Basal SFs were also connected to the twin boundary in both crystals. Based on simulation results, the authors in [\[129\]](#) attributed the formation mechanism of such SFs to only incoherent twin boundary migration, with no Shockley or Frank partial dislocations involved. However, they did not provide any experimental evidence for the zero contribution of partial dislocations.

The presence of basal SFs pinned to the twin boundary along with rectilinear  $\langle c \rangle$ -containing dislocations in the detwinned samples ([Figure 4.18](#) and [4.19](#)) is similar to the

characteristics of the twinned structures presented in the last section (Figure 4.11 and 4.12). Whether the  $\langle c \rangle$ -containing dislocations are partial dislocations that bound SFs, e.g.  $I_1$  partials based on Eq. (4.9), or other decomposition products of transmuted  $\langle c + a \rangle$  dislocations at the twin boundary, e.g.  $[0001]_{\text{twin}}$  based on Eq. (4.8), remains open. Whatever is the case, a characteristic defect structure is eventually developed inside the twinned and detwinned micropillars, where the  $\langle c \rangle$ -containing dislocations as well as the basal SFs reside in the wake of an advancing or a reversing twin boundary. Acknowledging the fact that the TEM investigations in Sections 4.3 and 4.4 were mostly conducted in samples interrupted within the plateau region of the stress-strain curves, it remains to be seen whether the observed defect structure associated with twinning or detwinning can establish a basis for subsequent post-plateau mechanical hardening in the tested samples.

## 4.5 The impact of twinning defect structure on the subsequent $c$ -axis hardening

The deformation curves obtained from microcompression of the three sets of micropillars machined for [0001] (Figure 4.4),  $[10\bar{1}0]$  (Figure 4.8) and  $[0001]/[10\bar{1}0]$  (Figure 4.15) orientations are represented for comparison in Figure 4.20. Interestingly, the initial yield stress for the original [0001] pillars (red curves) is higher than for the twinned (blue curves) and detwinned (black curves) samples; the initial yield stress for these pillars is considered as the twin migration stress, i.e. the plateau stress. On the other hand, the secondary yield stress shows the opposite trend. Secondary yielding occurs more readily in the reference [0001] pillars relative to the twinned and detwinned samples after the plateau. The stress-strain curves of the micropillars oriented for twinning ( $[10\bar{1}0]$ ) and detwinning ( $[0001]/[10\bar{1}0]$ ) show strong strain hardening when loaded beyond the plateau regimes, reaching much higher flow stresses than the reference [0001] single crystals. As confirmed by the EBSD cross-sections in Figures 4.9(e) and 4.16(e), the saturation point of the plateaus corresponds to microstructures that had been reoriented to a single crystal of the nominal [0001] orientation and hence, any subsequent straining beyond the plateau region is of the typical  $c$ -axis hardening. It follows that a comparison of the stress-strain behavior of the original single crystalline [0001] micropillars to those after the plateau regime in the single crystals of  $[10\bar{1}0]$  and bicrystals of  $[0001]/[10\bar{1}0]$  orientations gives insight into the impact of twinning (or detwinning) on the strain hardening response of Mg. The interpretation is limited to two characteristic features of the deformation curves beyond the plateau; the (second) yield stress and the work hardening rate.

In the case of microcompression testing, perfect contact between the flat punch and the micropillar top surface at the onset of deformation is hardly achievable due to surface roughness and small misalignments. This can lead to early plasticity. Such microplasticity is responsible for the typical compliant behavior at the early stages of microcompression. For this reason, the usual definition of yield stress using the 0.2% plastic strain offset convention is inappropriate [81]. In this study, the convention proposed by Kupka et al. [137] is employed, in which the slope of the load-displacement curve was used as a criterion to define the yield

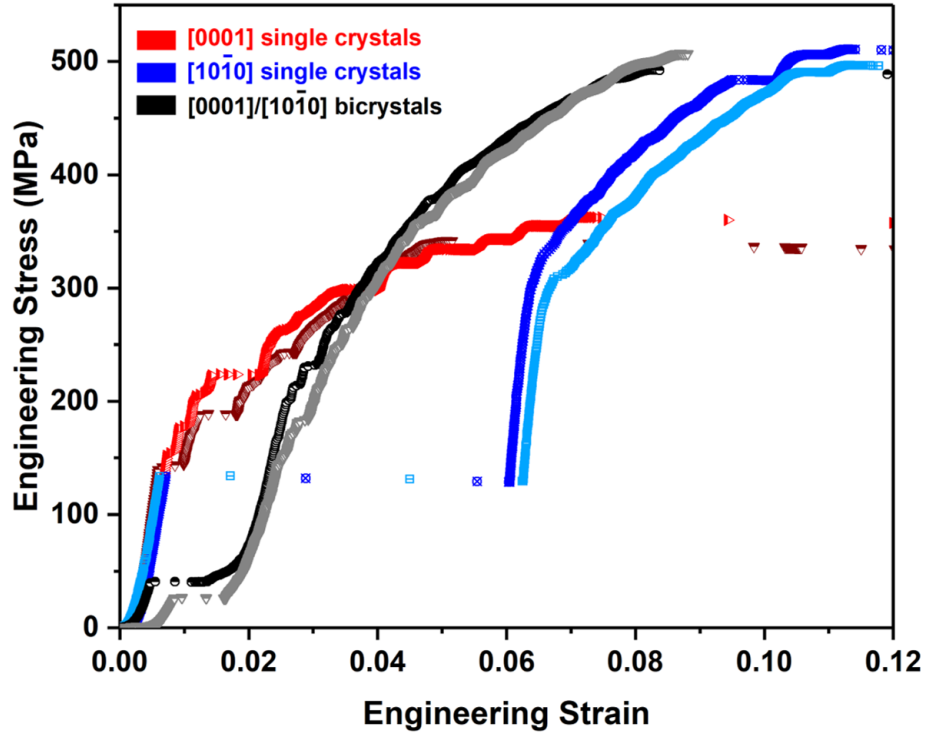


**Figure 4.20.** A comparative representation of the engineering stress-strain curves obtained from microcompression of  $[0001]$  (as reference) and  $[10\bar{1}0]$  oriented single crystals as well as  $[0001]/[10\bar{1}0]$  oriented bicrystals. The curves are re-presented from Figures 4.4, 4.8 and 4.15. Samples corresponding to the blue and black curves possess nominally a single crystal of  $[0001]$  orientation at the saturation of the plateaus, a same orientation as the reference red curves. A comparison of the stress-strain characteristic features beyond the plateaus with those reference curves is of great importance in studying the mechanical impact of twinning (or detwinning) on the  $c$ -axis hardening response.

stress. The local slope of the load-displacement curve, the loading stiffness, is determined using a linear fit over a range of  $\pm 30$  data points around each point of a loading curve (the data acquisition rate is 10 Hz). The maximum point of the loading stiffness curve,  $S_{\max}$ , is associated with the point of full contact. As is depicted in Figure 4.21, the yield point is defined here as the point where the slope of the loading curve becomes less than a threshold value of 25% of maximum loading stiffness ( $S_{\max}$ ).

The yield point criterion defined here was applied to a total of 51 micropillars compressed up to 12% engineering strain. For a reliable statistical comparison of the yield stress results, the best distribution function for each dataset was identified. While the limited number of samples in this work, i.e. on average 17 per initial state, in turn limits how definitive it is [84], the data sets appeared to be best described by a normal distribution function. It was used as a basis for comparison of the three sample types. The results are presented in Figure 4.22. The obtained normal probability curves including  $\pm 95\%$  confidence intervals show that the twinned and detwinned micropillars yield at  $289 \pm 30$  MPa and  $356 \pm 76$  MPa, respectively, both of which are stronger compared to the reference single crystals yielding at  $169 \pm 21$  MPa. The plot also reveals that the yield stress data for the twinned and reference pillars

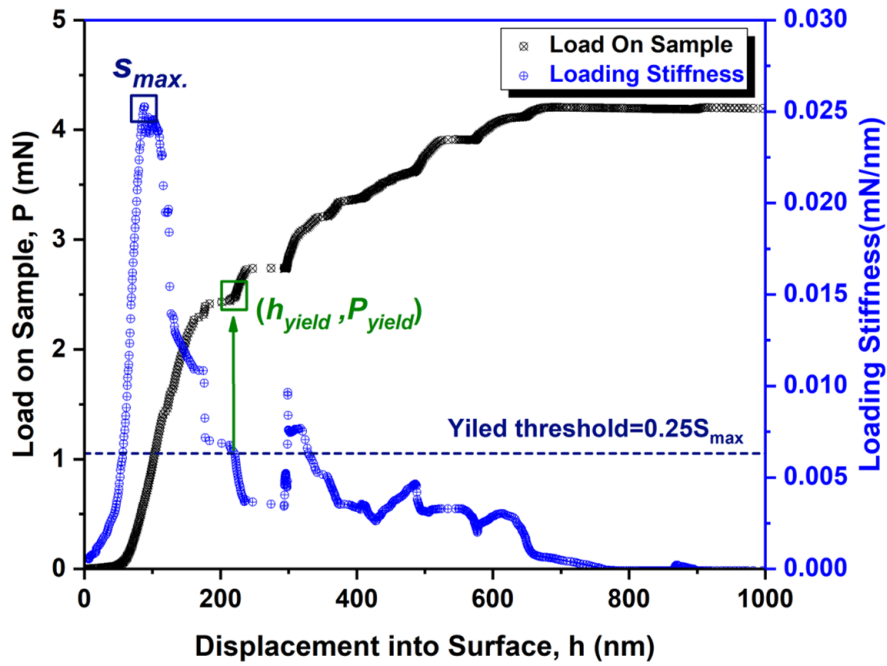


**Figure 4.21.** Definition of the yield point based on the load-displacement and loading stiffness curves of a compressed micropillar. The yield point,  $(h_{\text{yield}}, P_{\text{yield}})$ , is defined as the point where the loading stiffness becomes less than a threshold value of 25% of the maximum loading stiffness,  $S_{\text{max}}$ .

have quite comparable standard deviations and similar slopes for the best fit lines. However, the detwinned samples possess a larger confidence band along with a more inclined best fit line, relating to a larger standard deviation. The larger spread in the yield stress data for the bicrystalline micropillars after detwinning can be explained by the variation in volume of the detwinned region. The volume fraction of the included pre-existing twin varied for the bicrystalline micropillars, which is controlled by the inclination of the twin boundary and the distance from the pillar's longitudinal axis toward the boundary. This distance could not be kept exactly the same during the micropillars fabrication process. Whereas in the  $[10\bar{1}0]$  micropillars the entire sample is twinned, detwinning in the  $[0001]/[10\bar{1}0]$  bicrystals occurs in variable volumes and is responsible for the observed differences in the slope of the best fit as well as the size of the confidence bands.

Mg [0001] single crystals that underwent twinning or detwinning not only show a higher yield stress, but they also have higher strain hardening rates than the reference original crystals, indicating that (de)twinning itself significantly impacts strain hardening. Figure 4.23 shows the variation of the work hardening rate,  $\theta = d\sigma/d\varepsilon$ , as a function of engineering stress for an original, a twinned and a detwinned [0001] micropillar. Several spikes in  $\theta$  are found, associated with strain bursts in the stress-strain curves, leading to sudden slope changes in the stress-strain response and noise in the data. This is more noticeable for the reference micropillars (red curves), which show large slip steps on the outer surface of the samples, indicative of such bursts has been already shown in Figure 4.5. As is indicated in the work hardening curves, the [0001] single crystals that are products of twinning and detwinning

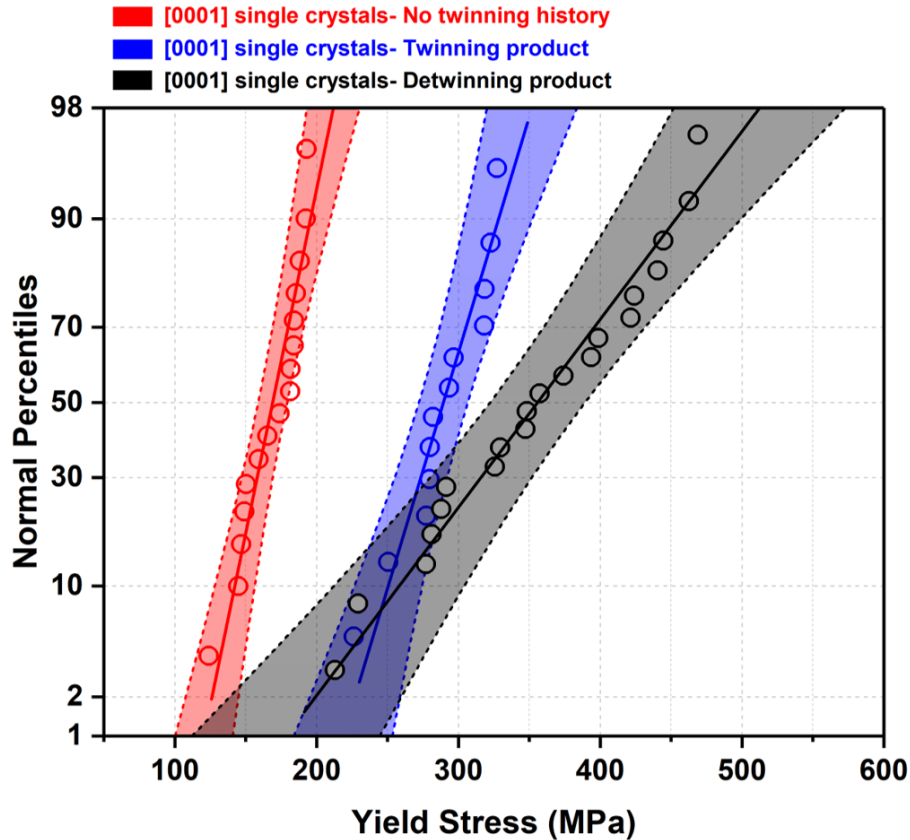


**Figure 4.22.** Normal probability plot of the yield stress data obtained from the stress-strain curves of totally 51 compressed micropillars up to 12% strain. Besides the best fits (solid lines),  $\pm 95\%$  confidence intervals are given in the colored regions with dashed line boundaries. For the twinning ( $[10\bar{1}0]$ ) and detwinning ( $[0001]/[10\bar{1}0]$ ) micropillars the yield criterion was applied for the stress-strain data beyond the stress plateaus, hence all the data correspond to a nominal  $\sim [0001]$  oriented single crystal, but with different twinning histories. The plot reveals higher yield stresses for the twinned and the detwinned micropillars relative to the reference samples.

show distinguishable higher hardening rates compared to the original reference crystals. As it is understood from Figures 4.21 and 4.22, the yield and work hardening data for the twinning and detwinning products do overlap to some extent. Hence, a clear differentiation between the twinning and detwinning effects is not considered in this work.

Once twinning and detwinning is exhausted, the micropillar is single crystalline of the same nominal orientation as the original  $[0001]$  samples. Yet, its stress-strain response shows significantly higher flow stress (yield stress) and strain hardening rate. This points to the influence of (de)twinning mechanisms on these two characteristics. While an increase in dislocation content can readily explain an increase in yield stress, this typically leads to a decrease in the strain hardening rate for the same material, i.e. the strain hardening rate of the reference pillars is a concave downward function. Therefore, the observations of a simultaneous increase in yield strength and hardening rate cannot be simply explained by the development of dislocation density during the plateau regime. Hardening due to deformation twinning is classically attributed to lattice reorientation from a soft into a hard orientation [138, 139], and dislocation-twin interactions in terms of twin boundaries acting as obstacles

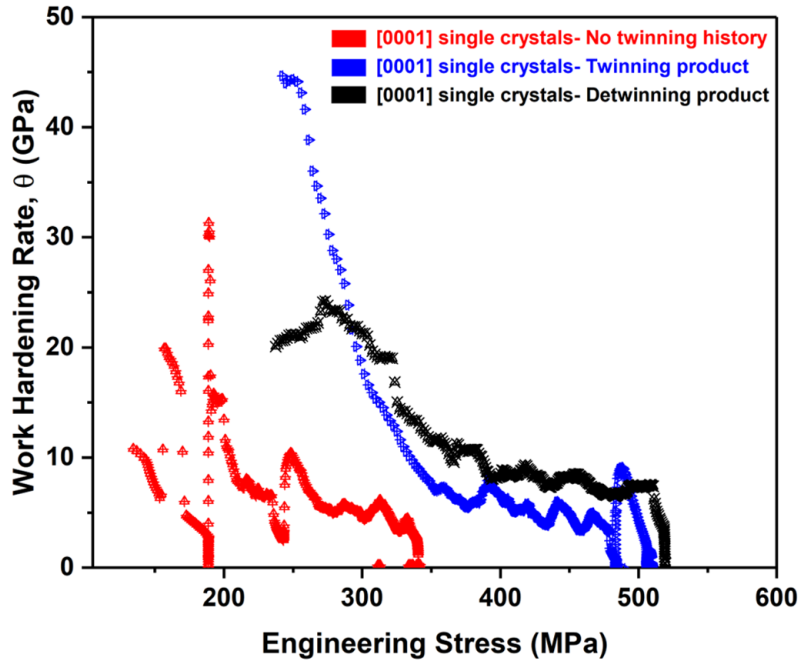


**Figure 4.23.** Work hardening rate,  $\theta$ , as a function of engineering stress for micropillars compressed up to 12%. The curves for the twinning and detwinning samples were plotted using the stress-strain data after the stress plateaus, hence all the data correspond to a nominal  $\sim[0001]$  oriented single crystal, but with different twinning histories. The plot shows a higher hardening rate for the twinned and detwinned micropillars relative to the reference samples.

to subsequent slip [17, 140]. The former is not playing any role in this work, because all of the samples have the same nominal orientation, i.e. [0001]. The exhaustion of (de)twinning capacity inside the micropillars at the end of the plateaus also negates the latter argument. A role of an active twin boundary is not considered anymore while loading beyond the plateau. Consequently, something more fundamental relating to the defect substructure inherited from a migrating twin boundary must be taken into account.

Micropillars interrupted at the saturation of the stress plateau do indeed provide the starting microstructure for the subsequent  $c$ -axis compression. Thus, characterizing the corresponding defect structure would help us to understand the origins of the observed mechanical hardening. An originally [0001] oriented single crystal (as reference), a  $[10\bar{1}0]$  twinning favored single crystalline micropillar and a  $[0001]/[10\bar{1}0]$  bicrystalline sample were interrupted at 5% strain, the corresponding deformation curves are shown in Figure 4.24. Reference single crystal (red curve) follows the typical stair-case hardening after yield stress governed by pyramidal slip. The micropillar of  $[10\bar{1}0]$  orientation is entirely twinned at the end of the stress plateau. The bicrystal shows a shorter plateau associated with detwinning, followed by hardening up to the unloading point. Up to the 5% strain, the reference sample deforms at much higher flow stresses than the other two micropillars. This is because the twinning and detwinning favored micropillars deform by easy twin migration at the early stages of compression rather than the hard  $\langle c+a \rangle$  slip associated with the original [0001] orientation. The behavior is reversed upon further loading beyond 5% strain, where the twinned and detwinned

micropillars are much stronger than the original sample, see Figure 4.20.

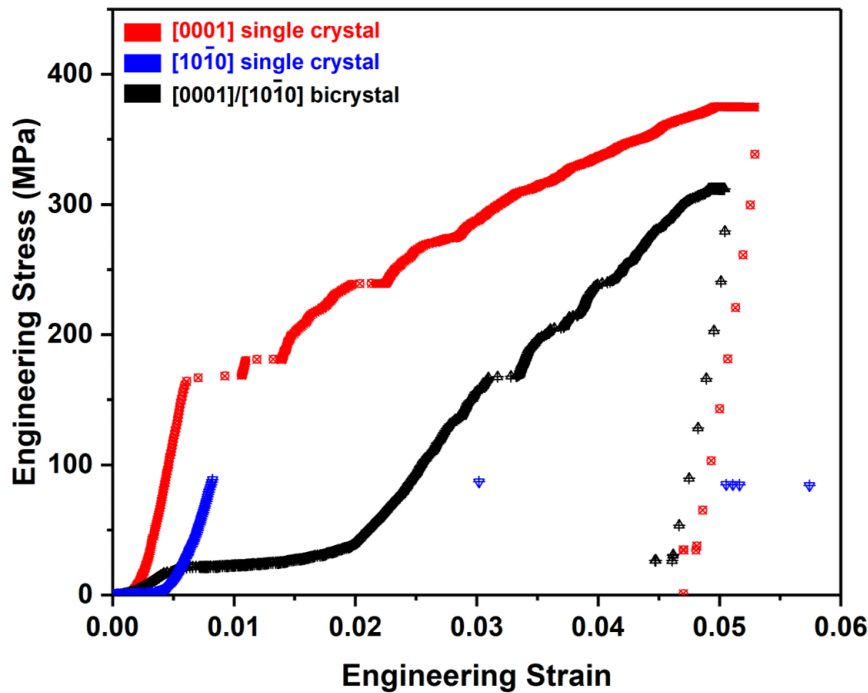


**Figure 4.24.** Engineering stress-strain curves of three micropillars holding single crystals of  $[0001]$  (red curve-as reference) and  $[10\bar{1}0]$  (blue curve) and bicrystal of  $[0001]/[10\bar{1}0]$  (black curve) orientations interrupted at 5% strain. The corresponding EBSD microstructures at the interruption strain have been already shown in Figures 4.5(e) for the red curve, 4.9(e) for the blue curve and 4.17(c) for the black curve. Analysis of defect structure in these same oriented crystals would shed light on the origins of post-(de)twinning mechanical hardening.

The corresponding EBSD cross-sections for the three samples have been already shown in Figures 4.5(e), 4.9(e) and 4.17(c). Thus, consideration of the local variations in orientation within and after the plateau points to a better explanation. To this end, the common kernel average misorientation (KAM) analysis (introduced in Section 3.4.2) was applied to the EBSD data to quantify the local deformations. The results are presented in Figure 4.25. It is apparent from the maps that the overall misorientation distribution is more heterogeneous in the twinned (Figures 4.25(e) and 4.25(f)) and detwinned (Figures 4.25(h) and 4.25(i)) micropillars compared to the single crystalline references (Figures 4.25(b) and 4.25(c)). Higher local misorientations in the micropillars compressed beyond the stress plateau, Figures 4.25(f), 4.25(h) and 4.25(i) suggests a higher accumulated density of geometrically necessary dislocations (GND) in the samples having a twinning history. It can therefore be argued that the higher local GND density would serve as an effective obstacle for dislocation glide, and thus resulting in hardening. To support this idea, the detwinned sample unloaded at 5% strain was selected for further analysis.

The stress-strain curve for this sample shown in Figure 4.24 (black curve) reveals that the sample starts to harden after a stress plateau, activated dislocations after the plateau might have interacted with those defects generated within the plateau. The TEM micrographs presented in Figures 4.11, 4.12 and 4.18 (particularly for this sample) revealed that a high

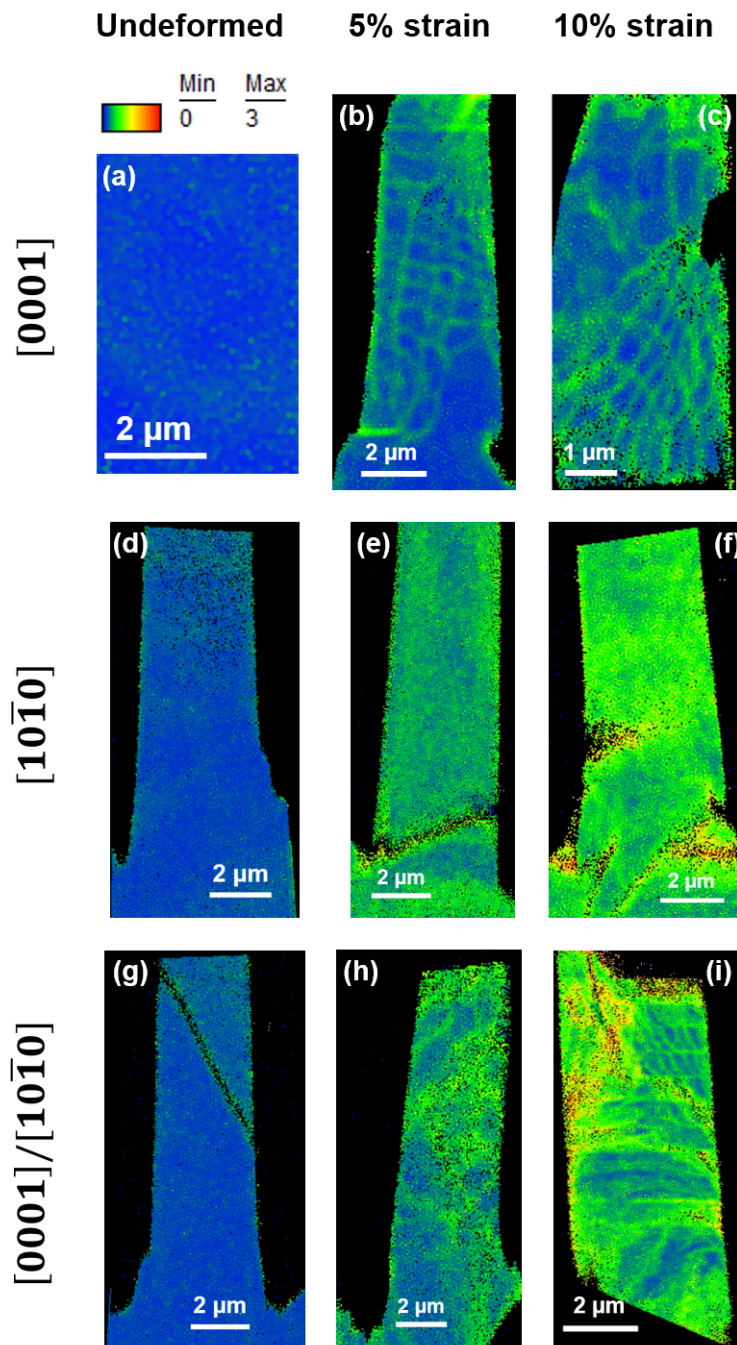


**Figure 4.25.** Maps of kernel average misorientation (KAM) for the compressed micropillars to varying strains constructed from EBSD maps of the samples cross-sections. (a-c) Original [0001] single crystals after 0% (a), 5% (b) and 10% (c) strain. (d-f) Single crystals of  $[10\bar{1}0]$  orientation after 0% (d), 5% (e) and 10% (f) strain. (g-i) Bicrystals of  $[0001]/[10\bar{1}0]$  orientation after 0% (g), 5% (h) and 10% (i) strain. The twinned and detwinned micropillars show inhomogeneous distribution of higher misorientations relative to the reference samples. The corresponding  $[100]$  IPF maps for (b-c) are found in [Figure 4.5](#), for (d-f) are shown in [Figure 4.9](#) and for (g-i) are given in [Figures 4.16](#) and [4.17](#). The deformation curves for (b), (e) and (h) are shown in [Figure 4.24](#).

density of long basal SFs along with rectilinear  $\langle c \rangle$ -containing dislocations are introduced within the plateau into the reoriented [0001] crystal. The  $\langle c \rangle$ -containing dislocations were imaged under the  $g = (01\bar{1}0)$  in the twin and thus they are suspected of being either pure  $\langle c \rangle$ , a product of dissociation of transmuted  $\langle c + a \rangle$  dislocations at the twin boundary, or non-dissociated transmuted  $\langle c + a \rangle$  dislocations. If they are pure  $\langle c \rangle$ , these dislocations would not move under loading along [0001] axis after the plateau since they reside on basal planes which are almost perpendicular to the loading direction. If they are non-dissociated  $\langle c + a \rangle$ , they would not contribute to plastic deformation at such low stress levels of about 25 MPa (detwinned sample) or 86 MPa (twinned sample) at the saturation of the plateau. This is because once the loading direction is approximately parallel to the crystal  $c$ -axis, the  $\langle c + a \rangle$  slip requires activation stresses higher than 150 MPa, see Figure 4.6. Consequently, the  $\langle c \rangle$ -containing dislocations are immobile right after the plateau.

Long basal SFs and sessile dislocations as remnants of the twin migration generate a locking defect structure inside the twin that is likely to contribute to the observed hardening in the (de)twinned [0001] samples. When the micropillar is highly faulted with the SFs, these SFs might interact with the gliding dislocations. The chance of this interaction is expected to be quite high, since the SFs are extended to over hundreds of nanometers. Such faulted sites pose an extra energy barrier for the dislocations to be overcome. This hardening mechanism can be rationalized by an enlarged view of the TEM microstructure already shown in Figure 4.18(b). As is seen from Figure 4.26, SFs no longer maintain their mostly straight planar morphology, this is the case for the twinned sample interrupted within the plateau (Figure 4.11). The SFs in the detwinned micropillar that was interrupted after the plateau were distorted and at some places cut by a potential interaction with the strain field of a gliding dislocation, see the arrows in Figure 4.26. Some SFs are also pitched off into shorter segments. The mobile dislocations that are activated beyond the plateau interact with a dense array of sessile  $\langle c \rangle$ -containing dislocations along with basal SFs that have been generated as debris behind the migrating twin boundary within the plateau regime. Thus, the defect structure inherited from (de)twinning is suggested to strongly contribute to the observed subsequent mechanical hardening in the  $c$ -axis oriented single crystals. The proposed mechanism can explain the higher local misorientations in the KAM maps for the twinned and detwinned samples; an environment including sessile linear and planar defects would increase the number of accumulated dislocations and thus the misorientation resulting from the associated lattice distortion.

The observed (de)twinning-mediated hardening in this work is in agreement with the classically known Basinski mechanism [141] proposed in 1997. Accordingly, glissile dislocations before twinning convert to sessile configurations within twinned areas after twinning shear transformation. Consequently, the transformed defects will harden slip inside the twinned region. Some few studies have mechanically characterized such twin hardening in hcp metals. Jian et al. [142] introduced an ultra-strong Mg alloy with a high density of SFs. As evidenced by TEM, the faults were effective in blocking and accumulating dislocations which could enhance the strain hardening rate of the tested material. TEM studies of deformed Zr also

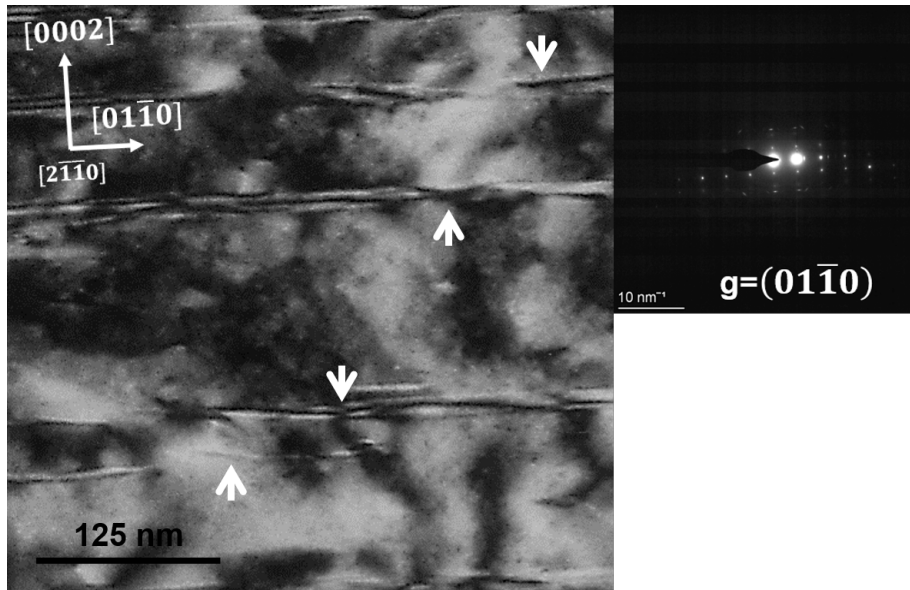


**Figure 4.26.** An enlarged view of the TEM micrograph shown in Figure 4.18(b) using an electron beam close to the  $[2\bar{1}\bar{1}0]$  zone axis at a  $g = (01\bar{1}0)$  two-beam reflection condition. The microstructure belongs to the detwinned micropillar interrupted beyond the stress plateau at 5% strain, the corresponding deformation curve is shown in Figure 4.24 in black. Basal SFs faults might have been distorted, cut and pinched off into shorter segments as they meet a gliding dislocation, some examples are indicated by white arrows. Such faults as debris from detwinning mechanism are suggested to strongly contribute to the post-plateau  $c$ -axis hardening.

showed that the presence of a high density of dislocations, as well as numerous SFs within deformation twins, would increase the resistance to dislocation plasticity in twins leading to hardening [143]. Lastly, incorporation of dislocation transmutation into latent hardening equations in crystal plasticity models has been shown to more accurately simulate the texture and the stress-strain response of Mg alloys [144, 145].

## 4.6 Chapter summary

Microcompression experiments were performed on [0001],  $[10\bar{1}0]$  single and [0001]/ $[10\bar{1}0]$  bicrystalline Mg micropillars to study the hardening mechanisms associated with twinning and detwinning of a single twin boundary. Single crystals of originally [0001] orientation, considered as reference samples, showed a typical stair-case  $c$ -axis hardening flow curve. EBSD and TEM microstructural examinations on pillar cross-sections revealed that compression along the crystal  $c$ -axis is mainly governed by (double) cross-slip of  $\langle c+a \rangle$  dislocations on equivalent pyramidal planes. No twinning was confirmed to contribute to the applied axial stress. Twinning and detwinning appeared as a stress plateau in the stress-strain response of the single  $[10\bar{1}0]$  and bicrystalline micropillars, respectively. At the saturation of the plateau, the twinned and detwinned pillars reoriented into the nominal [0001] orientation. Further straining of these samples beyond the plateau was associated with a strong  $c$ -axis hardening showing similar trends as found in the reference samples. However, a significantly higher yield

stress and a higher strain hardening rate was found for the twinned and detwinned micropillars compared to the reference ones. To understand the origins of such (de)twinning-mediated hardening, microstructural examinations were mostly conducted within the plateau regime, where the twinning defect structure prior to the subsequent loading can be characterized.

TEM observations revealed a unique defect substructure residing in the (de)twinning micropillars in the wake of a migrated twin boundary. Visualized with different two-beam reflection conditions, the micropillars interrupted within the plateau were comprised of a dense array of highly extended basal SFs along with numerous rectilinear  $\langle c \rangle$ -containing dislocations. Both of these defects were discussed to form as by-products of the so-called dislocation transmutation process; i.e. interaction of matrix  $\langle a \rangle$  dislocations with a migrating incoherent twin boundary, which results in a transformation of the  $\langle a \rangle_{\text{matrix}}$  to  $\langle c + a \rangle$  dislocations in the twin. A further dissociation of the transmuted  $\langle c + a \rangle_{\text{twin}}$  dislocations was proposed to leave immobile planar SFs and linear  $\langle c \rangle$  defects. Analysis of misorientation maps from EBSD data and TEM micrographs for a sample unloaded after the plateau let the author argue that the interaction of such sessile twinning-inherited defects with those dislocations activated after the plateau might play an important role in dictating the observed hardening in the micropillars having a twinning history. Despite similar findings in the studies of hcp microstructures within the stress plateau, to the author's knowledge, the results of this chapter is the first mechanical characterization of hardening resulted from the migration of a single twin boundary at the micron scale. The experimental results suggest that any continuum-based modelling approaches for understanding the deformation of Mg must include the concurrent mechanisms of twin migration and defect storage; simply reorienting the crystal upon twinning neglects the critical aspects of the hardening response.



# 5 Twinning and detwinning in Mg-4.7 wt.% Gd alloy

The Mg-Gd solid solution system is known to display a unique twinning behavior. Gd solutes can segregate into twin boundaries under thermal processing. Heat-treating of a Mg-Gd alloy would therefore establish a basis for changing the structure of twin boundaries. The impact of the twin boundary structure on the deformation behavior of Mg alloys at the micron scale is still lacking. The objective in this chapter is to understand the micromechanical effects of twinning and detwinning in a Mg-4.7 wt.% Gd alloy. Micropillars of the same orientation as the case in pure Mg,  $[0001]$ ,  $[10\bar{1}0]$  and  $[0001]/[10\bar{1}0]$ , are tested before and after heat-treatment. Particular focus is on the characterization of twin migration before and after decoration with Gd solutes in the  $[10\bar{1}0]$  and  $[0001]/[10\bar{1}0]$  micropillars and the subsequent hardening response in the  $[0001]$  orientation.

## 5.1 Experimental details

The initial material was an as-cast Mg-4.7 wt.% Gd alloy with the chemical composition already given in Table 3.1. The cast ingot was homogenized at 450°C for 24 hours, in order to remove the dendritic structure. In order to produce deformation twins in grains of interest, rectangular shape bulk samples were cut from the homogenized material and were macroscopically compressed to  $\sim 4.4$  strain (see Section 3.2). The IPF map of the sample surface before and after macrocompression is shown in Figure 5.1. The sample possesses a twin-free structure with random texture before deformation, see Figure 5.1(a). After macroscopic deformation of the bulk sample, deformation twins appear in some grains, as is seen in Figure 5.1(b). The regions of interest that mimic the orientations used for microcompression in pure Mg (Chapter 4) were identified. The selected grains for micropillar fabrication are labeled as **A**, **B** and **C** in Figure 5.1(b). The grain **A** is oriented for compression along the  $[0001]$  direction. The grain **B** is targeted for compression along the  $[10\bar{1}0]$  axis. The grain **C** is highly twinned and is appropriate for fabrication of  $[0001]/[10\bar{1}0]$  bicrystalline micropillars. The enlarged view of this grain in Figure 5.1(c) characterizes the common twin/matrix misorientation relationship for the  $\{10\bar{1}2\}$  twinning. Bicrystalline micropillars include the matrix and the twin. The matrix is compressed along the  $[0001]$  axis, whereas the twin is loaded parallel to the  $[10\bar{1}0]$  direction (Figure 5.1(c)). Microcompression in the selected grains along the viewing plane normal would activate deformation scenarios similar to what was planned in the pure Mg, see 4.2. These scenarios are expected to be pyramidal  $\langle c + a \rangle$  slip in the grain

**A**, extension twinning that reorients the crystal close to the  $[0001]$  direction in the grain **B** and detwinning in the bicrystalline micropillars in the grain **C**.

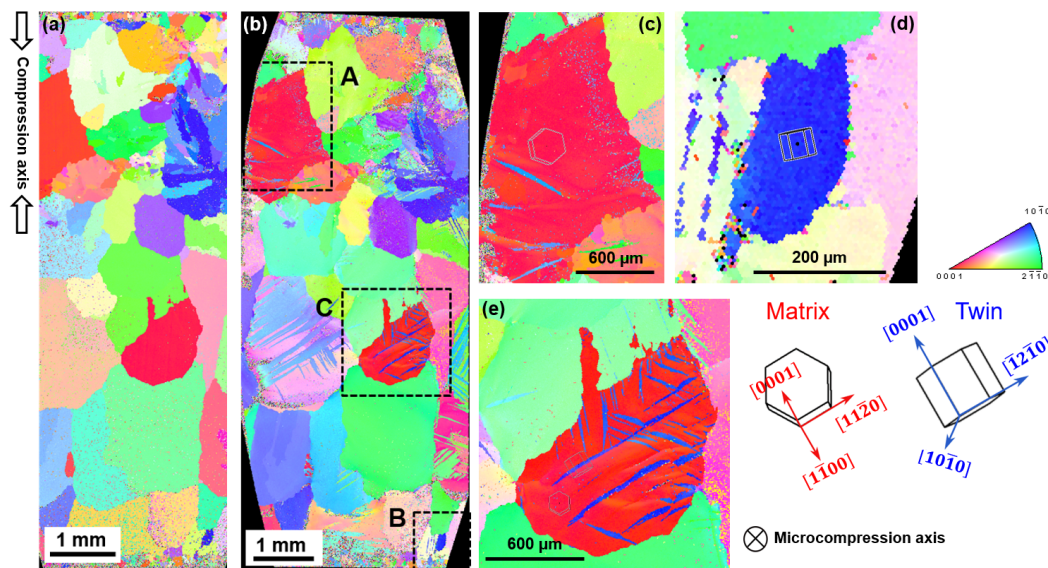


**Figure 5.1.**  $[001]$  IPF maps of a bulk polycrystalline Mg-Gd alloy sample, (a) before and (b) after macroscopic compression to approximately 4.4% strain. The grains of interest for micro-compression are marked by the dashed line areas labeled as **A**, **B** and **C**, their enlarged views are shown respectively in (c), (d) and (e). As is can be found from the color code IPF, the red grain **A** is oriented for compression of  $[0001]$  single crystals. The blue grain **B** is aligned for compression of  $[10\bar{1}0]$  single crystals. The grain **C** is selected for compression of  $[0001]/[10\bar{1}0]$  bicrystals. The orientation of the matrix (red) and the twin (blue) crystals are depicted in their hexagonal cells with the corresponding crystal axes. Microcompression is performed perpendicular to the viewing plane. The crystallographic information related to the selected grains is similar to the grains chosen in the pure Mg presented in Figure 4.2.

Series of micropillars were first fabricated and tested in the grains **A**, **B** and **C** in the as-homogenized alloy (Figure 5.1). The bulk sample was then heat-treated at  $300^\circ\text{C}$  for 3.5 hours. Next, the heat-treated sample was polished on a polishing cloth to make the surface appropriate for EBSD measurement and also for pillar fabrication. After the same grains were identified, a new array of micropillars were machined and tested in the heat-treated grains. In this way, the compression response of the three orientations before and after heat-treatment is compared. This comparison is specifically important in the  $[10\bar{1}0]$  (twinning) and  $[0001]/[10\bar{1}0]$  (detwinning) orientations, where the twin boundary structure is remarkably influenced by a potential segregation of Gd solutes in the twin boundaries. Thus, the twin boundary structure is first characterized in the following section, before presenting the results of microcompression testing.

## 5.2 Solute segregation at $\{10\bar{1}2\}$ twin boundary

High-angle annular dark-field scanning transmission electron microscopy (HAADF-STEM) is of particular interest in studying light metals alloyed with heavier rare-earth (RE) elements.

Combined with energy dispersive spectroscopy (EDS) mapping, the technique has been shown to be extremely powerful to reveal segregation of heavy RE elements in interfaces at (sub-)nanometer level [25, 26]. In order to see the effect of heat-treatment on the twin boundary structure, a TEM lamella was fabricated and lifted-out from a twin within the grain **C** in Figure 5.1(c) following the FIB procedure described in Section 3.4.1. The FIB lift-out process was first carried out on the selected twin before heat-treatment, in the as-homogenized state. After annealing the same twin band at 300°C for 3.5 hours, another lamella was taken out from the twin. The results of HAADF-STEM observation combined with EDS analysis are presented in Figure 5.2.

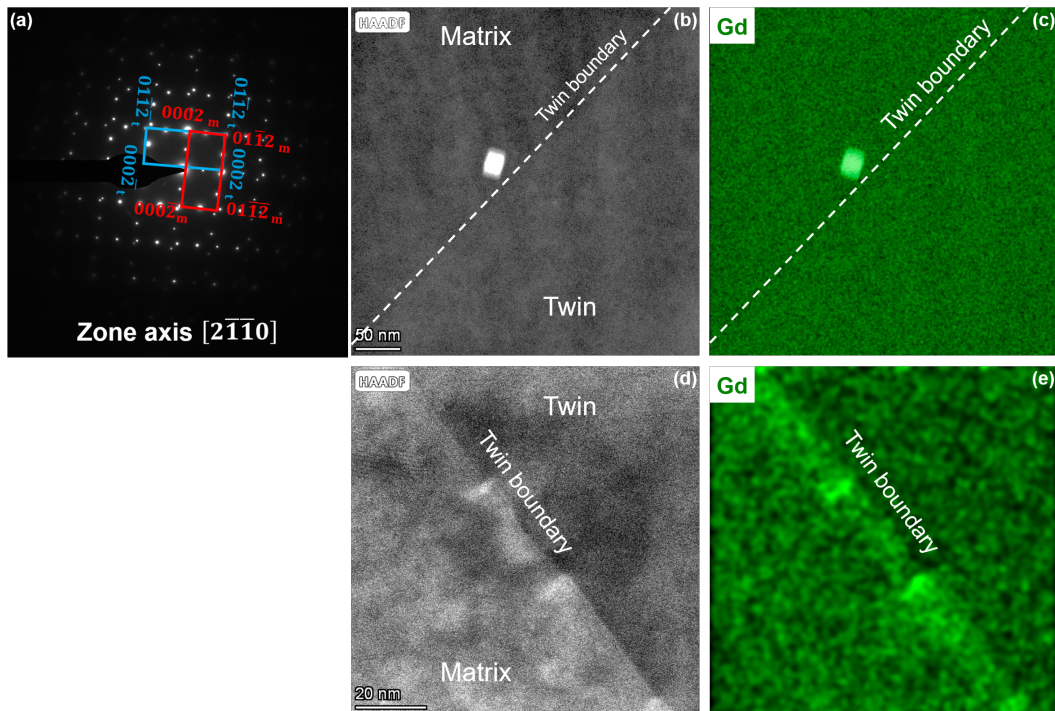


**Figure 5.2.** HAADF-STEM observation of the twin boundary structure in the Mg-Gd alloy, viewed along the  $\langle 2\bar{1}\bar{1}0 \rangle$  co-zone axis in the matrix and the twin. (a) Selected diffraction pattern confirming the crystallographic relationship associated with the  $\{10\bar{1}2\}$  twinning. Diffraction spots corresponding to the matrix (subscript m) and the twin (subscript t) are colored by red and blue, respectively. The HAADF micrographs and the corresponding STEM-EDS maps of Gd elements are shown in (b-c) before heat-treatment and in (d-e) after heat-treatment at 300°C for 3.5 hours. The twin boundary area is decorated with Gd solutes after heat-treatment. The scale bars in EDS maps are the same as in the corresponding HAADF micrographs.

As is shown in Figure 5.2(a), the diffraction pattern obtained from an electron beam close to the  $\langle 2\bar{1}\bar{1}0 \rangle$  co-zone axis in the matrix and the twin confirms the twin/matrix misorientation relationship measured from the EBSD and that the twin is  $\{10\bar{1}2\}$ . Inspection of the obtained HAADF-STEM image, Figure 5.2(b), and the corresponding STEM-EDS map, Figure 5.2(c), suggests that the twin boundary is free of solute segregation before heat-treatment. While the as-generated twin shows no evidence of Gd segregation, the bright intensity in the HAADF-STEM signal visible at the twin boundary area in Figure 5.2(d) indicates a different boundary structure after heat-treatment. The bright Z-contrast (see Section 3.4.3) near the

twin boundary implies a high concentration of Gd solutes, since the intensity of a HAADF image is approximately proportional to the square of the atomic number of the element [146], the atomic numbers of Mg and Gd is 12 and 64, respectively. In line with this idea, the corresponding STEM-EDS map in Figure 5.2(e) qualitatively shows that the concentration of Gd at the twin boundary vicinity is higher than that in regions remote from the twin boundary.

The observation suggests that the Gd solutes most likely segregated into the twin boundary after heat-treatment. The segregation of Gd solutes into the twin boundaries found here does not show the periodic type of segregation reported in coherent  $\{10\bar{1}2\}$  [26] and  $\{10\bar{1}1\}$  [146] twin boundaries in Mg-Gd alloy. Different resolutions might be the reason for this issue. Sub-nanometric imaging can verify such periodic solute segregation in twin boundaries in this thesis. The Gd-enrichment looks to be diffuse close to the twin boundary in Figures 5.2(d) and 5.2(e). This can arise from the twin boundary being oriented not exactly edge-on along the electron beam axis. Under such a condition, the buried out-of-focus Gd-rich points at the twin boundary are expected to contribute to the collected intensity, generating a short-range segregation band close to the twin boundary. Apart from the imaging condition, the diffuse segregation might be related to a concentration gradient extending from the twin boundary.

To consider this idea, a quantitative measurement of the solute fraction as a function of the distance from the twin boundary was performed. A STEM-EDS line scan was conducted across the heat-treated twin boundary, see Figure 5.3(a). The recorded concentration profiles for Gd and Mg elements are plotted in Figure 5.3(b). The temperature-dependent diffusion coefficients of Gd along the  $a$ - and  $c$ -axis in Mg can be written by the following expressions [147]:

$$D_{a\text{-axis}} = 1.27 \times 10^{-9} \exp(-79268/RT) \quad (5.1)$$

$$D_{c\text{-axis}} = 1.79 \times 10^{-9} \exp(-81687/RT) \quad (5.2)$$

in  $\text{m}^2/\text{s}$  where  $R = 8.314 \text{ JK}^{-1}\text{mol}^{-1}$  is the gas constant and  $T$  is the absolute temperature in K. Accordingly, diffusion coefficients of Gd along the  $a$ - and  $c$ -axis in Mg at  $300^\circ\text{C}$  are  $\sim 7.54 \times 10^{-17}$  and  $\sim 6.40 \times 10^{-17} \text{ m}^2/\text{s}$ , respectively. Taken the mean diffusion distance as  $\sqrt{Dt}$ , Gd solutes should be able to enrich twin boundaries from a maximum distance of  $\sim 1.0 \mu\text{m}$  during annealing at  $300^\circ\text{C}$  for 3.5 hours. Therefore, the observed 14 nm-thick segregation band around the twin boundary, as shown by the light gray area in Figure 5.3(b), is thermodynamically achievable under the applied heat-treatment. The concentration of Gd is peaked at the twin boundary and the Gd content at this point ( $\sim 6.1 \text{ wt.}\%$ ) is higher than the nominal concentration of Gd in the alloy (4.7 wt.%).

When the concentration of solute atoms is below the equilibrium solid solubility at the annealing temperature, segregation of Gd atoms within the Mg solid solution is not thermo-

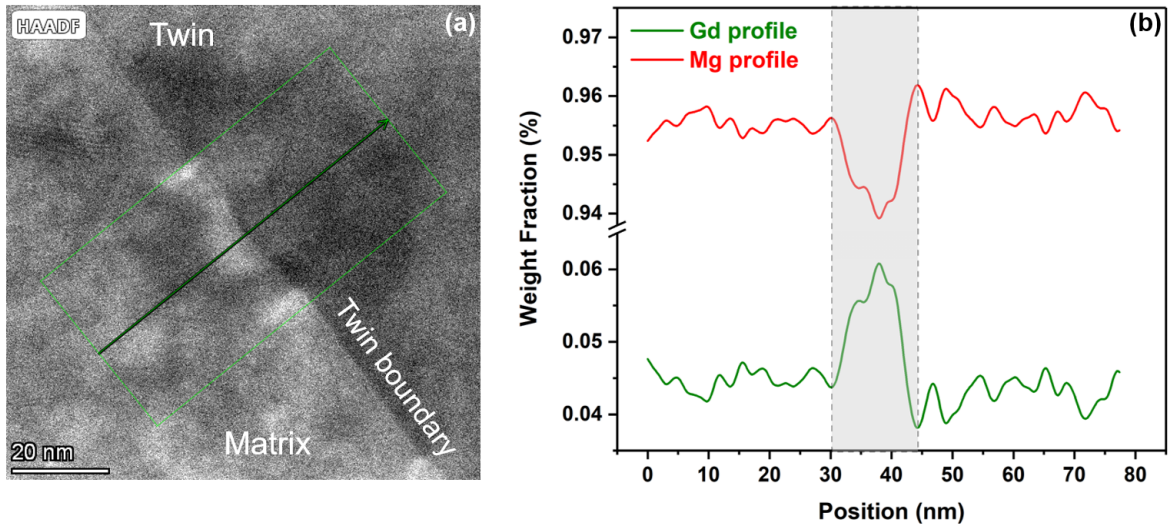


**Figure 5.3.** Line scan STEM-EDS analysis across a twin boundary in Mg-Gd alloy after heat-treatment at 300°C for 3.5 hours. (a) Survey micrograph showing the line profile crossing the twin boundary. The electron beam is close to the  $\langle 2\bar{1}10 \rangle$  co-zone axis in the matrix and the twin. (b) Mg and Gd weight fraction profiles across the twin boundary showing an area at the interface which is enriched in Gd and depleted in Mg as shown by light gray area.

dynamically anticipated. However, density functional theory (DFT) calculations have shown that when elastic strains associated with the twin boundary is introduced into the solid solution matrix, the strained sites are preferred locations for solute segregation in order to reduce elastic strain energies [26]. It has been reported that this elastic strain exists in the twin boundary where compression and extension sites are alternately distributed [26, 148]. The solute atoms larger than Mg segregate favorably to the extension sites, while smaller solutes segregate to the compression sites. This can be understood by considering a large solute in an Mg lattice, where the solute will displace the surrounding Mg atoms away from their normal lattice positions, creating a local strain. If the solute relocates to an extension site in a twin boundary, the strain in the lattice is removed, and the strain in the extension site at the twin boundary is reduced [148].

In this regard, DFT calculations performed by Nie et al. [26] indicated that the strains in the  $\{10\bar{1}2\}$  twin boundaries were reduced after segregation of Gd atoms. The atomic radii of Mg and Gd are 0.16 and 0.18 nm, respectively. Accordingly, substitution of a Mg atom with a Gd atom results in a large negative (compressive) misfit strain which can be balanced once Gd atoms are segregated into the extended region of dislocation cores at the twin boundaries. The strain energy at a twin boundary is estimated based on three components [26]. These are the strain energy caused by the size mismatch between a non-segregated atom and the solid solution matrix of Mg ( $U_1$ ), the energy component caused by the extension or compression of a Mg atom at the twin boundary ( $U_2$ ), and the energy arising from the size mismatch in the twin boundary after segregations of solute atoms into the extension or compression sites ( $U_3$ ). The difference between the strain energy values before and after the segregation defines the

strain energy change in the whole system as  $\Delta U = U_3 - (U_1 + U_2)$  [26]. The strain energy change of the system,  $\Delta U$ , has been calculated to be negative after Gd segregation into a twin boundary meaning that the segregation is energetically favorable [26]. Therefore, the solute segregation patterns observed in this study are thought to be driven by the minimization of the strain energy in the system and do indeed reach the equilibrium. High-resolution TEM studies have shown that the larger solute atoms are thermodynamically stable in a Mg matrix only at interfaces, such as twin [26, 146, 149] and grain [25, 77, 78] boundaries, where the local strain energy of the system is increased.

### 5.3 Microcompression of [0001] single crystals

The engineering stress-strain curves associated with compression of single crystalline micropillars machined into an [0001] oriented grain before and after heat-treatment is shown in Figure 5.4. The non-heat-treated micropillars deform largely elastic up to a yield point at a stress level of about 435 MPa followed by a stair-case hardening until a massive strain burst occurs at a stress level of around 615 MPa. The compression response follows the typical  $c$ -axis hardening behavior which was discussed in details in Section 4.2. Therefore, activation of equivalent pyramidal  $\langle c + a \rangle$  slip systems is suggested to account for the strain hardening in the tested micropillars. Based on the misorientation angle distribution analysis performed on the [0001] oriented single crystals in Section 4.2, a increased resolved shear stress on the basal planes at the final stages of compression can result into the massive basal strain bursts in Figure 5.4.

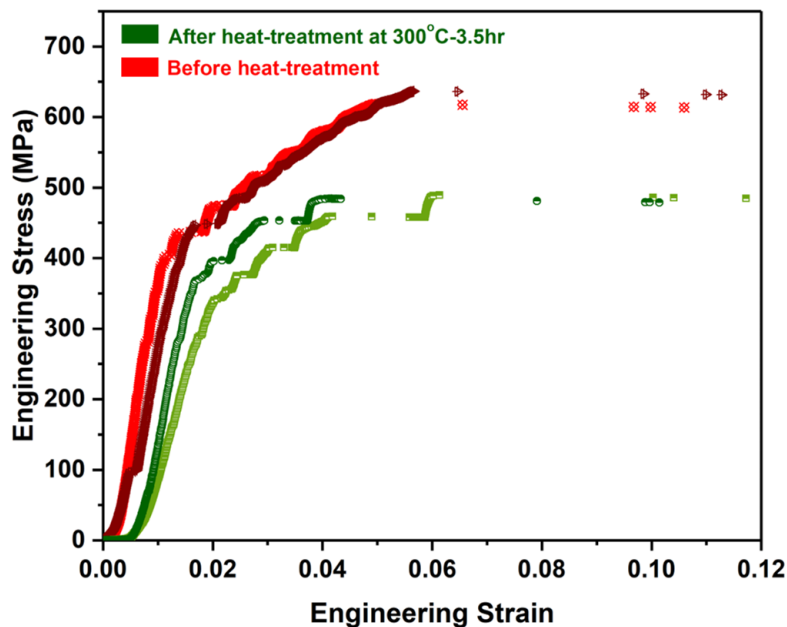


**Figure 5.4.** Engineering stress-strain curves obtained from microcompression of Mg-Gd [0001] single crystals to 12% strain before and after heat-treatment. For pre-compression condition, see the grain **A** in Figure 5.1.

The general features of the stress-strain curves after heat-treatment are similar to those

for the non-heat-treated samples, but the heat-treated micropillars deform by lower flow stress levels. The yield stress after heat-treatment drops to a stress level of about 380 MPa and the large strain burst occurs at about 490 MPa. Such flow softening is most likely related to the expected release of the stored energy after heat-treating the grain. Consequently, the annihilation and rearrangement of dislocations occurs leading to softening in the fabricated micropillars after heat-treatment.

## 5.4 Microcompression of $[10\bar{1}0]$ single crystals

The stress-strain curves obtained from microcompression of  $[10\bar{1}0]$  oriented micropillars before and after heat-treatment are presented in Figure 5.5. In both conditions, a stress increase up to a stress plateau ranging from 100 to 150 MPa is observed. The plateaus have an extension of about 6% strain and are followed by a strain hardening response, typical of the  $c$ -axis hardening trend. The  $[10\bar{1}0]$  compression behavior has been comprehensively discussed in Section 4.3. A comparison of the stress-strain curves shows that the applied heat-treatment has not remarkably affected the twin nucleation stress, i.e. the plateau stress, and also the subsequent hardening trend.

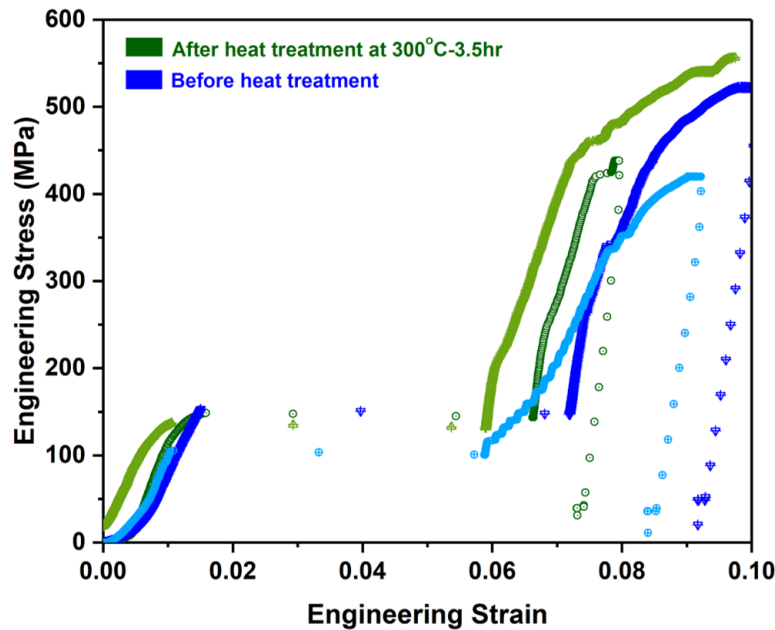


**Figure 5.5.** Engineering stress-strain curves for Mg-Gd  $[10\bar{1}0]$  single crystalline micropillars compressed to a maximum strain of 12% before and after heat-treatment. For pre-compression condition, see the grain **B** in Figure 5.1.

Deformation in this orientation is accompanied by nucleation and propagation of a  $\{10\bar{1}2\}$  twin in the tested micropillars (see Figure 4.9). The nucleated twin is assumed to be free of Gd solutes at the twin boundary, either for the micropillars that were fabricated before heat-treating the grain, or for the samples that were machined after the heat-treatment. In fact, this new twin can not be decorated with solutes before any additional annealing, see Figure

5.2. Therefore, the associated stress required for the twin to nucleate and also the extension achieved by the twin propagation is not influenced by the applied heat-treatment.

The explanation is also valid for the post-twinning hardening response. At the saturation point of  $\{10\bar{1}2\}$  twinning, the reoriented micropillar is of a nominal  $[0001]$  single crystal (Figure 4.9). The rate of work hardening,  $\theta$ , as a function of engineering stress was calculated for the micropillars tested in the  $[10\bar{1}0]$  grain before and after heat-treatment. The stress-strain data after the plateaus in Figure 5.5 were used to calculate the  $\theta$ . The presented results in Figure 5.6 show that after the twinning in Mg-Gd micropillars is complete, the  $[0001]$  hardening response during further loading is not greatly affected by the heat-treatment. Apart from some slight variations, the slope of the stress-strain curve remains mostly similar for the two samples at a constant engineering stress. The same defect structure is expected as debris in the twinned micropillars.

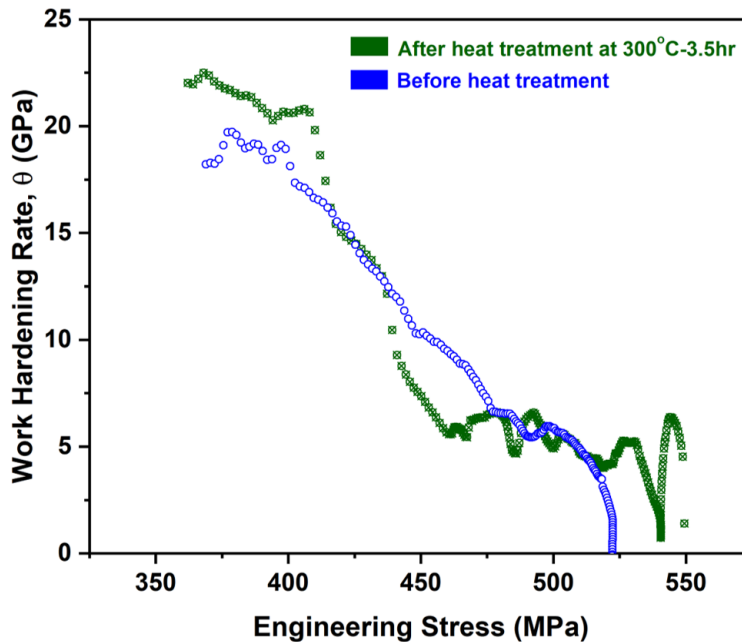


**Figure 5.6.** Work hardening rate,  $\theta$ , as a function of engineering stress for the Mg-Gd  $[10\bar{1}0]$  micropillars compressed to 12% before and after heat-treatment. The curves were plotted using the stress-strain data after the stress plateaus in Figure 5.5, hence all the data correspond to a nominal  $\sim[0001]$  single crystal, but with different thermal processing histories.

Presented in Figure 5.5, compression of non-heat-treated micropillars can show evidence of stair-case features in the post-twinning hardening behavior, see the light blue curve. One can assume these features to be a serrated flow that can be attributed to the dynamic interaction between diffusing solute atoms and moving dislocations, i.e. dynamic strain ageing [33]. This mechanism has been reported for binary Mg-Al [33], Mg-Y [150] and Mg-Gd [27] alloys tested at elevated temperatures, but not at room temperature. At room temperature, the diffusion rate of Gd is not high enough to create solute atmospheres during the arrest time between obstacles. Therefore, the dislocations are always subject to the same array of solutes at room temperature [27]. The observed stair-case features in the stress-strain curve

was further discussed using microstructural examinations on the cross-section of a Mg-Gd  $[10\bar{1}0]$  micropillar unloaded at 5% strain, a strain within the twinning plateau.

The micropillar shows a fully twinned microstructure at the unloaded strain, as is shown in the corresponding  $[100]$  IPF map in Figure 5.7(a). The twin boundary located at the pillar bottom appears to be largely serrated, indicating that the twin possesses an incoherent boundary after traversing through the column. A boundary along the pillar axis has been developed within the twinned crystal, as shown by the arrow. The grain boundary map presented in Figure 5.7(b) reveals that this boundary is a low-angle grain boundary. One end of the low-angle grain boundary is at the pillar top and the other end is pinned at the twin boundary at the pillar bottom. Such boundary is not seen in the matrix crystal and is limited inside the twin. Therefore, one can conclude that the observed low-angle grain boundary has left in the wake of advancing the incoherent twin boundary across the pillar axis.

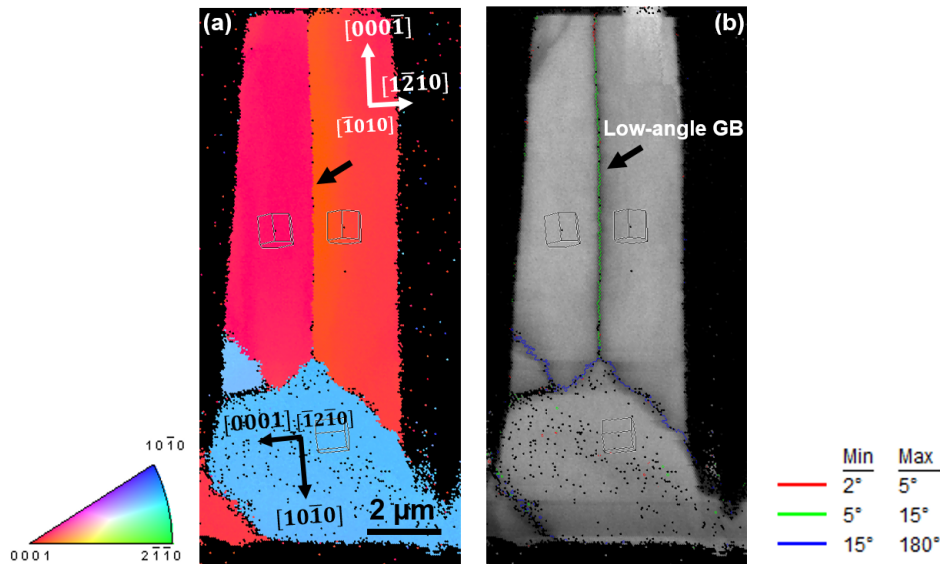


**Figure 5.7.** EBSD microstructural observation on the cross-section of a non-heat-treated Mg-Gd  $[10\bar{1}0]$  micropillar unloaded at 5% strain. (a)  $[100]$  IPF map showing a fully twinned structure. Blue represents the initial orientation of the  $[10\bar{1}0]$  matrix and red represents the twinned lattice. The arrow shows that a boundary appears in the twinned crystal that connects the pillar top to the twin boundary at the bottom. (b) The corresponding grain boundary map reveals that the boundary is a low-angle grain boundary (GB) in the twinned micropillar, as marked by the arrow. High-angle grain boundaries are represented by blue. Low-angle grain boundaries are represented by red and green.

Low-angle grain boundaries have been formed after migration of twin boundaries in Mg-Y [151] and Mg-Al-Zn (AZ series) [9] alloys. As reported by Cui et al. [9], the fraction of low-angle grain boundaries associated with twin migration increased more rapidly in the AZ alloys containing a larger amount of solute elements. This indicates that the solute elements can promote the formation of low-angle grain boundaries during twinning. To understand how alloying elements affect the formation of low-angle grain boundaries, the mechanisms of twinning should be considered. As atomic shearing does not necessarily moves all the

atoms into their right positions in the twin lattice, atomic shuffling is needed to complete the twinning process, see Section 2.2.2. The substitution of solute atoms for the Mg atoms leads to a misfit strain in the crystalline lattice, giving rise to more atoms deviating from the coherent twin boundary. It is therefore considered that more dislocations and defects are generated in the twin boundaries in Mg alloy during twin formation induced by the misfit strain in Mg with a solute concentration [9]. Consequently, these dislocations can be reserved in the prior locations of the advancing twin boundary forming a low-angle grain boundary (Figure 5.7). TEM examinations on compressed Mg-Y micropillars showing such low-angle boundaries along the pillar axis has indicated that these boundaries can effectively block  $\langle c \rangle$ -containing dislocations [151]. It is therefore suggested that the stair-case feature captured in the stress-strain curve in Figure 5.5 might originate from the interaction of moving dislocations with such boundaries.

The low-angle grain boundary can also be recognized as a kink boundary. Although kink deformation is an uncommon deformation mechanism in Mg alloys, it is observed frequently among the materials that show strong plastic anisotropy. Kinking is a major deformation mechanism in Mg alloys containing long-period stacking ordered (LPSO) phase when the loading condition favors twinning [152]. It has been repeatedly reported in Mg-Zn-Y [153, 154], Mg-Gd-Y-Zn-Zr [152] and Mg-Y [155] alloys. Wang et al. [155] observed a large kink band during in situ tensile loading of a Mg-Y alloy. The kink band was observed to form in a grain whose  $c$ -axis was almost parallel to the tensile direction, a loading condition that activates  $\{10\bar{1}2\}$  twinning. Small twins were identified in the vicinity of the kink band. The kink boundaries were therefore suggested to serve as heterogeneous sites for  $\{10\bar{1}2\}$  twin nucleation [155]. Inferred from the results in the RE-containing binary Mg alloys [151, 155], it is thus reasonable to believe that the twin in Figure 5.7 has likely nucleated from the low-angle (kink) boundary, the twin is still pinning the boundary after it has traversed the pillar axis, see Figure 5.7. Yamasaki et al. [154] suggested the low-angle kink boundaries form through a prismatic  $\langle a \rangle$  slip mode, which is thought to be active prior to twin nucleation in  $[10\bar{1}0]$  orientation [30, 73]. The observation in Figure 5.7 necessitates further TEM characterizations to understand how the low-angle boundaries will affect the plasticity after twin exhaustion.

## 5.5 Microcompression of $[0001]/[10\bar{1}0]$ bicrystals

Representative engineering stress-strain curves obtained from microcompression of Mg-Gd  $[0001]/[10\bar{1}0]$  bicrystalline micropillars to 12% strain before and after heat-treatment are shown in Figure 5.8. In the micropillars compressed before heat-treatment, the stress linearly increases up to a stress plateau ranging from 78 to 84 MPa. Further loading beyond the stress plateau shows a stress increase up to a secondary yield followed by a typical  $c$ -axis strain hardening up to stress values of 540-562 MPa. A similar deformation scenario as discussed in Section 4.4 is believed to be valid for the non-heat-treated bicrystalline micropillars. The stress plateau is associated with detwinning. After the detwinning is complete, the micropillar is of a single crystal holding a nominal  $[0001]$  orientation. Further compression of the detwinned

micropillar associates with activation of pyramidal  $\langle c + a \rangle$  dislocation resulting in the observed post-detwinning hardening. When the pre-existing twin boundary is exposed to the heat-treatment, compression response of bicrystals is obviously different.

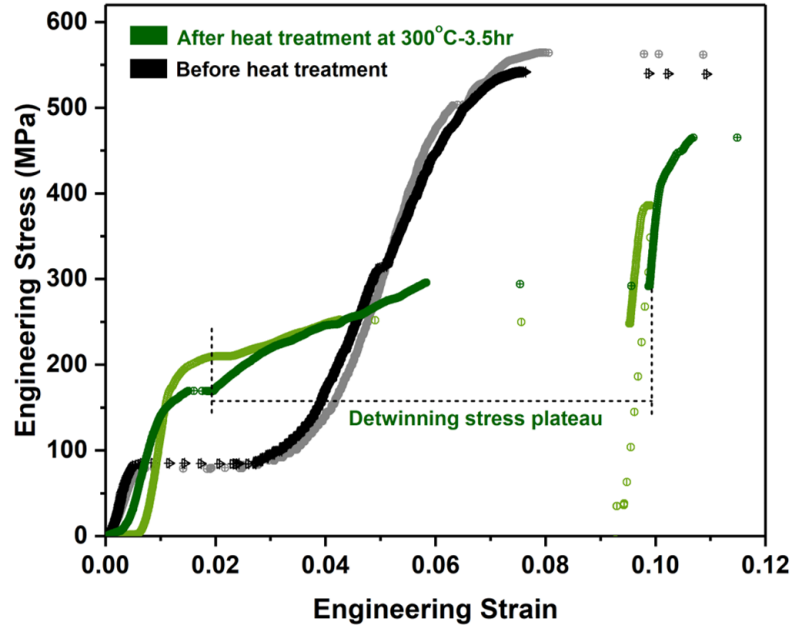


**Figure 5.8.** Engineering stress-strain curves for Mg-Gd  $[0001]/[10\bar{1}0]$  bicrystalline micropillars compressed to 12% strain before and after heat-treatment. The heat-treated pre-existing twin boundary shows a much higher migration stress, i.e. plateau stress, and a higher plateau strain. For pre-compression condition, see the grain C in Figure 5.1.

Interestingly, the heat-treated twin boundary shows a much higher detwinning plateau stress and a much higher plateau strain extension compared to the case before heat-treatment (see Figure 5.8). The stress has to increase to 250-294 MPa, in order for the single pre-existing twin boundary to migrate. Such a very high twin migration stress has never been reported in Mg and Mg alloys. In addition, the heat-treated bicrystalline micropillars have to be compressed to about 10% strain, strain at which the plateau saturates, to be entirely detwinned. The uncommon stress-strain characteristics associated with the detwinning plateau in the compressed micropillars after heat-treatment indicate that detwinning is strongly influenced by heat-treatment in Mg-Gd alloys. This is opposite to the case for twinning, where the compression response of  $[10\bar{1}0]$  micropillars were almost similar before and after heat-treatment, see Figure 5.5. Since the volume fraction of the included twins inside the  $[0001]/[10\bar{1}0]$  bicrystals are nearly the same, the observed hardening in detwinning should be related to the chemical composition of the pre-existing twin boundary influenced by heat-treatment.

Microstructural examinations were performed on the cross-sections of bicrystalline micropillars including heat-treated twin boundaries. The results for an undeformed sample and a micropillar interrupted at 5% strain are shown in Figure 5.9. After compression to 5% strain, a strain within the plateau regime, the pre-existing twin boundary shown in Figure 5.9(a) cannot completely detwin, as is obvious in Figure 5.9(b). The pre-existing twin has reversed to some extent and another twin has nucleated at the pre-existing twin boundary, see

**Figure 5.9(b)**. As evidenced by the STEM-EDS analysis presented in **Figures 5.2** and **5.3**, Gd solutes can segregate into twin boundaries during heat-treatment. The segregated solutes can thus induce a strong pinning effect on the twin boundary so that it can substantially increase the required stress and strain for detwinning. Consequently, plastic straining by detwinning must proceed by the nucleation of a new twin, which is solute free, rather than migration of the already existing twin. Nucleation of a new twin at the pre-existing twin boundary is also seen in the corresponding stress-strain data in **Figure 5.8**. While the detwinning stress plateau occurs at a fixed stress value in the non-heat-treated micropillars, the heat-treated micropillars show a non-flat stress plateau. After the very short flat part of the plateau, the stress increases until a second flat part occurs. According to the microstructure presented in **Figure 5.9(b)**, the hardening part of the detwinning stress plateaus in the heat-treated Mg-Gd bicrystalline micropillars can be related to the additional stress increase required for nucleating a new twin. Consistent to this idea, the stress increase within the detwinning plateau is about 126 MPa, a stress value that falls in the measured twin nucleation stress range of 100-150 MPa in **Figure 5.5**.

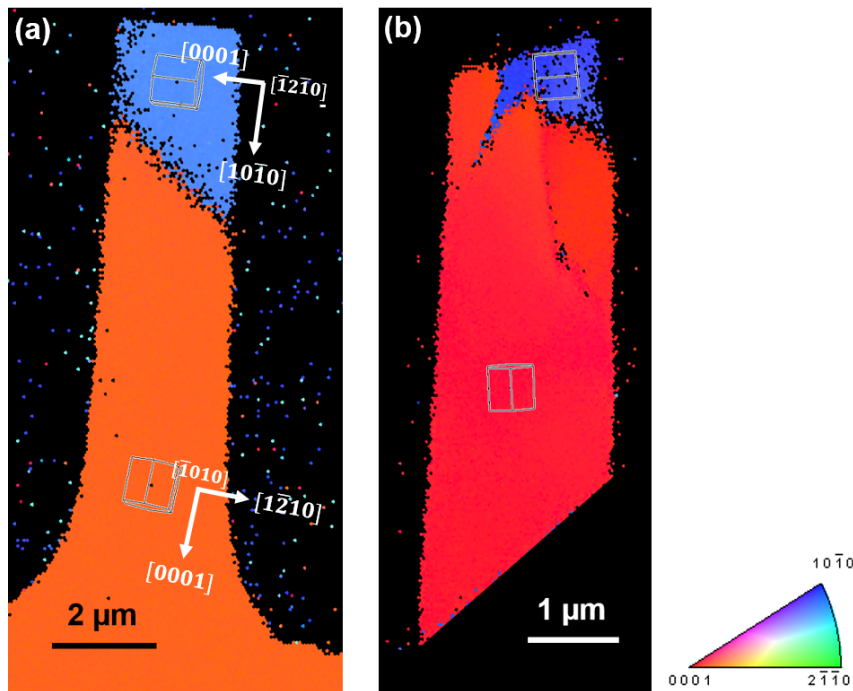


**Figure 5.9.** [100] IPF maps of heat-treated Mg-Gd [0001]/[10 $\bar{1}$ 0] bicrystalline cross-sections (a) before and (b) after unloading at 5% strain. The included pre-existing twin boundary is decorated with segregated Gd solutes at the interface, see **Figures 5.2** and **5.3**. A new twin has nucleated at the pre-existing twin boundary after compression in (b).

## 5.6 Chapter summary

Single and bicrystalline micropillars of [0001], [10 $\bar{1}$ 0] and [10 $\bar{1}$ 0]/[0001] orientations were compressed in a Mg-4.7 wt.% Gd alloy before and after heat-treatment at 300°C for 3.5 hours. A typical flow softening after annealing was observed for the [0001] single crystals. Heat-treatment in this orientation did not change the shape of the flow curves. The twin nucleation stress and the subsequent *c*-axis hardening response in [10 $\bar{1}$ 0] single crystals were not remarkably influenced by the heat-treatment. A unique stair-case feature was found in the stress-strain curve of an [10 $\bar{1}$ 0] micropillar before heat-treatment. Microstructural examinations on a micropillar interrupted within the twinning plateau showed the formation of a low-angle boundary at the twinning exhaustion. The boundary was discussed to have formed as a result of the migration of incoherent twin boundaries in the solid solution of Gd atoms. The observed low-angle boundary was also considered to be a kink boundary, which is frequently observed in RE-containing Mg alloys.

Microcompression of the [10 $\bar{1}$ 0]/[0001] bicrystals before heat-treatment followed the typical detwinning stress-strain characteristics. However, the stress and strain associated with detwinning were substantially different in the heat-treated samples. Using STEM-EDS analysis, it was confirmed that Gd solutes can segregate into the pre-existing twin boundaries during heat-treatment. The solute segregation increased the stress required for migration of a pre-existing twin inside the bicrystals up to about 294 MPa. Such a very high twin migration stress would be enough to activate even the hardest slip system,  $\langle c + a \rangle$  pyramidal slip, in hcp structure. Microstructural examinations on pillars cross-sections showed that the high twin migration stress hinders a complete detwinning of the decorated twin boundary. Instead, plasticity in this case would proceed by nucleation of a new solute-free twin at the pre-existing twin boundary. The results of this chapter can lead to new insights into the micromechanical influences of {10 $\bar{1}$ 2} twinning and detwinning in Mg-Gd solid solution in terms of the twin boundary structure.



## 6 A comparison of the microcompression results in pure Mg and Mg-4.7 wt.% Gd alloy

Micromechanical aspects of pyramidal slip, twinning and detwinning in pure Mg and Mg-4.7 wt.% Gd alloy were discussed respectively in Chapter 4 and Chapter 5. A comparison of the microcompression results in the two material systems would thus enable us to study the effect of Gd solutes on the dominant plasticity mechanisms of each orientation. This chapter presents such comparison in terms of the stress-strain, work hardening and microstructural characteristics that are reported in the previous chapters. Specifically, the microcompression results for the fabricated micropillars in the three orientations after heat-treating the pure Mg and Mg-Gd polycrystals are discussed. Additionally, a systematic comparison between the micromechanical effects of Gd solutes on the  $\langle c + a \rangle$  slip and  $\{10\bar{1}2\}$  (de)twinning found in this work with those reported for other solute elements in the literature is given. This further highlights how Gd solutes stand for the concept of modifying the relative ease of deformation systems in Mg alloys.

### 6.1 Effect of Gd solutes on the [0001] compression response

The stress-strain curves obtained from microcompression along the [0001] single crystals in pure Mg and Mg-Gd alloy are shown in Figure 6.1. As is seen from Figure 6.1, Mg-Gd [0001] micropillars deform obviously by higher flow stresses than pure Mg. The mechanical characteristics extracted from the [0001] stress-strain curves in pure Mg as well as Mg-Gd alloy are listed in Table 6.1. Some published data on microcompression of Mg and Mg alloys with [0001] orientation are also presented in this table.

Plasticity in the [0001] single crystals is dominated by slip of  $\langle c + a \rangle$  dislocations on first- and second-order pyramidal planes (Section 4.2). As is found from Table 6.1, single crystals of pure Mg yield at 169-250 MPa for the sample size range of 4.0-6.1  $\mu\text{m}$ . To facilitate comparisons with the literature, the resolved shear stress,  $\tau_{\text{RSS}}$ , on the pyramidal planes at the yield point and the peak strain hardening rate,  $\theta_{\text{max}}$ , were normalized by the elastic Young's modulus of Mg at room temperature. Generally speaking, the normalized resolved shear stress,  $\tau_{\text{RSS}}/E$ , and the peak strain hardening rates,  $\theta_{\text{max}}/E$ , associated with the activation of pyramidal slip in this work are comparable with those reported elsewhere [73, 75]. The normalized peak strain hardening rate for  $c$ -axis compression is in the range of 0.18-0.24. The normalized resolved shear stress for initiation of pyramidal slip falls within the range of 1.7-2.5

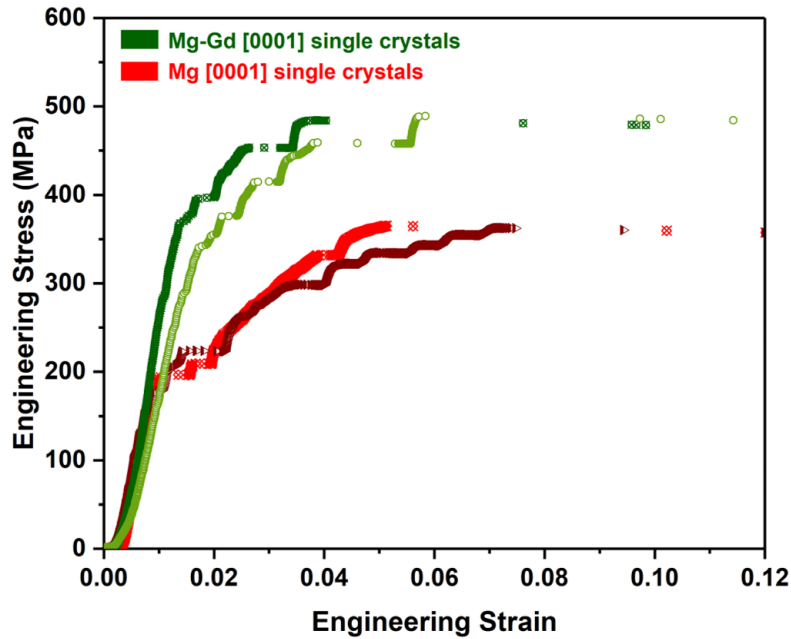


**Figure 6.1.** Engineering stress-strain curves obtained from microcompression of pure Mg and Mg-Gd [0001] single crystals to 12% strain. For pre-compression condition, see the grain **A** in Figures 4.1 and 5.1.

$\times 10^{-3}$ . The variation in the micromechanical characteristics of the [0001] micropillars may originate from the slight differences in the size of tested samples, the purity of the selected material, the deviations from the ideal [0001] loading direction and also the applied strain rates.

The addition of 4.7 wt.% Gd increases the compressive mean yield stress for pyramidal slip from 169 MPa to about 380 MPa, as is shown in this study. The measured increase in the yield stress does not, however, obey the solution strengthening relationship  $\Delta\sigma_{ss} \sim k_{ss}c^n$ , where  $\sigma_{ss}$  is the difference in the yield stress due to solid solution,  $k_{ss}$  is the strengthening coefficient,  $c$  is the solute content of Gd in at.% and  $n$  is the strengthening component [23]. Using the  $k_{ss} = 147$  MPa and  $n = 0.97$  measured for Mg-Gd polycrystalline alloy compressed at room temperature as taken from the literature [23], the  $\sigma_{ss}$  is about 113 MPa in the alloy studied here, where  $c = 0.76$  at.% (Section 3.1). As is found from Table 6.1, the resolved shear stress,  $\tau_{RSS}$ , on the pyramidal planes at the yield point is about 171 MPa for the Mg-Gd alloy, while a value of 76 MPa is measured for the pure sample. The normalized peak strain hardening rate,  $\theta_{max}/E$ , raises from 0.24 to 0.37 with the addition of 4.7 wt.% Gd. All of these measured parameters show a solute strengthening of pyramidal slip in the studied Mg-Gd alloy. Such solid solution strengthening of pyramidal slip due to Gd solutes is thought to be less effective than Zn solutes with  $\sigma_y = 455$  MPa and  $\tau_{RSS} = 203$  MPa [157], but more pronounced than Y elements with  $\sigma_y = 259$  MPa and  $\tau_{RSS} = 119$  MPa [151]. It is noteworthy that for the Mg-Zn alloy in Table 6.1 one should think of the smaller size of pillars compared to the current work and therefore the potential size effect that can affect our comparison of the mechanical effect of the solutes.

**Table 6.1.** The effect of solute elements on the mechanical characteristics of Mg and Mg alloys [0001] single crystals. The values of yield stress,  $\sigma_y$  and peak strain hardening rate,  $\theta_{\max}$ , were extracted from the corresponding stress-strain curves.  $E = 44.5$  GPa is the elastic Young's modulus of Mg at room temperature [156]. The resolved shear stress at the yield point,  $\tau_{\text{rss}}$ , is calculated by  $\tau_{\text{rss}} = m \times \sigma_y$ , where  $m$  is the highest Schmid factor for pyramidal slip.

Material	$\sigma_y$ (MPa)	$\tau_{\text{rss}}$ (MPa)	$\theta_{\max}/E$	$\tau_{\text{rss}}/E$ ( $\times 10^{-3}$ )	Sample size $\mu\text{m}$	Ref.
Mg	169 $\pm$ 21	76	0.24	1.71	4.0	This work
Mg	170	76.5	0.24	1.72	6.1	[75]
Mg	250	112.5	0.18	2.53	5.0	[73]
Mg-4.7 wt.% Gd	380 $\pm$ 20	171	0.37	3.84	4.0	This work
Mg-5.0 wt.% Zn	455 $\pm$ 80	203	-	4.56	2.0	[157]
Mg-0.4 wt.% Y	259	119 $\pm$ 2	-	2.67	4.5	[151]
Mg-4.0 wt.% Y	221	106 $\pm$ 2	-	2.38	4.5	[151]

The parameters listed for the Mg-Y alloys in Table 6.1 show that an increase in the Y content reduces the yield stress and the resolved shear stress in the [0001] single crystalline micropillars [151]. This means a solute softening of pyramidal slip with Y addition, opposite to the trend found for Gd addition in our results. As discussed in Section 2.1.1, addition of Y increases the activity of pyramidal  $\langle c + a \rangle$  dislocations in Mg. The underlying reason for the enhanced activity of  $\langle c + a \rangle$  slip in Mg-Y alloys is attributed to the modified stacking fault energy (SFE) of the system. The significantly decreased SFE through the addition of Y enables the nucleation of  $\langle c + a \rangle$  dislocations at lowered stresses, since the sessile defect structures associated with stacking faults act as heterogeneous nucleation sources for such dislocations [42, 46, 47]. Density functional theory calculations carried out by Sandlöbes et al. [46] showed that in addition to Y, all the lanthanides, comprising the 15 metallic chemical elements with atomic numbers 57–71 including Gd, reduce the SFE of the system relative to pure Mg. They experimentally showed that the mechanical properties of the alloys with predicted decreased SFEs are associated with a significantly increased room temperature ductility and, an increased activity of non-basal, in particular  $\langle c + a \rangle$ , dislocation slip. Considering this fact, the microcompression results in this thesis show that Gd is less effective in enhancing the  $\langle c + a \rangle$  activity compared to Y. With a similar content of the alloying elements and a comparable sample size as well as the same nominal orientation, it is the Mg-Gd alloy that yields at a much higher stress (see the data for Mg-4.7 wt.% Gd and Mg-4.0 wt.% Y in Table 6.1).

Such an increase in work hardening rate in RE-containing alloys has been reported elsewhere [158]. It is suggested that the influence of solute drag on dislocation dynamics would be the strongest contributor to the increase in the work hardening rate. In fact, glide of  $\langle c + a \rangle$  dislocations can be disrupted by the lattice distortions induced by larger Gd solute atoms.

## 6.2 Effect of Gd solutes on the $[10\bar{1}0]$ compression response

The engineering stress-strain response associated with microcompression of  $[10\bar{1}0]$  single crystals in pure Mg and Mg-Gd alloy are presented in Figure 6.2. At the first glance, it can be found from the stress-strain curves that the stress plateaus in the Mg-Gd micropillars can be higher than the pure Mg samples. The work hardening rate beyond the plateau looks also different in the two materials. Compression of the  $[10\bar{1}0]$  single crystals was identified to be associated with nucleation and propagation of  $\{10\bar{1}2\}$  twins, appearing as a stress plateau in the corresponding stress-strain curves (Section 4.3). Mechanical characteristics were extracted from the  $[10\bar{1}0]$  stress-strain curves in pure Mg as well as Mg-Gd alloy and were listed in Table 6.2. The published data on the mechanical behavior  $\{10\bar{1}2\}$  twinning in Mg and Mg alloys are also given for comparison.

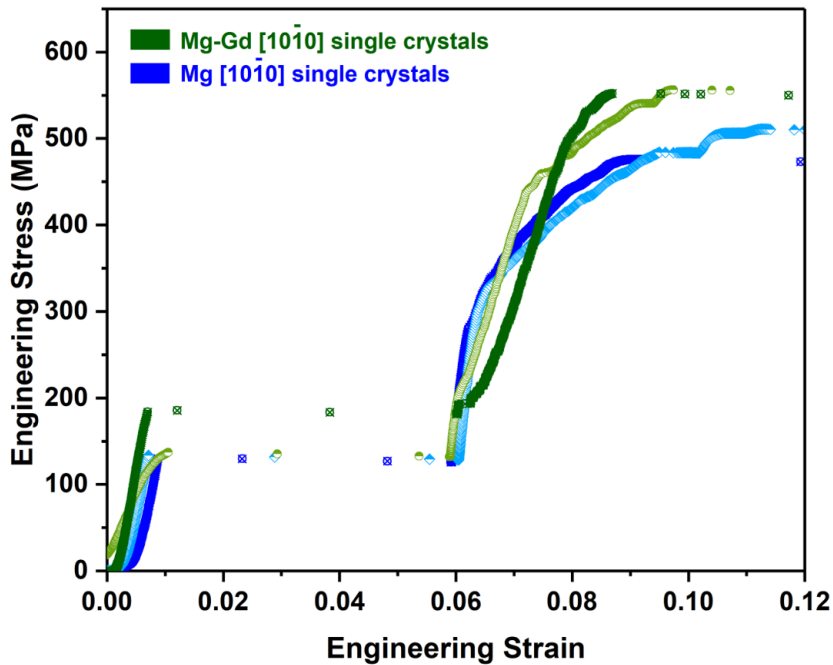


**Figure 6.2.** Engineering stress-strain curves obtained from microcompression of pure Mg and Mg-Gd  $[10\bar{1}0]$  single crystals to 12% strain. For pre-compression condition, see the grain **B** in Figures 4.1 and 5.1.

In order to make an appropriate comparison of the stress-strain characteristics to understand twinning behavior, the twin nucleation and twin boundary migration must be differentiated. Twin nucleation can appear differently in the corresponding stress-strain curves based on the load-controlled or displacement-controlled testing machines. The nucleation stress relates to stochastic factors, especially local stress or stress concentration at the pillar surface [74]. Therefore, quantifying the critical stresses associated with twin migration within the plateau is more straightforward than nucleation stresses in microcompression testing [73, 74]. The micromechanical data reported for  $\{10\bar{1}2\}$  twinning in Table 6.2 shows large scatter in the twinning plateau stress,  $\sigma_{\text{twin}}$ , and accordingly the resolved shear stress at the plateau,  $\tau_{\text{twin}}$  for pure Mg micropillars.

**Table 6.2.** The effect of solute elements on the mechanical characteristics of  $\{10\bar{1}2\}$  twinning in Mg and Mg alloys deformed along the  $[10\bar{1}0]$  and  $[11\bar{2}0]$  directions. The twinning plateau stress,  $\sigma_{\text{twin}}$  and peak strain hardening rate,  $\theta_{\text{max}}$ , were extracted from the corresponding stress-strain curves.  $\theta_{\text{max}}$  is calculated for the  $[10\bar{1}0]$  oriented micropillars that loaded beyond the plateau.  $E = 44.5$  GPa is the elastic Young's modulus of Mg at room temperature [156]. The resolved shear stress at the plateau,  $\tau_{\text{twin}}$ , is calculated by  $\tau_{\text{twin}} = m \times \sigma_{\text{twin}}$ , where  $m$  is the highest Schmid factor for  $\{10\bar{1}2\}$  twinning.

Material/orientation	$\sigma_{\text{twin}}$ (MPa)	$\tau_{\text{twin}}$ (MPa)	$\theta_{\text{max}}/E$	$\tau_{\text{twin}}/E$ ( $\times 10^{-3}$ )	Sample size $\mu\text{m}$	Ref.
Mg/ $[10\bar{1}0]$	118 $\pm$ 21	59	0.42	1.33	4.0	This work
Mg/ $[10\bar{1}0]$	50	25	-	0.56	5.0	[73]
Mg/ $[11\bar{2}0]$	60	22	-	0.49	5.0	[73]
Mg/ $[10\bar{1}0]$	$\sim$ 100	50	0.40	1.12	3.0	[120]
Mg/ $[10\bar{1}0]$	$\sim$ 60	29	-	0.65	3.0-10.0	[74]
Mg-4.7 wt.% Gd/ $[10\bar{1}0]$	152 $\pm$ 21	76	0.53	1.71	4.0	This work
Mg-5.0 wt.% Zn/ $[11\bar{2}0]$	191 $\pm$ 42	71	-	1.60	2.0	[157]
Mg-0.4 wt.% Y/ $[10\bar{1}0]$	98 $\pm$ 30	45 $\pm$ 12	-	1.01	4.5	[151]
Mg-4.0 wt.% Y/ $[10\bar{1}0]$	246 $\pm$ 5	113	-	2.54	4.5	[151]

Twinning occurs at 118 $\pm$ 21 MPa in the current study and the resolved shear stress at the plateau is measured as 59 MPa. This is different with the microcompression results performed elsewhere [73]. The values of  $\sigma_{\text{twin}}$  were 50 and 60 MPa for the twinning orientations of  $[10\bar{1}0]$  and  $[11\bar{2}0]$ , respectively. The higher twinning stress in the  $[11\bar{2}0]$  samples was ascribed to the lower Schmid factor for  $\{10\bar{1}2\}$  twinning while compressed along  $[11\bar{2}0]$ , 0.37, compared to the  $[10\bar{1}0]$  direction having a twinning Schmid factor of 0.5 [73]. Both of the tested orientations, however, showed much lower mechanical characteristics compared to the results of this thesis. This might originate from the smaller sample size in the current work, 4.0  $\mu\text{m}$ , compared to the 5.0  $\mu\text{m}$  pillars tested by Kim [73]. Among all the tested orientations, Kim found the strongest size effect for the two twinning orientations,  $[10\bar{1}0]$  and  $[11\bar{2}0]$ , and this was explained by the size dependency of the dislocation plasticity occurring concurrent with twin nucleation and propagation [73].

On the other hand, microcompression experiments of 3.0, 5.0 and 10.0  $\mu\text{m}$  pillars performed by Liu et al. [74] resulted in approximately a same twinning plateau stress of 60 MPa (a resolved shear stress of about 29 MPa), see Table 6.2. It is suggested that the micropillar geometry and boundary constraints of the microcompression testing can significantly affect the measurement of mechanics of twinning [159]. Changes in taper angle, presence of sharp corners in samples and misalignment between the indenter and the pillar top surface would therefore affect the measurements leading to variations in the critical stresses associated with twinning. The purity of the tested Mg micropillars would also affect the twinning stresses, as some slight differences in chemical composition would alter the behavior. The  $[10\bar{1}0]$  compression results in this thesis is closer to the work carried out by Prasad et al. [120], where a twinning plateau stress of  $\sim$ 100 MPa was reported. The similarity is also valid for the peak strain hardening rate,  $\theta_{\text{max}}/E$ , after the plateaus.

The critical stresses associated with twinning changes with Gd addition in this work. The

twinning plateau stress,  $\sigma_{\text{twin}}$ , increases from  $118 \pm 21$  in pure Mg to  $152 \pm 21$  MPa in Mg-4.7 wt.% Gd alloy (Table 6.2). The associated resolved shear stress in the alloy is calculated as 76 MPa, higher than the value for the pure sample, 59 MPa. The results suggest that Gd addition increases the activation stress required for  $\{10\bar{1}2\}$  twinning. The post-twinning work hardening rate has been also influenced by Gd solutes. The  $\theta_{\text{max}}/E$  value raises in the Mg-Gd alloy compared to the pure Mg. Consistent with the present results, increased critical stresses for twinning at the presence of Gd has been reported elsewhere [23].

The observed increase of the twin migration stress can be explained by the need for prismatic dislocations to be active prior to twinning. In-situ [30] and ex-situ [73] TEM observations of twinning-dominated deformation of Mg micropillars have confirmed that the activity and pile-up of prismatic  $\langle a \rangle$  dislocations act as a primary mechanism for twin generation. Since Gd has been shown to strengthen the prismatic slip system [28], it follows that the stress needed for twinning likewise increases.

In addition to the indirect effect of Gd on twinning via the increased stress for activating prismatic slip, a direct effect should also be considered. As described in Section 2.2.2, two atomic motions are involved in twinning, namely atomic shuffling and atomic shearing. The shuffles involved in the  $\{10\bar{1}2\}$  twin play an important role, since they can become larger than the shear. The experiments have shown that it is the atomic shuffling that is most affected by solute elements [50]. It has been suggested that solute atoms larger than Mg atoms, like Y and Gd, may inhibit this shuffling process [160] and therefore it is possible that the Gd increases the activation stress needed for twin boundary migration in the Mg-Gd micropillars. This can also explain the increased twinning stresses in Mg-Y alloys with increasing Y concentration, see Table 6.2. The increased twinning plateau stress from 98 to 246 MPa is probably associated with the increased solute Y content from 0.4 to 4.0 wt.% [151]. It has been shown that solute hardening of  $\{10\bar{1}2\}$  twins might result in activation of other deformation mechanisms, such as kink band formation [155] and other twinning modes like  $\{11\bar{2}1\}$  twins [160], to particularly accommodate deformation along the  $c$ -axis. Consistent to the idea, formation of a low-angle (kink) boundary was observed in a Mg-Gd micropillar interrupted after twinning saturation, see Figure 5.7.

The solute hardening of twinning in this work can also impact the coherency of the advancing twin boundary in the  $[10\bar{1}0]$  micropillars. Comparisons of the Figures 4.9(e) and 5.7a reveals that the Mg-Gd twin boundary is much more serrated than the boundary in pure Mg. This is consistent with previous reports that the inhomogeneous local strain caused by solute atoms, particularly those atoms that are larger than Mg, gives rise to an inhomogeneous migration of twin boundary leading to a higher level of twin boundary incoherency compared to pure Mg [9]. This is ascribed to the multiple interactions of solute atoms and dislocations at the twin boundary producing more facets at the twin interface, e.g. basal/prismatic facets [9] (see Figure 4.14 for the mechanism of facet formation at an advancing twin boundary). Atomic-resolution observation of the twin boundary structure and numerical calculation of the interaction energies between twinning dislocations and solute atoms and the resulting forces on the twin boundary movement would explain more clearly how Gd solutes influence

the twin boundary coherency during twin migration.

As for the higher work hardening rate after twinning in the Mg-Gd micropillars, Table 6.2, dislocation transmutation took place with higher frequency in Mg-RE alloys compared to pure Mg during twin growth [158]. This further enhances the work hardening rate after twinning. Indeed, a higher density of the sessile transmuted dislocations, see Section 4.5, produce a forest hardening effect that can serve as hard obstacles for glide of  $\langle c+a \rangle$  dislocations in the post-twinning  $c$ -axis compression.

### 6.3 Effect of Gd solutes on the $[0001]/[10\bar{1}0]$ compression response

Representative engineering stress-strain curves obtained from the microcompression of  $[0001]/[10\bar{1}0]$  bicrystals in pure Mg and Mg-Gd alloy are shown in Figure 6.3. Deformation of the bicrystals was identified to be associated with detwinning of the pre-existing  $\{10\bar{1}2\}$  twin, as discussed in Section 4.4. Detwinning appears as a stress plateau in the stress-strain curves. Although the volume fraction of the twin inside the bicrystalline micropillars is nearly the same for all pillars, a large difference in the compression response is observed. The detwinning stress, stress required for migration of the pre-existing twin, is obviously much higher in the Mg-Gd alloy. Mechanical characteristics were extracted from the  $[0001]/[10\bar{1}0]$  stress-strain curves in pure Mg as well as Mg-Gd alloy and were listed in Table 6.3.

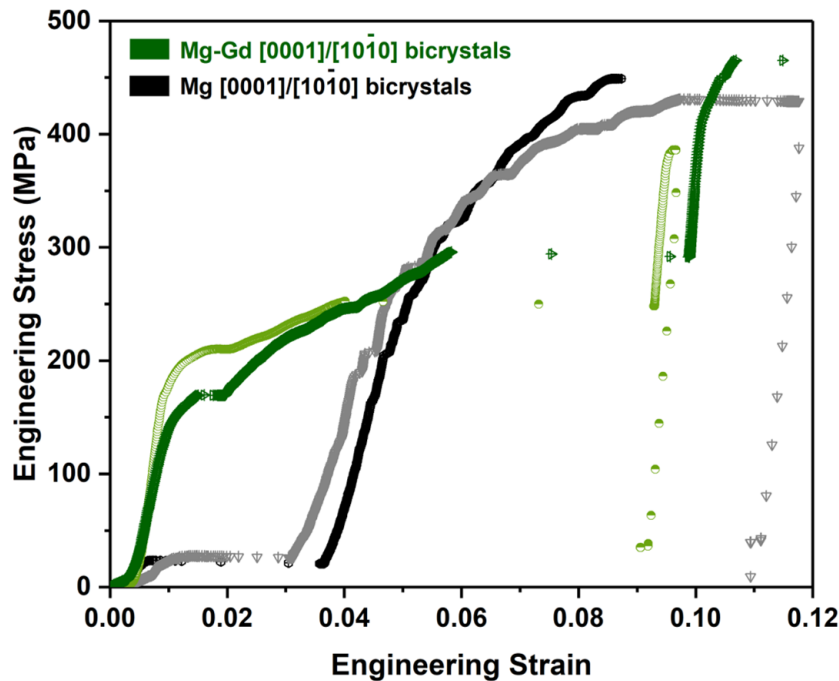


**Figure 6.3.** Engineering stress-strain curves obtained from microcompression of pure Mg and Mg-Gd  $[0001]/[10\bar{1}0]$  bicrystals to 12% strain. For pre-compression condition, see the grain C in Figures 4.1 and 5.1.

As is found from Table 6.3, pure Mg experiences detwinning at  $\sigma_{\text{detwin}} = 38 \pm 17$  MPa in

the current study and the resolved shear stress at the detwinning plateau,  $\tau_{\text{detwin}}$ , is measured as 19 MPa. The critical stresses for detwinning are much lower than those for twinning, as already given in Table 6.2. The difference is due to the nucleation-free nature of detwinning. Since a twin exists in the samples, the high stress needed for twin nucleation is not required to be achieved in the bicrystalline micropillars. The normalized peak strain hardening rate after the detwinning plateau,  $\theta_{\text{max}}/E = 0.5$ , is comparable to the value after the twinning plateau,  $\theta_{\text{max}}/E = 0.42$  (Table 6.2).

The addition of 4.7 wt.% Gd drastically increases the critical stresses for detwinning in the Mg-Gd bicrystalline micropillars. The detwinning stress plateau,  $\sigma_{\text{detwin}}$ , increases to  $250 \pm 33$  MPa and the resolved shear stress required for detwinning is correspondingly calculated as 125 MPa. This remarkable increase in detwinning stress is influenced by the different structure of  $\{10\bar{1}2\}$  twin boundary in the Mg-Gd alloy compared to the pure Mg. As already shown in Figure 5.2, compositional analysis of the twin interface revealed a segregation of Gd solutes into the twin boundary after heat-treatment. The results presented in Table 6.2 show that this solute segregation induces a strengthening effect on the migration of the pre-existing twin boundaries. More of the analysis of the solute segregation at twin boundaries has been discussed in Section 5.2.

**Table 6.3.** The effect of solute elements on the mechanical characteristics of  $\{10\bar{1}2\}$  detwinning in Mg and Mg alloy deformed along the  $[0001]/[10\bar{1}0]$  direction. The detwinning plateau stress,  $\sigma_{\text{detwin}}$  and peak strain hardening rate,  $\theta_{\text{max}}$ , were extracted from the corresponding stress-strain curves.  $\theta_{\text{max}}$  is calculated based on the stress-strain data after the plateaus.  $E = 44.5$  GPa is the elastic Young's modulus of Mg at room temperature [156]. The resolved shear stress at the plateau,  $\tau_{\text{detwin}}$ , is calculated by  $\tau_{\text{detwin}} = m \times \sigma_{\text{detwin}}$ , where  $m$  is the highest Schmid factor for  $\{10\bar{1}2\}$  twinning.

Material	$\sigma_{\text{detwin}}$ (MPa)	$\tau_{\text{detwin}}$ (MPa)	$\theta_{\text{max}}/E$	$\tau_{\text{detwin}}/E$ ( $\times 10^{-3}$ )	Sample size $\mu\text{m}$	Ref.
Mg	$38 \pm 17$	19	0.50	0.43	4.0	This work
Mg-4.7 wt.% Gd	$250 \pm 33$	125	-	2.81	4.0	This work

## 6.4 Effect of Gd solutes on the relative activities of slip and twinning

The ease of slip and twinning on different crystallographic planes is usually quantified by their critical resolved shear stress (CRSS), which can be measured in unconstrained single crystalline specimens where a unique slip or twinning system is activated. Glide of dislocations only occurs when the local resolved shear stress acting upon them equals the CRSS for that particular deformation system [161]. Recent experimental observations of Wang et al. [33] highlighted the experimental difficulties to extract quantitative, size-independent values of the CRSS for pure metals and alloys using micromechanical testing techniques such as micropillar compression, particularly at room temperature. During microcompression testing, amenable

dislocations are not always available inside the pillar volume. Consequently, the stress will continue to increase until a dislocation source is activated. The yield point in the flow curve does not represent the CRSS required to move a dislocation on the slip plane, but rather reflects the stress required to activate the sources that happen to be available within the pillar. In the twinning and detwinning orientations, the yield stress appeared as a plateau stress in the stress-strain curves. For the case of twinning or detwinning, the stress to yield the micropillar, i.e. the plateau stress, represents the stress required to nucleate and propagate a twin, or the stress needed to migrate an existing twin inside the pillar, respectively [157]. In the present work, the normalized values of the resolved shear stress at the yield point for [0001] ( $\tau_{\text{rss}}/E$ ),  $[10\bar{1}0]$  ( $\tau_{\text{twin}}/E$ ) and  $[0001]/[10\bar{1}0]$  ( $\tau_{\text{detwin}}/E$ ) micropillars listed respectively in Tables 6.1, 6.2 and 6.3 are used to approximate the relative activities of pyramidal slip, twinning and detwinning deformation systems in the pure Mg as well as Mg-Gd alloy. The corresponding data are shown in Figure 6.4 and compared with those reported for bulk pure Mg as well as Mg alloy micropillars.

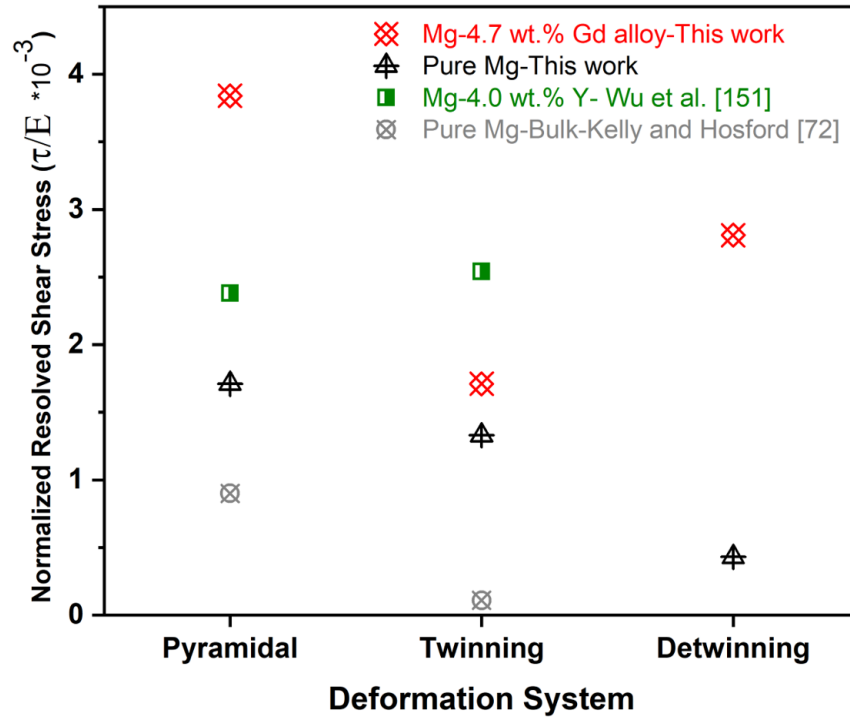


**Figure 6.4.** The effect of solute elements on the relative activity of pyramidal slip, twinning and detwinning in bulk [72] and micropillars of pure Mg, Mg-Gd and Mg-Y [151] alloys. The values of normalized resolved shear stress,  $\tau/E$ , were taken from Tables 6.1, 6.2 and 6.3.

The results of Kelly and Hosford [72] indicate a much easier activity of twinning compared to pyramidal slip in bulk single crystals of pure Mg. The trend is similar for the microcompression results of pure Mg in this thesis. However, a clear size effect in the activation stresses is observed. Evidently, the size effect is more pronounced for twinning than the pyramidal slip which may be due to the facilitated twin nucleation in constrained compression tests in [72]. While detwinning is the easiest strain accommodator along the crystal  $c$  direction in pure

Mg, twinning accommodates axial strain with the lowest required stress in Mg-Gd alloy. The activation stress for the three deformation systems changes from  $(\tau/E)_{\text{pyramidal}} > (\tau/E)_{\text{twin}} > (\tau/E)_{\text{detwin}}$  in pure Mg to  $(\tau/E)_{\text{pyramidal}} > (\tau/E)_{\text{detwin}} > (\tau/E)_{\text{twin}}$  in Mg-Gd alloy. Comparisons of the results in the current work implies that Gd exerts the highest strengthening on the detwinning mechanism followed by pyramidal slip and twinning. The effect is different from that reported by Kula et al. [23], in which Gd hardened the twinning mode more than the slip mode in polycrystalline Mg-Gd alloys. Furthermore, the effect of Y on the relative activity of pyramidal slip and twinning is found to be quite different compared to Gd. It can be inferred from Figure 6.4 that slip of  $\langle c + a \rangle$  dislocations on pyramidal planes requires an activation stress close to that needed for  $\{10\bar{1}2\}$  twinning [151]. This may lead to a higher mechanical isotropy at the presence of Y compared to Gd.

## 6.5 Chapter summary

Microcompression results from  $4\mu\text{m}$  size pillars machined in heat-treated polycrystals of pure Mg and Mg-Gd alloy were compared, and the effect of Gd solutes on the  $[0001]$ ,  $[10\bar{1}0]$  and  $[0001]/[10\bar{1}0]$  compression response were discussed. In the case of  $[0001]$  single crystals, the addition of 4.7 wt.% Gd increases the yield stress for pyramidal slip from 169 MPa to about 380 MPa. The peak strain hardening rate of pure Mg is also enhanced via alloying with Gd. The solute strengthening of pyramidal slip in the Mg-Gd alloy is shown to be more effective than Y elements, as presented in the literature [151], where the yield stress of  $\langle c + a \rangle$  slip is shown to decrease with increasing the Y solute content.

Gd addition increases the activation stress required for  $\{10\bar{1}2\}$  twinning in Mg. The twinning plateau stress increases from 118 to 152 MPa after alloying with Gd. The peak strain hardening rate after the twinning plateau is also higher for the Mg-Gd micropillars. The hardening in twin activity was discussed in terms of the effect of Gd solutes on the dislocation plasticity prior to twin nucleation and the strain hardening after twinning. It is suggested that the strengthening effect of Gd solutes on prismatic slip might hinder twin nucleation events to higher stresses. In addition, the higher hardening rate beyond the twinning plateau is ascribed to the higher rate of dislocation transmutation during twinning at the presence of solutes. The solutes are suggested to lead to an inhomogeneous twin boundary migration leading to a more serrated twin boundary compared to pure Mg.

The detwinning plateau stress significantly increases with Gd addition from 38 to about 250 MPa. This hardening of the critical stresses for detwinning is ascribed to the different structure of the pre-existing twin boundaries in pure Mg and Mg-Gd bicrystalline micropillars. Segregation of Gd to twin boundaries after heat-treatment was discussed to be the responsible mechanism for the observed effect. Comparison of the normalized resolved shear stresses reveals that addition of Gd changes the ease of activity of the deformation systems accommodating axial strain in pure Mg. While detwinning is the easiest mode to occur in pure Mg, it is the twinning that requires the least activation stress in Mg-Gd alloy. Such an effect may be different in other rare-earth containing systems like Mg-Y [151], where a higher

mechanical isotropy is anticipated due to the close values of activation stresses for pyramidal slip and twinning.



# 7 Concluding remarks and future directions

## 7.1 Concluding remarks

Microcompression experiments were carried out in this work to study the effects of twinning and detwinning on the concurrent slip activity in a pure Mg and a Mg-4.7 wt.% Gd alloy at room temperature. Particularly, single crystals of [0001] (pyramidal slip) and [10 $\bar{1}$ 0] (twinning) as well as bicrystals of [0001]/[10 $\bar{1}$ 0] (detwinning) orientation were compressed to understand (i) how {10 $\bar{1}$ 2} twinning and detwinning impact the  $c$ -axis hardening response of Mg in the two material systems, and (ii) how Gd solutes serve to influence the twinning, detwinning and pyramidal slip. Detailed microstructural characterizations were performed on focused ion beam (FIB)-prepared cross-sections of the compressed micropillars using electron backscatter diffraction (EBSD), scanning transmission electron microscopy (STEM) and high-angle annular dark-field (HAADF) imaging in STEM combined with energy dispersive spectroscopy (EDS) to identify the deformation mechanisms responsible for the recorded stress-strain behaviors. The main conclusions of the work based on the results presented in Chapters 4, 5 and 6 are given below as follows:

- Compression of pure Mg micropillars revealed a significant hardening in the yield stress and strain hardening rate of the [0001] single crystals after experiencing twinning and detwinning. The observed hardening in the  $\langle c + a \rangle$  dislocation slip, as the dominant plasticity mechanism in the [0001] orientation, was ascribed to the unique defect substructure residing in the (de)twinning micropillars in the wake of a migrated twin boundary. TEM observations at different reflection conditions revealed that the micropillars interrupted within the (de)twinning plateau comprise a dense array of highly extended basal stacking faults (SFs) and numerous rectilinear  $\langle c \rangle$ -containing dislocations. Detailed analysis of the TEM micrographs let us to consider such defect structure as by-products of interaction of matrix  $\langle a \rangle$  dislocations with a migrating incoherent twin boundary resulting in a transmutation of the  $\langle a \rangle_{\text{matrix}}$  dislocations to  $\langle c + a \rangle_{\text{twin}}$ . Considerations of the resolved shear stresses acting on the generated dislocations within the twin along with the high extension of the SFs, this was proposed to be an immobile defect environment that plays an important role in dictating the higher flow stress characteristics found for the [0001] single crystals with a (de)twinning history. The results in Chapter 4 provide the first micromechanical assessment of the dislocation transmutation process in Mg, highlighting the critical aspects of the concurrent mechanisms of twin migration and defect storage in the dislocation plasticity.

- Heat-treating of the Mg-4.7 wt.% Gd alloy showed an alteration of the  $\{10\bar{1}2\}$  twin boundary structure after heating. Using STEM-EDS analysis, a segregation of Gd solutes into twin boundaries was confirmed to occur after heat-treatment. The solute segregation enhanced the detwinning plateau stress in the Mg-Gd bicrystalline micropillars up to a maximum value of about 294 MPa, a very high stress that has never been reported for migration of a single twin boundary. Such a remarkable impact of heat-treatment on the detwinning mechanism was not observed for the single crystalline Mg-Gd micropillars oriented for pyramidal slip and twinning. While the compression response of the  $[0001]$  single crystalline pillars experienced a typical softening effect after heating, the stress-strain behavior of the  $[10\bar{1}0]$  samples was not noticeably influenced by the heat-treatment. EBSD microstructural examinations revealed that low-angle (kink) boundaries could form inside the twinned micropillars as a potential consequence of incoherent twin boundary migration within a solid solution containing Gd atoms larger than Mg. This was similar to the observations reported after twinning of rare-earth containing Mg alloys. The results in Chapter 5 present the first microcompression experiments of pyramidal slip, twinning and detwinning of Gd-decorated  $\{10\bar{1}2\}$  twin boundaries in Mg-Gd solid solution.
- The microcompression results of the  $[0001]$ ,  $[10\bar{1}0]$  and  $[0001]/[10\bar{1}0]$  micropillars in the pure Mg and Mg-Gd alloy were compared in Chapter 6 to understand the effect of Gd solutes on the pyramidal slip, twinning and detwinning. It was found that all these deformation modes are strengthened by addition of 4.7 wt.% Gd to pure Mg. The most strengthening effect was applied on the detwinning mechanism by Gd addition followed by pyramidal slip and twinning. This led to altering the relative ease of activity in these deformation modes in the Mg-Gd system compared to pure Mg. Accordingly, while detwinning and pyramidal slip were found to be respectively the easiest and hardest modes in pure Mg, twinning was the easiest mode in Mg-Gd alloy and pyramidal slip was still the hardest one. Comparisons of the results with the published data showed that the effect may be different for other rare-earth elements.

## 7.2 Future directions

Based on the microcompression experiments performed in this work and the remarkable differences found for the micromechanical response of the two material systems, the following ideas are proposed directing towards a complementary interpretation of the slip and (de)twinning mechanisms affected by Gd solutes:

- Comparison of the stress-strain characteristics associated with pyramidal slip (Table 6.1) showed a different, and to some extent opposite, effect that rare-earth elements may apply on the activity of  $\langle c + a \rangle$  dislocations. Evidently, more work of the type being carried out by Sandlöbes and colleagues [46] is required to determine the stacking fault energy of the binary Mg-Gd system using density functional theory calculations,

and its impact on the nucleation and cross-slip probability of different  $\langle a \rangle$  and  $\langle c + a \rangle$  dislocation types.

- The effect of Gd solutes on the mechanisms of twin migration in the  $[10\bar{1}0]$  orientation and the associated hardening effect on the critical stresses for twinning (Table 6.2) needs to be further clarified. As discussed in Section 6.2 the effect may be related to the hardened prismatic slip prior to twin nucleation and also the complex interaction of larger than Mg solid solution atoms with twin boundary dislocations during operation of atomic shearing and shuffling. An in-situ loading experiment may provide insights on the effect of Gd solutes on the slip activity required for a twin to nucleate. In addition, high-resolution TEM investigations is thought to be necessary in order to understand the local interactions of matrix dislocations with a migrating twin boundary in a solid solution environment and the resulting defects at the twin interface leading to a change into the twin boundary coherency.
- The results in Table 6.2 also indicated a higher work hardening rate after twinning in the Mg-Gd alloy, which was ascribed to a probable higher density of dislocation transmutation products compared to pure Mg [158]. The effect of Gd solutes on the dislocation transmutation process during  $\{10\bar{1}2\}$  twinning and TEM observation of the resulting debris inside the twin would provide an answer for the question of how Gd affects the frequency of defect generation inside the twin.
- Lastly, all the compression tests were performed in this work at room temperature, where the diffusion-controlled dynamic strain aging of moving dislocations by solute atoms is not operated. At elevated temperature there is a possibility that dislocations are not subject to the same array of solutes [27], providing a pinning and un-pinning effect on dislocations. Therefore, it is of great interest to investigate how pyramidal slip, twinning and detwinning mechanisms are influenced during in-situ micrompression testing at elevated temperatures.

## 8 Bibliography

- [1] M. M. Avedesian, H. Baker, et al., ASM specialty handbook: Magnesium and Magnesium Alloys, ASM international, 1999.
- [2] K. Hono, C. Mendis, T. Sasaki, K. Oh-ishi, Towards the development of heat-treatable high-strength wrought Mg alloys, *Scripta Materialia* 63 (7) (2010) 710 – 715, viewpoint set no. 47 Magnesium Alloy Science and Technology. [doi:https://doi.org/10.1016/j.scriptamat.2010.01.038](https://doi.org/10.1016/j.scriptamat.2010.01.038).
- [3] J. Tu, S. Zhang, On the  $\{10\bar{1}2\}$  twinning growth mechanism in hexagonal close-packed metals, *Materials & Design* 96 (2016) 143 – 149. [doi:https://doi.org/10.1016/j.matdes.2016.02.002](https://doi.org/10.1016/j.matdes.2016.02.002).
- [4] E. Aghion, B. Bronfin, D. Eliezer, The role of the magnesium industry in protecting the environment, *Journal of Materials Processing Technology* 117 (3) (2001) 381 – 385, containing keynote papers presented at the proceedings of THERMEC'2000, the International conference on Processing and manufacturing of Advanced Materials. [doi:https://doi.org/10.1016/S0924-0136\(01\)00779-8](https://doi.org/10.1016/S0924-0136(01)00779-8).
- [5] D. Fechner, N. Hort, K. Kainer, Magnesium recycling system prepared by permanent mould-and high pressure die casting, in: TMS Annual Meeting, San Francisco, USA, Minerals, Metals & Materials Soc, 2009, pp. 111–116.
- [6] V. J. J Brian Jordon, Victoria Miller, N. R. Neelameggham, *Magnesium Technology 2020*, Springer International Publishing, 2020. [doi:https://doi.org/10.1007/978-3-030-36647-6](https://doi.org/10.1007/978-3-030-36647-6).
- [7] M. Yoo, J. Lee, Deformation twinning in hcp metals and alloys, *Philosophical Magazine A* 63 (5) (1991) 987–1000. [doi:https://doi.org/10.1080/01418619108213931](https://doi.org/10.1080/01418619108213931).
- [8] X. Lou, M. Li, R. Boger, S. Agnew, R. Wagoner, Hardening evolution of AZ31B Mg sheet, *International Journal of Plasticity* 23 (1) (2007) 44 – 86. [doi:https://doi.org/10.1016/j.ijplas.2006.03.005](https://doi.org/10.1016/j.ijplas.2006.03.005).
- [9] Y. Cui, Y. Li, Z. Wang, X. Ding, Y. Koizumi, H. Bian, L. Lin, A. Chiba, Impact of solute elements on detwinning in magnesium and its alloys, *International Journal of Plasticity* 91 (2017) 134–159. [doi:https://doi.org/10.1016/j.ijplas.2016.09.014](https://doi.org/10.1016/j.ijplas.2016.09.014).

- 
- [10] M. A. Kumar, I. J. Beyerlein, R. J. McCabe, C. N. Tome, Grain neighbour effects on twin transmission in hexagonal close-packed materials, *Nature communications* 7 (1) (2016) 1–9. doi:<https://doi.org/10.1038/ncomms13826>.
- [11] X. Hong, A. Godfrey, W. Liu, Challenges in the prediction of twin transmission at grain boundaries in a magnesium alloy, *Scripta Materialia* 123 (2016) 77 – 80. doi:<https://doi.org/10.1016/j.scriptamat.2016.05.044>.
- [12] M. A. Kumar, I. Beyerlein, C. Tomé, Effect of local stress fields on twin characteristics in HCP metals, *Acta Materialia* 116 (2016) 143 – 154. doi:<https://doi.org/10.1016/j.actamat.2016.06.042>.
- [13] Q. Yu, J. Wang, Y. Jiang, R. J. McCabe, N. Li, C. N. Tomé, Twin–twin interactions in magnesium, *Acta Materialia* 77 (2014) 28 – 42. doi:<https://doi.org/10.1016/j.actamat.2014.05.030>.
- [14] B. Morrow, E. Cerreta, R. McCabe, C. Tomé, Toward understanding twin–twin interactions in hcp metals: Utilizing multiscale techniques to characterize deformation mechanisms in magnesium, *Materials Science and Engineering: A* 613 (2014) 365 – 371. doi:<https://doi.org/10.1016/j.msea.2014.06.062>.
- [15] J. Hirth, J. Wang, C. Tomé, [Disconnections and other defects associated with twin interfaces](https://doi.org/10.1016/j.pmatsci.2016.07.003), *Progress in Materials Science* 83 (2016) 417 – 471. doi:<https://doi.org/10.1016/j.pmatsci.2016.07.003>.  
URL <http://www.sciencedirect.com/science/article/pii/S0079642516300329>
- [16] M. Knezevic, A. Levinson, R. Harris, R. K. Mishra, R. D. Doherty, S. R. Kalidindi, Deformation twinning in AZ31: Influence on strain hardening and texture evolution, *Acta Materialia* 58 (19) (2010) 6230 – 6242. doi:<https://doi.org/10.1016/j.actamat.2010.07.041>.
- [17] D. Sarker, D. Chen, Detwinning and strain hardening of an extruded magnesium alloy during compression, *Scripta Materialia* 67 (2) (2012) 165 – 168. doi:<https://doi.org/10.1016/j.scriptamat.2012.04.007>.
- [18] C. Cáceres, A. Blake, On the strain hardening behaviour of magnesium at room temperature, *Materials Science and Engineering: A* 462 (1) (2007) 193 – 196, international Symposium on Physics of Materials, 2005. doi:<https://doi.org/10.1016/j.msea.2005.12.113>.
- [19] C. Cáceres, P. Lukáč, A. Blake, Strain hardening due to  $\{1012\}$  twinning in pure magnesium, *Philosophical Magazine* 88 (7) (2008) 991–1003. doi:<https://doi.org/10.1080/14786430701881211>.

- [20] M. D. Uchic, D. M. Dimiduk, J. N. Florando, W. D. Nix, Sample Dimensions Influence Strength and Crystal Plasticity, *Science* 305 (5686) (2004) 986–989. [arXiv:https://science.sciencemag.org/content/305/5686/986.full.pdf](https://science.sciencemag.org/content/305/5686/986.full.pdf), [doi:10.1126/science.1098993](https://doi.org/10.1126/science.1098993).
- [21] P. Shade, R. Wheeler, Y. Choi, M. Uchic, D. Dimiduk, H. Fraser, A combined experimental and simulation study to examine lateral constraint effects on microcompression of single-slip oriented single crystals, *Acta Materialia* 57 (15) (2009) 4580–4587. [doi:https://doi.org/10.1016/j.actamat.2009.06.029](https://doi.org/10.1016/j.actamat.2009.06.029).
- [22] A. Kula, X. Jia, R. Mishra, M. Niewczas, Flow stress and work hardening of Mg-Y alloys, *International Journal of Plasticity* 92 (2017) 96–121. [doi:https://doi.org/10.1016/j.ijplas.2017.01.012](https://doi.org/10.1016/j.ijplas.2017.01.012).
- [23] A. Kula, K. Noble, R. Mishra, M. Niewczas, Plasticity of Mg-Gd alloys between 4 K and 298 K, *Philosophical Magazine* 96 (2) (2016) 134–165. [doi:https://doi.org/10.1080/14786435.2015.1123820](https://doi.org/10.1080/14786435.2015.1123820).
- [24] A. Imandoust, C. Barrett, T. Al-Samman, K. Inal, H. El Kadiri, A review on the effect of rare-earth elements on texture evolution during processing of magnesium alloys, *Journal of Materials Science* 52 (1) (2017) 1–29. [doi:https://doi.org/10.1007/s10853-016-0371-0](https://doi.org/10.1007/s10853-016-0371-0).
- [25] M. Bugnet, A. Kula, M. Niewczas, G. Botton, Segregation and clustering of solutes at grain boundaries in Mg–rare earth solid solutions, *Acta Materialia* 79 (2014) 66 – 73. [doi:https://doi.org/10.1016/j.actamat.2014.06.004](https://doi.org/10.1016/j.actamat.2014.06.004).
- [26] J. F. Nie, Y. M. Zhu, J. Z. Liu, X. Y. Fang, Periodic Segregation of Solute Atoms in Fully Coherent Twin Boundaries, *Science* 340 (6135) (2013) 957–960. [arXiv:https://science.sciencemag.org/content/340/6135/957.full.pdf](https://science.sciencemag.org/content/340/6135/957.full.pdf), [doi:10.1126/science.1229369](https://doi.org/10.1126/science.1229369).
- [27] N. Stanford, I. Sabirov, G. Sha, A. La Fontaine, S. P. Ringer, M. R. Barnett, Effect of Al and Gd solutes on the strain rate sensitivity of magnesium alloys, *Metallurgical and Materials Transactions A* 41 (3) (2010) 734–743. [doi:https://doi.org/10.1007/s11661-009-0107-8](https://doi.org/10.1007/s11661-009-0107-8).
- [28] N. Stanford, D. Atwell, M. R. Barnett, The effect of Gd on the recrystallisation, texture and deformation behaviour of magnesium-based alloys, *Acta Materialia* 58 (20) (2010) 6773–6783. [doi:https://doi.org/10.1016/j.actamat.2010.09.003](https://doi.org/10.1016/j.actamat.2010.09.003).
- [29] S. Ando, K. Nakamura, K. Takashima, H. Tonda,  $\{11\bar{2}2\}\langle\bar{1}\bar{1}23\rangle$  Slip in Magnesium Single Crystal, *Journal of Japan Institute of Light Metals(Japan)* 42 (12) (1992) 765–771. [doi:10.2464/jilm.42.765](https://doi.org/10.2464/jilm.42.765).

- [30] J. Jeong, M. Alfreider, R. Konetschnik, D. Kiener, S. H. Oh, In-situ TEM observation of  $\{10\bar{1}2\}$  twin-dominated deformation of Mg pillars: Twinning mechanism, size effects and rate dependency, *Acta Materialia* 158 (2018) 407 – 421. [doi:https://doi.org/10.1016/j.actamat.2018.07.027](https://doi.org/10.1016/j.actamat.2018.07.027).
- [31] G. I. Taylor, Plastic strain in metals, *J. Inst. Metals* 62 (1938) 307–324.
- [32] M. Yoo, Slip, twinning, and fracture in hexagonal close-packed metals, *Metallurgical Transactions A* 12 (3) (1981) 409–418. [doi:https://doi.org/10.1007/BF02648537](https://doi.org/10.1007/BF02648537).
- [33] J.-Y. Wang, N. Li, R. Alizadeh, M. Monclús, Y. Cui, J. Molina-Aldareguía, J. LLorca, Effect of solute content and temperature on the deformation mechanisms and critical resolved shear stress in Mg-Al and Mg-Zn alloys, *Acta Materialia* 170 (2019) 155 – 165. [doi:https://doi.org/10.1016/j.actamat.2019.03.027](https://doi.org/10.1016/j.actamat.2019.03.027).
- [34] R. Sánchez-Martín, M. Pérez-Prado, J. Segurado, J. Bohlen, I. Gutiérrez-Urrutia, J. Llorca, J. Molina-Aldareguia, Measuring the critical resolved shear stresses in Mg alloys by instrumented nanoindentation, *Acta Materialia* 71 (2014) 283 – 292. [doi:https://doi.org/10.1016/j.actamat.2014.03.014](https://doi.org/10.1016/j.actamat.2014.03.014).
- [35] H. Somekawa, C. A. Schuh, Effect of solid solution elements on nanoindentation hardness, rate dependence, and incipient plasticity in fine grained magnesium alloys, *Acta Materialia* 59 (20) (2011) 7554 – 7563. [doi:https://doi.org/10.1016/j.actamat.2011.08.047](https://doi.org/10.1016/j.actamat.2011.08.047).
- [36] A. Akhtar, E. Teghtsoonian, Solid solution strengthening of magnesium single crystals—i alloying behaviour in basal slip, *Acta Metallurgica* 17 (11) (1969) 1339 – 1349. [doi:https://doi.org/10.1016/0001-6160\(69\)90151-5](https://doi.org/10.1016/0001-6160(69)90151-5).
- [37] A. Akhtar, E. Teghtsoonian, Solid solution strengthening of magnesium single crystals—ii the effect of solute on the ease of prismatic slip, *Acta Metallurgica* 17 (11) (1969) 1351 – 1356. [doi:https://doi.org/10.1016/0001-6160\(69\)90152-7](https://doi.org/10.1016/0001-6160(69)90152-7).
- [38] S. Agnew, M. Yoo, C. Tomé, Application of texture simulation to understanding mechanical behavior of Mg and solid solution alloys containing Li or Y, *Acta Materialia* 49 (20) (2001) 4277 – 4289. [doi:https://doi.org/10.1016/S1359-6454\(01\)00297-X](https://doi.org/10.1016/S1359-6454(01)00297-X).
- [39] F. E. Hauser, P. R. Landon, J. E. Dorn, Deformation and fracture of alpha solid solutions of lithium in magnesium, Minerals Research Laboratory, Institute of Engineering Research, University of California, Berkeley, 1956.
- [40] N. Stanford, M. Barnett, Solute strengthening of prismatic slip, basal slip and  $\{10\bar{1}2\}$  twinning in Mg and Mg–Zn binary alloys, *International Journal of Plasticity* 47 (2013) 165 – 181. [doi:https://doi.org/10.1016/j.ijplas.2013.01.012](https://doi.org/10.1016/j.ijplas.2013.01.012).

- [41] Y. Chino, M. Kado, M. Mabuchi, Enhancement of tensile ductility and stretch formability of magnesium by addition of 0.2wt%(0.035at%)Ce, *Materials Science and Engineering: A* 494 (1) (2008) 343 – 349, advances in microstructure-based modeling and characterization of deformation microstructures held at the TMS Annual Meeting 2007, Orlando, Florida. [doi:https://doi.org/10.1016/j.msea.2008.04.059](https://doi.org/10.1016/j.msea.2008.04.059).
- [42] S. Sandlöbes, S. Zaefferer, I. Schestakow, S. Yi, R. Gonzalez-Martinez, On the role of non-basal deformation mechanisms for the ductility of Mg and Mg–Y alloys, *Acta Materialia* 59 (2) (2011) 429 – 439. [doi:https://doi.org/10.1016/j.actamat.2010.08.031](https://doi.org/10.1016/j.actamat.2010.08.031).
- [43] V. Herrera-Solaz, P. Hidalgo-Manrique, M. Pérez-Prado, D. Letzig, J. Llorca, J. Segurado, Effect of rare earth additions on the critical resolved shear stresses of magnesium alloys, *Materials Letters* 128 (2014) 199 – 203. [doi:https://doi.org/10.1016/j.matlet.2014.04.144](https://doi.org/10.1016/j.matlet.2014.04.144).
- [44] Y. Chino, M. Kado, M. Mabuchi, Compressive deformation behavior at room temperature – 773k in Mg–0.2mass%(0.035at.%)Ce alloy, *Acta Materialia* 56 (3) (2008) 387 – 394. [doi:https://doi.org/10.1016/j.actamat.2007.09.036](https://doi.org/10.1016/j.actamat.2007.09.036).
- [45] T. Tsuru, Y. Udagawa, M. Yamaguchi, M. Itakura, H. Kaburaki, Y. Kaji, Solution softening in magnesium alloys: the effect of solid solutions on the dislocation core structure and nonbasal slip, *Journal of Physics: Condensed Matter* 25 (2) (2012) 022202. [doi:https://doi.org/10.1088/0953-8984/25/2/022202](https://doi.org/10.1088/0953-8984/25/2/022202).
- [46] S. Sandlöbes, Z. Pei, M. Friák, L.-F. Zhu, F. Wang, S. Zaefferer, D. Raabe, J. Neugebauer, Ductility improvement of Mg alloys by solid solution: Ab initio modeling, synthesis and mechanical properties, *Acta Materialia* 70 (2014) 92 – 104. [doi:https://doi.org/10.1016/j.actamat.2014.02.011](https://doi.org/10.1016/j.actamat.2014.02.011).
- [47] S. Sandlöbes, M. Friák, S. Zaefferer, A. Dick, S. Yi, D. Letzig, Z. Pei, L.-F. Zhu, J. Neugebauer, D. Raabe, The relation between ductility and stacking fault energies in Mg and Mg–Y alloys, *Acta Materialia* 60 (6) (2012) 3011 – 3021. [doi:https://doi.org/10.1016/j.actamat.2012.02.006](https://doi.org/10.1016/j.actamat.2012.02.006).
- [48] S. Agnew, J. Horton, M. Yoo, Transmission electron microscopy investigation of  $\langle c + a \rangle$  dislocations in Mg and  $\alpha$ -solid solution Mg–Li alloys, *Metallurgical and Materials Transactions A* 33 (3) (2002) 851–858. [doi:https://doi.org/10.1007/s11661-002-0154-x](https://doi.org/10.1007/s11661-002-0154-x).
- [49] D. Rodney, L. Ventelon, E. Clouet, L. Pizzagalli, F. Willaime, Ab initio modeling of dislocation core properties in metals and semiconductors, *Acta Materialia* 124 (2017) 633 – 659. [doi:https://doi.org/10.1016/j.actamat.2016.09.049](https://doi.org/10.1016/j.actamat.2016.09.049).
- [50] J. Christian, S. Mahajan, Deformation twinning, *Progress in Materials Science* 39 (1) (1995) 1 – 157. [doi:https://doi.org/10.1016/0079-6425\(94\)00007-7](https://doi.org/10.1016/0079-6425(94)00007-7).

- [51] . S. Mahajan, D. Williams, Deformation twinning in metals and alloys, *International Metallurgical Reviews* 18 (2) (1973) 43–61. [doi:https://doi.org/10.1179/imt1r.1973.18.2.43](https://doi.org/10.1179/imt1r.1973.18.2.43).
- [52] P. Partridge, The crystallography and deformation modes of hexagonal close-packed metals, *Metallurgical reviews* 12 (1) (1967) 169–194. [doi:10.1179/mt1r.1967.12.1.169](https://doi.org/10.1179/mt1r.1967.12.1.169).
- [53] B. Wu, Y. Zhang, G. Wan, M. Humbert, F. Wagner, C. Esling, Primary twinning selection with respect to orientation of deformed grains in ultra-rapidly compressed AZ31 alloy, *Materials Science and Engineering: A* 541 (2012) 120 – 127. [doi:https://doi.org/10.1016/j.msea.2012.02.012](https://doi.org/10.1016/j.msea.2012.02.012).
- [54] A. Serra, D. Bacon, R. Pond, The crystallography and core structure of twinning dislocations in H.C.P. metals, *Acta Metallurgica* 36 (12) (1988) 3183 – 3203. [doi:https://doi.org/10.1016/0001-6160\(88\)90054-5](https://doi.org/10.1016/0001-6160(88)90054-5).
- [55] A. Serra, D. Bacon, A new model for  $\{10\bar{1}2\}$  twin growth in hcp metals, *Philosophical Magazine A* 73 (2) (1996) 333–343. [doi:https://doi.org/10.1080/01418619608244386](https://doi.org/10.1080/01418619608244386).
- [56] B. A. Bilby, A. Crocker, The theory of the crystallography of deformation twinning, *Proceedings of the Royal Society of London. Series A. Mathematical and Physical Sciences* 288 (1413) (1965) 240–255. [doi:https://doi.org/10.1098/rspa.1965.0216](https://doi.org/10.1098/rspa.1965.0216).
- [57] B. Li, X. Zhang, Twinning with zero twinning shear, *Scripta Materialia* 125 (2016) 73 – 79. [doi:https://doi.org/10.1016/j.scriptamat.2016.07.004](https://doi.org/10.1016/j.scriptamat.2016.07.004).
- [58] X. Zhang, B. Li, Q. Sun, On the  $\{10\bar{1}2\}$  “twinning shear” measured from line deflection, *Scripta Materialia* 159 (2019) 133 – 136. [doi:https://doi.org/10.1016/j.scriptamat.2018.09.027](https://doi.org/10.1016/j.scriptamat.2018.09.027).
- [59] H. Khater, A. Serra, R. Pond, Atomic shearing and shuffling accompanying the motion of twinning disconnections in Zirconium, *Philosophical Magazine* 93 (10-12) (2013) 1279–1298. [doi:https://doi.org/10.1080/14786435.2013.769071](https://doi.org/10.1080/14786435.2013.769071).
- [60] A. Ostapovets, P. Molnár, On the relationship between the “shuffling-dominated” and “shear-dominated” mechanisms for  $\{10\bar{1}2\}$  twinning in magnesium, *Scripta Materialia* 69 (4) (2013) 287 – 290. [doi:https://doi.org/10.1016/j.scriptamat.2013.04.019](https://doi.org/10.1016/j.scriptamat.2013.04.019).
- [61] B. Li, E. Ma, Atomic Shuffling Dominated Mechanism for Deformation Twinning in Magnesium, *Phys. Rev. Lett.* 103 (2009) 035503. [doi:10.1103/PhysRevLett.103.035503](https://doi.org/10.1103/PhysRevLett.103.035503).
- [62] B.-Y. Liu, J. Wang, B. Li, L. Lu, X.-Y. Zhang, Z.-W. Shan, J. Li, C.-L. Jia, J. Sun, E. Ma, Twinning-like lattice reorientation without a crystallographic twin-

- ning plane, *Nature communications* 5 (1) (2014) 1–6. [doi:https://doi.org/10.1038/ncomms4297](https://doi.org/10.1038/ncomms4297).
- [63] B. Li, X. Zhang, Global strain generated by shuffling-dominated  $\{10\bar{1}2\}\langle 10\bar{1}\bar{1}\rangle$  twinning, *Scripta Materialia* 71 (2014) 45 – 48. [doi:https://doi.org/10.1016/j.scriptamat.2013.10.002](https://doi.org/10.1016/j.scriptamat.2013.10.002).
- [64] A. Serra, D. J. Bacon, R. C. Pond, Comment on ‘Atomic Shuffling Dominated Mechanism for Deformation Twinning in Magnesium’, *Phys. Rev. Lett.* 104 (2010) 029603. [doi:10.1103/PhysRevLett.104.029603](https://doi.org/10.1103/PhysRevLett.104.029603).
- [65] T. Braisaz, P. Ruterana, G. Nouet, R. Pond, Investigation of  $\{1012\}$  twins in Zn using high-resolution electron microscopy: Interfacial defects and interactions, *Philosophical Magazine A* 75 (4) (1997) 1075–1095. [doi:https://doi.org/10.1080/01418619708214012](https://doi.org/10.1080/01418619708214012).
- [66] J. Tu, X. Zhang, C. Lou, Q. Liu, HREM investigation of twin boundary and interface defects in deformed polycrystalline cobalt, *Philosophical magazine letters* 93 (5) (2013) 292–298. [doi:https://doi.org/10.1080/09500839.2013.769691](https://doi.org/10.1080/09500839.2013.769691).
- [67] X. Zhang, B. Li, X. Wu, Y. Zhu, Q. Ma, Q. Liu, P. Wang, M. Horstemeyer, Twin boundaries showing very large deviations from the twinning plane, *Scripta Materialia* 67 (10) (2012) 862 – 865. [doi:https://doi.org/10.1016/j.scriptamat.2012.08.012](https://doi.org/10.1016/j.scriptamat.2012.08.012).
- [68] H. El Kadiri, C. D. Barrett, J. Wang, C. N. Tomé, Why are  $\{10\bar{1}2\}$  twins profuse in magnesium?, *Acta Materialia* 85 (2015) 354 – 361. [doi:https://doi.org/10.1016/j.actamat.2014.11.033](https://doi.org/10.1016/j.actamat.2014.11.033).
- [69] F. Wang, S. R. Agnew, Dislocation transmutation by tension twinning in magnesium alloy AZ31, *International Journal of Plasticity* 81 (2016) 63 – 86. [doi:https://doi.org/10.1016/j.ijplas.2016.01.012](https://doi.org/10.1016/j.ijplas.2016.01.012).
- [70] F. Wang, K. Hazeli, K. Molodov, C. Barrett, T. Al-Samman, D. Molodov, A. Kontsos, K. Ramesh, H. El Kadiri, S. Agnew, Characteristic dislocation substructure in  $\{10\bar{1}2\}$  twins in hexagonal metals, *Scripta Materialia* 143 (2018) 81 – 85. [doi:https://doi.org/10.1016/j.scriptamat.2017.09.015](https://doi.org/10.1016/j.scriptamat.2017.09.015).
- [71] F. Wang, S. Agnew, Dislocation-twin interactions in magnesium alloy AZ31, in: *Magnesium Technology 2015*, Springer, 2015, pp. 139–144. [doi:https://doi.org/10.1007/978-3-319-48185-2\\_27](https://doi.org/10.1007/978-3-319-48185-2_27).
- [72] E. Kelley, W. Hosford, Plane-strain compression of magnesium and magnesium alloy crystals, *Trans Met Soc AIME* 242 (1) (1968) 5–13.
- [73] G. S. Kim, Small volume investigation of slip and twinning in magnesium single crystals, Ph.D. thesis, Grenoble (2011).

- [74] Y. Liu, N. Li, M. A. Kumar, S. Pathak, J. Wang, R. McCabe, N. Mara, C. Tomé, Experimentally quantifying critical stresses associated with basal slip and twinning in magnesium using micropillars, *Acta Materialia* 135 (2017) 411 – 421. [doi:https://doi.org/10.1016/j.actamat.2017.06.008](https://doi.org/10.1016/j.actamat.2017.06.008).
- [75] E. Lilleodden, Microcompression study of Mg (0001) single crystal, *Scripta Materialia* 62 (8) (2010) 532 – 535. [doi:https://doi.org/10.1016/j.scriptamat.2009.12.048](https://doi.org/10.1016/j.scriptamat.2009.12.048).
- [76] L. L. Rokhlin, Magnesium alloys containing rare earth metals: structure and properties, Crc Press, 2003. [doi:https://doi.org/10.1201/9781482265163](https://doi.org/10.1201/9781482265163).
- [77] J. Hadorn, T. Sasaki, T. Nakata, T. Ohkubo, S. Kamado, K. Hono, Solute clustering and grain boundary segregation in extruded dilute Mg–Gd alloys, *Scripta Materialia* 93 (2014) 28 – 31. [doi:https://doi.org/10.1016/j.scriptamat.2014.08.022](https://doi.org/10.1016/j.scriptamat.2014.08.022).
- [78] Y. Zhu, M. Bian, J. Nie, Tilt boundaries and associated solute segregation in a Mg–Gd alloy, *Acta Materialia* 127 (2017) 505 – 518. [doi:https://doi.org/10.1016/j.actamat.2016.12.032](https://doi.org/10.1016/j.actamat.2016.12.032).
- [79] M. D. Uchic, D. M. Dimiduk, A methodology to investigate size scale effects in crystalline plasticity using uniaxial compression testing, *Materials Science and Engineering: A* 400-401 (2005) 268 – 278, dislocations 2004. [doi:https://doi.org/10.1016/j.msea.2005.03.082](https://doi.org/10.1016/j.msea.2005.03.082).
- [80] M. D. Uchic, P. A. Shade, D. M. Dimiduk, Micro-compression testing of fcc metals: A selected overview of experiments and simulations, *Jom* 61 (3) (2009) 36–41. [doi:https://doi.org/10.1007/s11837-009-0038-2](https://doi.org/10.1007/s11837-009-0038-2).
- [81] C. A. Volkert, E. T. Lilleodden, Size effects in the deformation of sub-micron Au columns, *Philosophical Magazine* 86 (33-35) (2006) 5567–5579. [doi:https://doi.org/10.1080/14786430600567739](https://doi.org/10.1080/14786430600567739).
- [82] D. Kaufmann, R. Mönig, C. Volkert, O. Kraft, Size dependent mechanical behaviour of tantalum, *International Journal of Plasticity* 27 (3) (2011) 470 – 478. [doi:https://doi.org/10.1016/j.ijplas.2010.08.008](https://doi.org/10.1016/j.ijplas.2010.08.008).
- [83] D. Kaufmann, A. Schneider, R. Mönig, C. Volkert, O. Kraft, Effect of surface orientation on the plasticity of small bcc metals, *International Journal of Plasticity* 49 (2013) 145 – 151. [doi:https://doi.org/10.1016/j.ijplas.2013.03.004](https://doi.org/10.1016/j.ijplas.2013.03.004).
- [84] N. Malyar, B. Grabowski, G. Dehm, C. Kirchlechner, Dislocation slip transmission through a coherent {111} copper twin boundary: Strain rate sensitivity, activation volume and strength distribution function, *Acta Materialia* 161 (2018) 412 – 419. [doi:https://doi.org/10.1016/j.actamat.2018.09.045](https://doi.org/10.1016/j.actamat.2018.09.045).

- [85] N. Malyar, G. Dehm, C. Kirchlechner, Strain rate dependence of the slip transfer through a penetrable high angle grain boundary in copper, *Scripta Materialia* 138 (2017) 88 – 91. [doi:https://doi.org/10.1016/j.scriptamat.2017.05.042](https://doi.org/10.1016/j.scriptamat.2017.05.042).
- [86] N. Malyar, J. Micha, G. Dehm, C. Kirchlechner, Size effect in bi-crystalline micropillars with a penetrable high angle grain boundary, *Acta Materialia* 129 (2017) 312 – 320. [doi:https://doi.org/10.1016/j.actamat.2017.03.003](https://doi.org/10.1016/j.actamat.2017.03.003).
- [87] G. Dehm, B. Jaya, R. Raghavan, C. Kirchlechner, Overview on micro- and nanomechanical testing: New insights in interface plasticity and fracture at small length scales, *Acta Materialia* 142 (2018) 248 – 282. [doi:https://doi.org/10.1016/j.actamat.2017.06.019](https://doi.org/10.1016/j.actamat.2017.06.019).
- [88] I. N. Sneddon, The relation between load and penetration in the axisymmetric boussinesq problem for a punch of arbitrary profile, *International Journal of Engineering Science* 3 (1) (1965) 47–57. [doi:https://doi.org/10.1016/0020-7225\(65\)90019-4](https://doi.org/10.1016/0020-7225(65)90019-4).
- [89] H. Fei, A. Abraham, N. Chawla, H. Jiang, Evaluation of micro-pillar compression tests for accurate determination of elastic-plastic constitutive relations, *Journal of Applied Mechanics* 79 (6).
- [90] J. Li, T. Malis, S. Dionne, Recent advances in FIB–TEM specimen preparation techniques, *Materials Characterization* 57 (1) (2006) 64 – 70. [doi:https://doi.org/10.1016/j.matchar.2005.12.007](https://doi.org/10.1016/j.matchar.2005.12.007).
- [91] L. N. Brewer, D. P. Field, C. C. Merriman, Mapping and assessing plastic deformation using EBSD, *Electron backscatter diffraction in materials science* (2009) 251–262 [doi:https://doi.org/10.1007/978-0-387-88136-2\\_18](https://doi.org/10.1007/978-0-387-88136-2_18).
- [92] P. O. Guglielmi, M. Ziehmer, E. T. Lilleodden, On a novel strain indicator based on uncorrelated misorientation angles for correlating dislocation density to local strength, *Acta Materialia* 150 (2018) 195–205. [doi:https://doi.org/10.1016/j.actamat.2018.03.009](https://doi.org/10.1016/j.actamat.2018.03.009).
- [93] D. B. Williams, C. B. Carter, *Transmission Electron Microscopy: A Textbook for Materials Science*, Vol. 1, New York: Springer, 2009.
- [94] S. G. Wolf, M. Elbaum, Chapter 10 - CryoSTEM tomography in biology, in: T. Müller-Reichert, G. Pigino (Eds.), *Three-Dimensional Electron Microscopy*, Vol. 152 of *Methods in Cell Biology*, Academic Press, 2019, pp. 197–215. [doi:https://doi.org/10.1016/bs.mcb.2019.04.001](https://doi.org/10.1016/bs.mcb.2019.04.001).
- [95] A. Howie, Image contrast and localized signal selection techniques, *Journal of Microscopy* 117 (1) (1979) 11–23. [doi:https://doi.org/10.1111/j.1365-2818.1979.tb00228.x](https://doi.org/10.1111/j.1365-2818.1979.tb00228.x).

- [96] S. Kadkhodazadeh, High resolution STEM of quantum dots and quantum wires, *Micron* 44 (2013) 75–92. doi:<https://doi.org/10.1016/j.micron.2012.10.004>.
- [97] M. M. L. da Cunha, S. Trepout, C. Messaoudi, T.-D. Wu, R. Ortega, J.-L. Guerquin-Kern, S. Marco, Overview of chemical imaging methods to address biological questions, *Micron* 84 (2016) 23–36. doi:<https://doi.org/10.1016/j.micron.2016.02.005>.
- [98] M. D. Nave, M. R. Barnett, Microstructures and textures of pure magnesium deformed in plane-strain compression, *Scripta Materialia* 51 (9) (2004) 881 – 885. doi:<https://doi.org/10.1016/j.scriptamat.2004.07.002>.
- [99] P. Imrich, C. Kirchlechner, G. Dehm, Influence of inclined twin boundaries on the deformation behavior of Cu micropillars, *Materials Science and Engineering: A* 642 (2015) 65 – 70. doi:<https://doi.org/10.1016/j.msea.2015.06.064>.
- [100] H. Tang, K. W. Schwarz, H. D. Espinosa, Dislocation-Source Shutdown and the Plastic Behavior of Single-Crystal Micropillars, *Phys. Rev. Lett.* 100 (2008) 185503. doi:[10.1103/PhysRevLett.100.185503](https://doi.org/10.1103/PhysRevLett.100.185503).
- [101] S.-W. Lee, W. D. Nix, Geometrical analysis of 3D dislocation dynamics simulations of FCC micro-pillar plasticity, *Materials Science and Engineering: A* 527 (7) (2010) 1903–1910. doi:<https://doi.org/10.1016/j.msea.2009.11.020>.
- [102] C. M. Byer, K. Ramesh, Effects of the initial dislocation density on size effects in single-crystal magnesium, *Acta Materialia* 61 (10) (2013) 3808 – 3818. doi:<https://doi.org/10.1016/j.actamat.2013.03.019>.
- [103] T. Obara, H. Yoshinga, S. Morozumi,  $\{11\bar{2}2\}\langle\bar{1}\bar{1}23\rangle$  slip system in magnesium, *Acta Metallurgica* 21 (7) (1973) 845 – 853. doi:[https://doi.org/10.1016/0001-6160\(73\)90141-7](https://doi.org/10.1016/0001-6160(73)90141-7).
- [104] J. Geng, M. Chisholm, R. Mishra, K. Kumar, An electron microscopy study of dislocation structures in Mg single crystals compressed along  $[0\ 0\ 0\ 1]$  at room temperature, *Philosophical Magazine* 95 (35) (2015) 3910–3932. doi:[10.1080/14786435.2015.1108531](https://doi.org/10.1080/14786435.2015.1108531).
- [105] B.-Y. Liu, F. Liu, N. Yang, X.-B. Zhai, L. Zhang, Y. Yang, B. Li, J. Li, E. Ma, J.-F. Nie, Z.-W. Shan, Large plasticity in magnesium mediated by pyramidal dislocations, *Science* 365 (6448) (2019) 73–75. doi:[10.1126/science.aaw2843](https://doi.org/10.1126/science.aaw2843).
- [106] B. Syed, J. Geng, R. Mishra, K. Kumar,  $[0001]$  compression response at room temperature of single-crystal magnesium, *Scripta Materialia* 67 (7) (2012) 700 – 703. doi:<https://doi.org/10.1016/j.scriptamat.2012.06.036>.
- [107] J. Jain, P. Cizek, K. Hariharan, Transmission electron microscopy investigation on dislocation bands in pure Mg, *Scripta Materialia* 130 (2017) 133 – 137. doi:<https://doi.org/10.1016/j.scriptamat.2016.11.035>.

- [108] S. Ando, H. Tonda, T. Gotoh, Molecular dynamics simulation of  $\langle c + a \rangle$  dislocation core structure in hexagonal-close-packed metals, *Metallurgical and Materials Transactions A* 33 (3) (2002) 823–829. [doi:https://doi.org/10.1007/s11661-002-0151-0](https://doi.org/10.1007/s11661-002-0151-0).
- [109] X.-Z. Tang, Y.-F. Guo, S. Xu, Y.-S. Wang, Atomistic study of pyramidal slips in pure magnesium single crystal under nano-compression, *Philosophical Magazine* 95 (19) (2015) 2013–2025. [doi:https://doi.org/10.1080/14786435.2015.1043970](https://doi.org/10.1080/14786435.2015.1043970).
- [110] J. Morris, K. Ho, K. Chen, G. Rengarajan, M. Yoo, Large-scale atomistic study of core structures and energetics of dislocations in hexagonal close packed metals, *Modelling and Simulation in Materials Science and Engineering* 8 (1) (2000) 25. [doi:https://doi.org/10.1088/0965-0393/8/1/303](https://doi.org/10.1088/0965-0393/8/1/303).
- [111] M. Yoo, J. Morris, K. Ho, S. Agnew, Nonbasal deformation modes of hcp metals and alloys: role of dislocation source and mobility, *Metallurgical and Materials Transactions A* 33 (3) (2002) 813–822. [doi:https://doi.org/10.1007/s11661-002-0150-1](https://doi.org/10.1007/s11661-002-0150-1).
- [112] S. Sandlöbes, M. Friák, J. Neugebauer, D. Raabe, Basal and non-basal dislocation slip in Mg–Y, *Materials Science and Engineering: A* 576 (2013) 61 – 68. [doi:https://doi.org/10.1016/j.msea.2013.03.006](https://doi.org/10.1016/j.msea.2013.03.006).
- [113] B. Li, Q. Zhang, S. Mathaudhu, Basal-pyramidal dislocation lock in deformed magnesium, *Scripta Materialia* 134 (2017) 37 – 41. [doi:https://doi.org/10.1016/j.scriptamat.2017.02.040](https://doi.org/10.1016/j.scriptamat.2017.02.040).
- [114] B. Greenberg, M. Ivanov, O. Antonova, A. Vlasova, The first observation of dislocation blocking in pure metal without external stress, *Crystallography Reports* 57 (4) (2012) 541–548. [doi:https://doi.org/10.1134/S1063774512040062](https://doi.org/10.1134/S1063774512040062).
- [115] J. F. Stohr, J. P. Poirier, Etude en microscopie electronique du glissement pyramidal  $\{11\bar{2}\}\langle 1123 \rangle$  dans le magnesium, *Philosophical Magazine* 25 (6) (1972) 1313–1329. [doi:https://doi.org/10.1080/14786437208223856](https://doi.org/10.1080/14786437208223856).
- [116] J. Geng, M. F. Chisholm, R. Mishra, K. Kumar, The structure of  $\langle c + a \rangle$  type dislocation loops in magnesium, *Philosophical magazine letters* 94 (6) (2014) 377–386. [doi:https://doi.org/10.1080/09500839.2014.916423](https://doi.org/10.1080/09500839.2014.916423).
- [117] P. Price, Nonbasal Glide in Dislocation-Free Cadmium Crystals. ii. The  $(11\bar{2}2)[\bar{1}\bar{1}23]$  System, *Journal of Applied Physics* 32 (9) (1961) 1750–1757. [doi:https://doi.org/10.1063/1.1728430](https://doi.org/10.1063/1.1728430).
- [118] B. C. Wonsiewicz, Plasticity of magnesium crystals., Ph.D. thesis, Massachusetts Institute of Technology (1966).
- [119] A. Chapuis, J. H. Driver, Temperature dependency of slip and twinning in plane strain compressed magnesium single crystals, *Acta Materialia* 59 (5) (2011) 1986 – 1994. [doi:https://doi.org/10.1016/j.actamat.2010.11.064](https://doi.org/10.1016/j.actamat.2010.11.064).

- [120] K. E. Prasad, K. Rajesh, U. Ramamurty, Micropillar and macropillar compression responses of magnesium single crystals oriented for single slip or extension twinning, *Acta Materialia* 65 (2014) 316 – 325. [doi:https://doi.org/10.1016/j.actamat.2013.10.073](https://doi.org/10.1016/j.actamat.2013.10.073).
- [121] C. Mallmann, A. Simar, E. Ferrié, M. Fivel, E. Lilleodden, Influence of Y<sub>2</sub>O<sub>3</sub> nanoparticles on the twinning of single crystalline magnesium, *Scripta Materialia* 138 (2017) 79 – 82. [doi:https://doi.org/10.1016/j.scriptamat.2017.05.016](https://doi.org/10.1016/j.scriptamat.2017.05.016).
- [122] F. Wang, C. D. Barrett, R. J. McCabe, H. E. Kadiri], L. Capolungo, S. R. Agnew, Dislocation induced twin growth and formation of basal stacking faults in {10 $\bar{1}2$ } twins in pure Mg, *Acta Materialia* 165 (2019) 471 – 485. [doi:https://doi.org/10.1016/j.actamat.2018.12.003](https://doi.org/10.1016/j.actamat.2018.12.003).
- [123] P. Partridge, E. Roberts, The formation and behaviour of incoherent twin boundaries in hexagonal metals, *Acta Metallurgica* 12 (11) (1964) 1205 – 1210. [doi:https://doi.org/10.1016/0001-6160\(64\)90103-8](https://doi.org/10.1016/0001-6160(64)90103-8).
- [124] J. Chen, Y. Liu, R. McCabe, J. Wang, C. Tomé, Quantifying elastic strain near coherent twin interface in magnesium with nanometric resolution, *Materials Characterization* 160 (2020) 110082. [doi:https://doi.org/10.1016/j.matchar.2019.110082](https://doi.org/10.1016/j.matchar.2019.110082).
- [125] M. A. Kumar, B. Clausen, L. Capolungo, R. McCabe, W. Liu, J. Tischler, C. Tomé, Deformation twinning and grain partitioning in a hexagonal close-packed magnesium alloy, *Nature communications* 9 (1) (2018) 1–8. [doi:https://doi.org/10.1038/s41467-018-07028-w](https://doi.org/10.1038/s41467-018-07028-w).
- [126] M. A. Kumar, A. Kanjarla, S. Niezgoda, R. Lebensohn, C. Tomé, [Numerical study of the stress state of a deformation twin in magnesium](https://doi.org/10.1016/j.actamat.2014.10.048), *Acta Materialia* 84 (2015) 349–358. [doi:https://doi.org/10.1016/j.actamat.2014.10.048](https://doi.org/10.1016/j.actamat.2014.10.048).  
URL <https://www.sciencedirect.com/science/article/pii/S135964541400812X>
- [127] S. Song, G. Gray III, Transmission electron microscopy examination and analysis of an anomalous stacking fault in hcp metals, *Philosophical Magazine A* 71 (2) (1995) 263–274. [doi:https://doi.org/10.1080/01418619508244355](https://doi.org/10.1080/01418619508244355).
- [128] D. Zhang, B. Zheng, Y. Zhou, S. Mahajan, E. J. Lavernia, Prism stacking faults observed contiguous to a {10 – 12} twin in a Mg–Y alloy, *Scripta Materialia* 76 (2014) 61 – 64. [doi:https://doi.org/10.1016/j.scriptamat.2013.12.015](https://doi.org/10.1016/j.scriptamat.2013.12.015).
- [129] X. Zhang, B. Li, Q. Liu, Non-equilibrium basal stacking faults in hexagonal close-packed metals, *Acta Materialia* 90 (2015) 140 – 150. [doi:https://doi.org/10.1016/j.actamat.2015.02.036](https://doi.org/10.1016/j.actamat.2015.02.036).
- [130] Q. Sun, Q. Zhang, B. Li, X. Zhang, L. Tan, Q. Liu, Non-dislocation-mediated basal stacking faults inside {10 $\bar{1}1$ } twins, *Scripta Materialia* 141 (2017) 85 – 88. [doi:https://doi.org/10.1016/j.scriptamat.2017.07.036](https://doi.org/10.1016/j.scriptamat.2017.07.036).

- [131] Y. Zhu, A. Morton, M. Weyland, J. Nie, Characterization of planar features in Mg–Y–Zn alloys, *Acta Materialia* 58 (2) (2010) 464 – 475. [doi:https://doi.org/10.1016/j.actamat.2009.09.025](https://doi.org/10.1016/j.actamat.2009.09.025).
- [132] H. Yu, Q. Dong, Z. Yao, M. R. Daymond, Stacking faults observed in  $\{10\bar{1}2\}$  extension twins in a compressed high Sn content Zr alloy, *Scripta Materialia* 141 (2017) 72 – 75. [doi:https://doi.org/10.1016/j.scriptamat.2017.07.028](https://doi.org/10.1016/j.scriptamat.2017.07.028).
- [133] Q. Sun, X. Zhang, Y. Shu, L. Tan, Q. Liu, Two types of basal stacking faults within  $\{10\bar{1}2\}$  twin in deformed magnesium alloy, *Materials Letters* 185 (2016) 355 – 358. [doi:https://doi.org/10.1016/j.matlet.2016.09.019](https://doi.org/10.1016/j.matlet.2016.09.019).
- [134] M. Niewczas, Lattice correspondence during twinning in hexagonal close-packed crystals, *Acta Materialia* 58 (17) (2010) 5848 – 5857. [doi:https://doi.org/10.1016/j.actamat.2010.06.059](https://doi.org/10.1016/j.actamat.2010.06.059).
- [135] D. Tomsett, M. Bevis, The formation of stacking faults in  $\{10\bar{1}2\}$  twins in zinc as a result of slip dislocation-deformation twin interactions, *Philosophical Magazine* 19 (159) (1969) 533–537. [doi:https://doi.org/10.1080/14786436908216310](https://doi.org/10.1080/14786436908216310).
- [136] Z. Wu, W. Curtin, The origins of high hardening and low ductility in magnesium, *Nature* 526 (7571) (2015) 62–67. [doi:https://doi.org/10.1038/nature15364](https://doi.org/10.1038/nature15364).
- [137] D. Kupka, N. Huber, E. Lilleodden, A combined experimental-numerical approach for elasto-plastic fracture of individual grain boundaries, *Journal of the Mechanics and Physics of Solids* 64 (2014) 455 – 467. [doi:https://doi.org/10.1016/j.jmps.2013.12.004](https://doi.org/10.1016/j.jmps.2013.12.004).
- [138] B. Clausen, C. Tomé, D. Brown, S. Agnew, Reorientation and stress relaxation due to twinning: Modeling and experimental characterization for Mg, *Acta Materialia* 56 (11) (2008) 2456 – 2468. [doi:https://doi.org/10.1016/j.actamat.2008.01.057](https://doi.org/10.1016/j.actamat.2008.01.057).
- [139] G. Proust, C. N. Tomé, A. Jain, S. R. Agnew, Modeling the effect of twinning and detwinning during strain-path changes of magnesium alloy AZ31, *International Journal of Plasticity* 25 (5) (2009) 861 – 880. [doi:https://doi.org/10.1016/j.ijplas.2008.05.005](https://doi.org/10.1016/j.ijplas.2008.05.005).
- [140] A. Serra, D. Bacon, R. Pond, Twins as barriers to basal slip in hexagonal-close-packed metals, *Metallurgical and materials transactions A* 33 (13) (2002) 809–812. [doi:https://doi.org/10.1007/s11661-002-0149-7](https://doi.org/10.1007/s11661-002-0149-7).
- [141] Z. Basinski, M. Szczerba, M. Niewczas, J. Embury, S. Basinski, The transformation of slip dislocations during twinning of copper-aluminum alloy crystals, *Revue de mEtallurgie* 94 (9) (1997) 1037–1044. [doi:https://doi.org/10.1051/metal/199794091037](https://doi.org/10.1051/metal/199794091037).

- [142] W. Jian, G. Cheng, W. Xu, H. Yuan, M. Tsai, Q. Wang, C. Koch, Y. Zhu, S. Mathaudhu, Ultrastrong Mg alloy via nano-spaced stacking faults, *Materials Research Letters* 1 (2) (2013) 61–66. [doi:https://doi.org/10.1080/21663831.2013.765927](https://doi.org/10.1080/21663831.2013.765927).
- [143] D. Bhattacharyya, E. Cerreta, R. McCabe, M. Niewczas, G. Gray, A. Misra, C. Tomé, Origin of dislocations within tensile and compressive twins in pure textured Zr, *Acta Materialia* 57 (2) (2009) 305 – 315. [doi:https://doi.org/10.1016/j.actamat.2008.09.014](https://doi.org/10.1016/j.actamat.2008.09.014).
- [144] H. El Kadiri, A. Oppedal, A crystal plasticity theory for latent hardening by glide twinning through dislocation transmutation and twin accommodation effects, *Journal of the Mechanics and Physics of Solids* 58 (4) (2010) 613 – 624. [doi:https://doi.org/10.1016/j.jmps.2009.12.004](https://doi.org/10.1016/j.jmps.2009.12.004).
- [145] Q. Ma, H. El Kadiri, A. Oppedal, J. Baird, B. Li, M. Horstemeyer, S. Vogel, Twinning effects in a rod-textured AM30 magnesium alloy, *International Journal of Plasticity* 29 (2012) 60 – 76. [doi:https://doi.org/10.1016/j.ijplas.2011.08.001](https://doi.org/10.1016/j.ijplas.2011.08.001).
- [146] Y. Zhu, S. Xu, J. Nie,  $\{10\bar{1}1\}$  twin boundary structures in a Mg–Gd alloy, *Acta Materialia* 143 (2018) 1 – 12. [doi:https://doi.org/10.1016/j.actamat.2017.09.067](https://doi.org/10.1016/j.actamat.2017.09.067).
- [147] S. K. Das, Y.-B. Kang, T. Ha, I.-H. Jung, Thermodynamic modeling and diffusion kinetic experiments of binary Mg–Gd and Mg–Y systems, *Acta Materialia* 71 (2014) 164 – 175. [doi:https://doi.org/10.1016/j.actamat.2014.02.029](https://doi.org/10.1016/j.actamat.2014.02.029).
- [148] C. He, Z. Li, H. Chen, N. Wilson, J.-F. Nie, Unusual solute segregation phenomenon in coherent twin boundaries, *Nature communications* 12 (1) (2021) 1–8. [doi:https://doi.org/10.1038/s41467-021-21104-8](https://doi.org/10.1038/s41467-021-21104-8).
- [149] X. Chen, L. Xiao, Z. Ding, W. Liu, Y. Zhu, X. Wu, Atomic segregation at twin boundaries in a Mg–Ag alloy, *Scripta Materialia* 178 (2020) 193 – 197. [doi:https://doi.org/10.1016/j.scriptamat.2019.11.025](https://doi.org/10.1016/j.scriptamat.2019.11.025).
- [150] L. Gao, R. Chen, E. Han, Solid solution strengthening behaviors in binary Mg–Y single phase alloys, *Journal of Alloys and Compounds* 472 (1) (2009) 234–240. [doi:https://doi.org/10.1016/j.jallcom.2008.04.049](https://doi.org/10.1016/j.jallcom.2008.04.049).
- [151] J. Wu, S. Si, K. Takagi, T. Li, Y. Mine, K. Takashima, Y. L. Chiu, Study of basal  $\langle a \rangle$  and pyramidal  $\langle c+a \rangle$  slips in Mg–Y alloys using micro-pillar compression, *Philosophical Magazine* 100 (11) (2020) 1454–1475. [doi:https://doi.org/10.1080/14786435.2020.1725250](https://doi.org/10.1080/14786435.2020.1725250).
- [152] J. Shao, Z. Chen, T. Chen, R. Wang, Y. Liu, C. Liu, Texture evolution, deformation mechanism and mechanical properties of the hot rolled Mg–Gd–Y–Zn–Zr alloy containing LPSO phase, *Materials Science and Engineering: A* 731 (2018) 479–486. [doi:https://doi.org/10.1016/j.msea.2018.06.062](https://doi.org/10.1016/j.msea.2018.06.062).

- [153] T. Matsumoto, M. Yamasaki, K. Hagihara, Y. Kawamura, Configuration of dislocations in low-angle kink boundaries formed in a single crystalline long-period stacking ordered Mg-Zn-Y alloy, *Acta Materialia* 151 (2018) 112–124. doi:<https://doi.org/10.1016/j.actamat.2018.03.034>.
- [154] M. Yamasaki, K. Hagihara, S. ichi Inoue, J. P. Hadorn, Y. Kawamura, Crystallographic classification of kink bands in an extruded Mg-Zn-Y alloy using intragranular misorientation axis analysis, *Acta Materialia* 61 (6) (2013) 2065–2076. doi:<https://doi.org/10.1016/j.actamat.2012.12.026>.
- [155] L. Wang, J. Sabisch, E. Lilleodden, Kink formation and concomitant twin nucleation in Mg-Y, *Scripta Materialia* 111 (2016) 68–71. doi:<https://doi.org/10.1016/j.scriptamat.2015.08.016>.
- [156] G. Simmons, Single crystal elastic constants and calculated aggregate properties, Tech. rep., Southern Methodist Univ Dallas Tex (1965).
- [157] J. Wang, N. Stanford, Investigation of precipitate hardening of slip and twinning in Mg5%Zn by micropillar compression, *Acta Materialia* 100 (2015) 53–63. doi:<https://doi.org/10.1016/j.actamat.2015.08.012>.
- [158] A. Imandoust, C. D. Barrett, H. El Kadiri, Effect of rare earth addition on  $\{10\bar{1}2\}$  twinning induced hardening in magnesium, *Materials Science and Engineering: A* 720 (2018) 225–230. doi:<https://doi.org/10.1016/j.msea.2018.02.067>.
- [159] J. Wang, M. Ramajayam, E. Charrault, N. Stanford, Quantification of precipitate hardening of twin nucleation and growth in Mg and Mg-5Zn using micro-pillar compression, *Acta Materialia* 163 (2019) 68–77. doi:<https://doi.org/10.1016/j.actamat.2018.10.009>.
- [160] N. Stanford, R. Marceau, M. Barnett, The effect of high yttrium solute concentration on the twinning behaviour of magnesium alloys, *Acta Materialia* 82 (2015) 447–456. doi:<https://doi.org/10.1016/j.actamat.2014.09.022>.
- [161] W. Hutchinson, M. Barnett, Effective values of critical resolved shear stress for slip in polycrystalline magnesium and other hcp metals, *Scripta Materialia* 63 (7) (2010) 737–740, viewpoint set no. 47 *Magnesium Alloy Science and Technology*. doi:<https://doi.org/10.1016/j.scriptamat.2010.05.047>.

# A Appendix

## A.1 Conversion from Miller-Bravais notation to orthonormal coordinate system

The procedure described below involves conversion of indices of crystallographic planes and directions from hexagonal Miller-Bravais notation to an orthogonal system. The defined hexagonal axes, ( $a_1$ ,  $a_2$ ,  $a_3$  and  $c$ ), with respect to Cartesian axes, ( $e_1$ ,  $e_2$  and  $e_3$ ) are shown in Figure A.1. The  $a_1$  axis is defined to be parallel to the  $e_1$  axis and the  $c$ -axis is defined to be aligned with the  $e_3$  axis. The transformation is performed in two steps. First, a transformation of  $(hkil)$  planes and  $[uvw]$  directions in Miller-Bravais notation to rhombohedral  $(HKL)$  planes and  $[UVW]$  directions in Miller system and then a further transformation to orthonormal  $(H'K'L')$  planes and  $[e_1e_2e_3]$  directions in Cartesian system. The transformation for crystallographic directions and planes are performed using different matrices.

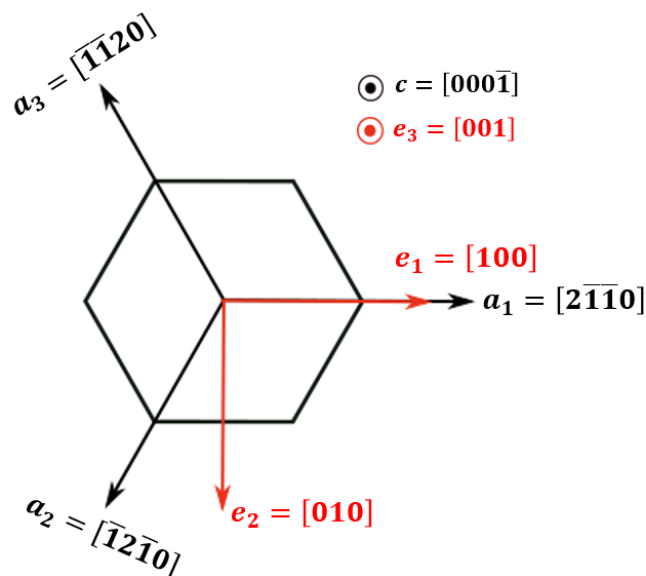


**Figure A.1.** Definition of the hexagonal axis, ( $a_1$ ,  $a_2$ ,  $a_3$  and  $c$ ), with respect to Cartesian orthonormal axes, ( $e_1$ ,  $e_2$  and  $e_3$ ). Viewing direction is along  $c$  or  $e_3$ .

### A.1.1 Transformation of directions (shear)

Conversion of shear directions from  $[uvw]$  Miller-Bravais notation to  $[UVW]$  rhombohedral is performed by:  $U = u-t$ ,  $V = v-t$  and  $W = w$ . Further transformation of the converted  $[UVW]$  notation to Cartesian orthonormal  $[e_1e_2e_3]$  is obtained by the following matrix operation:

$$\begin{bmatrix} e_1 \\ e_2 \\ e_3 \end{bmatrix} = \begin{bmatrix} 1 & -0.5 & 0 \\ 0 & \sqrt{3}/2 & 0 \\ 0 & 0 & c/a \end{bmatrix} \begin{bmatrix} U \\ V \\ W \end{bmatrix} \quad (\text{A.1})$$

Accordingly, Equation (A.1) shows the matrix transformation of shear directions from rhombohedral (Miller) to orthonormal (Cartesian) system, where  $e_1 = U - V/2$ ,  $e_2 = \sqrt{3}V/2$  and  $e_3 = (c/a)W$ .

### A.1.2 Transformation of plane normals

In the hexagonal system, a plane normal is not necessarily the same-indexed direction, as is the case in cubic structures. Exceptions are  $\{0001\}$  and  $\{hki0\}$  planes. The indices of  $(hkil)$  plane normals can be written in the Miller-Bravais format as [52]:  $\left[ h \ k \ i \ \frac{3}{2}\left(\frac{a}{c}\right)^2 l \right]$ . Conversion of the Miller-Bravais notated plane normal direction  $\left( \left[ h \ k \ i \ \frac{3}{2}\left(\frac{a}{c}\right)^2 l \right] \right)$  to rhombohedral (Miller) system,  $[UVW]$ , gives:  $\left[ 2h + k \ h + 2k \ \frac{3}{2}\left(\frac{a}{c}\right)^2 l \right]$ . To find out the indices of plane normal directions in the Cartesian orthonormal system,  $(H'K'L')$ , the transformation matrix presented in Eq. (A.1) is then applied to the Miller-notated plane normal direction as follows, considering the fact that  $h = H$ ,  $k = K$  and  $l = L$ :

$$\begin{bmatrix} 1 & -0.5 & 0 \\ 0 & \sqrt{3}/2 & 0 \\ 0 & 0 & c/a \end{bmatrix} \begin{bmatrix} 2H + K \\ H + 2K \\ \frac{3}{2}\left(\frac{a}{c}\right)^2 L \end{bmatrix} = \begin{bmatrix} H' \\ K' \\ L' \end{bmatrix} \quad (\text{A.2})$$

Further simplification results the Eq. (A.3), where the matrix transformation of plane normals from the Miller to the orthonormal coordinate system is given:

$$\begin{bmatrix} H' \\ K' \\ L' \end{bmatrix} = \begin{bmatrix} 3/2 & 0 & 0 \\ \sqrt{3}/2 & \sqrt{3} & 0 \\ 0 & 0 & 3/2(c/a) \end{bmatrix} \begin{bmatrix} H \\ K \\ L \end{bmatrix} \quad (\text{A.3})$$

To sum up, for transformation of the  $(hkil)[uvw]$  plane-direction Miller-Bravais notation system to the  $(H'K'L')[e_1e_2e_3]$  plane-direction orthonormal Cartesian system, an intermediate conversion of planes and directions to  $(HKL)[UVW]$  rhombohedral Miller notation is necessary. After this conversion, shear directions and plane normals can be transformed to

orthonormal system using expressions Eq. (A.1) and Eq. (A.3), respectively.

## A.2 Schmid factor for different slip and twinning systems

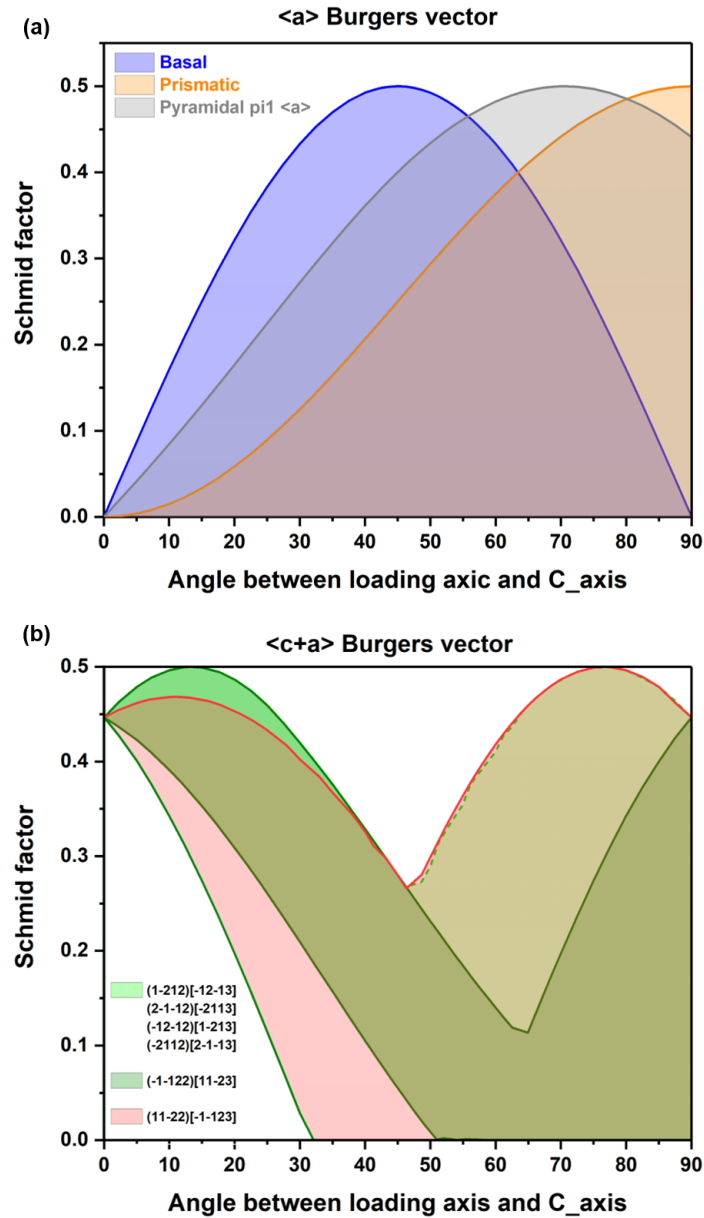


**Figure A.2.** Variation of Schmid factor with the angle between the crystal  $c$ -axis and the loading axis for different slip systems of (a) basal, prismatic and pyramidal  $\pi_1$  with  $\langle a \rangle$ -type Burgers vector, and (b) pyramidal  $\pi_2$  with  $\langle c + a \rangle$ -type Burgers vector.

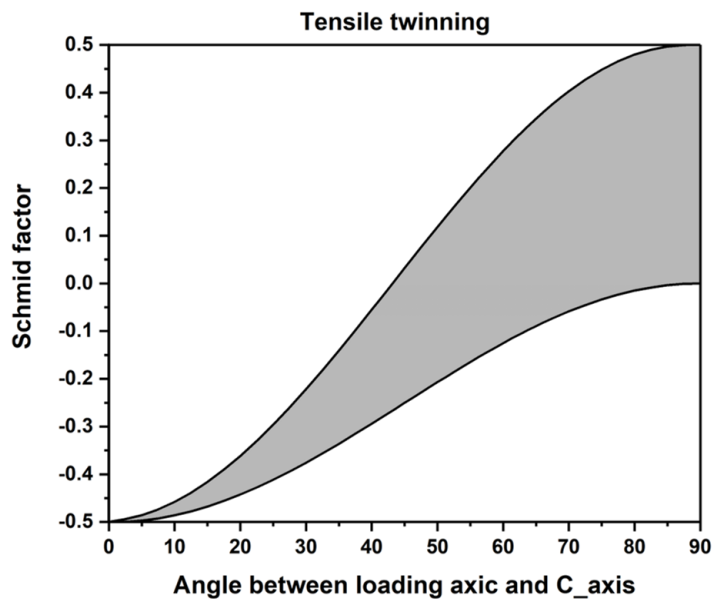


**Figure A.3.** Variation of Schmid factor with the angle between the crystal  $c$ -axis and the loading axis for  $\{10\bar{1}2\}$  tensile twinning activating under compression perpendicular to the  $c$ -axis.

## B Curriculum vitae

<b>Sure name</b>	Maghsoudi
<b>First name</b>	Mohammadhadi
<b>Date of birth</b>	30.06.1988
<b>Place of birth</b>	Tehran, Iran
<b>09.1995 - 09.2000</b>	Primary School in Tehran
<b>09.2000 - 09.2003</b>	Middle School in Tehran
<b>09.2003 - 09.2007</b>	High School in Tehran
<b>09.2007 - 09.2011</b>	Bachelor Degree (B.Sc.) in Materials Science and Engineering, Sharif University of Technology, Tehran, Iran
<b>09.2011 - 09.2014</b>	Master Degree (M.Sc.) in Materials Engineering-Metal Forming, University of Tehran, Tehran, Iran
<b>10.2014 - 02.2016</b>	Research Assistant, University of Tehran, Tehran, Iran
<b>03.2016 - 05.2016</b>	Sales Engineer, Shahid Bahonar Copper Ind. Co, Tehran, Iran
<b>06.2016 - 11.2016</b>	Teaching Assistant, Northern Arizona University, Arizona, United States
<b>12.2016 - Current</b>	PhD Student, Helmholtz-Zentrum Geesthacht, Institute of Materials Mechanics, Geesthacht, Germany